THE THERMAL SUNYAEV – ZEL'DOVICH EFFECT AS A PROBE OF CLUSTER PHYSICS AND COSMOLOGY

Ryan Warne

University of KwaZulu-Natal

UNIVERSITY OF KWAZULU-NATAL

THE THERMAL SUNYAEV – ZEL'DOVICH EFFECT AS A PROBE OF CLUSTER PHYSICS AND COSMOLOGY

by

Ryan Russell Warne

Submitted in fulfilment of the
academic requirements for the degree of
Doctor of Philosophy (Science),
in the
School of Mathematical Sciences,
University of KwaZulu-Natal

Westville
March, 2010

As the candidate's supervisor I have approved this dissertation for submission.

Signed: ..... Name: ..... Date: .....

ABSTRACT

The universe is a complex environment playing host to a plethora of macroscopic and microscopic processes. Understanding the interplay and evolution of such processes will help to shed light on the properties and evolution of the universe. The juxtaposition is that in order to study small scale effects one needs to observe large scale structure as the latter objects trace the history of our universe. Galaxy groups and clusters are the largest known objects in the universe and thus provide a means to probe the evolution of structure formation in the universe as well as the underlying cosmology. In this thesis we investigate how clusters observed through the Sunyaev-Zel'dovich (SZ) effect can be used to constrain cosmological models. In addition, we present the first results of the Atacama Cosmology Telescope (ACT), a mm-wave telescope measuring the small-scale microwave background anisotropy, and conclude with preliminary SZ cluster detection performed on the latest ACT sky maps.

In the first part of this thesis we investigate the ability of high resolution cosmic microwave background (CMB) experiments to detect hot gas in the outer regions of nearby group halos. We construct two hot gas models for the halos; a simpler adiabatic formalism with the gas described by a polytropic equation of state, and a more general gas description which incorporates feedback effects in line with constraints from X-ray observations. We calculate the thermal Sunyaev-Zel'dovich (tSZ) signal in these halos and compare it to the sensitivities of upcoming and current tSZ survey experiments such as ACT, PLANCK and the South Pole Telescope (SPT). Through the application of a multi-frequency Wiener filter, we derive mass and redshift based tSZ detectability limits for the various experiments, incorporating effects of galactic and extragalactic foregrounds as well as the CMB. In this study we find that galaxy group halos with virial masses below $10^{14} M_{\odot}$ can be detected at $z \lesssim 0.05$ with the mass limit dropping to $3 - 4 \times 10^{13} M_{\odot}$ at $z \lesssim 0.01$. Probing such halos with the tSZ effect allows one to map the hot gas in the outer regions, providing a means to constrain gas processes, such as feedback, as well as the distribution of baryons in the local universe.

In the fourth chapter, we extend this analysis and determine the ability of ACT to constrain galactic feedback and star formation in clusters and groups using the tSZ effect. We present a new microwave deblender, which provides a means of extracting accurate halo fluxes and radial profiles from maps of the tSZ effect. Considering various surveys that could be performed by ACT, we use multi-frequency filtering on simulated sky maps to predict how well such surveys will constrain gas properties using a Fisher matrix analysis. We find that the current ACT survey will be unable to constrain any gas parameters. However, if ACT were to survey a smaller area then we will be able to constrain feedback. Furthermore, with greater sensitivity, we will be able to place interesting constraints on the gas feedback, and baryon and stellar fractions.

The fifth chapter in this thesis concerns itself with the first results of the Atacama Cosmology Telescope Project. In this section we discuss the map-making method as well as telescope beam characterisation, an understanding of which is important in any subsequent map analyses. In addition, we present maps of eight clusters observed at 148 GHz via the SZ effect, and provide flux and signal to noise estimates of the clusters.

In the final chapter we present a preliminary analysis of the latest 148 GHz ACT maps from the 2008 observing season. We study the sky maps using single frequency wiener filtering, allowing for CMB, dust and correlated noise contamination. To substantiate our results, we compare the number counts, recovered fluxes and sample purity from simulated sky maps. The compounding effects of CMB and correlated noise result in high contamination levels below a signal to noise ratio of 6, however our investigation shows that above 8σ our cluster sample is $\approx 80\%$ pure. A cluster list containing 44 detections, of which 8 are previously known, is also presented, along with a Table listing the candidate cluster positions and fluxes. The candidate cluster catalogue will be used for follow-up studies using optical and X-ray observations.

ACKNOWLEDGMENTS

First and foremost I would like to thank my supervisor Prof. Kavilan Moodley for his guidance, hard work and motivation throughout my PhD. Moreover, I am eternally grateful for the confidence he instilled in me, nurturing me from a freshly graduated honours student, to a fully fledged PhD, ready to accept any challenge presented before me. I would also like to thank Dr. Catherine Cress and Dr. Matt Hilton, who were always on hand during the rough times that are part of any PhD journey.

Throughout my PhD, I have been lucky enough to travel abroad many times, particularly as part of the Atacama Cosmology Telescope (ACT) project. Being involved in such a project has not only allowed me to visit wonderful countries and institutions, but has brought forth many new relationships - both personal and academic. My time in Princeton would not have been as enjoyable or productive without the following people; Tobias Marriage, Adam Hincks, Robert Lupton, James Gunn and Mindy Lipman who helped me in various ways during many of visits. In particular David Spergel and Lyman Page, who always made me feel at home and totally welcome. Two important colleagues who were at Princeton but have since moved to Harvard are Hy Trac and Doug Finkbeiner. Hy Trac has been a fellow collaborator on three projects and a person always willing to answer my endless questions. Doug was the first person I worked with during my inaugural visit to Princeton. He not only guided me through the challenging projects, but also introduced me to the game of 'four-square', for which I am very grateful!

My PhD also took me to the shores of Spain where I collaborated with Jose Marie Diego through the South Africa-Spain bilateral collaboration. During these visits, Chema - as he is known to friends, served as a mentor and introduced me to the finer living that is the Spanish custom.

My PhD would not have been possible without the financial support of the National Research Foundation and the Square Kilometre Array *Human Capital Development* fund. Within the SKA program, I had the opportunity of meeting leading researchers from around globe, striking up projects and feeding off their wealth of knowledge.

I would like to extend thanks to the University of KwaZulu-Natal (UKZN) for giving me the opportunity to study for a PhD. UKZN has been home for nearly 10 years, and I will cherish many fond memories from it. These include frequent visits to the Drakensburg for collaboration and reflection, organised by Sunil Maharaj, and the delicious bunny chows that became my stable diet near the end of my thesis.

This thesis would not have been possible without my family, friends and adorable dog Kane (fondly known as 'my son'). My mom and dad have been a constant source of inspiration, always pushing me to give of my best and never accept second place. To my friends, I owe many thanks, particularly for putting up with my attitude when projects were not going as planned. To my family and friends, 'thank-you' for your love and understanding and always believing in me.

Last but not least I would like to thank Nicolette Caister. To put in words her unwavering support and love during this journey, is not possible. As I look back over my PhD and her contribution to it, the one thing that stands out is her ability to ask the right questions-when to me the road forward was filled with obscurity. Her academic contribution to my thesis is minuscule however, compared to the emotional support she provided throughout this endeavour. She was my constant companion and the single person always there to bring me that hot cup of tea in the middle of the night.

PREFACE

The study described in this thesis was carried out in the School of Mathematical Sciences, University of KwaZulu-Natal, and the Astrophysics Department at Princeton University, United States of America, during the period May 2006 to March 2010. This dissertation was completed under the supervision of Prof. K. Moodley.

This study represents original work by the author and has not been submitted in any form for any degree or diploma to any another tertiary institution. Where use was made of the work of others it has been duly acknowledged in the text.

DECLARATION OF NON-PLAGIARISM

I, ... declare that

1. The research reported in this thesis, except where otherwise indicated, is my original research.

2. This thesis has not been submitted for any degree or examination at any other university.

3. This thesis does not contain other persons' data, pictures, graphs or other information, unless specifically acknowledged as being sourced from other persons.

4. This thesis does not contain other persons' writing, unless specifically acknowledged as being sourced from other researchers. Where other written sources have been quoted, then:

    - Their words have been re-written but the general information attributed to them has been referenced.
    - Where their exact words have been used, then their writing has been placed in italics and inside quotation marks, and referenced.

5. This thesis does not contain text, graphics or tables copied and pasted from the Internet, unless specifically acknowledged, and the source being detailed in the thesis and in the References sections.

Signed in Westville, KwaZulu-Natal: ..... Date: .....

DECLARATION OF PUBLICATIONS

Details of contribution to publications that form part and/or include research presented in this thesis:

Chapter 3

Detection of Hot Gas in Galaxy Groups via the Thermal Sunyaev-Zel'dovich Effect

Moodley, K., Warne, R., Goheer, N., & Trac, H. 2009, Astrophys. J., 697, 1392

For this paper I contributed to the model development, signal detection analysis and wrote up the results. The form of the publication has been altered slightly to adhere to the formatting requirements of this thesis.

Chapter 4

Constraining Feedback and Star Formation in Galaxy Clusters with Measurements of the Thermal Sunyaev-Zel'dovich Effect

Warne, R., Moodley, K., Crichton, D., & Trac, H. 2010, in prep

For this paper I undertook the analysis and wrote up the results under the supervision of Dr. K. Moodley.

Chapter 5

The Atacama Cosmology Telescope (ACT): Beam Profiles and First SZ Cluster Maps

Hincks, A. D., et al. 2009, arXiv:0907.0461

For this paper I contributed to the cluster detection and analysis. The form of the publication has been altered slightly to adhere to the formatting requirements of this thesis.

Contents

List of Figures

List of Tables

CHAPTER 1

Introduction

Cosmology is the study of our universe, bringing forth ideas and explanations about its birth, evolution and ultimate fate. On smaller scales, it provides an observationally motivated framework describing the constituents of the universe and their complex interconnected dynamics. The last few decades have been the golden age for cosmology. High quality data coupled with instruments capable of looking back to the very beginnings of the cosmos, suggest that we live in a universe that is close to homogeneous and isotropic on large scales (see for example Tago et al., 2006; Hinshaw et al., 2007). Furthermore, observations of Type Ia supernovae suggest that the universe is dominated by unknown forms of energy and expanding at an accelerating rate (Riess et al., 1998; Perlmutter et al., 1999; Riess et al., 2004, 2007; Wood-Vasey et al., 2007; Kowalski et al., 2008; Kessler et al., 2009; Hicken et al., 2009; Biswas and Wandelt, 2009).

Investigations indicate that during the earliest epoch, about 14 billion years ago, the universe underwent a phase of rapid expansion originating from a singularity known as the Big Bang. During this epoch, the universe was permeated with radiation and baryonic matter as well as two more mysterious constituents, namely: cold dark matter and dark energy. Many theories have sought to explain this phenomenon. To date, perhaps the most widely accepted theory is that of inflation (Guth, 1981) - which offers a possible explanation of how perturbations were

seeded in the early universe, providing building blocks for future structure formation. Over the last decade, advances in computing power and instrumentation have allowed stringent tests of this hot Big Bang model, finding strong evidence in its support. One prediction of this model is the existence of a matter dominated epoch. The transition from radiation to matter domination defines the origin of structure formation and is described by a surface in time known as matter-radiation equality. During matter domination, primordial perturbations in the Cosmic Microwave Background (CMB) grew through gravitational attraction - a process no longer impeded by the hot plasma that dominated the early universe. Growing perturbations gave rise to hierarchical structure formation, and after billions of years yielded the stars, galaxies and clusters we observe today.

The visible universe however, comprises only a very small fraction of the matter content in the cosmos. Within the Big Bang theory there is the allowance for a non-luminous form of dark matter which amplifies perturbations in the CMB to the large scale structures existing today. One of the first hints of the existence of this component arose from observations of clusters by Zwicky in 1933 (Zwicky, 1933). He noticed that, given the large line-of-sight radial velocities of cluster galaxies and the deficit of galactic mass necessary for gravitational stability, clusters would break apart unless there existed another form of 'invisible' matter. These results are supported by many more recent studies: gravitational lensing (see for example Mellier, 1999; Bartelmann and Schneider, 2001; Treu and Koopmans, 2004; Adelman-McCarthy et al., 2006); stellar dynamics in clusters (Treu and Koopmans, 2004; Koopmans et al., 2006); distribution of intracluster gas (Sarazin, 1986), as well as galaxy rotation curves (*e.g.* Rubin et al., 1980).

A desire to understand the state of the universe, in particular its 'dark side', has led to a prolific increase in observations. Supernovae experiments, coupled with observations of large scale structure distribution (Percival et al., 2001; Tegmark et al., 2006), and analyses of CMB anisotropies (Spergel et al., 2007; Hinshaw et al., 2009; Komatsu et al., 2009) have led to the current 'concordance' model. This model describes the universe as geometrically flat and expanding, comprising 4% visible baryonic matter, 23% dark matter and 73% dark energy. In

spite of estimates of the contribution of the dark component to the total energy and mass of the universe, the actual mechanisms governing it and particles it comprises, are yet to be understood.

Since the early work of Zwicky, galaxy clusters have been used as probes of cosmology and astrophysical laboratories. Galaxy clusters typically have masses between 10^{14} and 10^{15} solar masses and thus represent the largest virialised objects in the universe. Given their large masses, clusters represent the final form of the collapse of density perturbations with comoving scales measuring ~ 10 Mpc. In light of this, clusters mark the transition between two distinct dynamical epochs.

On scales above ~ 10 Mpc, structure formation is driven mainly by gravitational forces, and thus the evolution feels the imprint of cosmological initial conditions. In the cold dark matter (CDM) paradigm, structure formation proceeds hierarchically (Davis et al., 1985), in that the first objects to form are low mass structures, such as dwarf galaxies followed by progressively larger structures such as Milky Way type galaxies, and finally galaxy groups and clusters. Thus the process of structure formation and its dynamics depends sensitively on cosmological initial conditions. Moreover, if the universe has a high matter density, expansion is decelerated and structures can grow against the Hubble flow. In such a scenario, structure formation is continuous and clusters would have formed very recently. On the other hand, if the universe comprised a low matter density and a cosmological constant (a form of dark energy), expansion would be rapid and structures would have to form early, otherwise they would not be able to collapse against the expansion. Therefore, the abundance or number density of clusters is a proxy for the underlying cosmology and can be used to constrain various parameters, such as the average of the matter density to the critical density, Ω_M, the normalisation of the primordial density perturbation power spectrum, σ_8, and the dark energy equation of state, w (see for example Holder et al., 2001; Haiman et al., 2001; Rosati et al., 2002; Pierpaoli et al., 2003; Battye and Weller, 2003; Voit, 2005; Marian and Bernstein, 2006; Frieman et al., 2008; Sahlén et al., 2009).

Below scales of ~ 1 Mpc, baryon dynamics play an important role in addition to gravitational forces. During cluster formation, intergalactic gas is initially heated to X-ray emitting temperatures, typically $10^7 - 10^8$ K, by shocks and adiabatic compression, eventually settling

into hydrostatic equilibrium within cluster potential wells. Once the intracluster gas is dense enough, it cools to form stars and can accrete onto supermassive black holes, which are thought to be at the centres of all reasonably massive galaxies. Star formation and black hole accretion can result in feedback processes through supernovae or active galactic nuclei. Such events inject large amounts of heat into the intracluster medium (ICM), spreading heavy elements throughout the cluster.

Recent studies into the baryon content of our universe (Fukugita et al., 1998; Fukugita and Peebles, 2004) suggest that there is a deficit of baryons in the local universe. At high redshift, studies of the CMB anisotropy (Dunkley et al., 2009), light element abundances (Steigman, 2007) and the Lyα forest (Kirkman et al., 2003) yield a consistent baryon fraction of $\Omega_b \approx 0.044$. At low redshifts however, almost thirty to forty percent of the baryons are 'missing'. The current understanding is that these 'dark' baryons lie within the hot gas of galaxy groups and far outskirts of clusters. Studies by Sun et al. (2009) have measured the baryon content of galaxy groups out to a radius of r_{500}, and claim to have detected approximately half of these dark baryons. This suggests that roughly fifteen to twenty percent is still missing and possibly located in rarefied gas regions at the edges of groups and clusters (see for example Tripp et al., 2000; Sembach et al., 2003; Tumlinson et al., 2005, for studies of this missing component).

An early test for the presence of this hot thermal plasma was first prescribed by Sunyaev and Zel'dovich in the early 1970s (Sunyaev and Zeldovich, 1970, 1972). They suggested that electrons within the intracluster medium would have a unique effect on CMB photons passing through the cluster. Free-streaming primordial photons would be inverse Compton scattered to higher energies by the hot electrons, creating a frequency dependent signature for the hot gas. Since the total photon number is conserved in such a process, microwave observations of the sky toward clusters would see the sky dimmer at lower frequencies and brighter at higher frequencies. Observations of the hot gas within clusters and groups using the Sunyaev-Zel'dovich Effect (SZE) has many advantages over other techniques, such as those employing X-rays. X-ray studies depend strongly on luminosity and gas density. These factors mean that X-ray observations are redshift limited and are not able to probe the outskirts of galaxy groups and clusters

where the gas is more rarefied. In contrast, the SZE is redshift independent and has a weaker dependence on gas density, making it an efficient tool for detecting hot gas and the baryons that lie within it. In light of the above, observations employing the SZE yield a mass selected sample, in that one detects all clusters in the universe above a particular mass threshold. This threshold depends on factors such as telescope characteristics, galactic foregrounds as well as atmospheric contamination (in the case of ground based experiments).

Since the early pioneering work of Sunyaev and Zel'dovich, the SZE has been observed with many telescopes, typically of two forms; single dish and interferometric. Single dish observations provided the first detection of this phenomenon at centimetre wavelengths. However, these early measurements were plagued by systematic errors and led to inconsistent results. Perhaps the first reliable SZE results were produced by Birkinshaw using the Owens Valley Radio Observatory (OVRO) 40 m telescope (Birkinshaw et al., 1978a,b, 1991). Following this work, the OVRO 5 m telescope at 32 GHz measured the SZE in several intermediate redshift clusters (Herbig et al., 1995; Myers et al., 1997; Mason et al., 2001). The introduction of sensitive bolometer detectors over the last decade has produced a plethora of SZE detections. The first telescopes to use this technology for measurements of the SZE were the Swedish-ESO Submillimeter (SEST) and Institut de Radioastronomie Millimétrique (IRAM) telescopes, which detected several clusters at 140 GHz (Andreani et al., 1996a, 1999; Desert et al., 1998; Pointecouteau et al., 1999, 2001). In addition, the Nobeyama 45 m telescope has been used at 21 GHz, 43 GHz and 150 GHz to produce maps of the SZE effect in several clusters at high signal-to-noise (Komatsu et al., 1999, 2001). Sky mapping, through drift scanning techniques[1], has been employed using the Sunyaev-Zel'dovich Infrared Experiment (SuZIE) and has produced strip maps of the SZE in a number of clusters. This data, combined with complementary X-ray information, allowed constraints to be placed on the Hubble constant (Holzapfel et al., 1997; Mauskopf et al., 2000).

In the last few years, new generation single dish telescopes aimed at probing the SZE have come on-line. These include, the Atacama Cosmology Telescope (ACT; Kosowsky, 2006), the

[1]Drift scanning is an observational technique whereby the telescope remains in a fixed position, while the rotation of the Earth moves the beam across the sky.

South Pole Telescope (SPT; Ruhl et al., 2004), the Atacama Path-Finder Experiment (APEX-SZ; Dobbs et al., 2006) and the prototype-One Centimeter Receiver Array (OCRA-p; Lancaster et al., 2007). In addition PLANCK, the latest CMB satellite mission, has been successfully launched and is currently observing the entire sky (The Planck Collaboration, 2006).

Interferometry provides a stable method to measure the SZE, because these instruments perform differential sky measurements over well defined spatial frequencies. Moreover, the use of different baseline lengths allows one to remove contamination from radio point sources, which plague single dish measurements. The first detection of the SZE using an interferometer was made with the Ryle Telescope (RT), which is located in Cambridge, England (Jones et al., 1993). Since then, many new interferometers have initiated observations of the CMB such as; the Cosmic Background Imager (CBI; Padin et al., 2002), the Sunyaev-Zel'dovich Array (SZA; Muchovej et al., 2007) and the Array for Microwave Background Anisotropy (AMiBA; Ho et al., 2009), revealing structures at arcminute resolutions. Recently, multi-wavelength investigations into the properties of 38 clusters, using SZ data from OVRO/BIMA (LaRoque et al., 2006a) and X-ray data from *Chandra X-ray Observatory*, have shown good agreement with expectations from a self-similar model for cluster formation (Bonamente et al., 2008). In addition, measurements of cluster mass and integrated SZ fluxes (Compton Y parameter) performed without X-ray data, were found to correlate well with those made from joint SZ and X-ray observations.

Although single dish and interferometric SZ observations probe the same effect, their observational capabilities and expertise are different. Interferometry involves high resolution targeted imaging while single dish experiments, such as ACT and SPT, have faster mapping speeds, and are thus capable of performing blind surveys.

With the large amounts of data available from these experiments, one will have a secure platform to study the macroscopic and microscopic picture of galaxy groups and clusters. Catalogues produced by these telescopes will allow one to place constraints on cosmological parameters and provide insight into the state of our universe. Moreover, Battye and Weller (2003) suggest that upcoming SZ surveys will be able to constrain σ_8 and Ω_m to within an error of 10% at 1σ. On smaller scales, the high signal to noise maps of clusters and groups will permit studies of the hot

gas in these structures, thus placing constraints on the dark baryon distribution and density as well as shedding light on the complex feedback processes taking place within these objects.

The work presented in this thesis extends the study of galaxy clusters and groups by using the SZE as a probe of the hot gas present in such structures. In chapter 2 we present a theoretical background to the thesis detailing the current understanding of the universe, as well as the properties and observational tools used in the detection and study of galaxy groups and clusters. In chapter 3 we explore the dynamics of the hot gas in galaxy groups. In addition, we examine the detectability of different gas models by current and upcoming CMB experiments using the SZE. We also discuss how the the detection of this gas will allow one to constrain various gas properties, such as entropy injection and baryon fraction.

In chapter 4 we introduce a novel method of microwave deblending and use realistic simulations of the SZE to place constraints on hot gas properties. We find that deblending is able to obtain accurate flux measurements over a large mass range, by mitigating effects of contamination arising from overlapping objects. In addition, we observe that deblending allows one to accurately reconstruct SZ profiles for groups and clusters out to large radii. Furthermore, we provide constraints on gas properties including, feedback energy, baryon fraction and star formation expected from various ACT cluster surveys. Moreover, assuming different noise specifications for surveys with ACT, we forecast constraints on halo gas parameters including feedback, stellar and baryon fractions using multi-frequency filtering and Fisher matrix analyses.

In chapter 5 we present the first results from the ACT project. We describe the beam properties of the telescope and present detections and subsequent analyses of eight previously detected clusters. In chapter 6, we present filtering analyses of the latest ACT survey maps and compare them to simulations. We introduce a two-dimensional Wiener weight function, designed to accommodate for spatial noise variations, and apply it to real and simulated ACT data quoting completeness, sample purity as well as cluster number counts. In addition we present a list of cluster candidates, containing 44 detections of which 36 are new candidates. Finally in chapter 7 we summarise our results and present a discussion of planned extensions to the various projects.

CHAPTER 2

Cosmological Framework

The study of large scale structure and its applications to cosmology requires an understanding of general cosmological principles and theories. In this chapter we discuss the properties of the cosmological model of the universe, including theories of its origins and dynamics. In addition, we explain the evolution and characteristics of large scale structure as well as observations aimed at understanding cosmology through the study of such phenomena.

2.1 The Standard Model of Cosmology

The standard model can be broadly split into two distinct parts: the properties and dynamics of the homogeneous background and, the origin and subsequent evolution of perturbations. These fluctuations give rise to large scale structure and the observed distribution of matter in the universe. The present edifice of the standard cosmological model is robust, supported by the following 'pillars':

- Homogeneous and isotropic cosmology, expanding from a hot initial phase known as the Big Bang.

- The basic components of the universe take the form of baryons, photons, neutrinos, dark matter and dark energy.
- The spatial sections of space-time are geometrically flat or Euclidean.
- Primordial perturbations were generated in an inflationary epoch and imprinted on the anisotropy of the CMB.
- The time evolution of density perturbations through gravitational processes has produced the large scale structure in the universe.

In order to understand the attributes of the model, we will frame it within the Friedmann - Robertson - Walker formalism.

Friedman – Robertson – Walker Cosmology: The Metric

A homogeneous, isotropic and expanding universe comprising a four-dimensional space-time can be described by the symmetric Friedman – Robertson – Walker metric. This relation can be written in terms of a line element ds^2

$$ds^2 = g_{\alpha\beta}\, dx^\alpha dx^\beta = dt^2 - a^2(t)\left(\frac{dr^2}{1-kr^2} + r^2 d\theta^2 + r^2 \sin^2\theta\, d\phi^2\right), \tag{2.1.1}$$

where $g_{\alpha\beta}$ is the metric tensor and dx^α is this difference between two events in space-time within dimension α. The Greek indices in the above relation run from 0 to 3, symbolising the four dimensions of the space-time. The coordinates (t, r, θ, ϕ) represent the comoving coordinates of a fundamental observer[1], while the constant k is a measure of the local universe geometry. Moreover, $k = 0$ describes a flat geometry, while $k > 0$ and $k < 0$ corresponds to a spherical (closed) and hyperbolic (open) universe respectively. The comoving coordinate r is related to the proper length measure, x, by $x(t) = a(t)r$, where $a(t)$ is the scale factor of the universe. Units have been chosen such that the speed of light is unity. The expansion of the universe distorts observable quantities. For example, photons emitted with a wavelength λ in a universe with a

[1] A fundamental observer is a frame in which the universe appears homogeneous and isotropic.

scale factor given by $a(t)$ will be measured with wavelength λ_0 today (signified by subscript 0), where $\lambda_0/\lambda = a_0/a(t)$. Since $\lambda_0 > \lambda$ in an expanding universe, the photons are 'redshifted', with redshift defined as $z = (\lambda_0/\lambda) - 1$.

Friedman – Robertson – Walker Cosmology: The Friedmann Equation

The time evolution of the scale factor governs the behaviour of a homogeneous and isotropic universe. The link between the dynamics of the universe and its contents is provided by Einstein's general theory of relativity. The Einstein Field equation relates the constituents of the universe, given by the stress-energy tensor $T_{\alpha\beta}$, to the geometry described by the metric g. In addition, it portrays how the presence of matter curves space-time. This equation is expressed by

$$G_{\alpha\beta} = 8\pi G T_{\alpha\beta} + \Lambda g_{\alpha\beta}, \tag{2.1.2}$$

where $G_{\alpha\beta}$ is the Einstein tensor, G is the Gravitational constant and Λ is the cosmological constant. If one assumes a perfect fluid source of stress-energy, then upon solving the time-time component of Einstein's Field equation one arrives at the time evolution equation for the scale factor (*i.e.* the Friedmann equation)

$$\left(\frac{\dot{a}}{a}\right)^2 = \frac{8\pi G\rho}{3} - \frac{k}{a^2} + \frac{\Lambda}{3}, \tag{2.1.3}$$

where $\rho(t)$ is the energy density of the fluid. Similarly from the space-space component we can obtain the acceleration equation

$$\frac{\ddot{a}}{a} = \frac{-4\pi G}{3}(\rho + 3p) + \frac{\Lambda}{3}, \tag{2.1.4}$$

where $p(t)$ is the pressure. Finally from energy-momentum conservation we obtain the continuity relation

$$\dot{\rho} + \frac{3\dot{a}}{a}(\rho + p) = 0. \tag{2.1.5}$$

In essence, the dynamics of the scale factor depend on the properties of the perfect fluid, governed in part by its equation of state w. This parameter links the pressure of the fluid to its density by $p = w\rho$ and is constant for a perfect fluid.

The Makeup of the Universe

The Friedmann equation represented in Eq. (2.1.3) can be simplified to a form which reflects the contents of the universe. Using the Hubble parameter, defined as $H = \dot{a}/a$ and the critical density $\rho_c = 3H^2/(8\pi G)$ the equation becomes

$$\begin{aligned} 1 &= \frac{\rho_m}{\rho_c} + \frac{\rho_R}{\rho_c} + \frac{\rho_k}{\rho_c} + \frac{\rho_\Lambda}{\rho_c} \\ &= \Omega_m + \Omega_R + \Omega_K + \Omega_\Lambda, \end{aligned} \tag{2.1.6}$$

where $\rho_k = -3k/(8\pi G a^2)$ and $\rho_\Lambda = \Lambda/(8\pi G)$. The key components of our universe are thus, pressureless gravitating matter Ω_m, relativistic matter (*e.g.* radiation) Ω_R and cosmological vacuum energy (widely known as dark energy) Ω_Λ. The deviation of the total energy density from unity gives rise to curvature and consequently can be represented by a curvature energy density Ω_K. The pressureless matter density minimally comprises three components: baryonic matter, cold dark matter and possibly massive neutrinos, the first mentioned being responsible for all visible matter within the universe. The relativistic component is comprised almost entirely of the CMB and relic neutrinos of the Big Bang. The dark energy density is more difficult to explain as it can take the form of 'exotic', non-clustering matter with a variable equation of state or in the simplest case a cosmological constant with a constant equation of state. Regardless of the flavour of dark energy, it has the effect of accelerating the expansion of the universe, a theory that is corroborated by type 1a supernovae observations (Riess et al., 1998; Perlmutter et al., 1999; Kowalski et al., 2008). Present day values for these parameters have been provided by the Wilkinson Microwave Anisotropy Probe (WMAP; Komatsu et al., 2009) as follows: $\Omega_b = 0.0456 \pm 0.0015$, $\Omega_{cdm} = 0.228 \pm 0.013$ and $\Omega_\Lambda = 0.726 \pm 0.015$.

The state of the universe can be described in a 'Cosmic Triangle' (Bahcall et al., 1999, and references therein) shown in Fig. 2.1. The axes demonstrate the fundamental questions regarding the background cosmology, namely; what is the geometry of our universe, is our universe expanding, and how much does non-relativistic matter contribute to the energy density of the universe? The triangle on the right overlays constraints on the various cosmological models from observations of type 1a supernovae, large-scale structure (LSS) and the CMB. Current ob-

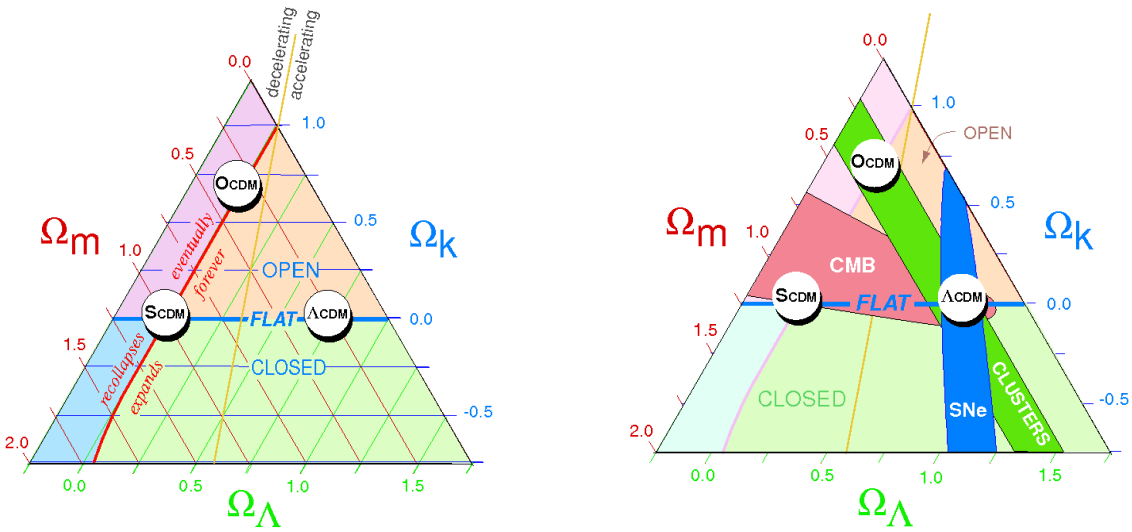

Figure 2.1: This schematic termed the Cosmic Triangle, represents the chief parameters governing the composition of our universe namely, Ω_m, Ω_Λ and Ω_K. Each point within the triangle satisfies the addition rule $\Omega_m + \Omega_\Lambda + \Omega_K = 1$. The blue horizontal line designates a flat universe ($\Omega_m + \Omega_\Lambda = 1$) and serves as the threshold between an open and closed universe. The red line ($\Lambda \approx 0$) on the left triangle separates an ever expanding universe ($\Lambda > 0$) from one that will inevitably collapse ($\Lambda < 0$). The yellow, almost vertical line, differentiates a universe that is accelerating from one that is decelerating. The position of the three key models is highlighted in the triangles: (flat) standard cold dark matter (SCDM); flat (ΛCDM); and open CDM (OCDM). The coloured bands displayed in the right hand triangle signify constraints ($\sim 1\sigma$) from Large Scale Structure (LSS), high redshift supernovae Type Ia and CMB observations. The complementarity of the observations is maximal at the concordance model – a flat model with $\Omega_m \approx 0.3$ and $\Omega_\Lambda = 0.7$. Figure taken from Bahcall et al. (1999).

servations place our universe firmly in the ΛCDM region, far removed from past cosmological models.

The evolution of the universe involves epochs in which its various constituents dominate its development. By substituting the equation of state into the continuity equation, Eq. (2.1.5), one arrives at $\rho \propto a^{-3(1+w)}$. As eluded to earlier, the energy density, ρ, contains relativistic and non-relativistic components. Relativistic particles or radiation have an equation of state with

$w = -1/3$ and thus the density evolves as $\rho \propto a^{-4}$. Non-relativistic matter on the other hand is pressureless so its density evolves as $\rho \propto a^{-3}$. In a similar vein, the curvature contribution has $\rho_k \propto a^{-2}$ while the dark energy component or cosmological constant behaves as $\rho \propto$ const. From the above analysis, it is clear that the radiation component decays faster than the matter component. While we inhabit a universe that appears to be dominated by matter and possibly a cosmological constant, at very early times its density would have been dominated by a relativistic component. The transition epoch between matter and radiation dominated universes is termed 'matter-radiation equality' and took place at $z \sim 3500$ in a ΛCDM universe. Late times would then be dominated by a cosmological constant.

Having placed the current cosmological model in context, by describing the equations governing the universe's large scale dynamics and composition, we now proceed to explain theories regarding its origins.

The Big Bang Model

One of the pillars of modern cosmology is that the universe expanded rapidly from a hot initial phase (often dubbed the singularity) known as the Big Bang. Three pieces of evidence support this theory: the expansion of the universe, the primordial abundance of light elements and the existence of the CMB.

Hubble Expansion

The expansion of the universe is manifested in the systematic recession of distant galaxies – a phenomenon first discovered by Edwin Hubble in 1929 (Hubble, 1929). Hubble's law as it is now dubbed, states that the recession velocity of a galaxy is proportional to its distance away from us:

$$v = H_o D, \tag{2.1.7}$$

where H_o is the constant of proportionality between the velocity v and the distance D of the galaxy. Measurements made of distant galaxies by the Hubble Space Telescope Key Project

(Freedman et al., 2001) provided a measurement of $h = 0.72 \pm 0.08$, where $H_o = 100h$ km sec^{-1} Mpc^{-1}.

Abundance of Light Elements

Expansion implies that there must have been a time where the universe was much hotter and denser. In the early universe temperatures above $T \sim 1$ MeV inhibited the formation of bound nuclei. However, as the universe cooled below the binding energies of specific nuclei, light elements such as Hydrogen (H), Helium (^{4}He), Lithium (Li) and Deuterium (D), began to form in a process termed Big Bang nucleosynthesis (BBN). The particular abundance of these elements can be precisely calculated by knowing the conditions of the early universe, in particular its temperature and expansion rate (Olive et al., 2000). Fig. 2.2 presents the measured abundances of the various elements, which, except for Li^7, are all consistent with predictions – a crucial piece of evidence supporting the Big Bang model. In the case of the 'Lithium problem', recent studies by Cyburt et al. (2008) suggest that primordial abundances predicted by BBN and the WMAP baryon density are discrepant by a factor of 2.3-4.3 from abundances inferred from observations of Population II stars. This issue is currently a source of investigation.

Cosmic Microwave Background

The CMB was first discovered by Arno Penzias and Robert Wilson in 1965 (Penzias and Wilson, 1965). It is relic radiation from the early universe that was formed when matter and radiation decoupled approximately $370,000$ years after the Big Bang, corresponding to z ≈ 1100. This event defines a surface in the thermal history of the universe which is often termed: 'the surface of last scattering', as at this juncture the electron-photon interaction length exceeded the scale of the universe. The brightness profile of the CMB is well described by a blackbody spectrum with T $= 2.725$K. The existence and blackbody nature of the CMB is central to the Big Bang theory of the universe and was predicted by Gamow (1946); Alpher and Herman (1948, 1949).

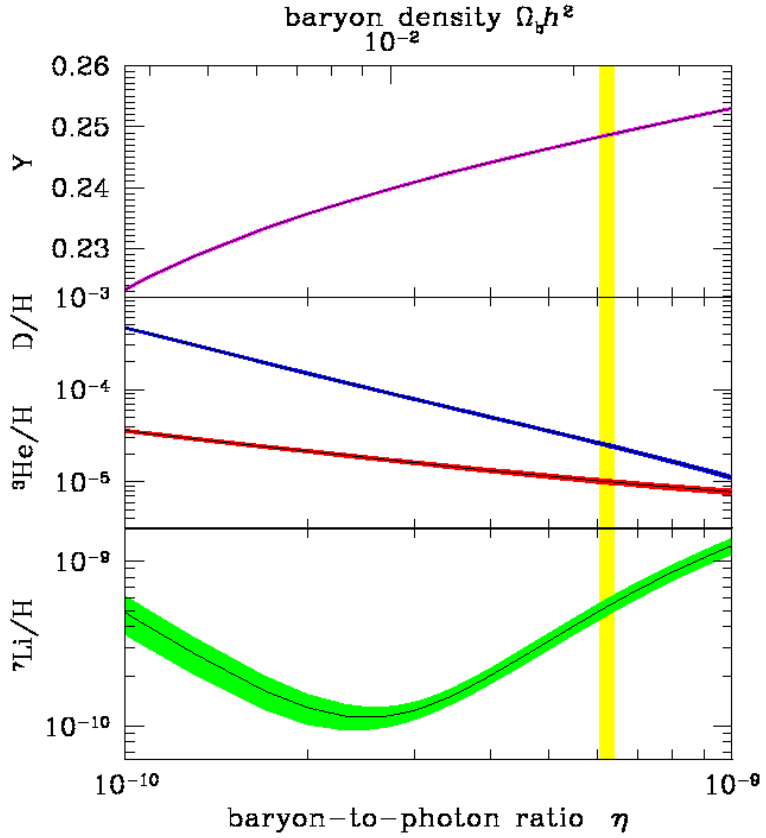

Figure 2.2: The curves show the primordial abundances of He^4, Li and D with respect to H, as a function of baryon-to-photon ratio, as predicted by the standard model of Big Bang nucleosynthesis. The band thickness represents 1σ errors in the element abundances. The yellow stripe is the WMAP baryon-to-photon ratio, η. Figure taken from Cyburt et al. (2008).

The spectrum of the CMB has been modified ever since its creation in the early universe, and hence its profile encodes the history of the universe. Information regarding the large scale structure of the universe are imprinted in the integrated properties of the CMB, whilst details of structures formed at late-time, such as galaxy clusters, *etc.*, are encoded in the small scale properties of the CMB brightness spectrum. Since the first discovery of these anisotropies by the Cosmic Background Explorer (COBE) satellite's Differential Microwave Radiometer (DMR) instrument (Smoot et al., 1992), much effort has been invested into mapping the sky at higher sensitivities and angular resolutions. Instruments aboard ground-based, balloon-borne and satel-

lite experiments have contributed to CMB measurements over the last few decades, with perhaps the most well-known being WMAP (Bennett et al., 2003a). The latter produced full-sky maps of the CMB in five frequency bands and led to the confirmation of the 'Standard or Concordance Model of Cosmology.'

2.2 Large Scale Structure Formation and Growth of Clusters

Cosmological models of the universe must not only describe the behaviour of the homogeneous background universe, but also the dynamics and properties of the perturbed universe. Furthermore, it must account for the generation, evolution and finally the formation of large scale structure in the universe. Much progress in cosmology over the last few years has been borne out of the interplay between observational improvements and refinements to the theories of structure formation. In this section we will explain how perturbations seeded in the early universe evolve to form structures visible in the universe today.

2.2.1 Density Perturbations

The universe contains a multitude of structures varying in scale from photons and electrons to galaxies and clusters. The very existence of these objects means that the universe is inhomogeneous, and must have evolved from a time where the matter density was irregular. At this early time, these perturbations give rise to an overdensity field

$$\delta(\mathbf{x}) = \frac{\rho_M(\mathbf{x}) - \langle \rho_M \rangle}{\langle \rho_M \rangle}, \tag{2.2.8}$$

where $\langle \rho_M \rangle$ is the mean density of the universe. The Fourier representation of the density contrast is given by

$$\delta_{\mathbf{k}}(k) = \int \delta(\mathbf{x}) e^{i\mathbf{k}\cdot\mathbf{x}} d^3x. \tag{2.2.9}$$

Assuming that $\delta(\mathbf{x})$ is isotropic, the density field can be described by an isotropic power spectrum of the form

$$P(k) = \left\langle |\delta_k|^2 \right\rangle. \tag{2.2.10}$$

In addition, if $\delta(\mathbf{x})$ is a Gaussian random field, then $P(k)$ is a complete description of the primordial perturbation spectrum.

In order to understand how density perturbations give rise to large scale structure formation we need to understand the physical meaning of the perturbation spectrum $P(k)$. For the following discussion we assume a power-law form for the primordial spectrum, with $P(k) \propto k^{n_s}$, and consider the mass variance within identical volume elements each with a length scale k^{-1}. The expression for the mass perturbation is given by

$$\frac{\delta M}{M}(\mathbf{r}) = \int \delta(\mathbf{x}) W(|\mathbf{x} - \mathbf{r}|) d^3x, \tag{2.2.11}$$

where $W(r)$ is a spherical window function encompassing the following properties: its integral over all space is unity; and the function value tends quickly to zero beyond a radius r_W. By using the convolution theorem, one can write the variance in the mass, σ^2, on this mass scale as

$$\sigma^2 = \left\langle \left| \frac{\delta M}{M} \right|^2 \right\rangle = \frac{1}{(2\pi)^3} \int P(k) |W(k)|^2 d^3k, \tag{2.2.12}$$

where $W(k)$ is the Fourier transform of $W(r)$. Since the window function damps out modes with $k \gg {r_W}^{-1}$, the variance in mass on scale k for a power law spectrum is $\sigma^2 \propto k^{n_s+3}$. Thus, the typical mass fluctuation is given by

$$\frac{\delta M}{M} \propto M^{-\frac{n_s+3}{6}}. \tag{2.2.13}$$

The natural question to ask is, what is the value of the power law index n_s? Inflationary models for the seeding of primordial perturbations suggest a Gaussian density field with an index close to $n_s = 1$, which is consistent with recent measurements of the anisotropies in the CMB (Komatsu et al., 2010).

2.2.2 Growth of Linear Perturbations

After inflation ceased, the density perturbations seeded by this evolutionary phase, grew through gravitational attraction, as slightly overdense regions gravitationally strip matter from underdense regions. To describe this process we utilise a model consisting of a uniform-density sphere,

which is slightly denser than the surrounding region. The equation governing the dynamics for the radius of a uniform sphere is analogous to the equation of motion of the universe. Thus, by integrating Eq. (2.1.4) using Eq. (2.1.5), with $\Lambda = 0$ and $a = R/R_o$, where R_o is the fiducial radius at which $\rho = \rho_o$, we obtain

$$\frac{\dot{R}^2}{2} - \frac{4\pi G \rho_o R_o^{3+3w}}{3} R^{-(1+3w)} = \epsilon, \tag{2.2.14}$$

where ϵ is related to the spatial curvature, or in energy terms, the net specific energy of the sphere. As mentioned earlier, structure grows through the gravitational interaction of nearby structures. To simulate these effects we consider two similar spheres each expanding from a common origin located at $R = 0$ and $t = 0$, but with slightly different specific energies, $\delta\epsilon \ll \dot{R}^2/2$. As the two spheres evolve in time, their individual radii will deviate from each other by an amount $R_2 - R_1 = \delta R$. This behaviour satisfies the following relation

$$\int_0^R \frac{dR_1}{\dot{R}_1} = \int_0^{R+\delta R} \frac{dR_2}{\dot{R}_2}. \tag{2.2.15}$$

Since we are only considering growth in the linear regime, we can make the simplification $\dot{R}_2^{-1} = \left(1 - \dot{R}_1^{-2}\delta\epsilon\right)\dot{R}_1^{-1}$. If we choose the sphere with radius R_1 as the descriptor for the universe, then Eq. (2.2.15) can be solved to obtain

$$\frac{\delta R}{R} = \frac{\delta\epsilon}{R_o^2}\frac{\dot{a}}{a}\int_0^a \frac{da}{\dot{a}^3}. \tag{2.2.16}$$

Since $\delta\rho/\rho = -3\,(1+w)\,\delta R/R$, Eq. (2.2.16) can be rewritten to obtain the linear perturbation growth function for this particular model

$$D(a) \propto \frac{\delta\rho}{\rho} \propto \frac{\dot{a}}{a}\int_0^a \frac{\dot{a}}{a}, \tag{2.2.17}$$

which is normalised such that $D(a) = 1$ at $z = 0$. The above relation is independent of the scale of the perturbation. This implies that density perturbations grow at the same rate regardless of their scale.

In the case where the universe contains a constant dark energy density, the growth function can be approximated by

$$D(z) = \frac{5\Omega_m(z)}{2\,(1+z)}\left\{\Omega_m(z)^{4/7} - \Omega_\Lambda(z) + \left[1 + \frac{\Omega_m(z)}{2}\right]\left[1 + \frac{\Omega_\Lambda(z)}{70}\right]\right\}^{-1} \tag{2.2.18}$$

(see Carroll et al., 1992; Lahav et al., 1991).

If the universe contains a time-dependent yet homogeneous dark energy density, then the dark energy density within the perturbed sphere of radius R_2 is radially invariant. In this case, assuming a universe with negligible radiation density, the linear evolution of $\delta \equiv \delta\rho/\rho$ is described by the following differential equation

$$\ddot{\delta} + 2\frac{\dot{a}}{a}\dot{\delta} = 4\pi G\rho_M(z)\delta, \tag{2.2.19}$$

where the above relation is derived by differentiating $R_2 = R_1(1-\delta/3)$ twice with respect to time and keeping only terms of the lowest order. For this particular scenario, Wang and Steinhardt (1998) derived the following approximation to the growth function

$$D(a) \approx a \exp\left(\int_a^1 \left\{1 - [\Omega_M(z)]^{\alpha_w}\right\} \frac{da}{a}\right), \tag{2.2.20}$$

where α_w is given by

$$\alpha_w = \frac{3}{5 - w/(1-w)} + \frac{3}{125}\frac{(1-w)(1-3w/2)}{(1-6w/5)^3}\left[1 - \Omega_m(z)\right]. \tag{2.2.21}$$

The approximation to the growth function provided above reproduces the actual growth function given by Eq. (2.2.17) to better than 1% for $\Omega_m(z) > 0.2$.

The growth functions described here are only valid in the regime where pressure gradients do not effect the behaviour of the perturbation. Pressure gradients are ineffectual when the perturbation scale exceeds the Hubble length cH^{-1}, but as the universe ages, perturbations of increasingly larger scale enter the horizon - giving birth to additional physical effects. These processes imprint themselves on the initial scale free perturbation spectrum, $P(k)$. As the universe evolves, $P(k)$ changes in parallel, keeping a record of the evolution. All the effects that alter $P(k)$ can be collectively described by a quantity known as the transfer function

$$T(k) \equiv \frac{\delta_k(z=0)}{\delta_k D(z)}, \tag{2.2.22}$$

where k refers to comoving modes of wavenumber $(1+z)k$ in physical space. In this definition, the redshift z is deemed large enough so that at that surface in time, the perturbation

spectrum, $\delta_k(z)$, reflects the primordial or initial spectrum seeded by inflation or another such process. Thus, the transfer function describes all the effects imprinted onto the original perturbation spectrum throughout the evolution of the universe, except of course those involving nonlinear mode growth. Using this formalism, the linear perturbation power spectrum can be rewritten as $P(k) \propto k^{n_s} T^2(k)$.

2.2.3 The Cold Dark Matter Power Spectrum

The most widely accepted models for large scale structure formation involve cold dark matter (CDM). These particles exert negligible pressure, interact only through gravity, and have small individual random velocities (non-relativistic at the time of decoupling). They are thus not be able to escape the deep potential wells existing within the said structures and thus damp out the density perturbations. In this model, where the universe contains only CDM and radiation, the transfer function contains only one feature, corresponding to the wavenumber of the mode that crossed the horizon at z_{eq} – a time known as matter-radiation equality. The comoving size of such a mode is $l_{eq} \sim cH_o^{-1}(\Omega_m z_{eq})^{-1/2} \sim 20(\Omega_m h^2)^{-1}$Mpc.

Growth of modes which entered the horizon prior to equality (*i.e.* have smaller comoving wavelengths than l_{eq}) are stunted until z_{eq} is reached, as the radiation pressure prior to equality is strong enough to resist gravitational compression. Thus, these short-wavelength perturbations miss out on a growth factor proportional to $(kl_{eq})^2$, which is analogous to the square of the difference in the scale factor from the time of matter radiation equality to the time at which the mode crossed into the horizon. Long-wavelength perturbations however continue to grow unhindered during this time. The dynamics of the CDM transfer function in these two regimes is; $T(K) \approx 1$ for $k \ll l_{eq}^{-1}$ (long wavelengths) and $T(K) \approx (kl_{eq})^2$ for $k \gg l_{eq}^{-1}$ (short wavelengths). Thus, for a power law index $n_s = 1$, these scalings result in mass fluctuations of $\delta M/M \sim M^{-2/3}$ and $\delta M/M \sim const$, on large and small scales respectively. This result suggests that structure formation in a cold dark matter universe is a hierarchical process, with small scale perturbations reaching the nonlinear evolutionary phase before large scale ones.

2.2.4 Spherical Collapse

Cluster formation is a hierarchical process resulting from perturbations in the CDM density distribution. In the earliest epoch of structure formation, density perturbations have larger amplitudes on smaller scales. As a consequence, smaller subclumps of matter are the first to dissociate from the Hubble flow and undergo gravitational collapse. These subclumps then coalesce and merge with larger clumps as perturbations on larger mass scales enter the horizon and reach the nonlinear regime. Understanding the intricacies of structure formation requires large scale numerical and hydrodynamical simulations, a description of which is beyond the scope of this thesis. The key concepts can however be elucidated by a spherically symmetric model of structure formation (*e.g.* Bertschinger, 1985; Fillmore and Goldreich, 1984; Gunn and Gott, 1972).

In this formalism, the matter, that eventually ends up within a cluster, begins as a low-amplitude density perturbation that expands along with the Hubble flow. As the universe evolves, the gravitational attraction of the perturbation slows the expansion of that matter, and eventually causes it to collapse and form clusters of matter. The rate at which matter accumulates onto the cluster is determined by the radial density distribution of the initial perturbation.

Assuming a spherically symmetric geometry, the dynamics of a single mass shell in a region containing a homogeneous generalised dark energy field is governed by the following equation of motion

$$\ddot{r}_{sh} = -\frac{GM_{sh}}{r_{sh}^2} - \frac{1+3w}{2}\Omega_\Lambda H_o^2 (1+z)^{3(1+w)} r_{sh}, \tag{2.2.23}$$

where M_{sh} is the mass enclosed within radius r_{sh} of the shell. During the early stages of spherical perturbation evolution, the mass contained within a shell remains constant. Moveover, if the dark energy is negligible, then the radial behaviour of the shell is governed by the following parametric equation

$$r_{sh} = r_{ta}\left[\frac{1-\cos\theta_M}{2}\right], \qquad t = t_c\left[\frac{\theta_M - \sin\theta_M}{2\pi}\right], \tag{2.2.24}$$

where $r_{ta} = \left[\left(2GM_{sh}t_c^2\right)/\pi^2\right]^{1/3}$ is the turnaround radius and t_c is the collapse time. The above solution is not much different from the case where dark energy is included, since dark energy comprises $\lesssim 15\%$ of the matter, during the time when the shells collapse to the origin. In this

scenario we are making the implicit assumption that the in-falling dark matter does not effect the dark energy density (see Wang and Steinhardt, 1998; Weinberg and Kamionkowski, 2003).

Once a shell collapses, its mass no longer remains constant, as other shells on separate trajectories interpenetrate, owing to the collisionless form of the dark matter. As a result, the radii of collapsed shells oscillate symmetrically about the origin, with the oscillations slowly damping with time, as mass belonging to other collapsed shells accrues within the turning points of each oscillation (Gunn, 1977).

The process of mass accretion is not as symmetric in real clusters. Instead, the gravitational interaction between infalling matter generates a time varying gravitational potential field. This field randomises the velocities of the collapsing matter particles resulting in a Maxwellian velocity distribution, where the temperature is proportional to the particle mass. This process equilibrates the cluster and is known as 'violent relaxation' (Lynden-Bell, 1967). A cluster in this state is said to be in virial equilibrium, a state described by the following equation

$$E_G + 2E_K = 4\pi P_b r_b^3, \tag{2.2.25}$$

where E_K is the kinetic energy, E_G is the total gravitational potential energy and P_b denotes the effective pressure resulting from in-falling matter at the boundary, r_b, of the collapsed structure. By setting P_b equal to zero, one arrives at the usual formalism for the virial theorem of gravitationally bound systems.

Estimating the location of a cluster's outer boundary, *i.e.* r_b, is often achieved through the application of a spherical top-hat toy model. For this scenario, the perturbation leading to the cluster is given by a spherical region of uniform density. Furthermore, all the mass shells in such a perturbation evolve together and simultaneously collapse to the origin. In this situation, the virial theorem states that the location of the boundary, after the shells collapse and virialise, will be in the region of half the turnaround radius.

Even with a simple toy model, such as the spherical top-hat model, one can have different definitions for the virial radius. If one follows the prescription that all the mass in the original perturbation ends up within $r_{ta}/2$, then the mass density in the resulting cluster is $6M/\pi r_{ta}^3$. In

a universe dominated by matter and with zero dark energy, this density is equivalent to $\Delta_v = 8\pi^2/(Ht)^2$ multiplied by the critical density ρ_c (derived by using the mass density defined above and the right hand side of Eq. (2.2.24)). Therefore, for a matter-dominated, geometrically flat universe, where $Ht = 2/3$, the average density of a recently collapsed perturbation is $18\pi^2 \approx 178\rho_c$. Bryan and Norman (1998) provide the following approximation for Δ_v in terms of a flat universe with a non-zero cosmological constant ($w = -1$):

$$\Delta_v = 18\pi^2 + 82\left[\Omega_M(z) - 1\right] - 39\left[\Omega_M(z) - 1\right]. \tag{2.2.26}$$

In reality the bounding radius of a cluster is not distinct. This fact has prompted an alternative approach for the definition of the virial radius, whereby it is defined as the radius within which the density is $\Delta_v\rho_c$ (Eke et al., 1996). A common alternative, inspired by the numerical value of Δ_v in a flat, matter dominated universe, is the scale radius r_{200}, within which the density is $200\rho_c$. As long as $\Omega_M(z) \approx 1$, the scale radius is nearly identical to the virial radius. However, since $\Omega_M \approx 0.3$, the scale radius is actually smaller than the virial radius. The vagueness of the cluster radius is a source of confusion, although each definition has its own part to play in certain applications.

2.2.5 Cluster Mass Profiles

It is well known that the velocity dispersion of galaxies within clusters is nearly constant with distance from the cluster centre. This observation implies an underlying mass-density profile of the form

$$\rho_M(r) \propto r^{-2}. \tag{2.2.27}$$

The most elementary cluster model consistent with this density formalism is the isothermal sphere. In this singular model, the velocity dispersion, σ_ν, is isotropic and constant within a cluster with the density profile given by

$$\rho_M(r) = \frac{\sigma_M^2}{2\pi G r^2}, \tag{2.2.28}$$

(*e.g.* Binney and Tremaine, 1987). The aforementioned model is useful for analytical estimates of various cluster properties, however, it does not describe the complete picture since the total cluster mass diverges with radius.

Numerical simulations of large structure formation suggest an alternative form for the density profile. The dark matter halos produced in these simulations comprise density profiles with slopes shallower than isothermal at small radii and steeper slopes at large radii. This behaviour is described by a two component density profile

$$\rho_M(r) = \frac{\rho_s}{r^p \left(r + r_s\right)^{p-q}}, \tag{2.2.29}$$

where ρ_s is the density at the scale radius, r_s (defined as the point where the slope changes), and the variables, p and q, are the slopes of the inner and outer radii respectively. There is still considerable disagreement regarding the actual values of these slope parameters, although simulations suggest that $1 \lesssim p \lesssim 1.5$ and $2.5 \lesssim q \lesssim 3$. A few examples of different density profiles include the Narraro-Frenk-White (NFW) profile, where $p = 1$ and $q = 3$ (Navarro et al., 1997), the Moore profile, where $p = 1.5$ and $q = 3$, and the Rasia profile (Rasia et al., 2004) with $p = 1$ and $q = 2.5$. Cluster density profiles of this form are well supported by X-ray and optical observations, although discrepancies are found especially in the innermost regions of clusters (Carlberg et al., 1997; Lewis et al., 2003; Pratt and Arnaud, 2002). Measuring the inner slope p is currently of great interest, as the cuspiness of dark matter density profiles at the centre of clusters is a major test of the CDM model of structure formation (Navarro et al., 2004).

The transition from shallow to steep in the dark matter density profile is elucidated by the concentration parameter $c = r_b/r_s$, which defines the outer radius of the cluster in terms of the scale radius, r_s. The actual value for the concentration parameter varies depending on the bounding radius chosen for the cluster. Nevertheless, typical concentration values lie in the range $3 \lesssim c \lesssim 10$ with a scatter in $\log c$ of $0.2 - 0.3$ (Jing, 2000).

2.2.6 Cluster Mass

As eluded to earlier, a cluster's mass and all scaling relations linking this property to other observable quantities depends on the definition of the cluster's outer boundary. The best option is to define a boundary that facilitates simple scalings between observables. In reality however, a single definition is not optimal in all situations.

The most straightforward way to couple observations to theoretical models is to cast the mass of cluster into a general form, namely M_{Δ}. This definition describes the amount of matter contained within a spherical structure of radius r_{Δ}, where the mean density is $\Delta \cdot \rho_c$. Spherical top-hat models, such as the one described earlier, suggest that Δ_v is a suitable descriptor for the density threshold. In spite of this, observers tend to use higher thresholds, namely $\Delta = 200$ or $\Delta = 500$. This decision is motivated by the following: cluster properties are easier to study in regions where the density has a higher contrast than the surrounding area and simulations suggest that substructure within r_{500} is more relaxed than the region within r_v.

Converting between the more general mass form, M_{Δ}, and the virial mass, M_v, is simple, provided the cluster concentration is known. Assuming the cluster mass is given by $M = 4/3\pi r^3 \rho$, then the relationship is

$$\frac{M_{\Delta}}{M_v} = \frac{\Delta}{\Delta_v} \left(\frac{c_{\Delta}}{c_v} \right)^3 , \tag{2.2.30}$$

where c_{Δ} and c_v are the concentrations within r_{Δ} and r_v respectively.

Alternative forms for the cluster mass are useful in particular contexts. As an example, cluster masses derived from gravitational lensing are measured in a cylinder along the line of sight. Within the simulations arena, cluster masses are often estimated using a 'friends-of-friends' algorithm, which links neighbouring mass particles together, eventually forming the entire cluster structure (Davis et al., 1985). This method however often leads to irregular cluster boundaries, making its application to observations more difficult (White, 2001). Cluster masses based on spherical geometry also have their disadvantages, particularly in the cases of cluster mergers. Nevertheless, this approximation provides the most straightforward link between observations and theoretical models.

2.2.7 Cluster Mass Function

Tracing the evolution of galaxy clusters over cosmic time has provided some of the most powerful constraints on cosmological models. Observations of individual galaxy cluster evolution are impossible however, due to the length of cosmological time scales. To circumvent this, observations of how the demographics of the cluster ensemble change with redshift can be studied. An important tool in such an investigaton is the cluster mass function, $n_M(M)$, which gives the number density of clusters in a comoving volume element with mass greater than, M. Pioneering work by Press and Schechter (1974) which was later refined and extended upon by Bond et al. (1991); Bower (1991); Lacey and Cole (1993), provided a semi-analytical method for expressing the cluster mass function in terms of cosmological parameters. By combining spherical top-hat collapse with the growth function for linear pertubations one arrives at the cluster mass function (in differential form)

$$\frac{dn_M}{d\ln\sigma^{-1}} = \sqrt{\frac{2}{\pi}}\frac{\Omega_M\rho_c}{M}\frac{\delta_c}{\sigma}e^{-\frac{\delta_c^2}{2\sigma^2}}, \tag{2.2.31}$$

where $\sigma^2(M,z)$ is the variance of the initial density fluctuation field and is given by

$$\sigma^2(M,z) = \frac{D^2(z)}{(2\pi)^3}\int P(k)|W_k(M)|^2 d^3k. \tag{2.2.32}$$

In the above formulae, δ_c is the critical overdensity for spherical collapse and $W_k(M) = 3\left(\sin kr_M - kr_M\cos kr_M\right)/\left(kr_M\right)^3$ with $r_M = \left(3M/4\pi\Omega_M\rho_{cr0}\right)^{1/3}$, is the Fourier transform of a spherical top-hat window function that encloses mass M. In the above formalism, we assume all density perturbations continue to evolve according to the linear growth rate given by $D(z)$. The normalisation of the power spectrum, $P(k)$, is set such that $\sigma(M_8,0) = \sigma_8$ for $M_8 \equiv \left(8h^{-1}\text{Mpc}\right)^3 H_0^2\Omega_M/2G = 6.0\times10^{14}\Omega_M h^{-1}M_\odot$.

Extending this treatment by assuming perturbations to be ellipsoidal rather than spherical, improved the agreement with numerical simulations (Sheth et al., 2001). Moreover, Sheth and Tormen (1999) demonstrated that a mass function of the form

$$\frac{dn_M}{d\ln\sigma^{-1}} = A_s\sqrt{\frac{2a_s}{\pi}}\left[1+\left(\frac{\sigma^2}{a_s\delta_c^2}\right)^{p_s}\right]\times\frac{\Omega_M\rho_c}{M}\frac{\delta_c}{\sigma}e^{-\frac{a_s\delta_c^2}{2\sigma^2}}, \tag{2.2.33}$$

with $A_s = 0.3222$, $a_s = 0.707$, and $p_s = 0.3$ correlates well with mass functions arising from different numerical simulations.

While such models are useful, they require calibration against cosmological simulations. Furthermore, since they do not encompass the complete complexity of halo formation, their accuracy is likely to be inadequate for precision cosmological constraints (Tinker et al., 2008).

The foundation for precision determination of the mass function from simulations was initiated by Jenkins et al. (2001) and Evrard et al. (2002), whose fitting function for the halo abundance was accurate to $\sim 10\% - 20\%$. Extension and improvement to this work has come from many authors, including Tinker et al. (2008) who not only showed their halo mass function to have an accuracy of $\lesssim 5\%$, but also demonstrated halo mass function 'non-universality' – the same functional form and parameters for the mass function cannot be used for different cosmologies and redshifts. The universality and evolution of the halo mass function are currently the source of much interest and research.

2.3 Cluster Probes

The complex mechanisms existing inside clusters allow one to probe their dynamics through various observational techniques. In the following sections we outline several methods employed to detect and study clusters.

2.3.1 Clusters in Optical Light

Optical identification of clusters has been ongoing for many decades. Moreover, Charles Messier and William Herschel in the late eighteenth century had already recognised clustering of galaxies in the constellations of Virgo and Coma Berencies. With the improvement of telescope observing power and software analysis techniques, optical cluster catalogues continued to grow over the next two centuries, resulting in the extensive cluster catalogues described in Abell (1958); Abell et al. (1989). The forementioned contain most nearby clusters and have provided a foundation for our understanding of clusters and their physical processes. More recently, large area surveys

using the latest detector technology as well as automated cluster detection techniques have produced large catalogues of galaxy clusters (see for example: Koester et al., 2007; Postman et al., 2001, 1996; Gal et al., 2009, 2003, 2000; Gladders and Yee, 2005).

Each cluster observation method has advantages and disadvantages. Clusters are inherently rare objects and therefore we require large survey areas to locate a significant sample. Optical observations offer the opportunity to cover wide areas of the sky with large CCD frames coupled to telescopes with large fields of view. In addition, studies of the colour magnitude relation in red galaxies have allowed accurate distance measurements of clusters out to $z \sim 1$ (Gladders and Yee, 2005).

It is well known that cluster studies at this wavelength band have disadvantages. Since optical observations measure flux, which decreases with distance from the source, this technique is distance or redshift limited. To make matters worse, projection effects caused by background or foreground galaxies along the line of sight can contaminate cluster detection results. Moreover, in order for clusters to be cosmologically useful (in terms of parameter estimation) their masses are required. This parameter is difficult to measure straightforwardly from optical means. These issues served to motivate studies of clusters at other frequencies, particularly in X-rays.

2.3.2 Clusters in X-rays

A census of baryons in the local universe indicate that only about a tenth of the universe's baryons lie within stars in galaxies, leaving the remainder in intergalactic space. These baryons are difficult to detect, however the large potential wells inherent to clusters compress the associated baryonic gas to $T \sim 10^7$ K causing clusters to be conspicuous at X-ray wavelengths. If the gas shares the same properties as the cluster member galaxies, then the temperature is given by

$$k_B T \simeq \mu m_p \sigma_v^2 \simeq 6 \left(\frac{\sigma_v}{10^3 \text{kms}^{-1}} \right)^2 \text{ keV}, \tag{2.3.34}$$

where m_p is the proton mass and μ is the mean molecular weight - typically 0.6 for a primordial composition with 76% hydrogen.

At the high temperatures described by the above relation, the intra-cluster medium (ICM) is analogous to a fully ionized plasma, whose major emission mechanism is thermal bremsstrahlung. The emissivity of such a process occurring at frequency ν scales as

$$\epsilon_\nu \sim n_e n_i g(\nu, T) T^{-1/2} \exp\left(\frac{-h\nu}{k_B T}\right), \tag{2.3.35}$$

where n_e and n_i are the electron and ion number densities respectively, and $g(\nu, T) \propto \log(k_B T/h\nu)$ is the Gaunt factor. By integrating Eq. (2.3.35) over the gas distribution and X-ray emission energy range, one obtains typical luminosities of $L_{\rm X} \sim 10^{43} - 10^{45}{\rm erg\,s^{-1}}$. These luminosities make it possible to identify clusters at high redshift at X-ray wavelengths.

The connection between local gas pressure, p, and density ρ_g, is easily understood if one assumes spherical symmetry and hydrostatic equilibrium:

$$\frac{dp}{dR} = -\frac{GM(<R)\rho_g(R)}{R^2}. \tag{2.3.36}$$

Furthermore, by substituting the equation of state for a perfect gas into Eq. (2.3.36) one obtains an expression for the total mass with radius R

$$M(<R) = -\frac{k_B T R}{G\mu m_p}\left(\frac{d\log\rho_g}{d\log R} + \frac{d\log T}{d\log R}\right). \tag{2.3.37}$$

If R denotes the virial radius, then at redshift z the mass enclosed is $M \propto R^3 \bar{\rho}_0 (1+z)^3 \Delta_v(z)$, where $\bar{\rho}_0$ is the cosmic mean density at the present time, and Δ_v is the mean density at the virial radius (as defined in §2.2.6). Furthermore, if one makes the assumption that the universe is of the Einstein-de-Sitter form, then Δ_v is constant, and the temperature of an isothermal gas distribution is related to the mass by $T \propto M^{2/3}(1+z)$. Thus, in addition to providing an efficient technique for cluster detection, X-ray observations of the ICM also provide a means to determine cluster masses, which is the parameter predicted by cosmological models of the universe. To complement this, X-ray emission in clusters depends on the square of the gas density, hence clusters standout strongly from regions of lower density. This property, in combination with the relatively low surface density of X-ray sources, mitigates projection effects which tend to plague cluster detection studies at other wavelengths

Since the first attempts in the 1970s to map the X-ray sky (Giacconi et al., 1979), observations in this wavelength band have been prolific. Numerous surveys in the 1990s, such as those using the ROSAT satellite, have helped to constrain cosmological parameters (see Rosati et al., 2002, for a review of several cosmologically significant X-ray surveys). Today we are in the era of XMM-Newton and *Chandra* satellites, which together with the large survey area of XMM-Newton and the high angular resolution of *Chandra*, have started to shed light on the interplay between the complex dynamics of the intra-cluster medium and the detailed physics of star formation.

Unfortunately, X-ray and optical studies suffer a common drawback. Both of these methods depend on cluster luminosity and thus suffer from redshift dimming. In the next section we introduce the microwave regime as a novel method for cluster detection and outline its advantages over clusters studies at other wavelengths.

2.3.3 Clusters in the Microwave

Two decades after the prediction of the existence of the SZE (Sunyaev and Zeldovich, 1970, 1972) there were still only a few cluster detections, but in the following decade many new clusters were located at high significance using this phenomenon (Birkinshaw, 1999; Carlstrom et al., 2002). As we now enter the forth decade of SZE observations, improved detector sensitivity and large scale surveys, such as the Atacama Cosmology Telescope (ACT; Kosowsky, 2006), South Pole Telescope (SPT; Ruhl et al., 2004) and PLANCK (The Planck Collaboration, 2006), allow one to fully exploit the power of the SZE. Experiments, such as the aforementioned, will provide not only detailed images of clusters, enabling one to study the intra-cluster medium (ICM), but also large catalogues of SZE selected clusters over a wide range of redshift, permitting accurate measurements of cosmological parameters.

The SZE as an observational tool is particularly useful for deep surveys since the detection limit of a particular survey is fixed by the mass of the cluster. Furthermore, SZE surveys will be able to detect all clusters above a particular mass threshold independent of their redshifts. This remarkable property arises due to the fact that although the CMB suffers redshift dimming, the

ratio of the SZE to the CMB does not, since it is a direct, redshift independent measurement of the cluster gas pressure integrated along the line of sight (see Eq. (2.4.42)).

Most observations employing the SZE have concentrated on galaxy clusters, but with new high sensitivity telescopes, such as those mentioned above, there is now the possibility of detecting hot gas in lower mass group or galaxy sized halos. The total SZE flux measured from a cluster or group is $S_{\rm tSZ} \propto M^{5/3}/{d_A}^2$, where the denominator is the angular diameter distance of the halo. This property suggests that significant SZE flux can be detected from low mass halos with large angular sizes.

The SZE as a cosmological tool is hampered by our lack of understanding of the structure, formation and gas dynamics of groups and clusters. Gas processes such as feedback and star formation for example, alter the observed SZE signal. With deep surveys and high sensitivity measurements of the CMB, coupled with accurate gas models, one can constrain these effects.

2.4 The Sunyaev-Zel'dovich Effect

Compton scattering is one of the chief mechanisms that couples radiation to matter. The importance of this process is often stressed in high energy environments, for example self compton scattering may be responsible for the X-radiation emitted by active galactic nuclei (Fabian et al., 1986). Compton scattering however, also has observable consequences in low energy transfers. The SZE is perhaps the most important astrophysical example of such a process. This effect provides a cosmological tool to probe the properties of intra-cluster gas and has been proposed as a means to measure the motions of galaxies within clusters. In the following we will discuss the properties of the thermal and kinetic Sunyaev-Zel'dovich effect, although the main theme of this research revolves around the thermal effect.

2.4.1 Thermal Sunyaev-Zel'dovich Effect

The thermal Sunyaev-Zel'dovich effect (tSZ) is a spectral distortion of the CMB caused by the inverse Compton scattering of CMB photons by free elections located in the hot gas within

galaxies and clusters. As photons stream through the centre of massive clusters, the probability of their path intersecting with hot ICM electrons is $\approx 1\%$. The resulting interaction boosts the energy of CMB photons resulting in a ≤ 1mK distortion in the CMB spectrum.

The dynamics of the interaction between non-relativistic electrons and a radiation field is well described by the Kompaneets equation (Kompaneets, 1956). Assuming the electron temperature, T_e, is larger than the radiation field temperature, T, the Kompaneets equation can be written as

$$\frac{\partial \langle n \rangle}{\partial t} = \frac{k_B T_e}{m_e c} \frac{\sigma_T n_e}{x^2} \frac{\partial}{\partial x} \left(x^4 \frac{\partial \langle n \rangle}{\partial x} \right), \tag{2.4.38}$$

where, $\langle n \rangle$ is the average photon occupation number, σ_T is the Thompson scattering cross section, n_e is the electron number density and finally $x = h\nu/k_B T$ is the dimensionless frequency component. Rephaeli (1995) suggests an alternative form for the scattering kernel that includes relativistic corrections. However, since we are concerned with weak scattering and small electron temperatures (in the case of small to medium-sized clusters), the two kernels are equivalent, we consequently follow the simpler Kompaneets approximation from here on. In light of the low energy scattering environment, a Bose-Einstein distribution for $\langle n \rangle$ can be assumed. In this notation, the spectral intensity is given by

$$I = \frac{2 \left(kBT_{CMB} \right)^3}{\left(hc \right)^2} x^3 \langle n \rangle . \tag{2.4.39}$$

The specific intensity (a convention common in microwave SZE observations) can be derived by integrating along the line of sight

$$\Delta I_{tSZ} = \frac{2 \left(kBT_{CMB} \right)^3}{\left(hc \right)^2} y_c g(x), \tag{2.4.40}$$

where $g(x)$ is the spectral distortion term which can be expressed as

$$g(x) = \frac{x^4 e^x}{\left(e^x - 1 \right)^2} \left(x \frac{e^x + 1}{e^x - 1} - 4 \right) \left(1 + \delta_{tSZ}(x, T_e) \right), \tag{2.4.41}$$

where $\delta_{tSZ}(x, T_e)$ is the correction to the frequency dependence due to relativistic effects. The Compton parameter y_c in Eq. (2.4.40) is measure of the gas pressure integrated along the line of sight. Fig. 2.3 demonstrates the effect of the tSZ on the CMB spectrum for a cluster 1000

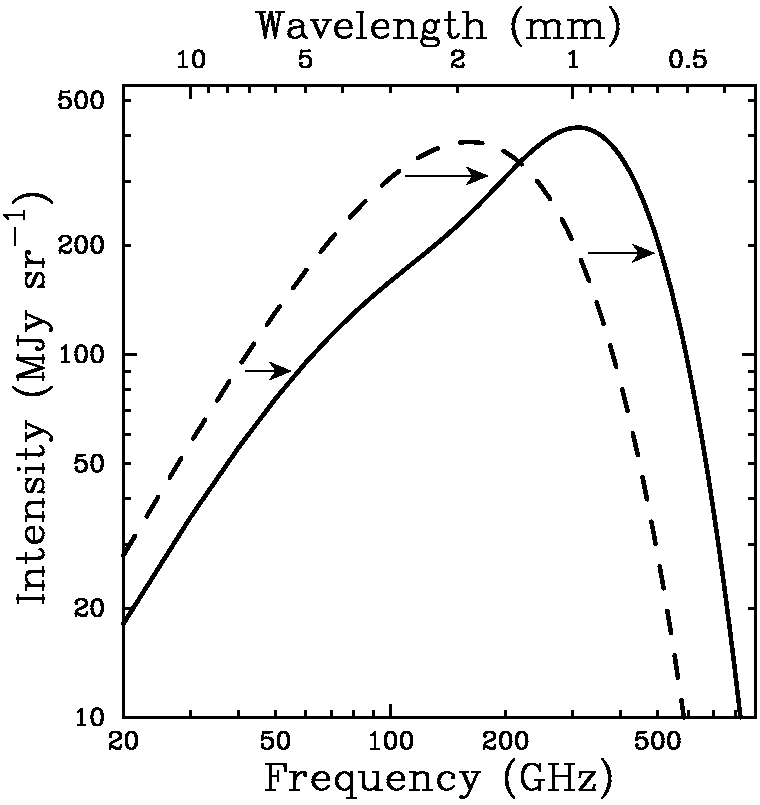

Figure 2.3: Distortion of the CMB spectrum caused by the tSZ for a fictional cluster 1000 times more massive than a typical cluster. The undistorted CMB spectrum is shown as the dashed line, while the distorted one is shown as the solid line. This figure is taken from Carlstrom et al. (2002).

times more massive than a typical cluster. The distortion is seen as a decrease in photon energy at frequencies below ≈ 218 GHz and an increase above this frequency.

The spectral distortion of the CMB can equivalently be expressed as a temperature change $\Delta T_{tSZ}/T_{CMB}$ expressed by

$$\frac{\Delta T_{tSZ}}{T_{CMB}} = f(x)y = f(x)\int n_e \frac{k_B T_e}{m_e c^2}\sigma_T dl, \tag{2.4.42}$$

where $m_e c^2$ is the election rest mass energy and the integration is performed along the line of sight. The frequency dependence of the tSZ in this formalism is contained within $f(x)$ as

$$f(x) = \left(x\frac{e^x+1}{e^x-1} - 4\right)\left(1 + \delta_{tSZ}(x, T_e)\right). \tag{2.4.43}$$

The derivative of the blackbody with respect to temperature, $|dB_\nu/dT|$ is the coupling factor between T_{tSZ} and ΔI_{tSZ}. Fig. 2.4 depicts the distortion of the CMB spectrum due to the SZE, measured in intensity units. The tSZ distortion is easily distinguishable from a CMB temperature fluctuation unlike the kSZ in the non-relativistic regime.

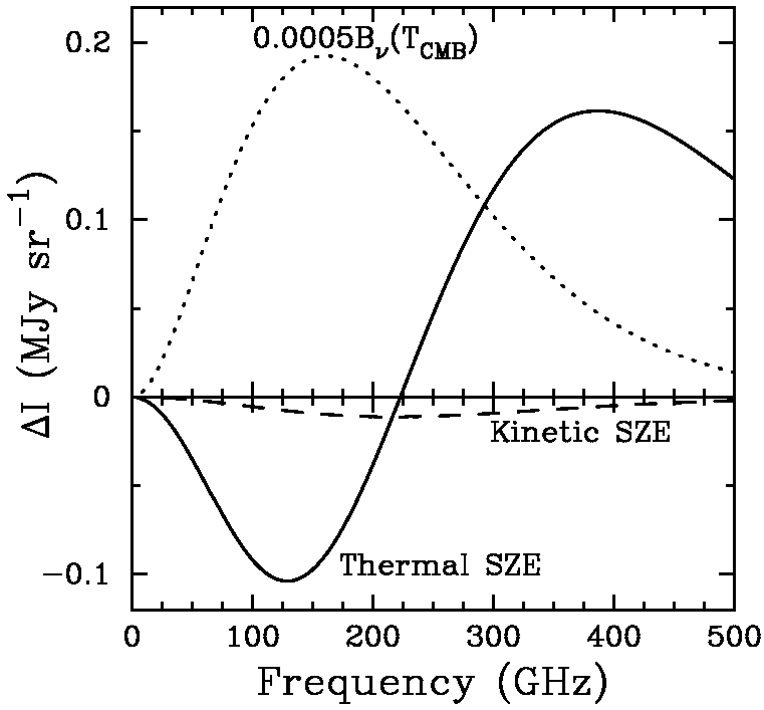

Figure 2.4: Distortion of the CMB spectrum caused by the SZE for a realistic cluster comprising a Compton y parameter of 10^{-4}, electron temperature of 10 keV and peculiar velocity of 500 kms^{-1}. The tSZ is depicted by the solid line, while the kinetic SZE is shown by the dashed line. For comparative purposes, the CMB intensity, scaled by 0.0005, is shown as the dotted line. This figure is taken from Carlstrom et al. (2002).

An observable of particular importance for SZE cluster surveys is the integrated tSZ signal. The total tSZ signal, derived by integrating over the entire cluster, is proportional to the integrated Compton parameter Y_{SZ} where

$$Y_{SZ}{D_A}^2 = \left(\frac{\sigma_T}{m_e c^2}\right) \int P dV, \tag{2.4.44}$$

where D_A is the angular diameter distance to the cluster. The gas pressure within clusters is an excellent proxy for the gravitational potential, and thus $Y_{SZ}{D_A}^2$ is expected to be closely related to the cluster mass.

The salient features of the tSZ are: (1) it is a weak distortion of the CMB spectrum which is proportional to the cluster gas pressure along the line of sight; (2) the effect is independent of redshift; (3) it comprises a unique frequency dependence (with a decrease of the CMB intensity for frequencies < 218 GHz, zero effect at the null ≈ 218 GHz, and an increase of intensity for frequencies higher than the null); (4) the total tSZ signal is proportional the inverse of the squared angular diameter distance implying that SZE surveys will comprise redshift independant thresholds particularly at high redshifts.

2.4.2 Kinetic Sunyaev-Zel'dovich

The kinetic Sunyaev-Zel'dovich (kSZ) effect arises when the gas medium within a cluster is moving with respect to the CMB or Hubble flow. This effect is manifested as a distortion of the CMB spectrum caused by the Doppler effect of the bulk velocity on the scattered CMB photons. In the non-relativistic regime the kSZ is a pure thermal distortion given by

$$\frac{\Delta T_{kSZ}}{T_{CMB}} = -\tau_e \left(\frac{v_{pec}}{c}\right), \tag{2.4.45}$$

where v_{pec} is the cluster peculiar velocity along the line of sight and τ_e is the optical depth of the cluster. Fig. 2.4 depicts the kSZ effect compared to a scaled version of the CMB as a function of frequency. The distorted CMB spectrum is still Planckian but at a marginally different temperature.

Perhaps the most pertinent feature of the kSZ effect is that it provides a measure of the line of sight peculiar velocity of a cluster at high redshift. Moreover, if the bulk flows can be measured over a range of redshifts, they can be used to place constraints on the process of structure formation (Davis et al., 1992). Unfortunately, the sensitivity of today's experiments cannot probe this feature, but rapid progress is being made in this regard.

2.5 Observations of SZE Clusters

The plethora of new telescopes either already observing or in the process of becoming operational will provide not only accurate measurements of the CMB, but also large catalogues of SZE selected clusters. In this section we outline two new ground based experiments in the form of the Atacama Cosmology Telescope and the South Pole Telescope, as well as ESA's (European Space Agency) latest satellite mission, PLANCK. Moreover, we discuss the expected outcomes of such experiments and how they will impinge on cosmology.

2.5.1 The Atacama Cosmology Telescope

The Atacama Cosmology Telescope (ACT) is a new generation instrument that is current producing arcminute-resolution and micro-Kelvin sensitivity maps of the CMB over several hundred degrees of the sky. The telescope, which operates in three microwave channels, namely: 148 GHz, 219 GHz and 277 GHz, will probe not only the high multipole primary anisotropies, but also secondary effects of the CMB, such as the SZE. These three observing bands were chosen in order to probe the increment, null and decrement of the SZE. The telescope comprises a 6m primary mirror and receiver known as the Millimeter Bolometer Array Camera (MBAC). Probing secondary CMB effects requires not only high sensitivity but also high quality data. To this end, ACT is located on Cerra Toco in Chile at an altitude of 5200 m, a site chosen to minimise the effects of atmospheric fluctuations and precipitable water vapour. To date, the telescope has observed three full seasons over 2007, 2008 and 2009 and aims to continue for the next few years. The fiducial specifications for ACT are presented in Table 2.1

The first cluster and power spectrum results have already been completed. In the first paper (Hincks et al., 2009), presented in Chapter 5, eight previously known clusters were detected using the SZE and subsequently analysed. The second paper (Fowler et al., 2010) provides a measurement of the CMB power spectrum in the multipole range $600 < l < 8000$.

ACT is expected to observe hundreds of clusters over the sky. Understanding the cluster detection properties involves simulations and forecasts. In addition, with the plethora of new

clusters that will be observed by ACT, important cosmological questions can be answered. These include addressing the shortfall of baryons in the local universe, and trying to understand the dynamics of clusters and their formation. In this thesis we investigate the performance of ACT and other new generation experiments, as well as place constraints on cosmological parameters through the analysis of galaxy clusters and groups.

2.5.2 South Pole Telescope

The South Pole Telescope (SPT) (Ruhl et al., 2004) is another ground-based experiment aimed at measuring the CMB as well as detecting clusters through the SZE. The SPT is an off-axis Gregorian telescope comprising a 10m primary mirror and five synchronous observing channels (sky mapped at multiple frequencies simultaneously). The SPT is well suited to observing clusters because its angular resolution, in several of its frequency bands, matches cluster scales, and it possesses high sensitivity over a large field of view (≈ 1 deg^2). To complement this, the SPT is situated approximately one kilometre from the geographic South Pole - a region with the best atmosphere for millimetre astronomy. In Table 2.1 we present the specifications of the SPT as defined by Ruhl et al. (2004).

The SPT is expected to survey hundreds of square degrees of sky finding thousands of clusters through the SZE. This well defined cluster sample can be used to constrain various cosmological parameters. In addition, the SPT aims to measure the CMB on angular scales of several arcminutes or less. In this regime, characterised by $l \gtrsim 2000$, secondary anisotropies dominate over the primordial CMB angular power spectrum. The largest source of anisotropy in this multipole range is believed to be the SZE. Thus, measuring the power spectrum in this regime, including or removing clusters detected in the SZE survey, can place constraints on parameters such as σ_8 and Ω_m, which are complementary to those constraints derived from the cluster survey.

In early 2009, the SPT released its first cluster results (see Staniszewski et al. (2009)), which presented four new clusters discovered through the SZE. Later that year, Plagge et al. (2009) presented an analysis of 15 X-ray selected clusters and compared derived quantities, such as Y_{SZ}, to X-ray properties of the clusters. More recently, Vanderlinde et al. (2010) presented a

Table 2.1: Summary of ACT, SPT and PLANCK Specifications

	ACT			SPT					PLANCK								
ν (GHz)[a]	148	218	277	95	150	219	274	345	30	44	70	100	143	217	353	545	857
$\delta\nu$ (GHz)[b]	18.4	17.0	20.9	24.0	38.0	35.0	67.0	27.0	6.0	8.8	14.0	30.0	42.9	65.1	105.9	163.5	257.1
NET_{CMB} ($\mu K\sqrt{s}$)[c]	300	500	700	278	259	551	774	4975	170	200	270	50	62	91	277	1998	91000
Θ_{fwhm} ($'$)[d]	1.41	1.01	0.94	1.58	1.00	0.69	0.56	0.44	33.4	26.8	13.1	9.2	7.1	5.0	5.0	5.0	5.0

[a] Instrumental frequency.
[b] Defines the instrument's frequency window or bandwidth.
[c] Noise equivalent temperature in CMB temperature units.
[d] Full width at half-maximum of the telescope beam.

catalogue of 21 SZE selected galaxy clusters, with the optical follow-up studies of these clusters discussed in (High et al., 2010).

2.5.3 PLANCK

For over 40 years the CMB has been used to answer questions regarding the geometry and contents of our universe. To date however, only a very small fraction of the information stored within the CMB has been mined. PLANCK is the third satellite mission after COBE and WMAP and aims to extract all the information stored in the CMB anisotropies. In addition, PLANCK will measure the polarisation of the CMB anisotropies which encodes cosmological information, such as the possible existence of gravitational waves, as well as provides a unique data set to probe the thermal history of the universe. The PLANCK satellite was successfully launched on May 14th 2009 from Kourou space port in French Guyana and will conduct an all sky survey.

The PLANCK satellite comprises nine observing frequencies ranging from 30 GHz to 857 GHz. This telescope is particularly well suited to observing the SZE owing to its frequency dependence and the fact that the multiple channels will allow accurate and straightforward foreground removal. Table 2.1 presents a summary of the PLANCK telescope specifications derived from The Planck Collaboration (2006). PLANCK's best angular resolution is $5'$ which is significant lower than current ground based experiments such as SPT and ACT. Consequently, PLANCK will be less sensitive to lower mass, high redshift clusters than new generation ground based experiments. This constraint means PLANCK will be unable to probe the cluster gas profile – a measurement which is needed to constrain the Hubble constant. On the positive side,

PLANCK will observe thousands of clusters over the entire sky with a well defined selection function. This catalogue will be invaluable in studies of cosmological models and our understanding of large scale structure evolution.

In this chapter we have outlined the current cosmological model for the universe and its constituents, including the evolution and properties of large scale structure. To complement this, we described methods of probing the dynamics of such structures through multi-wavelength observations. In the following chapters we present studies of galaxy clusters thus providing insight into their properties and applications to cosmology.

CHAPTER 3

Detection of Hot Gas in Galaxy Groups via the Thermal Sunyaev-Zel'dovich Effect

3.1 Introduction

Through the distinctive signatures that cosmological parameters, such as the baryon density, matter density and spatial curvature have on the cosmic microwave background (CMB) anisotropy, recent measurements of the CMB temperature and polarisation spectra (Nolta et al., 2009, and references therein) have placed precise constraints on these parameters, thereby establishing a cosmological model that is consistent with a wide range of astronomical observations Dunkley et al. (2009, and references therein). Moreover, because the physics underlying the CMB anisotropy is to a good approximation linear on these scales, the CMB provides a powerful probe into the physics of the early universe and the primordial perturbations (Komatsu et al., 2009, and references therein).

Whereas on large angular scales the CMB anisotropy is fairly well described, apart from a late-time integrated Sachs-Wolfe (ISW) contribution (Sachs and Wolfe, 1967), by the geometrical projection of inhomogeneities at the last scattering surface onto our celestial sphere, the so-called primary anisotropies, on smaller angular scales of around an arcminute CMB photons are more significantly affected by gravitational and scattering processes along the line of sight.

These secondary anisotropies provide an effective probe of the physics of the low-redshift universe.

The most significant secondary anisotropy on scales of around a few arcminutes comes from inverse Compton scattering of CMB photons off hot gas in galaxy clusters along the line of sight, the so-called thermal Sunyaev-Zel'dovich (tSZ) effect (Sunyaev and Zeldovich, 1970). The population of hot electrons in the cluster gas imparts energy to photons in the Rayleigh-Jeans part of the spectrum pushing them into the Wien tail. This distorts the thermal CMB spectrum by creating a deficit of photons at low frequencies and an excess of photons at high frequencies with no distortion at the tSZ null frequency, $\nu \simeq 218$ GHz. The galaxy cluster appears as a cold spot on the sky at frequencies below the tSZ null and as a hot spot above the tSZ null. The unique spectral signature of the tSZ effect will allow multi-frequency, high-resolution CMB experiments to make a relatively clean separation of the thermal SZ effect from the primary CMB and other contaminants such as point sources and galactic foregrounds.

The utility of the thermal SZ effect as a cosmological probe arises from the fact that the Compton distortion of the CMB is a scattering effect, so that the central decrement towards a cluster is independent of the redshift of the cluster. Moreover the angular diameter distance flattens out at $z \sim 1$ so that the angular size of the cluster is approximately constant at high redshift. This means that the tSZ effect does not suffer from the strong redshift dimming of its optical and X-ray counterparts with the consequence that a microwave background tSZ cluster survey can detect a larger proportion of lower mass clusters out to higher redshifts. The thermal SZ effect can thus be used to construct galaxy cluster catalogues with a well defined selection function, thereby providing a potentially powerful probe of cosmology through the evolution of the cluster abundance (for a review see Carlstrom et al. (2002)).

While most work has focused on the detection of the tSZ effect in galaxy clusters and its cosmological application, there is an intriguing possibility that high resolution CMB experiments with sufficient sensitivity may be able to detect hot gas in lower mass galaxy or galaxy group halos. Whereas the central tSZ distortion scales roughly in proportion to the mass of the halo, the total tSZ flux, $S_{\rm tSZ} \propto M^{5/3}/d_A^2$, has an additional dependence on the angular diameter distance

of the halo. This means that nearby low mass halos with a large angular size could produce a significant tSZ flux. This fact was exploited in Taylor et al. (2003) to study the possibility of detecting the tSZ effect in the halo of our neighbouring galaxy, M31, with the upcoming PLANCK surveyor. In this chapter we focus on how well current and forthcoming CMB experiments will detect the tSZ effect in nearby galaxy and group halos. Such a detection will provide unique insights into the distribution of baryons and the properties of hot gas in the outskirts of galaxy and group halos.

Indeed, in a census of baryons in the local universe (Fukugita et al., 1998; Fukugita and Peebles, 2004) it has been argued that most of the uncertainty in the baryon budget comes from the uncertainty in the mass in ionised plasma associated with groups of galaxies. Whereas the baryon fraction inferred from light element abundances (e.g., Steigman (2007)), the CMB anisotropy (Dunkley et al., 2009) and the high redshift Lyα forest (Kirkman et al., 2003) give a consistent baryon fraction of $\Omega_b \approx 0.044$, only about ten percent of these baryons are observed to be in stars, hot gas in clusters, and neutral and molecular gas in galaxies at low redshift. Cool plasma in and around groups of galaxies indirectly detected through quasar absorption lines (Penton et al., 2000, 2004) makes up twenty to twenty five percent of the baryon budget, while the warm-hot gas residing in the filamentary large-scale structure is believed to account for another thirty to thirty five percent of the baryons (Davé et al., 2001; Cen and Ostriker, 2006). The remaining thirty to forty percent of baryons is likely to be tied up in galaxy groups in a low density, warm-hot plasma. Recent X-ray observations (Sun et al., 2009) that report average gas fractions, $f_{\rm gas} \approx 0.08$, out to r_{500} in galaxy groups may have detected roughly half of these baryons. When combined with the fact that the gas fraction profiles inferred from these measurements are still rising at r_{500} (see also Vikhlinin et al. (2006)) this indicates that a large fraction, perhaps as much as fifteen to twenty percent, of baryons in the universe may be in the outskirts of galaxy halos and in the intragroup medium beyond r_{500}. Recent evidence for this warm-hot component has come from quasar absorption lines in the ultraviolet (O VI; e.g., Tripp et al. (2000); Sembach et al. (2003); Tumlinson et al. (2005)) and in X-rays (OVII and OVIII; e.g., Fang et al. (2003)) observed around galaxies and groups of galaxies but these detections only map the two-

dimensional gas distribution along a few lines of sight to allow a complete study of its spatial properties.

More detailed observations of this warm-hot component will yield important clues into the impact of galactic feedback on the distribution of gas in the intragroup medium. The relative dearth of hot gas observed in the central regions of galaxies and galaxy groups results in these halos being less X-ray luminous for a given temperature as compared to more massive galaxy clusters. The resulting break in the luminosity-temperature relation observed in X-ray clusters and groups (McCarthy et al., 2004) suggests that non-gravitational processes that modify the entropy structure in the central regions of low mass clusters and groups are responsible for departures from the cluster scaling relations expected in self-similar models. Several models have been proposed to explain the excess entropy (for a recent review see Voit (2005)), including preheating of infalling gas before it was shock-heated to the virial temperature, radiative cooling of low entropy gas to form stars, and feedback from supernovae and active galactic nuclei that increased the temperature and reduced the density of gas in the central regions of galaxies and groups. While a combination of radiative cooling and feedback seems to reproduce the central entropy excess in low mass clusters and groups, it is clear that improved measurements of the properties of hot gas in these halos are necessary to understand the exact details of entropy injection. Whereas X-ray observations lack sensitivity to the hot gas beyond r_{500} because the X-ray luminosity scales as the square of the (decreasing) gas density, the tSZ effect scales linearly with the density and thus provides a potentially more sensitive probe of the hot gas in the outskirts of galaxy and group halos. Moreover, the tSZ effect measures the projected gas pressure which is a complementary probe to the X-ray luminosity and can provide new constraints on models of the intracluster and intragroup medium. While the tSZ effect has been detected in a number of galaxy clusters by single-dish and interferometric experiments (for a review see Carlstrom et al. (2002)) it has not not yet been convincingly detected in any galaxy groups. However, a new generation of high resolution CMB experiments with superior detector sensitivity offers the hope of detecting and constraining the properties of the hot gas in galaxy groups.

The outline of this chapter is as follows. In §3.2 we construct models of the hot gas in virialized halos of a given mass and redshift, over the mass range $M_{\rm vir} = 10^{13} M_{\odot} - 10^{15} M_{\odot}$ and redshift range $z = 0 - 1.5$. The models take into account constraints on the temperature, entropy injection and gas fraction from X-ray observations. In §3.3 we utilise multi-frequency filtering techniques to determine the detectability of hot gas in nearby halos with current and forthcoming microwave background experiments such as the Atacama Cosmology Telescope (ACT; Kosowsky (2006)), the South Pole Telescope (SPT; Ruhl et al. (2004)) and the PLANCK mission (The Planck Collaboration, 2006). In a final section we summarise our findings and discuss how detection of the tSZ effect in group halos will constrain gas models and allow a measurement of physical parameters such as the entropy injection and baryon fraction in these halos. Throughout this study we assume a flat ΛCDM cosmological model with parameters $h = 0.72,\ \Omega_m = 0.26,\ \Omega_b = 0.044,\ \Omega_{\rm de} = 0.74,\ w_{\rm de} = -1.0$, and $\sigma_8 = 0.8$ that provide a best fit to the WMAP 5 year data (Dunkley et al., 2009).

3.2 Hot Gas Halo Models

Historically the isothermal β model (Cavaliere and Fusco-Femiano, 1976) has been used to describe the spatial distribution of hot gas in galaxy clusters, primarily to model the X-ray emission originating from thermal bremsstrahlung of the hot intracluster gas (Sarazin, 1986). The β model provides a convenient analytical form that has been popular for X-ray surface brightness profile fitting. However, over the past decade it has been realised that X-ray observations of density profiles at large radii do not favour the β model: the isothermal model provides a poor description of the temperature profiles of intracluster gas, with observed temperature profiles declining at large radii and cooling flows observed in the central regions of some clusters (Vikhlinin et al., 2006). Furthermore, it has been shown that there is a fundamental incompatibility between the β model parameters fitted using X-ray data, and those fitted using data based on the tSZ effect (Hallman et al., 2007a; Atrio-Barandela et al., 2008), indicating that the simple β model is not sufficiently realistic to describe the observed cluster gas physics.

We will study two different models for the hot gas in dark matter halos. Our first model, which we will refer to as the polytropic model, assumes that the hot gas follows a polytropic equation of state and traces the dark matter in the outskirts of the halo (e.g. Komatsu and Seljak (2001a, 2002)). As discussed in Komatsu and Seljak (2001a) this model is in good agreement with observed X-ray surface brightness profiles and the mass-temperature relation above temperatures of a few keV. Our second model, which we refer to as the entropy model, builds upon the first and attempts to account for non-gravitational feedback by adding entropy to the hot gas, similar to Voit et al. (2002). In both cases, the hot gas is in hydrostatic equilibrium with the underlying dark matter potential.

3.2.1 Dark Matter Halo

We define a dark matter halo at redshift z with virial mass $M_{\rm vir}$ and radius $r_{\rm vir}$ to have a characteristic average density equal to $\Delta_{\rm vir}(z)$ times the critical density,

$$\rho_c(z) = \frac{3H^2(z)}{8\pi G} \, . \tag{3.2.1}$$

The Hubble parameter relative to its present value is given by

$$\frac{H(z)}{H_0} = \left[\Omega_m(1+z)^3 + \Omega_{\rm de}(1+z)^{3(1+w_{\rm de})}\right]^{1/2} \, , \tag{3.2.2}$$

where $\Omega_{\rm m}$ and $\Omega_{\rm de}$ represent the density of the matter and dark energy components, respectively, relative to the critical density today.

In the spherical collapse model (Peebles, 1980) for a SCDM cosmology with $\Omega_m = 1$ and $\Omega_{de} = 0$, the virial collapse factor has a constant value $\Delta_{\rm vir}(z) = 18\pi^2$. Using numerical simulations, Bryan and Norman (1998) found for ΛCDM cosmologies that the parametric form

$$\Delta_{\rm vir}(z) = 18\pi^2 + 82[\Omega(z) - 1] - 39[\Omega(z) - 1]^2 \, , \tag{3.2.3}$$

where

$$\Omega(z) \equiv \Omega_m(1+z)^3 \left[\frac{H_0}{H(z)}\right]^2 \, , \tag{3.2.4}$$

provides a good fit over a wide range of ΛCDM cosmological models. Once the characteristic average density is chosen, the virial mass and radius become uniquely related.

We assume that the dark matter density follows the self-similar NFW profile (Navarro et al., 1997),

$$\rho_{dm}(x) = \frac{\rho_s}{x(1+x)^2}, \qquad x \equiv r/r_s \ , \tag{3.2.5}$$

where r_s is the scale radius of the halo. By integrating the density profile and equating the mass found within the virial radius to $M_{\rm vir}$, we obtain the density normalisation,

$$\rho_s = \frac{M_{\rm vir}\ c^3}{4\pi r_{\rm vir}^3\ m(c)} \ , \tag{3.2.6}$$

where the function,

$$m(x) = \ln(1+x) - \frac{x}{1+x} \ , \tag{3.2.7}$$

is the dimensionless dark matter mass profile. The concentration parameter is defined as $c = r_{\rm vir}/r_s$ and we adopt the fitting formula,

$$c(M_{\rm vir}, z) = \frac{7.5}{1+z}\left[\frac{M_{\rm vir}}{M_{*0}}\right]^{-0.1} \ , \tag{3.2.8}$$

to describe the dependence on virial mass and redshift following Dolag et al. (2004). The dependence on cosmological parameters is captured by scaling the virial mass by the nonlinear mass M_{*0}. In the spherical collapse model, the nonlinear mass is defined as the mass $M = (4/3)\pi\bar{\rho}R^3$ enclosed within a sphere of radius R for which the variance of the linear density field δ, smoothed by a tophat filter, equals the square of the critical overdensity threshold $\delta_c = 1.68$. For the chosen cosmology, the nonlinear mass is $M_{*0} = 2.818 \times 10^{12} h^{-1} M_\odot$ at redshift $z = 0$.

The exact dependence of the concentration parameter on mass and redshift is still uncertain as various parametrisations have been used in the literature (e.g. Navarro et al. (1997); Seljak (2000); Bullock et al. (2001)). However, as previously observed (Komatsu and Seljak, 2002) we find that our results are insensitive to the exact choice of the concentration parameter. This is due to the fact that the tSZ effect is less sensitive to the central regions, where the changes in the concentration parameter are most important.

During the formation of virialized halos, the collisionless dark matter undergoes violent relaxation and the collisional baryons get shockheated. According to the virial theorem, the internal energy of a virialized halo is twice its gravitational potential energy. From this relation, we can define a characteristic velocity dispersion for the dark matter and a virial temperature,

$$\begin{aligned} T_{\rm vir} &= \frac{1}{3} G\,\mu\, m_p\, \frac{M_{\rm vir}}{r_{\rm vir}} \\ &= 0.034 \left(\frac{M_{\rm vir}}{10^{12} M_\odot}\right)^{2/3} \left(\frac{\Delta_{\rm vir}(z)}{100}\right)^{1/3} \left(\frac{H(z)}{H_0}\right)^{2/3} {\rm keV}\,, \end{aligned} \tag{3.2.9}$$

for the shockheated gas. We assume a fully ionised gas with a mean molecular weight $\mu = \frac{4}{3+5X_H} = 0.588$ for a hydrogen mass fraction of $X_H = 0.76$.

3.2.2 Polytropic Model

We first consider a model where the gas follows a polytropic equation of state, $P_g \propto \rho_g^\gamma$, with polytropic index γ. The gas density and temperature profiles can be parametrised as,

$$\rho_g(x) = \rho_{g,0} y_{\rm poly}(x)\,, \tag{3.2.10}$$

$$T_g(x) = T_{g,0} y_{\rm poly}^{\gamma-1}(x)\,, \tag{3.2.11}$$

where $y_{\rm poly}(x)$ is the dimensionless gas density profile and the coefficients $\rho_{g,0} \equiv \rho_g(0)$ and $T_{g,0} \equiv T_g(0)$ are two boundary conditions. Assuming that the gas is in hydrostatic equilibrium with an NFW potential, we obtain the analytical solution (e.g. Komatsu and Seljak (2001a)),

$$\begin{aligned} y_{\rm poly}(x) &= [1 - B f(x)]^{1/(\gamma-1)}\,, \\ f(x) &= 1 - \frac{\ln(1+x)}{x}\,, \\ B &= \left(\frac{\gamma-1}{\gamma}\right)\left(\frac{3T_{\rm vir}}{T_0}\right)\left[\frac{c}{m(c)}\right]\,. \end{aligned} \tag{3.2.12}$$

For a given mass and redshift, there are 3 free parameters: the polytropic index γ, the central gas temperature $T_{g,0}$, and the central gas density $\rho_{g,0}$. In Komatsu and Seljak (2001a, 2002)

these parameters were specified by requiring that the gas density profile matches the dark matter density profile in the outer parts of the halo. This assumption is known to be in good agreement with adiabatic hydrodynamic simulations, but it remains unclear how valid it is for radiative simulations which include cooling, star formation, and feedback. We will take an alternative approach, choosing appropriate values for the free parameters such that they are in agreement with hydrodynamic simulations, are complimentary with other recent semi-analytical models, and are flexible enough for us to apply them to our non-polytropic model.

We set the polytropic index to be $\gamma = 1.2$ as suggested by hydrodynamic simulations and used in other recent semi-analytical models (see Ostriker et al. (2005), and references therein). This value is also consistent with the range of values used by Komatsu and Seljak (2001a, 2002), who parametrised the polytropic index as a function of the concentration parameter and found that it varies only weakly with c. In reality, the effective polytropic index $\gamma_{\rm eff} \equiv \mathrm{d}\ln P_g/\mathrm{d}\ln\rho_g$ is likely to be a function of radius. Towards the centre of the halo where cooling is more efficient because of the higher densities, the temperature can decrease, resulting in $\gamma_{\rm eff} < 1$. In the outskirts of the halo beyond the virial radius where shockheating is less efficient, the effective polytropic index will approach the characteristic value $\gamma_{\rm eff} = 1.62$ for the IGM (Hui and Gnedin, 1997). Furthermore, non-gravitational feedback can also change the equation of state. In our second model, we consider a profile where the effective polytropic index is scale dependent.

Halos found in adiabatic hydrodynamic simulations are generally well described by the virial theorem. The temperature at the virial radius is close to the virial temperature and the central and average temperature are found to be slightly higher (e.g., Frenk et al. (1999); Rasia et al. (2004)). Therefore, we choose to equate the temperature at the virial radius, $T_{g,c} \equiv T_g(c)$, to $T_{\rm vir}$ and this fixes the central temperature as,

$$T_{g,0} = T_{\rm vir} + 3T_{\rm vir}\left(\frac{\gamma-1}{\gamma}\right)\left[\frac{cf(c)}{m(c)}\right] \ . \tag{3.2.13}$$

Our chosen values for $T_{g,0}$ and $T_{g,c}$ are also consistent with the range of values used by (Komatsu and Seljak, 2001a, 2002).

We normalise the density profile by fixing the mass of hot gas within the virial radius, $r_{\rm vir}$, and compare the gas fractions predicted by this model to X-ray constraints within r_{500}. X-ray observations of hot clusters have demonstrated that the cumulative gas fraction within r_{500} approaches a constant value that lies in the range $f_{\rm gas,500} \approx 0.10$ to 0.16 independent of cluster mass (Sun et al. (2009); LaRoque et al. (2006b)). Furthermore there is good evidence that $f_{\rm gas}(< r_{200})$ converges to the universal baryon fraction f_b (Vikhlinin et al., 2006; Sanderson et al., 2003; McCarthy et al., 2007). These results agree with cosmological hydrodynamic simulations, which also suggest that for massive clusters, there is very little evolution of the gas fraction with redshift within $r_{\rm vir}$ (Kay et al., 2004; Eke et al., 1998; Ettori et al., 2004; Kravtsov et al., 2005; Kay et al., 2007).

Observational constraints on the gas fraction in the cooler halos of galaxies and groups of galaxies are much weaker than the cluster measurements. However, there is evidence for a decrease of $f_{\rm gas}(< r_{500})$ with decreasing halo mass. It also appears that $f_{\rm gas}(< r_{200})$ does not approach the universal baryon fraction f_b (Sanderson et al. (2003), see also McCarthy et al. (2007)). The main process that changes the gas fraction while maintaining the baryon fraction is condensation of cold, low entropy gas into stars. The lower value of $f_{\rm gas}$ for smaller halos is consistent with the higher stellar fraction measured for lower mass halos (Lin et al., 2003; Gonzalez et al., 2007) combined with the fact that lower mass halos are more sensitive to non-gravitational heating which can expel gas from their shallower potentials. There are few observational constraints on the evolution of the gas fraction with redshift for cooler systems, but simulations suggest that there is little evolution of the baryon fraction from $z = 1$ to $z = 0$ down to the galactic scales of $M_{\rm vir} \simeq 10^{12} M_{\odot}$ (Crain et al., 2007).

Taking these uncertainties into account, we assume that the baryon fraction within the virial radius is given by the cosmic fraction Ω_b/Ω_m, but allow for a fraction $f_* = 0.1$ of baryons in the form of stars. We also assume that $f_{\rm gas,vir}$ is redshift-independent (for $z \lesssim 1$) for all halo masses ($M_{\rm vir} = 10^{13} - 10^{15} M_{\odot}$) that we consider. The central gas density is then given by,

$$\rho_{g,0} = \frac{(1 - f_*)\frac{\Omega_b}{\Omega_m} M_{\rm vir}}{4\pi r_s^3 \int_0^c y_{\rm poly}(x) x^2 dx} \,. \tag{3.2.14}$$

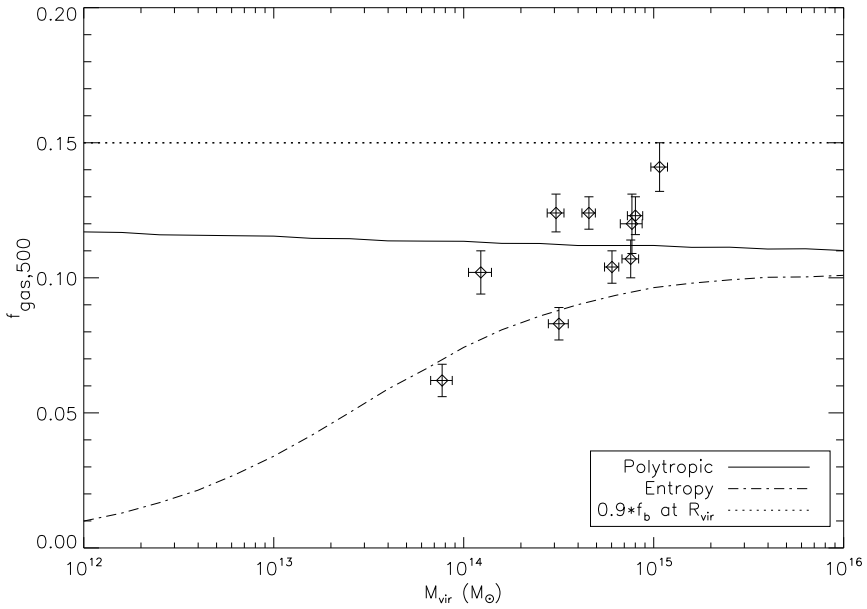

Figure 3.1: Integrated gas fraction within r_{500} for the polytropic (solid curve) and entropy injection (dot-dashed curve) models, each normalised as described in the text. The model curves are compared to the universal baryon fraction, as measured from the WMAP 5 year data, with 10% removed to account for stars (dotted curve). The data points were obtained by Vikhlinin et al. (2006) from a CHANDRA sample of nearby relaxed galaxy clusters.

Note that Komatsu and Seljak (2001a, 2002) chose to fix the gas fraction at the virial radius to the cosmic value, without any explicit allowance for stars. In general, the integrated gas mass and pressure within the virial radius from our model agrees well with theirs with typical differences of order ten percent. We note that this simple parametrisation does indeed fit X-ray observations as can be seen from Fig. 3.1.

Now that the density and temperature of the gas are completely specified for the polytropic model, we can write down additional quantities that are relevant to tSZ and X-ray observations. The electron pressure and entropy are given as,

$$P_e = n_e k T_e = P_{e,0} y_{\rm poly} \ , \tag{3.2.15}$$

and

$$S_e = T_e n_e^{-2/3} = S_{e,0} y_{\rm poly}^{\gamma - 5/3} \ , \tag{3.2.16}$$

where $P_{e,0} \equiv n_{e,0} k T_{e,0}$ and $S_{e,0} \equiv T_{e,0} n_{e,0}^{-2/3}$ are the central electron pressure and entropy, respectively. The electron number density n_e is calculated from the gas density assuming a fully ionised gas and the electron temperature is assumed to be equal to the gas temperature.

3.2.3 Entropy Model

Observations indicate that in the inner regions of low-temperature clusters there is excess entropy above the predictions of the self-similar model (Ponman et al., 1999; Lloyd-Davies et al., 2000; Finoguenov et al., 2007). Together with the observed departure from the simple scaling relations suggested by purely gravitational physics (Arnaud and Evrard, 1999), this means that non-gravitational effects should be included when modeling the ICM gas distribution. Various authors have suggested that the ICM was heated by some energy input, e.g., via star formation, SN explosions or AGN feedback. For example, Voit et al. (2003) showed that preheating can explain the entropy profiles of groups. This model was also studied (Reid and Spergel, 2006) in the context of tSZ observations. Ostriker et al. (2005) constructed a model including various non-gravitational processes that could be used to match the observed scaling relations of clusters (see also Bode et al. (2007)).

Similar to Voit et al. (2002) (see also Balogh et al. (2006) and Younger and Bryan (2007)), we allow for an additive term $S_{\rm inj}$ to the polytropic entropy profile that incorporates the combined effect of non-gravitational processes, such as feedback from supernovae and galactic nuclei, and radiative cooling and star formation. $S_{\rm inj}$ is constant with radius so that

$$S = S_0 \, y_{\rm ent}^{\gamma-5/3} + S_{\rm inj} \, , \tag{3.2.17}$$

The addition of an entropy term modifies the temperature profile according to

$$T_g(x) = T_{g,1} \, y_{\rm ent}^{\gamma-1}(x) + T_{\rm inj} \, y_{\rm ent}^{2/3} \, , \tag{3.2.18}$$

so that the central temperature is now $T_g(0) = T_{g,1} + T_{\rm inj}$. Here $T_{\rm inj}$ is the amount of injected thermal energy per particle, and relates to the amount of injected entropy via

$$S_{\rm inj} = 100 \left(\frac{T_{\rm inj}}{1{\rm keV}} \right) \left(\frac{n_{e0}}{10^{-3}{\rm cm}^{-3}} \right)^{-2/3} \ {\rm keV \ cm}^2. \tag{3.2.19}$$

The form of heating proposed here is effective at increasing the temperature in the inner regions of the halo but has little effect in the outskirts of the halo for all but the lowest mass halos (see Fig. A.2). The additional entropy due to the non-gravitational heating term breaks the self-similarity of the cluster physics. This very simple model provides a good phenomenological description that is adequate for our purposes in spite of its shortcomings.

We assume that the gas remains in hydrostatic equilibrium with the dark matter, which yields an implicit equation for the modified profile $y_{\rm ent}$, which we solve numerically. For a given mass and redshift, there are 4 free parameters in this model: the index γ that characterises the polytropic part of the temperature, the central gas temperature, the central gas density and the amount of injected energy $T_{\rm inj}$. In general the gas will not retain a polytropic equation of state and its profile will be altered. However, we want to continue to associate the polytropic-like terms with virialisation and shockheating, thus we keep $\gamma = 1.2$ and normalise the polytropic term in the temperature equation just like in the polytropic model. That means we set the value at the virial radius to be equal to the virial temperature, which fixes the constant $T_{g,1}$ via

$$T_{g,1} = \frac{T_{\rm vir}}{y_{\rm ent}^{\gamma-1}(c)}. \tag{3.2.20}$$

Note that we implicitly assume that the gas has first settled in the gravitational potential set up by the dark matter before being redistributed by the injection of entropy.

We normalise the gas density by assuming that the gas pressure at the virial radius remains unchanged by the entropy injection, i.e. $P_{\rm gas}^{\rm ent}(r_{\rm vir}) = P_{\rm gas}^{\rm poly}(r_{\rm vir})$. This means that we assume that the gas settles back into a pressure balanced hydrostatic equilibrium at the virial radius after the energy injection. Note that with our choices, the entropy model reduces to the polytropic model when $T_{\rm inj}$ goes to zero. The resulting electron temperature, density, pressure and entropy profiles for the polytropic model and entropy injection model are shown in Figs. A.2-A.4 in Appendix A, where they are discussed in more detail.

In order to adjust the amount of heating $T_{\rm inj}$, we construct a fitting function for $T_{\rm inj}$ such that $S_{\rm inj} \approx 100$ keV cm^2 independent of halo mass and redshift. It has been shown that this form and amount of feedback reproduces the observed scaling relations of clusters (McCarthy et al.,

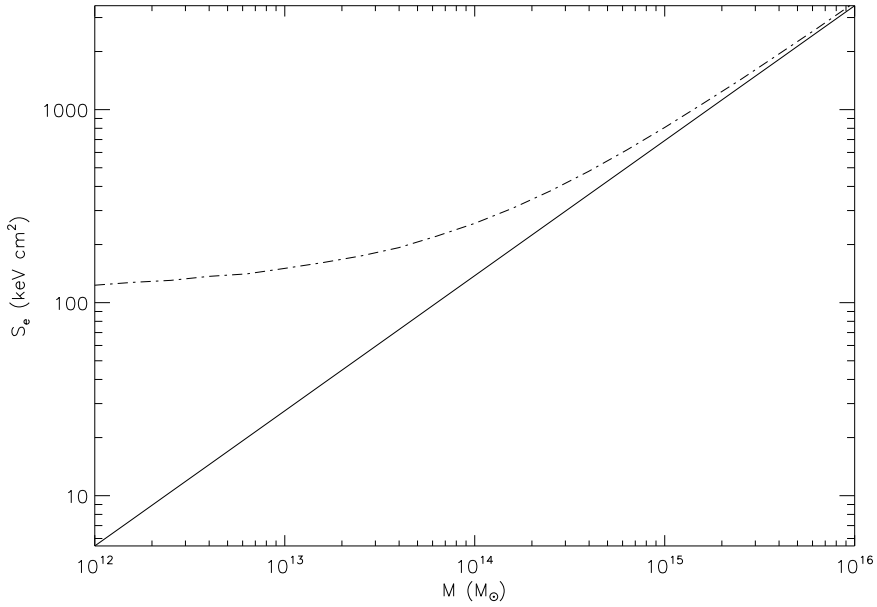

Figure 3.2: Entropy at $0.1\,r_{\rm vir}$ against halo mass, $M_{\rm vir}/M_\odot$, for the polytropic model (solid curve) and the entropy model (dot-dashed curve), showing a break in the scaling of the core entropy scaling as suggested by X-ray observations.

2004) (see Voit (2005) for a detailed discussion of the feedback energy available from physical processes such as supernovae or AGN heating).

In Fig. 3.2 we plot the entropy, S_e at $0.1\,r_{\rm vir}$ against virial mass for the different models. It can be seen that the entropy model has more central entropy in group halos. This results from the feedback that heats the gas and flattens the density profile, by pushing more gas from the centre to the outskirts, thereby breaking the scale invariance of the entropy-mass relation. We also note that the level of feedback chosen in our entropy injection model provides an entropy floor of $S \approx 100 - 200\,{\rm keV\,cm^2}$ which agrees with entropy profiles derived from X-ray observations (see Ponman et al. (1999); Lloyd-Davies et al. (2000)) and simulations (see Finoguenov et al. (2003)) of galaxy clusters and groups.

An additional constraint on the entropy injection parameter comes from the X-ray luminosity-temperature relation. The X-ray luminosity within radius r_X is

$$L_X(< r_X) = \quad 1.41 \times 10^{35}\,\mathrm{erg\ s^{-1}} \left(\frac{n_{e0}}{10^{-3}\mathrm{cm}^{-3}}\right)^2 \left(\frac{T_{e0}}{\mathrm{keV}}\right)^{1/2} \times \left(\frac{r_s}{\mathrm{kpc}}\right)^3 \times 4\pi \int_0^{r_X/r_s} \mathcal{Y}_X(x_p)\, x_p\, dx_p \tag{3.2.21}$$

where the projected radius is $r_p = x_p\, r_s = \sqrt{r^2 - l^2\, r_s^2}$. In the case of the entropy model the integrand $\mathcal{Y}_X$ is given in terms of $y_{\rm gas}$, the dimensionless gas profile, as

$$\mathcal{Y}_X(r) = \sqrt{y_{\rm gas}^{\gamma+3}(r) + (T_{\rm inj}/T_{e0}) y_{\rm gas}^{14/3}(r)}$$

while in the case of the polytropic model $\mathcal{Y}_X$ is simply obtained by setting $T_{\rm inj} = 0$ in the above expression.

In Fig. 3.3 we plot the integrated X-ray luminosity within r_{500} against the emission weighted electron temperature. We see that the entropy injection model has significantly lower X-ray luminosity for group halos, resulting in the observed break of the scale invariant $L_X - T_X$ relation on group scales.

3.3 Multi-Frequency Filtering of the Halo tSZ Signal

We now study the significance with which the halo tSZ signal from nearby groups and galaxies can be detected with forthcoming multi-frequency CMB experiments. Microwave maps contain not only the thermal SZ, but a host of contaminants including primary CMB anisotropies, kinetic SZ, microwave emission from galactic dust, infrared and radio point sources, over and above the detector noise of the experiment. The importance of utilising the tSZ as a cosmological probe has prompted several authors to develop specialised techniques for detecting galaxy clusters through the tSZ effect. Proposed techniques include the maximum entropy method (Hobson et al., 1998), fast independent component analysis (Maino et al., 2002b), matched filter analysis (Herranz et al., 2002a), wavelet filtering (Pierpaoli et al., 2005) and Wiener filtering (Tegmark

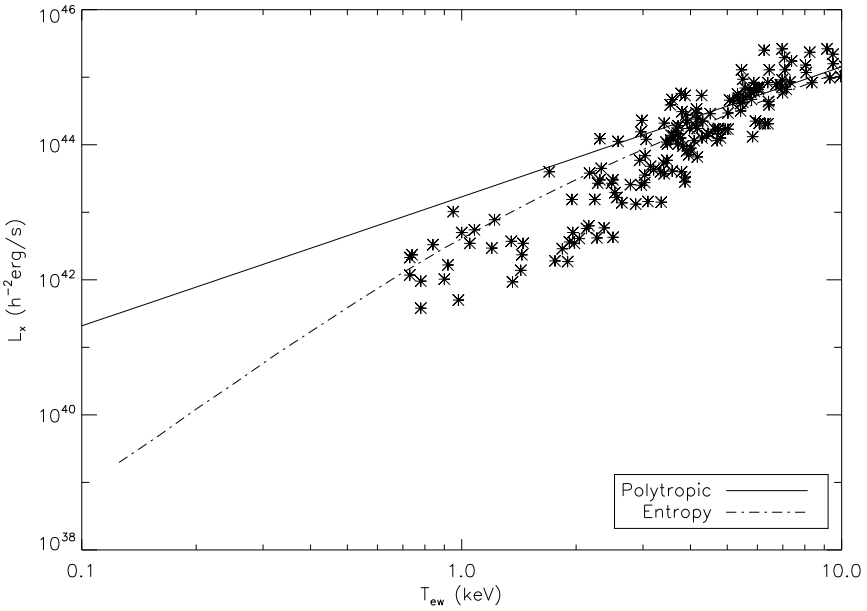

Figure 3.3: Integrated X-ray luminosity within r_{500} against emission-weighted gas temperature, $T_{\rm ew}$, in the polytropic model (solid curve) and the entropy model (dot-dashed curve). The data points were obtained by McCarthy et al. (2004) from a compilation of CHANDRA and XMM-NEWTON data.

and Efstathiou, 1996). Map filtering, in general, utilises both the spatial and frequency information to separate galactic foreground emission and extragalactic point source contamination from the primary CMB and thermal SZ signals.

For the purposes of this investigation, which involves assessing the level of detection of a tSZ halo, we utilise a simple multi-frequency Wiener filtering technique as described in Tegmark and Efstathiou (1996) to separate the halo tSZ signal from other components. The method allows us to determine the level of residual noise in the filtered maps and a signal-to-noise ratio for each halo. Foreground and noise subtraction is done in harmonic space which allows one to exploit the fact that contaminants such as the CMB, galactic dust and extragalactic point sources have power spectra that differ from that of the thermal SZ effect. We also include a contribution from the thermal SZ background that has the same frequency dependence as the halo tSZ signal. The contamination arising from the superposition of tSZ sources along the line of sight has the

potential to reduce detectability and distort observable properties of the halo tSZ signal (Holder et al., 2007).

3.3.1 Multi-Frequency Wiener Filter

We assume that we have microwave sky maps $d_i(\mathbf{r})$ at pixel position $\mathbf{r}$ for $\mathcal{M}$ different frequencies. The signal in each map originates from $\mathcal{N}$ components $s_j(\mathbf{r})$ such as the primary CMB anisotropy, tSZ sources, galactic foregrounds and extragalactic point sources, so that

$$\Delta T(\mathbf{r}, \nu) = \sum_j f_j(\nu) s_j(\mathbf{r})$$

where $f_j(\nu)$ is the frequency dependence of the jth component. In addition to these components each map contains detector noise $n_i(\mathbf{r})$ which we treat as random in each pixel. Then we can write our observation as

$$d_i(\mathbf{r}) = F_{ij} s_j(\mathbf{r}) + n_i(\mathbf{r})$$

where the $\mathcal{M} \times \mathcal{N}$ frequency response matrix F is defined as $F_{ij} = \int w_i(\nu) f_j(\nu) d\nu$. It is convenient to absorb the beam response factor into the definition of the pixel noise (Knox, 1995) which allows us to set the response coefficients w_i to unity.

We assume that the noise has zero mean $\langle n_i \rangle = 0$ with covariance

$$\langle \tilde{n}_i(\boldsymbol{\ell}) \tilde{n}_j^*(\boldsymbol{\ell}') \rangle = (2\pi)^2 \delta(\boldsymbol{\ell} - \boldsymbol{\ell}') \tilde{N}_{ij}(l).$$

We will consider the case of white noise, for which $\tilde{N}_{ij}(\boldsymbol{\ell})$ is constant. We assume that the signal and foreground components have means

$$\langle s_i(\mathbf{r}) \rangle = A_i$$

with covariance

$$\langle (\tilde{s}_i(\boldsymbol{\ell}) - A_i)(\tilde{s}_j^*(\boldsymbol{\ell}') - A_j) \rangle = (2\pi)^2 \delta(\boldsymbol{\ell} - \boldsymbol{\ell}') \tilde{S}_{ij}(\ell).$$

The condition that the signal and noise components are uncorrelated ensures that the signal covariance matrix, $\tilde{S}_{ij}(\ell) = \delta_{ij} \tilde{C}_{\ell,(j)}$, and noise covariance matrix, $\tilde{N}_{ij}(\ell) = \delta_{ij} \tilde{N}_{\ell,(j)}$, are diagonal. In what follows we will drop the tilde on harmonic space quantities.

The most general linear estimator $\hat{\mathbf{s}}$ of the signal can be constructed from the data $\mathbf{d}$ as

$$\hat{\mathbf{s}}(\mathbf{r}) = \int W(\mathbf{r}-\mathbf{r}')\mathbf{d}(\mathbf{r}')d^2\mathbf{r}',$$

where W, is an $\mathcal{N}\times\mathcal{M}$ weight matrix. We use the flat sky approximation and work in harmonic coordinates. Some signals e.g., the primordial CMB, have a zero mean, $A_i = 0$. For a signal with non-zero mean, the condition of an unbiased estimator requires that

$$\langle \hat{s}_i(\mathbf{r})\rangle = \int \sum_{j=1}^{\mathcal{M}} W_{ij}(\boldsymbol{\ell})\, s_j(\boldsymbol{\ell})\, d^2\boldsymbol{\ell} = A_i,$$

where we have used Parseval's theorem.

The residual error in the maps from the noise and foregrounds is given by

$$\langle \Delta_i(\mathbf{r})^2\rangle = \langle (\hat{s}_i(\mathbf{r}) - s_i(\mathbf{r}))^2\rangle = \int \Delta_i^2(\ell)\, d^2\boldsymbol{\ell}. \tag{3.3.22}$$

where

$$\Delta_i^2(\ell) = \sum_{j=1}^{\mathcal{N}} |(W_\ell F - I)_{ij}|^2 S_{\ell,j} + \sum_{j=1}^{\mathcal{M}} |W_{\ell,ij}|^2 N_{\ell,j}.$$

The first term accounts for the contamination of the desired signal by other components while the second term measures the detector noise. A non-zero mixing arises when two or more components have similar frequency dependence. Requiring that the residual error is minimised we derive the Wiener filter weights

$$W_\ell = S_\ell F^T [F S_\ell F^T + N_\ell]^{-1}.$$

To set the threshold for detection we compare the mean tSZ signal to the residual noise and define the signal-to-noise ratio as

$$\mathrm{S/N} = \frac{\langle \hat{s}_{\rm tsz}(\mathbf{r})\rangle}{\langle \Delta_{\rm tsz}(\mathbf{r})^2\rangle^{1/2}} = \frac{\int \hat{s}_{tsz}(\ell)\, \ell\, d\ell}{\left[\int \Delta^2_{\rm tsz}(\ell)\, \ell\, d\ell\right]^{1/2}},$$

where the recovered signal is given by

$$\hat{s}_{tsz}(\ell) = \sum_{j=1}^{\mathcal{M}} W_{{\rm tsz},j}(\ell)\, s_{tsz}(\ell).$$

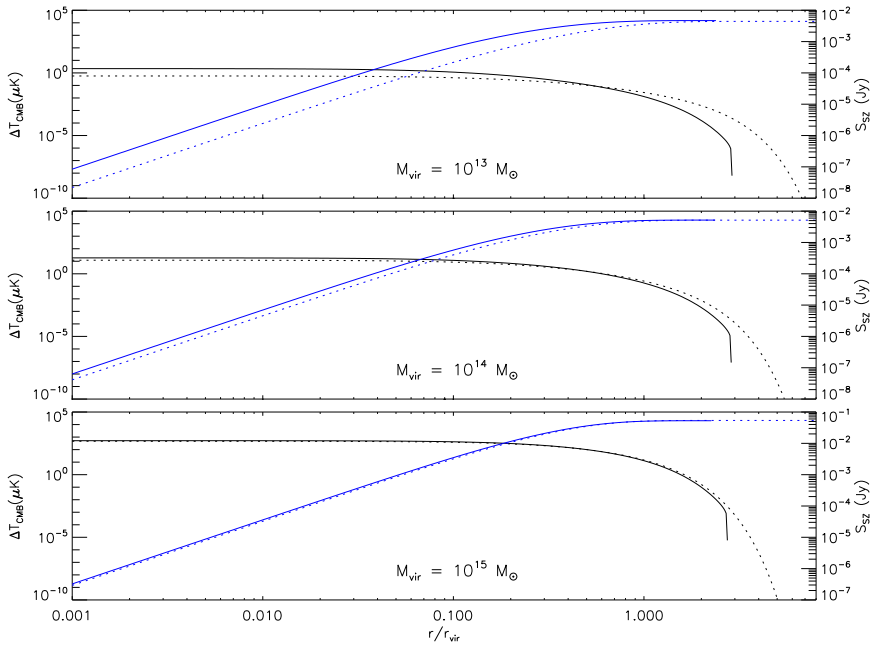

Figure 3.4: tSZ temperature distortion profile (black curves, decreasing from left to right) and integrated flux profile (blue curves, increasing from left to right) plotted against $r/r_{\rm vir}$ for the polytropic model (solid curves) and the entropy model (dotted curves). The panels from top to bottom show the tSZ distortion and integrated flux profiles for halo masses $M_{\rm vir} = 10^{13}, 10^{14}$ and $10^{15}\ M_\odot$ respectively. The sharp fall-off that is visible in the temperature distortion profile for the polytropic model is a result of the Gaussian smoothing described in the text, and occurs at larger radius for the entropy injection model.

The signal-to-noise ratio depends on the range of ℓ over which the integration is performed. We chose ℓ_{min} and ℓ_{max} to give the maximum signal-to-noise over this ℓ range – in practice this would correspond to applying the appropriate high pass and low pass filters to the recovered map.

In the above derivation we have assumed a perfect knowledge of the frequency response of the instrument to the various components. In practice the bandpasses are only known to within some error, which results in leakage of flux between components when applying the multi-frequency filter to separate components. Following Church et al. (2003) we have computed the mixing matrix that quantifies the leakage between components due to an imperfect knowledge of the bandpass error, using a five-component model that includes the CMB, the tSZ signal, galactic

dust, radio point sources and infrared point sources. In the case of both the ACT and PLANCK experiments we have found that the error resulting from the leakage of other components into the tSZ component dominates the reconstruction error from the multi-frequency Wiener filter, $\Delta_{tSZ}(\ell)$, on large scales, $\ell \lesssim 300$. Most of this error is due to the CMB which has significant large-scale power and the largest mixing component with the tSZ. On smaller scales, however, where practically all of the signal-to-noise accumulates for the tSZ cluster and group detections, the bandpass leakage error is sub-dominant to the reconstruction error for both the ACT and PLANCK experiments. This permits us to ignore the bandpass leakage error when studying the detection of individual tSZ clusters and groups.

3.3.2 Halo Thermal Sunyaev-Zel'dovich Signal

The upscattering of microwave background photons by hot electrons in the halo results in a projected Compton profile

$$y_{\rm comp}(r_p) = y_{\rm c0} \times 2 \int_0^{r_{\rm max}/r_s} \mathcal{Y}_{\rm tSZ}(r) dl \tag{3.3.23}$$

where the central Compton distortion is

$$y_{\rm c0} = 8.0 \times 10^{-3} \left(\frac{n_{e0}}{10^{-3}{\rm cm}^{-3}}\right) \left(\frac{T_{e0}}{\rm keV}\right) \left(\frac{r_s}{\rm Mpc}\right) \tag{3.3.24}$$

and the projected radius is $r_p = x_p\, r_s = \sqrt{r^2 - l^2\, r_s^2}$. In the case of the entropy model the projected pressure is given by

$$\mathcal{Y}_{\rm tSZ}(r) = \sqrt{y_{\rm gas}^{\gamma}(r) + (T_{\rm inj}/T_{e0}) y_{\rm gas}^{5/3}(r)}$$

where $y_{\rm gas}$ is the dimensionless gas profile, while in the polytropic model the corresponding expression is obtained by setting $T_{\rm inj} = 0$.

The resulting thermal SZ temperature distortion is given by

$$\Delta T(\theta) = j(x)\, T_{\rm cmb}\, y_{\rm comp}(\theta) \tag{3.3.25}$$

where $\theta = r_p/d_A$, the CMB temperature is $T_{\rm cmb} = 2.73$ K and the frequency dependence is given by

$$j(x) = \frac{x(e^x+1)}{(e^x-1)} - 4\,, \qquad x = \nu/56.9\ \text{GHz}. \tag{3.3.26}$$

The projected temperature distortion profiles are shown in Fig. 3.4. We note that the polytropic and entropy injection models are almost indistinguishable for the most massive halos. In Fig. 3.4 we also show the cumulative tSZ flux within radius $r_{\rm tSZ}$, which is given by

$$S_{\rm tSZ}(< r_{\rm tSZ}) = I_{\rm cmb}\ g(x)\ \times 2\pi \int_0^{r_{\rm tSZ}/r_s} y_{\rm comp}(x_p)\ x_p\ dx_p \tag{3.3.27}$$

where

$$g(x) = j(x)\,\frac{x^4 e^x}{(e^x-1)^2}, \qquad I_{\rm cmb} = 0.27\ \text{GJy}. \tag{3.3.28}$$

While the tSZ signatures of the largest clusters are nearly identical, it is clear from Fig. 3.4 that the tSZ temperature distortions of less massive group halos are sensitive to feedback effects even for models which have the same tSZ flux at the virial radius.

The relevant quantities in harmonic space for determining the detectability of a given tSZ halo are the Bessel transform of the halo tSZ distortion

$$s_{\rm tsz}(\ell) = 2\pi \int_0^{\theta_{\rm max}} [\Delta T(\theta)/j(x)]\, J_0(\ell\,\theta)\,\theta\,d\theta \tag{3.3.29}$$

where J_0 is the Bessel function of order zero, and the tSZ halo power spectrum

$$C_{\ell,tsz} = 2\pi \int_0^{\theta_{\rm max}} [\Delta T(\theta)/j(x)]^2\, J_0(\ell\,\theta)\,\theta\,d\theta \tag{3.3.30}$$

which enters the reconstruction error if the filter weights are not diagonal in the tSZ component i.e., $(WF)_{i\,tsz} \neq \delta_{i\,tsz}$.

The sharp cutoff in the Bessel transform, combined with the fact that the tSZ distortion has not fallen to zero at $\theta_{\rm max}$, results in ringing of the profile spectrum and power spectrum in ℓ-space. We therefore smooth the density profile using a Gaussian profile so that $\rho_{gas}(r) \rightarrow \rho_{gas}(r)e^{-r^2/\xi r^2_{\rm max}}$ where ξ is chosen to ensure that the total gas mass is unchanged. The smoothed profile falls off sharply after $r_{\rm max}$ so in practice we integrate out to $\theta^{\rm smooth}_{\rm max}$ that is a few times

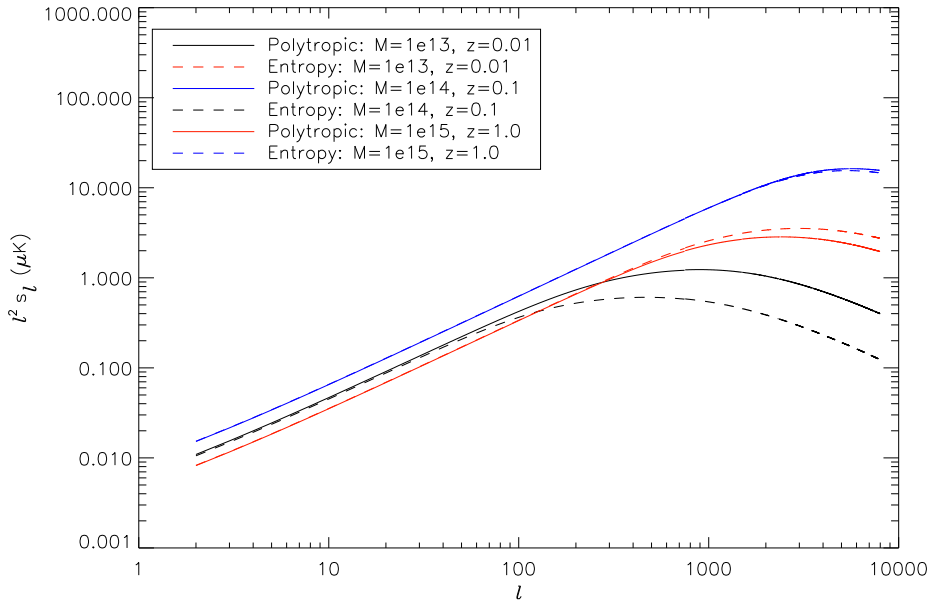

Figure 3.5: Halo spectra, $s_{\rm tsz}(\ell)$, for the polytropic model (solid curves) and entropy injection model (dashed curves). The curves from top to bottom show the spectra for halo masses $M_{\rm vir} = 10^{13}, 10^{14}$ and $10^{15}\ M_\odot$ (blue, red and black) respectively.

larger than $\theta_{\rm max}$, which suffices to remove the ringing. The resulting spectra have slightly more ($\sim$ few percent) power on intermediate and large scales with the power going smoothly to zero at large ℓ.

In Fig. 3.5 we compare the tSZ halo spectrum $s_{\rm tsz}(\ell)$ in the polytropic and entropy injection models for halos of mass $M_{\rm vir} = 10^{13} M_\odot$ at redshift $z = 0.01$, mass $M_{\rm vir} = 10^{14} M_\odot$ at redshift $z = 0.1$, and mass $M_{\rm vir} = 10^{15} M_\odot$ at redshift $z = 1.0$. In the largest mass halo we note that both our gas models produce nearly identical spectra due to the fact that the heating is small relative to the thermal energy of the hot gas. For the lower mass halos we observe that the polytropic model produces a larger amplitude tSZ signal due to the higher density of gas in the central regions of the halo. The temperature increase that occurs in the entropy injection models is insufficient to compensate for the reduced density, which results in a tSZ profile with smaller amplitude for larger entropy injection. The trend is monotonic suggesting that, for experiments with sufficient

sensitivity and frequency coverage to extract the tSZ halo signal, the amount of entropy injection may be measurable from these tSZ observations.

3.3.3 Foreground Components

We assume that the spatial and frequency dependence of each foreground component can be written as a product

$$\Delta T^2_{(i)}(\nu, \ell) = A^2_{(i)} f^2_{(i)}(\nu) C_{\ell,(i)} \ ,$$

where $f_{(i)}(\nu)$ measures the average frequency dependence of a component, C_ℓ is its spatial power spectrum and $A_{(i)}$ is its amplitude. It is useful to make use of both the spectral and spatial properties of the various sources, since signals displaying similar spatial properties, can often be distinguished from one another though their unique frequency dependence and vice versa.

Note that $f_{(i)}(\nu)$ gives the frequency dependence of the RMS fluctuations in thermodynamic temperature referenced to the CMB blackbody. We normalise the frequency term, $f_{(i)}(\nu)$, to be unity at $\nu_* = 56.9$ GHz and the spatial term $C_{\ell,(i)}$ to be unity at $\ell_* = 2$ so that the units are absorbed into the overall amplitude $A_{(i)}$. We now consider models for each of the foreground components in turn.

Galactic Dust Emission

We model the frequency dependence of thermal galactic dust emission as

$$f_{\rm dust}(\nu) = c(x)\, c_*(x)\, \frac{x^{3+\alpha}_{\rm dust}}{e^{x_{\rm dust}} - 1}, \qquad x_{\rm dust} = h\nu / k_B T_{\rm dust}. \tag{3.3.31}$$

where α is the emissivity index and

$$c(x) = \left(\frac{2 \sinh \frac{x}{2}}{x} \right)^2, \quad c_*(x) = \frac{1}{x^2} \frac{1}{2k} \left(\frac{hc}{k_B T_{cmb}} \right)^2 \tag{3.3.32}$$

convert antenna temperature to thermodynamic temperature and specific intensity to antenna temperature respectively. In our model we assume an emissivity index α =1.7 and a dust temperature T_{dust} =18 K (Tegmark et al., 2000; Draine and Lazarian, 1999; Ponthieu et al., 2005).

We model the spatial power spectrum of the thermal dust component as a power law

$$C_{l,\mathrm{dust}} = (\ell/\ell_*)^{-\beta}, \tag{3.3.33}$$

where β is the power law index. We set $\beta = 3$ which was the value derived from an analysis of the DIRBE maps (Wright, 1998). We fix the amplitude of the galactic dust emission to be $A = 10.2\,\mu$K at 56.9 GHz.

An analysis of the FIRAS and DIRBE datasets (Schlegel et al., 1998; Finkbeiner and Schlegel, 1999) has provided evidence for two dust components with different temperatures and emissivities. We account for uncertainty in the emissivity by introducing a residual dust component with the same spatial power spectrum but with scatter, $\delta\alpha$, in the emissivity index. We choose $\delta\alpha = 0.3$ as suggested by the analysis of Finkbeiner et al. (1999), which is consistent with the results of Draine and Lazarian (1999). The top left and top right panels of Fig. 3.6 display the power spectra of the dust and residual dust components respectively. In reality dust is not homogeneous nor Gaussian, which is assumed in this study. To accout for such effects more complex component separation methods are available such as: maximum entropy method (Hobson et al., 1998), and fast independent component analysis (Maino et al., 2002b).

Radio and Infrared Point Sources

We consider two point source populations: radio sources e.g., blazars, and infrared point sources e.g., early dusty galaxies. We model radio sources using a fit to the WMAP Q-band ($\nu_o = 41$ GHz) data (Bennett et al., 2003b):

$$\frac{dN}{dS_\nu} = \frac{N_o}{S_o}\left(\frac{S_\nu}{S_o}\right)^{-2.3} \tag{3.3.34}$$

where $N_o = 80\,\mathrm{deg}^{-2}$ and $S_o = 1$ mJy. Since we are mostly concerned with fluxes at the mJy level, the slope of the distribution was altered to -2.3 from the fiducial slope of -2.7 (White and Majumdar, 2004). In the case of infrared point sources we use the fit (Borys et al., 2003) to SCUBA observations (Holland et al., 1999) at $\nu_o = 350$ GHz, given by

$$\frac{dN}{dS_\nu} = \frac{N_o}{S_o}\left[\left(\frac{S_\nu}{S_o}\right) + \left(\frac{S_\nu}{S_o}\right)^{3.3}\right]^{-1}, \tag{3.3.35}$$

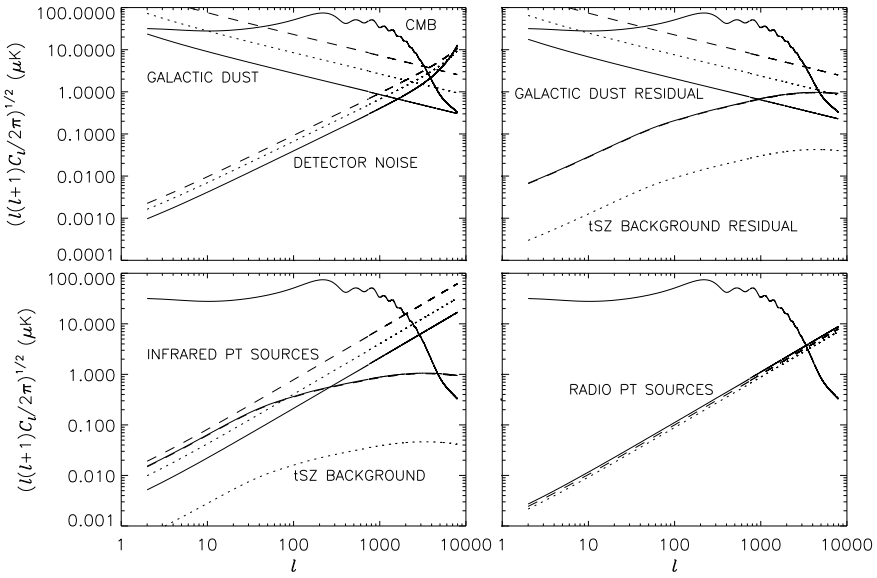

Figure 3.6: Angular power spectra of the foreground components and ACT detector noise at 145 GHz (solid curves), 215 GHz (dotted curves) and 280 GHz (dashed curves) respectively. The top left panel displays the power spectra of the galactic dust, thermal SZ (tSZ) background and detector noise. The top right panel displays the power spectra of the residual tSZ background and residual galactic dust. The bottom left and bottom right panels display the spectra of infrared and radio point sources respectively. All spectra are compared to the lensed CMB spectrum (bold solid curve) in each panel.

where $N_o = 1.5 \times 10^4\,\mathrm{deg}^{-2}$ and $S_o \simeq 1.8\,\mathrm{mJy}$. The sources fluxes were extrapolated to the frequencies of the various CMB experiments using a power law, $S_\nu \propto (\nu/\nu_o)^\alpha$. We use a spectral index $\alpha = 0$ for radio sources and $\alpha = 2.5$ for infrared sources (White and Majumdar, 2004).

The power spectra of the point sources is calculated from

$$C_l = \left(\frac{dB}{dT}\right)^{-2} \int_0^{S_{cut}} \frac{dN}{dS_\nu} S_\nu^2 dS_\nu, \tag{3.3.36}$$

where dB/dT is the derivative of the Planck spectrum and S_{cut} is the imposed flux cut, which we assume to be 5 mJy for ACT and SPT (White and Majumdar, 2004) and 250 mJy for PLANCK (Vielva et al., 2001). We assume that the point sources are spatially uncorrelated on the sky, thus the power is constant at all multipoles. In reality, point sources exhibit clustering, especially infrared sources, which can lead to complications with source detection and flux measurement.

Experiment	ν (GHz)	σ_p (μK/pixel)	θ_b ($^\circ$)
PLANCK: all-sky	100.0	4.5	0.18
	143.0	5.5	0.13
	217.0	11.8	0.092
	353.0	39.3	0.083
	545.0	401.3	0.083
ACT: 200 deg^2 (4000 deg^2)	145.0	2.0 (8.9)	0.028
	215.0	5.2 (23.3)	0.018
	280.0	8.8 (39.4)	0.015
SPT: 4000 deg^2 (200 deg^2)	95.0	9.1 (2.0)	0.026
	150.0	13.4 (3.0)	0.017
	219.0	41.2 (9.2)	0.012
	274.0	71.4 (16.0)	0.009
	345.0	583.9 (130.6)	0.007

Table 3.1: Experimental specifications for the PLANCK (The Planck Collaboration, 2006), ACT (Kosowsky, 2006) and SPT (Ruhl et al., 2004) experiments. In addition to the nominal ACT and SPT surveys, the specifications for a wider ACT survey and deeper SPT survey are also listed, where we have assumed a fixed total integration time in rescaling the pixel noise.

In this study however, we ignore such effects and defer this analysis to future work. The power spectra of infrared and radio point sources are displayed in the bottom left and bottom right panels of Fig. 3.6 respectively.

Cosmic Microwave Background

The cosmic microwave background anisotropy has a constant frequency dependence with reference to the blackbody temperature so that $f_{\rm cmb}(\nu) = 1$. The CMB power spectrum, C_ℓ, was calculated using the CAMB software package [1] using the WMAP 5 year best fit cosmological model. The lensed CMB angular power spectrum is shown in Fig. 3.6.

[1] CAMB: http://www.camb.info

tSZ Background

The projection of tSZ sources of varying mass and redshift along the line of sight creates a diffuse tSZ background which can contaminate halo tSZ observables. To account for the contamination of the foreground halo signal by background clusters, we model the tSZ background statistically by using its power spectrum. Ideally one would utilise a simulated map of tSZ halos to study the contamination due to projection effects but we defer this investigation to a future publication. This map would also take into account the contamination from hot gas outside collapsed structures, though Hernández-Monteagudo et al. (2006) have shown that this component does not significantly contribute to the thermal SZ power spectrum.

The frequency dependence of the thermal SZ background is the same as that of the thermal SZ halo signal given in Eq. (3.3.26). The power spectrum of the tSZ background is computed following Komatsu and Seljak (2002) over the mass range $10^{12} - 10^{16} M_{\odot}$. We also allow for an uncertainty in the tSZ background which we conservatively model as arising from background halos smaller than $5 \times 10^{14} M_{\odot}$. The top left and top right panels of Fig. 3.6 display the power spectra of the tSZ background and residual tSZ background.

3.3.4 Detector Noise and Experimental Specifications

We model the detector noise as an additional sky signal (Knox, 1995) with power spectrum

$$N_{\ell,i} = w_i^{-1} e^{\theta_{b,i}^2 \ell(\ell+1)} \tag{3.3.37}$$

in a given frequency band, i. In this case each of the sky signals is not convolved with the experimental beam. We assume that the experimental beam is a Gaussian of width $\theta_{b,i}$ so that the full width at half maximum is given by $\mathrm{FWHM}_i = \sqrt{8 \ln 2}\, \theta_{b,i}$. The inverse noise weight

$$w_i^{-1} = \sigma_{p,i}^2 \times \theta_{b,i}^2 \tag{3.3.38}$$

is defined as the noise variance per pixel times the pixel area in steradians.

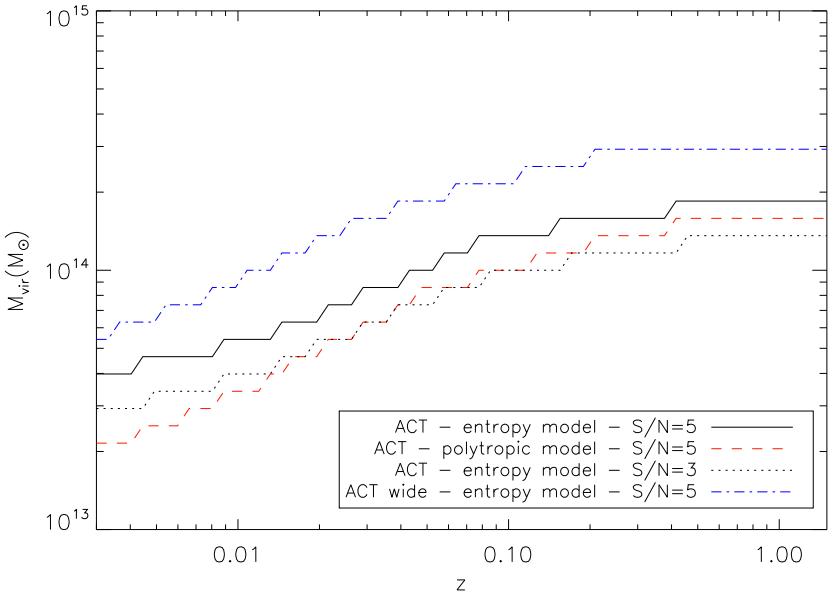

Figure 3.7: The minimum detectable mass, $M_{\rm vir}$, of tSZ halos as a function of redshift, z, for the ACT experiment. The minimum detectable mass is plotted for an entropy model with $S/N = 5$ (solid curve) and $S/N = 3$ (dotted curve), and a polytropic model with S/N=5 (dashed curve) for the nominal ACT survey. Also shown is the minimum detectable mass with the ACT wide survey for an entropy model with $S/N = 5$ (dot-dashed curve).

We consider three nominal experiments, a shallow all sky tSZ survey by the PLANCK surveyor [2], a 200 deg^2 tSZ survey by the Atacama Cosmology Telescope (ACT) [3] and a 4000 deg^2 survey by the South Pole Telescope (SPT) [4]. We also consider a wider ACT survey (over 4000 deg^2) and a deeper SPT survey (over 200 deg^2) where we have rescaled the pixel noise using a fixed total integration time. Specifications for the various experiments are listed in Table 3.1 (Kosowsky, 2006; The Planck Collaboration, 2006; Ruhl et al., 2004). The top left panel of Fig. 3.6 displays the detector noise power spectra for the ACT experiment.

[2]PLANCK: http://www.rssd.esa.int/index.php?project=planck
[3]ACT: http://www.physics.princeton.edu/act/
[4]SPT: http://pole.uchicago.edu/

3.4 Detectability of the Halo tSZ Signal

We now study the detectability of tSZ halos in our mass and redshift range for the polytropic and entropy injection models presented above. In Fig. 3.7 we plot the minimum detectable halo mass, or threshold mass, as a function of redshift for the ACT experiment using a detection significance of $S/N = 3$ and $S/N = 5$. Similar plots for the PLANCK and SPT experiments are presented in Fig. 3.8 and Fig. 3.9 respectively.

At high redshift ($z \sim 1$) the ACT experiment reaches a threshold mass of $2 \times 10^{14} M_{\odot}$ for a signal-to-noise ratio of five and sky coverage of 200 deg^2, which is similar to the completeness limit presented in (Sehgal et al., 2007). The threshold mass at high redshift is similar for the SPT experiment but larger ($\sim 10^{15} M_{\odot}$) for the all-sky PLANCK survey which has larger pixel noise. At low redshift, however, it is interesting to note that the threshold mass for ACT, in the case of the entropy injection model, drops below $10^{14} M_{\odot}$ at $z \approx 0.05$ and as low as $4 \times 10^{13} M_{\odot}$ at $z \approx 0.005$ ($\approx 20\,\mathrm{Mpc}$), and is similar in the case of the SPT-deep survey. Although the threshold mass at low redshift is higher for the SPT wide (4000 deg^2) survey and the all-sky PLANCK survey it is still possible to detect group-sized halos below $10^{14} M_{\odot}$ at $z < 0.02$. This indicates that the thermal SZ effect in nearby group-sized halos can be detected with multi-frequency observations that reach pixel sensitivities of a few μK, and that the detectability of these halos can be improved with longer integration times.

For the polytropic model the detection levels are more optimistic because the tSZ signal is larger due to the gas being more concentrated, however, as discussed in the previous section this model is less realistic, particularly for low mass clusters and groups. To determine the significance with which one can distinguish the entropy model from the polytropic model via measurements of the tSZ distortion in these halos we computed the χ^2 statistic that compares the difference in spectra between these models to the residual noise and foreground level from the nominal ACT experiment. In particular we were interested in the leverage one gains from the detection of galaxy groups and low mass clusters. In Fig. 3.10 we plot the χ^2 statistic as a function of virial mass. We observe that the information gained from group halos is of the same

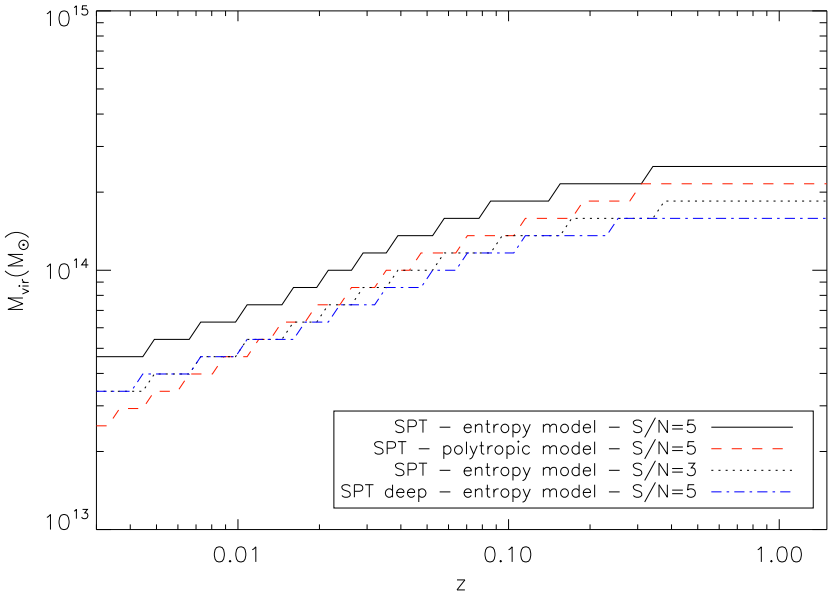

Figure 3.8: The minimum detectable mass, $M_{\rm vir}$, of tSZ halos as a function of redshift, z, for the SPT experiment. The minimum detectable mass is plotted for an entropy model with $S/N = 5$ (solid curve) and $S/N = 3$ (dotted curve), and a polytropic model with S/N=5 (dashed curve) for the nominal SPT survey. Also shown is the minimum detectable mass with the SPT deep survey for an entropy model with $S/N = 5$ (dot-dashed curve).

order of magnitude as the information gained from larger clusters because the larger differences in the tSZ spectra, that results from the increased impact of the entropy injection in lower mass halos, compensates the larger residual noise. For group halos detected with higher significance these measurements will provide useful joint constraints on the gas fraction and level of entropy injection in these halos. It is important to note that in our polytropic and entropy models we have assumed that all the baryons not in the form of stars are in the form of gas. If this turned out not to be the case and the gas fraction is in fact lower than what we have assumed, the significance of detections quoted here will be lower due to the reduced tSZ signal.

It is interesting to quantify the yield of galaxy groups and low mass clusters that are detectable in these surveys. We calculate the yield by integrating the cluster abundance from the minimum survey threshold mass to a cutoff mass of $2 \times 10^{14} M_\odot$, which is roughly the minimum mass quoted for the detection of clusters in upcoming tSZ cluster surveys e.g., Sehgal et al. (2007). In

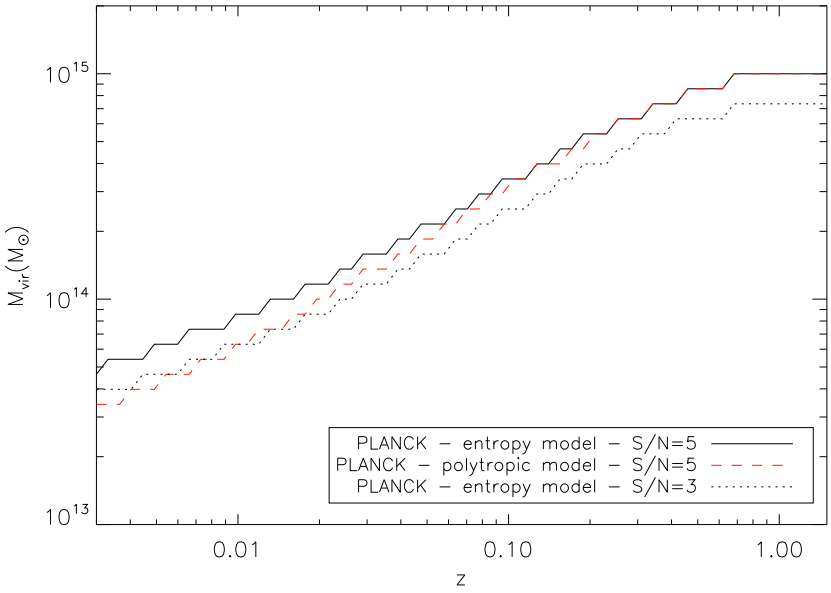

Figure 3.9: The minimum detectable mass, $M_{\rm vir}$, of tSZ halos as a function of redshift, z, for the PLANCK experiment. The minimum detectable mass is plotted for an entropy model with $S/N = 5$ (solid curve) and $S/N = 3$ (dotted curve), and a polytropic model with S/N=5 (dashed curve).

choosing this cutoff mass our aim is to quantify the additional yield of tSZ halos, over and above the yield of more massive clusters, in these surveys. The anticipated number of detectable galaxy groups and low mass clusters are given in Table 3.2 for the different surveys. We note that the mass function is steep so the yield is very sensitive to the minimum and maximum mass limits, consequently the numbers quoted here should only be taken as a rough guide to the anticipated yields. We observe that all surveys will yield a reasonable number of detectable halos below the mass cutoff at the $S/N = 5$ level, with the numbers increasing significantly for halos detected at the lower significance of $S/N = 3$, though the contamination will be higher at this level. It is generally the case that the deep surveys produce a higher yield than the wide surveys for a given model, presumably because the mass function is so steep in this mass range. This trend is reversed in the case of the SPT wide survey at the $S/N = 3$ level, however, because the increased sky area is sufficient to compensate for the reduced sensitivity. We also note that the yields for

the polytropic model are larger than those for the entropy model due to the larger signal in the polytropic model.

In Fig. 3.11 we compare detection curves for the ACT experiment to the distribution of nearby groups in the USGC (UZC-SRSS2 Group Catalogue) (Ramella et al., 2002) and a group catalogue compiled from the Sloan Digital Sky Survey (SDSS) (Yang et al., 2007). The USG catalogue is based on the updated Zwicky Catalogue (UZC) and Southern Sky Redshift Survey (SRSS2), and contains 1168 groups of galaxies out to a redshift of $z \simeq 0.04$ and over a solid angle of 4.69 sr, while the group catalogue based on the SDSS contains 301237 groups from $z = 0.02$ to $z = 0.2$. Comparing the ACT detection curves to the USGC we find that there are 429 groups and clusters in the catalogue out to a redshift $z = 0.04$ that can be detected at a level $S/N = 5$, with 222 of these halos having a mass below $2 \times 10^{14} M_{\odot}$. At a signal-to-noise level of $S/N = 3$ the numbers increase to 488 halos with 281 of these halos having a mass below $2 \times 10^{14} M_{\odot}$. At redshifts beyond those probed by the USGC the SDSS catalogue contains additional groups that are above the minimum detectable mass level of tSZ experiments. The comparison of the threshold mass curves to these catalogues suggests that there are a large number of galaxy groups already detected in redshift surveys that can be detected through targeted observations with upcoming tSZ experiments.

3.5 Discussion and Conclusions

We have investigated the detectability of tSZ groups using an analytic prescription for the hot gas in these halos. The models that we studied were based on hot gas being in hydrostatic equilibrium with the dark matter halo, and described by a polytropic equation of state, or an equation of state modified to include an entropy injection term. We have found that the entropy models are distinguishable from the polytropic models via measurements of their tSZ distortion, even in low mass clusters and galaxy groups. While these models provide a useful starting point to evaluate the detectability of tSZ groups, an improved analysis will include a more realistic

Experiment	Model	$S/N = 3$	$S/N = 5$
ACT Deep	Entropy	1520	696
ACT Deep	Polytropic	3570	813
ACT Wide	Entropy	307	23
ACT Wide	Polytropic	1371	87
SPT Wide	Entropy	5487	131
SPT Wide	Polytropic	15856	759
SPT Deep	Entropy	2323	706
SPT Deep	Polytropic	3845	1465
PLANCK	Entropy	653	227
PLANCK	Polytropic	1110	418

Table 3.2: Anticipated yield of tSZ halos detectable by the ACT, PLANCK and SPT experiments, calculated by integrating the cluster abundance from the minimum detectable mass for a given survey and S/N level to an upper mass limit of $M_{\rm vir} = 2 \times 10^{14} M_{\odot}$.

treatment of the gas distribution as provided by high resolution cosmological simulations, which we intend to pursue in forthcoming studies.

Another issue that we have only partially addressed here, through the inclusion of an tSZ background contaminant, is the confusion caused by the superposition of tSZ distortions from hot gas in halos along the line of sight (see for e.g., Holder et al. (2007); Hallman et al. (2007b)). Here again a large volume cosmological simulation will help to quantify the impact of the tSZ background on the detection of group halos and their recovered flux. By taking advantage of the fact that nearby group halos produce a more extended tSZ signal, we aim to mitigate the impact of the tSZ background by devising algorithms to separate the group signal from the tSZ emission at smaller angular scales produced by higher redshift clusters. Finally the combination of maps of the various foreground contaminants with simulated tSZ maps will allow us to undertake a more accurate treatment of the foreground contamination. While we have been relatively conservative in our modelling of the foreground contaminants, we have not included effects such as the clustering of infrared point sources, which could turn out to be a significant contaminant in the

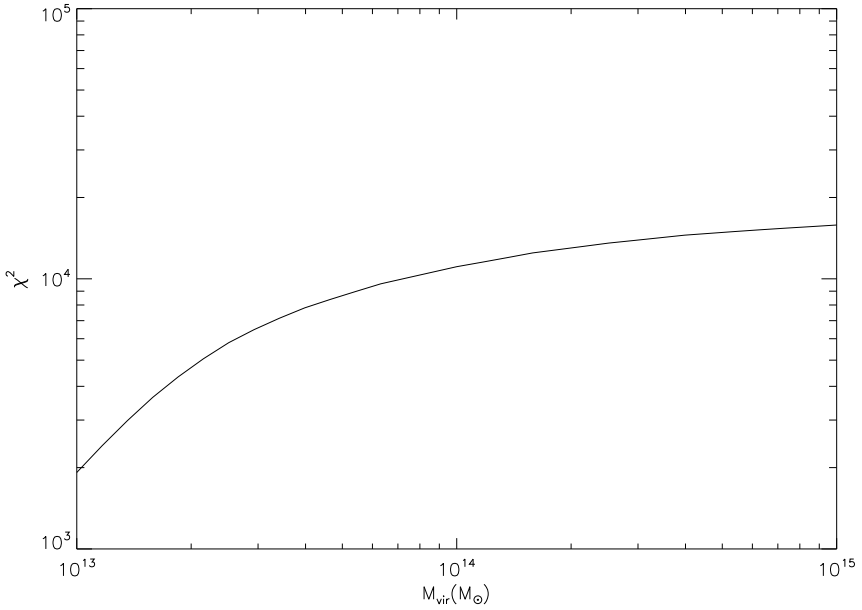

Figure 3.10: Significance with which the entropy model can be distinguished from the polytropic model by the nominal ACT survey as a function of halo mass, $M_{\rm vir}$. The χ^2 statistic is calculated by comparing the difference between model spectra to the residual noise and foreground level of the ACT experiment.

extraction of tSZ halos (Righi et al., 2008). We have also not included the kinetic SZ effect as a possible contaminant because it has the same frequency dependence as the primary CMB but a much smaller amplitude on the relevant angular scales. For the same reason we have not attempted to detect the halo via its kinetic SZ signal, though we note that a detection of the kinetic SZ signal could be enhanced by cross-correlation with optical or X-ray observations of the halo or the thermal SZ signal.

Prospects for detection of tSZ clusters have been studied previously in the case of PLANCK (Malte Schäfer and Bartelmann, 2007; Melin et al., 2006), ACT (Pace et al., 2008; Sehgal et al., 2007) and SPT (Melin et al., 2006), but these studies have mainly focused on the statistics of tSZ detections above the mass completeness limit of the respective surveys. Pace et al. (2008) found that ACT could detect tSZ halos down to $6 \times 10^{13} h^{-1} M_\odot$ fairly independent of redshift, whereas we have found that these halos become hard to detect at higher redshifts. The analysis of Pace

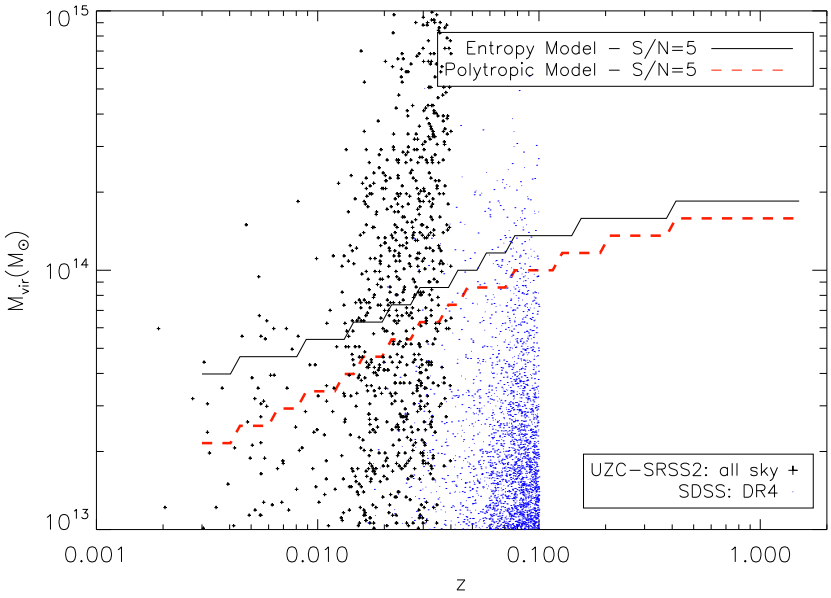

Figure 3.11: The minimum detectable mass, $M_{\rm vir}$, of tSZ halos as a function of redshift, z, for the ACT experiment compared to a compilation of groups (plotted as crosses) from the USGC (Ramella et al., 2002) and a galaxy group catalogue (plotted as dots) based on the Sloan Digital Sky Survey (SDSS DR4; Yang et al. (2007)). The SDSS groups are only shown up to a redshift of $z = 0.1$. The minimum detectable mass is plotted for an entropy model with $S/N = 5$ (solid curve) and $S/N = 3$ (dashed curve).

et al. (2008) only included the CMB as a foreground so it is conceivable that the inclusion of point source foregrounds would degrade their forecasts for low mass halos at high redshift, as we have found to be the case in our analysis. We also note that the analysis of Malte Schäfer and Bartelmann (2007) found that PLANCK could detect halos of mass $6 \times 10^{13} M_\odot/h$ below $z = 0.1$ when they included the CMB and all galactic foregrounds. In our analysis we have emphasised that smaller halos, with $M \simeq 3 - 4 \times 10^{13} M_\odot$, could be detected at $z \lesssim 0.01$.

The detection of hot gas in these galaxy groups and low mass clusters with the upcoming set of tSZ survey experiments will provide an interesting probe of galaxy formation and its effect on the distribution and state of the hot gas, which is most prominent in these halos. A measurement of the tSZ distortion at the virial radius of these halos will set a joint constraint on the level of entropy injection and the baryon fraction, which can be compared to the predictions from galaxy

formation models. In particular a measurement of the baryon fraction in the outskirts of galaxy groups and low mass clusters will provide a unique update to the baryon census in the local universe.

While the upcoming generation of tSZ experiments have been designed to carry out blind surveys of galaxy clusters, a targeted survey of galaxy groups already detected in optical and X-ray observations would yield a very interesting set of objects to study. The measurement of a diffuse signal on the scale of tens of arcminutes will be challenging though, and carefully planned and executed observations will be necessary to control systematic effects and produce high fidelity maps of the tSZ distortion in these halos. In combination with existing optical and X-ray observations of these halos, these measurements will enhance our knowledge of the physics of galaxy formation and its effect on the intragroup medium.

CHAPTER 4

Constraining Feedback and Star Formation in Galaxy Clusters with Measurements of the Thermal Sunyaev-Zel'dovich Effect

4.1 Introduction

The study of the nature and properties of the Cosmic Microwave Background (CMB), particularly in the last decade, has significantly improved our understanding of the universe. CMB experiments, either planned or underway – such as the Atacama Cosmology Telescope Project (ACT; Kosowsky, 2006), the South Pole Telescope (SPT; Ruhl et al., 2004) and Planck (The Planck Collaboration, 2006), will produce high resolution multi-frequency maps of the sky. An important goal of these experiments will be the detection of galaxy clusters through the Sunyaev-Zel'dovich (SZ) effect , caused by the interaction of CMB photons with cluster gas. Galaxy clusters allow one to study the evolution and distribution of matter over cosmic time, and provide a means for probing the underlying cosmology through their abundance as a function of redshift (Bahcall et al., 1999; Rosati et al., 2002; Voit, 2005). In light of this, several experiments have already presented analyses of galaxy clusters detected via the SZ effect (Hincks et al., 2009; Staniszewski et al., 2009; Plagge et al., 2009; Vanderlinde et al., 2010; High et al., 2010).

Cosmological studies demand statistically sound cluster catalogues with well defined selection criteria. A particular surveys selection function is linked to the properties of the instrument and the data reduction techniques applied to it. In light of this, considerable effort has been made by many researchers to develop methods to optimally detect and extract clusters via the SZ effect. Many types of filters have been utilised to isolate and measure the SZ signal in CMB maps. Such techniques include, Wiener filtering (see Tegmark and Efstathiou, 1996; Aghanim et al., 1997), fast independent component analysis (Maino et al., 2002b), maximum entropy method (Hobson et al., 1998, 1999; Stolyarov et al., 2002), matched filter analysis (Herranz et al., 2002b,a) and wavelet filters (Pierpaoli et al., 2005). To characterise the statistical properties of these detections many authors have applied cluster detection techniques to simulations (see, e.g., Melin et al., 2006; Vale and White, 2006; Malte Schäfer and Bartelmann, 2007). These studies concerned themselves with analytic or semi-analytic prescriptions for the clusters within the simulations, excluding gas physics (such as feedback), which alters the appearance of clusters (see for example Bonaldi et al., 2007). In light of this, Pace et al. (2008) presented analyses of SZ and X-ray cluster detections using single and multi-band filtering applied to simulations incorporating gas dynamics as well as other processes including feedback, star formation and radiative cooling.

Crucial to using clusters for cosmology is understanding how to relate observables, such as SZ flux, to quantities that can be predicted by theory, namely mass. Using such scaling relations, the final goal is to produce theoretical predictions for the distribution of cluster observables as a function of redshift and cosmological parameters. A non-negligible source of error in this type of analysis is scatter in the various scaling relations. Shaw et al. (2008) found that the internal dynamics of clusters, such as feedback effects, will introduce significant scatter (at least 20%) into the mass-SZ flux relation, brought about by variations in the cluster gas fraction. Accurate measurements of cluster gas properties will help to mitigate this scatter and allow a more robust sample of clusters for cosmology. In this chapter we show how well SZ observations can be used to constrain gas physics within clusters, such as feedback and the baryon and stellar fractions.

Another source of scatter in the SZ flux-mass scaling relation is flux measurement error brought about by projection effects (White, 2001; Holder et al., 2007; Hallman et al., 2007b).

It has been shown in Motl et al. (2005), that integrating the thermal SZ flux of clusters out to a significant fraction of the virial radius, permits a robust measure of cluster mass, by suppressing scaling scatter caused by heating or cooling effects in the core. However, as one probes the outer regions of halos, contamination due to undetected groups and clusters becomes prominent. In light of this, Shaw et al. (2008) derived optimal SZ flux integration limits aimed at minimising projection effects. They found that a maximum angular radius of $\approx 1'$ for a cluster of mass, $M \approx 1.4 \times 10^{14} M_{\odot}$ will provide the tightest SZ-flux to mass relationship. In this chapter we study projection effects from a different angle. We introduce a new deblending technique which improves the accuracy of halo profile extraction and flux estimation in low mass clusters by deblending contaminant sources out of the measurement. Such a method will be crucial in upcoming CMB experiments which will be signal rather than noise dominated.

The structure of the chapter is as follows. We summarise the main properties of the SZ effect in §4.2. In §4.3 we outline the sky simulations used in this study. The microwave deblender is described in §4.4. Analyses of group and cluster properties is presented in §4.5 and finally, our results are summarised and discussed in §4.6.

4.2 The Sunyaev-Zel'dovich Effect

The SZ effect is produced by the inverse Compton scattering of CMB photons by electrons in the intracluster gas. The thermal SZ (tSZ) effect results from the thermal motion of the electrons, whilst the kinetic SZ (kSZ) is caused by the bulk motion of the cluster itself. The kSZ is typically an order of magnitude weaker than its thermal counterpart. The tSZ effect is characterised by the dimensionless Compton parameter y_c as:

$$y_c = \frac{k_B \sigma_T}{m_e c^2} \int dl T_e n_e, \tag{4.2.1}$$

where k_B is the Boltzmann constant, σ_T is the Thompson cross-section, m_e is the electron mass, c is the speed of light, T_e and n_e are the temperature and number density of the gas electrons respectively, and the integral is performed along the line of sight. The change in the CMB

brightness temperature due to the tSZ effect is described by

$$\frac{\Delta T}{T} = y_c f(x), \tag{4.2.2}$$

where $f(x)$ is the tSZ spectrum

$$f(x) = \left(x \frac{e^x + 1}{e^x - 1} - 4 \right), \tag{4.2.3}$$

as a function of the dimensionless frequency $x = h\nu / k_B T_{cmb}$. The kSZ effect on the other hand, produces fluctuations in the brightness temperature of the form

$$\frac{\Delta T}{T} = -\frac{\sigma_T}{c} \int dl n_e v_r, \tag{4.2.4}$$

where v_r is the radial peculiar velocity of the cluster along the line of sight, defined to be positive for receding clusters. The kSZ effect is independent of frequency and is thus best estimated from observations near the tSZ null at $\nu \approx 218$ GHz.

4.3 ACT Sky Simulations

Simulated sky maps comprising the CMB, SZ effect (thermal and kinetic) and dust in the frequency channels relevant to ACT (148, 219 and 277 GHz) were produced for two cluster gas models; adiabatic and standard. The adiabatic model comprised a polytropic equation of state, while the standard model incorporated the effects of entropy through feedback processes as well as star formation. The individual source maps were provided by Sehgal et al. (2010) and are available freely at NASA's Lambda website[1]. Fig. 4.1 depicts the survey region covered by the extended and deep sky surveys (discussed later). This region was chosen because it is relatively free of dust contamination and corresponds to a portion of the actual ACT observing strip.

To simulate the ACT instrument characteristics, the sky maps at each of the ACT frequency channels, were convolved with a Gaussian beam of full-width at half-maximum equal to $1.4'$, $1.1'$ and $0.9'$ respectively. Varying levels of Gaussian random noise were then added to the maps to simulate different observing seasons. The noise levels included in this study, as well as the ACT characteristics are presented in Table 4.1.

[1]The website for the maps can be found at: http://lambda.gsfc.nasa.gov/toolbox/tb_cmbsim_ov.cfm

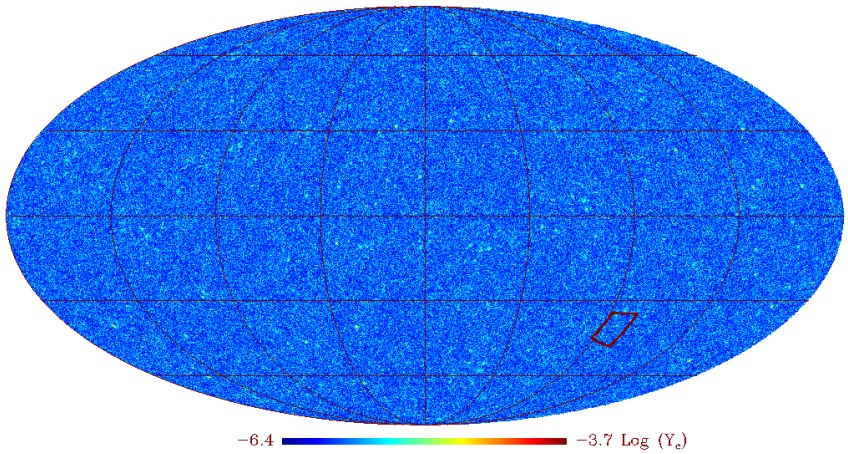

Figure 4.1: Mollweide projection of the input tSZ map. The 200 deg^2 survey area is depicted by the outlined region. Map units are presented in $\log_{10} \mathrm{Y}_c$.

4.4 The Microwave Deblender

Cosmology with the SZ effect relies on the application of the SZ flux to mass relation. Moreover, we expect the total flux to correlate with the intrinsic mass of the cluster Bartlett (see 2001), as predicted by numerical simulations (Motl et al., 2005; Nagai, 2006; da Silva et al., 2004). Accurate photometric measurements are crucial if one is to obtain reliable fluxes and consequent masses.

Flux recovery is a delicate art in which one has to balance algorithm generality and adaptivity to computational time restrictions. The redshift independence of the SZ effect introduces contamination due to projection effects along the line of sight (Holder et al., 2007). This effect is problematic especially when one attempts to recover the fluxes of galaxy groups. To overcome this issue we developed a microwave deblender which aims to deblend SZ halos and recover their individual fluxes, as well as to extract radial profiles.

Disentangling overlapping objects in astronomical images is a classical problem with a long history. Whenever one wishes to extract properties of non-isolated objects, deblending becomes necessary. There are many deblending codes that have been developed for optical astronomy.

For example, *COSMOS* which is described in Beard et al. (1990), *SExtractor* (see Bertin and Arnouts (1996)) and *FOCAS* (see Jarvis and Tyson (1981)) to name but a few. The deblender presented here is similar to the one used in the Sloan Digital Sky Survey (SDSS), but has been adapted for use with microwave data. For a thorough overview of the technical details, which are relevant to this deblender, one can refer to Lupton (2001).

4.4.1 The Map Deblending Algorithm

The first step in the deblending process is to segment the input map with dithering. This procedure decreases the computational time required since the algorithm is very sensitive to the number of pixels contained within the map blend. The deblending operation then proceeds in two stages. Firstly, sources (defined as children hereafter) are identified within the blend – which we shall call the parent. Secondly, the child templates are constructed by comparing the intensities of pairs of pixels situated symmetrically about the peak pixel and replacing both by the lower of the two. The latter stage does not mean that the final deblended child comprises any particular symmetry since shape symmetry is only enforced in the construction of the templates. In one dimension the problem is exemplified below:

$$P_i \approx \sum_{r=1}^{n} w_r T_{r,i}, \tag{4.4.5}$$

$$P_{cost} \equiv \sum_{i} \left(P_i - \sum_{r=1}^{n} w_r T_{r,i} \right)^2, \tag{4.4.6}$$

where P_i is the intensity of the parent at pixel position i, where i runs over the pixels in the blend and r runs over the n children. Essentially, the parent, P_i, is the sum of the individual child templates, $T_{r,i}$, multiplied by a particular weight function, where the weights, w_r, are calculated by minimising the chi-squared or cost value of the blend (P_{cost} in the above relation). Finally, the children in the blend are calculated by assigning flux for the r^{th} child, C_r, at pixel i as:

$$C_{r,i} = P_i \frac{w_r T_{r,i}}{\sum_{r=1}^{n} w_r T_{r,i}}. \tag{4.4.7}$$

In two dimensions the procedure is essentially the same except that we assume two-fold rotational symmetry about the object centre to construct the child templates. To explain further, we

create two dimensional templates for each child by extracting flux through an adaptive aperture which changes morphology automatically based on the object shape. Two-fold rotational symmetry is enforced by comparing pixels placed symmetrically about the centre of each child - where symmetric pixels are found simply by incrementing the angular position of pixel i by π radians. In this way we produce the templates for each child, which are then weighted to construct the final set of deblended children, in a manner which is identical to the one-dimensional case.

Through this process we produced a catalogue of deblended objects which can be photometrically analysed. The fluxes of the children were subsequently computed using an aperture. To compare the accuracy of this new deblender, object fluxes were compared to *SExtractor* as discussed below.

4.4.2 Statistics of tSZ Detections

The very strength that makes the SZ effect a powerful probe of cosmology, the redshift independence of the SZ source flux, means that the SZ sky will comprise not only well-defined sources but a plethora of weak signals super-imposed on one another, due mainly to unresolved clusters and groups spanning a range of masses and redshifts (Holder et al., 2007). To understand this effect, we created a ≈ 200 deg^2 map containing tSZ halos and 2μK per beam instrumental noise. The map contained halos ranging in mass from $2 \times 10^{11} M_{\odot}$ to $2 \times 10^{15} M_{\odot}$ within the redshift range $0 < z < 3$. Since the survey mass limit is significantly higher than the minimum mass object present in the maps, the data represents an adequate sample to study projection effects. The particular mass threshold chosen for the maps does not significantly effect the results, since the SZ power spectrum is dominated by clusters of the order of $10^{14} M_{\odot}$ (see Holder et al., 2007, and references therein).

To compare the efficiencies and accuracies of both algorithms in recovering cluster fluxes, we utilised the same object catalogue for both algorithms. To explain further, *SExtractor* was first run on the composite map. An output catalogue consisting of the positions of objects detected above 3σ were created and then passed to the deblender. The catalogue created in this way was

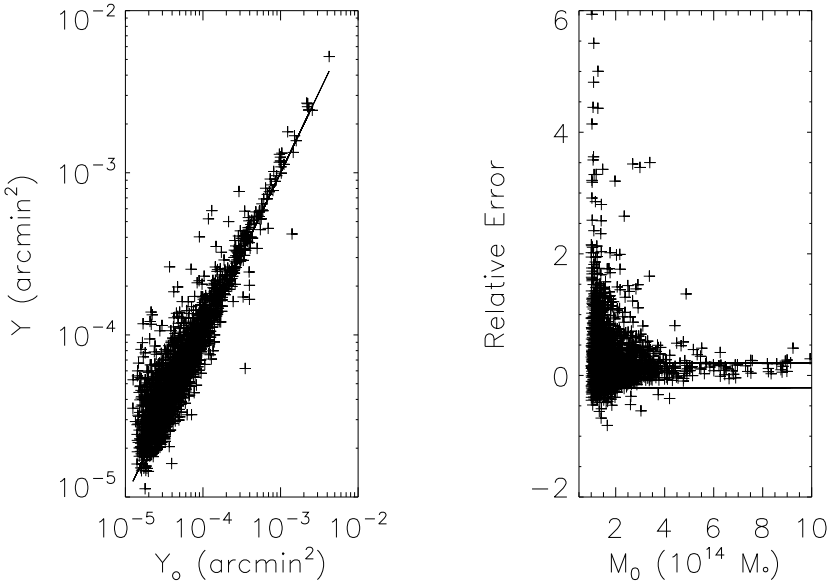

Figure 4.2: Flux recovery statistics for *SExtractor*. The solid lines in the right panel indicate 20% errors.

found to have approximately 80% purity. This technique ensures our conclusions are not biased by the cluster sample or by any other selection criteria. Photometric analysis was then performed by both *SExtractor* and the deblender, with the analysed halos matched to the simulation input catalogue to produce completeness and flux recovery statistics. Catalogue matching was performed using a matching length of $\approx 1.8'$ – which corresponds to the central radius of a typical cluster (similar to the half-light radius). All catalogue halos within this radius were flagged as candidates. The final match was taken to be the candidate whose mass was highest. If two objects were matched to the same object, the closest match was kept and the other was flagged as a contaminant. The recovered cluster fluxes (Y) obtained by *SExtractor* and the deblender are plotted against the halo catalogue fluxes (Y_o) to produce the left hand panels of Figs. 4.2 and 4.3 while the relative error given by:

$$error = \frac{Y - Y_o}{Y_o}, \tag{4.4.8}$$

is plotted in the right hand panel.

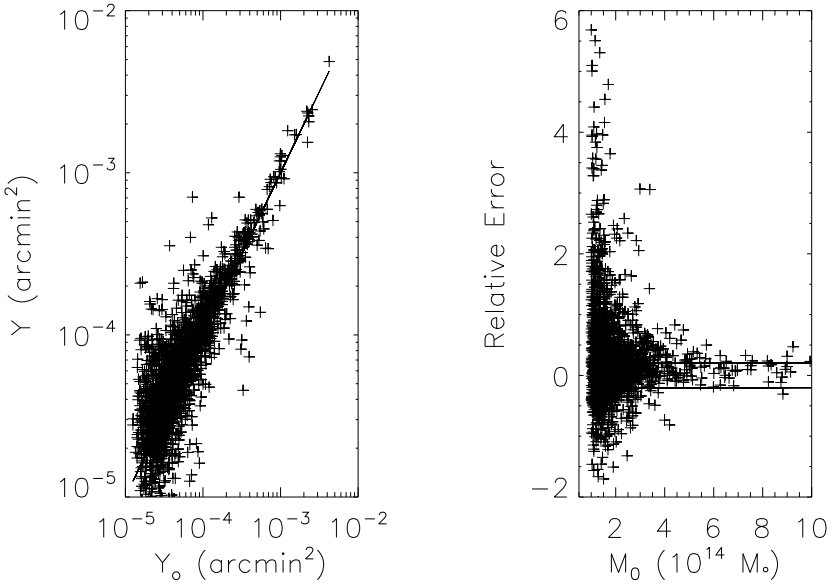

Figure 4.3: Flux recovery statistics for the deblender. The solid lines in the right panel indicate 20% errors.

The bias in the flux error for *SExtractor*, particularly at low fluxes, suggests that lower mass halos extracted by this algorithm suffer from contamination due to projection effects along the line of sight. The deblender has the same problem but to a lesser extent. The relative error for the latter indicates a more uniform distribution about the zero level. To quantify this error further, in Figs. 4.4-4.5, we present a histogram containing the errors in various mass bins for each of the algorithms. Also presented is the skewness (presented as a dimensionless quantity rescaled to the standard deviation) of the total error distribution. In the case of the deblender the skewness was found to be 0.0027, while in the case of *SExtractor* it was 0.0048–almost a factor of two larger, indicating that the deblender provides more uniform flux errors, particularly noticeable at low masses. Both algorithms do exhibit a slightly positive tail, particularly in the low mass bins. This is due to unresolved low mass halos that could not be removed, and thus caused a small projection effect.

The ability to measure low mass objects has a compounding effect on the quality of the overall catalogue. Moreover, the accurate description of these low mass objects allows one to

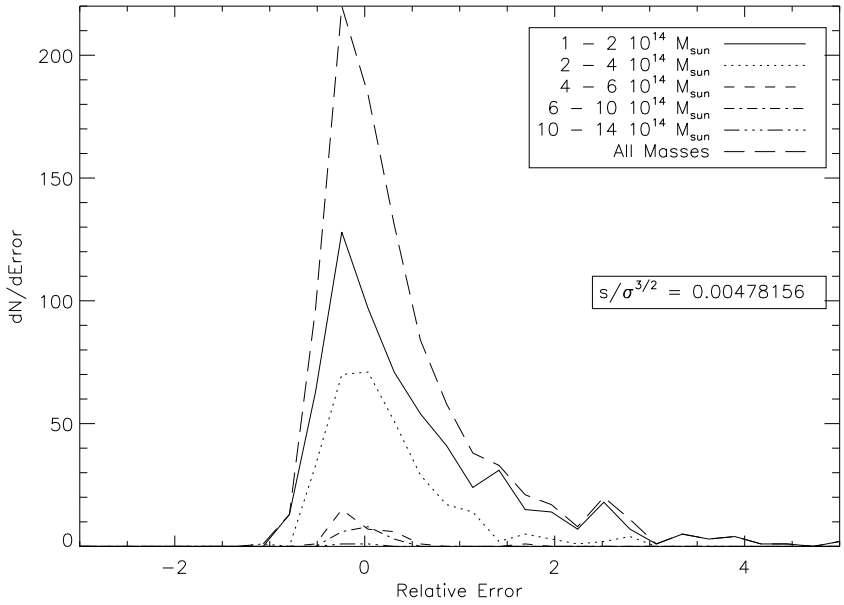

Figure 4.4: Histogram of flux recovery errors for *SExtractor* in five mass bins (signified by the different linestyles in the legend). The rescaled skewness of the total distribution is also presented.

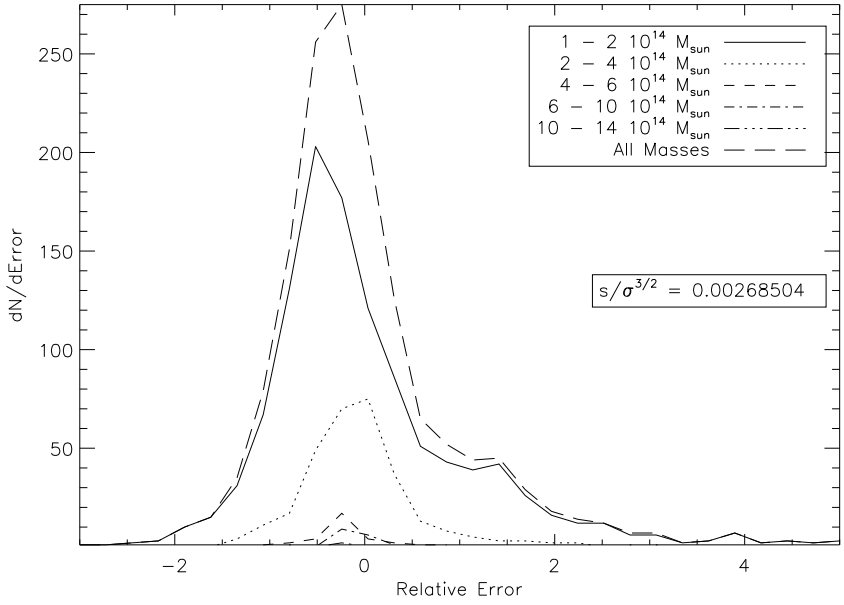

Figure 4.5: Histogram of flux recovery errors for the deblender in five mass bins (signified by the different linestyles in the legend). The rescaled skewness of the total distribution is also presented.

remove their contamination effects from higher mass objects, thus creating a cleaner catalogue throughout a large mass range. It must be said, that current telescope sensitivity is not at the level where these issues will skew results significantly, however, next generation experiments reaching sensitivities of a few μK will have to take into account such effects.

Another important attribute of the deblender is the ability to accurately probe the outer regions of clusters, which is especially useful when estimating radial profiles of objects. After a cluster has been detected, its centre is found by a simple centroiding algorithm. Concentric annuli, of thickness equal to the pixel resolution of the map in question (or the beam width in the case of beam-convolved maps), are then constructed around this centre. To estimate the sky level in each annulus, we place up to 30 annuli (analogous to dithering) around the local region of the cluster. We found that a minimum of 20 dithers were required for sky level convergence. We then take the median, in a pixel-by-pixel basis, of the set of annuli and subtract this final annulus from the object flux annulus yielding the final flux for that particular aperture.

The total error associated with each bin in the radial profile was calculated to be the summation (in quadrature) of the sky annulus error as well as the error in the estimation of the total background sky. The latter was determined by the standard deviation of the map pixels contained within an annulus extending from $\sqrt{3}R_{\rm vir}$ to $2R_{\rm vir}$ away from the cluster centre. The sky annulus error was determined using a similar method as the sky estimation discussed above. After dithering the set of annuli, each annulus was totalled to yield a set of sky values. We then calculated the standard deviation of this distribution to yield the sky error in each annulus. In Fig. 4.6 we illustrate the binned radial profile error for the deblender against direct profile extraction (where the profile is measured directly from the map without source removal) for two different mass bins. The radial profiles were extracted from a slightly larger area of sky than discussed previously, in order to increase the number of statistics. The fractional error, $\delta(\mathbf{r})$, was calculated as follows:

$$\delta(\mathbf{r}) = \frac{\sum_{N_{halo}} \left| \frac{\Delta T_{map}(\mathbf{r}) - \Delta T_{model}(\mathbf{r})}{\Delta T_{model}(\mathbf{r})} \right|}{N_{halo}}, \tag{4.4.9}$$

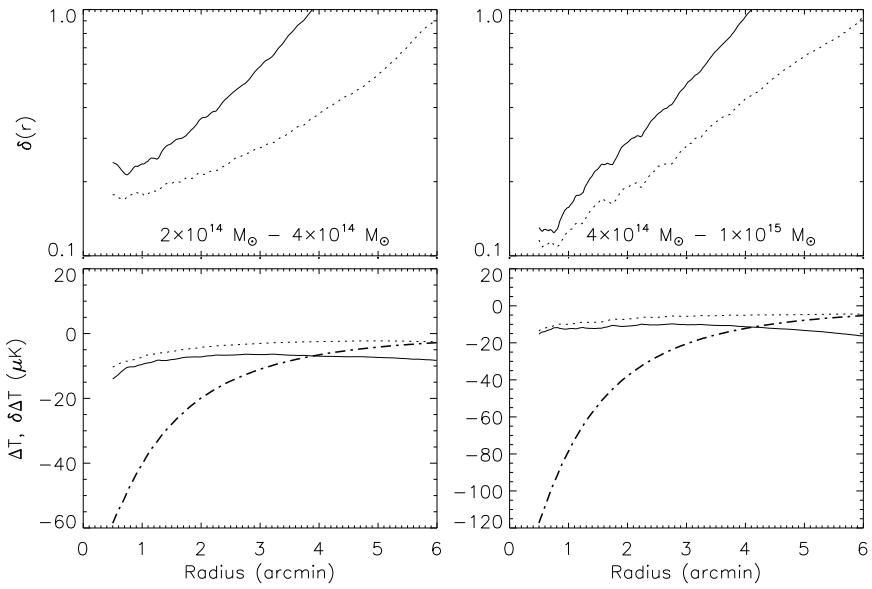

Figure 4.6: Direct (solid line) versus deblended (dotted line) radial profile extraction for two mass bins. The top panel illustrates the binned fractional error for the two extraction techniques, while the bottom panel expresses the error, compared to the average model profile (dot-dashed line). The lefthand side represents the mass bin $2 \times 10^{14}\mathrm{M}_{\odot} - 4 \times 10^{14}\mathrm{M}_{\odot}$, while the righthand side pertains to $4 \times 10^{14}\mathrm{M}_{\odot} - 1 \times 10^{15}\mathrm{M}_{\odot}$.

where ΔT_{model} is the model tSZ profile, ΔT_{map} is the extracted tSZ profile and N_{halo} is the number of halos in the particular bin. The fractional error shown in the top panel is significantly smaller for the deblender (dotted line) across the entire radial range. In the bottom panel we express this error as a fraction of the average SZ profile within the bin. At the centre of each halo the errors are comparable, however in the outskirts, the deblended profile is more accurate since contaminating objects are deblended out of each halo profile.

Although the overall integrated flux estimated from the blended or deblended profiles will be similar, owing to the low flux in the outskirts, the accuracy of profile estimation is improved. This is due to the fact that one is able to fit over a larger dynamic range. Furthermore, contamination removal allows more accurate shape fitting, which effects parameters such as β in the well known 'beta model'. As alluded to earlier, many studies of clusters currently do not use deblending since

the maps are dominated largely by noise, but in future studies, deblending of overlapping signals will be necessary.

4.5 Physical Properties of Clusters and Groups

In this section we utilise the simulated tSZ maps to study the accuracy with which physical parameters describing the structure of the intracluster medium can be measured. Our parametrised model for the distribution of hot gas in simulated clusters follows the prescription of Bode et al. (2009), on which the method of populating dark matter halos in the simulations with hot gas is based. We investigate how variations in the cluster model parameters modify the radial Compton profiles of simulated tSZ halos and utilise a Fisher matrix approach to quantify how accurately these physical parameters can be measured in realistic tSZ surveys.

4.5.1 Statistics of tSZ Detections

We first studied the statistics of detections of simulated tSZ halos using a Wiener filter with realistic assumptions for noise (for a given tSZ cluster survey) and foreground contamination in multi-frequency CMB maps. The Wiener filter, which recovers a minimum variance SZ map, is given by

$$W = SF^T \left[FSF^T + N\right]^{-1} = SF^T D^{-1}, \tag{4.5.10}$$

where S, D and N are the covariances of the signal, data and noise respectively, and F includes the beam and frequency dependence of the various signals. The template for the signal is based on a model for the gas distribution that is described in the next section. We found that the detection statistics of tSZ halos are only weakly dependent on the form of the template used, as long as the template is a reasonable approximation to the underlying signal. In addition to the instrumental noise, other components included in our analysis were the primary CMB, the kinetic SZ (which is small relative to the CMB) and galactic dust. More details of the foreground components are given in Sehgal et al. (2010). Although radio and infrared point sources do exist in the suite of simulations, we did not include them in this work, but plan to study their effects

on our results in a forthcoming paper. We expect flux and purity statistics to be adversly effected by their inclusion.

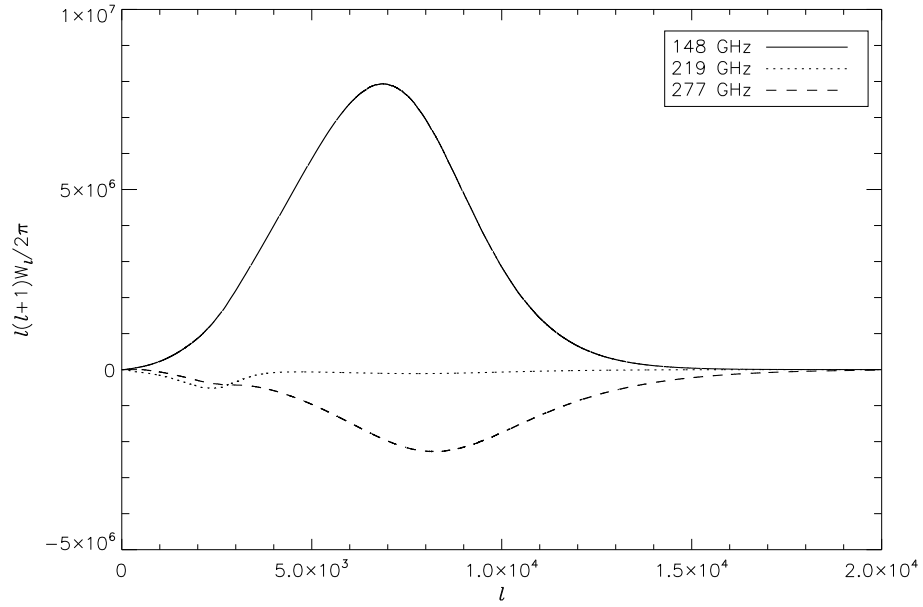

Figure 4.7: The multi-frequency Wiener filter weights plotted against multipole, l. We have multiplied the weights by $\frac{\ell(\ell+1)}{2\pi}$ to compare to the conventional way of plotting the CMB power spectrum. The weights for 148 GHz, 219 GHz and 277 GHz are signified by the solid, dotted and dashed lines respectively.

We considered an experiment with three frequency channels, namely, 148 GHz, 219 GHz and 277 GHz, the same as those used in the ACT experiment (Kosowsky, 2006). The filter profile for each frequency channel was generated by modelling the power spectra of each foreground component (see Moodley et al., 2009, for a detailed discussion). Fig. 4.7 presents the filter weights, W_ℓ, that are applied to the maps in each frequency band. We note that in the case of the 148 GHz and 277 GHz channels the weight function is peaked, but with opposite sign (due to the change in sign of the tSZ signal), at multipoles in the region of a few thousand where the tSZ signal template (taken to be that of a $4 \times 10^{14} M_\odot$ cluster at $z = 0.1$) peaks, whereas it is practically zero over this range of multipoles for the 219 GHz channel, since at these frequencies the tSZ signal is null. At low multipoles ($\ell < 2000$) the filter weights tend to zero to suppress

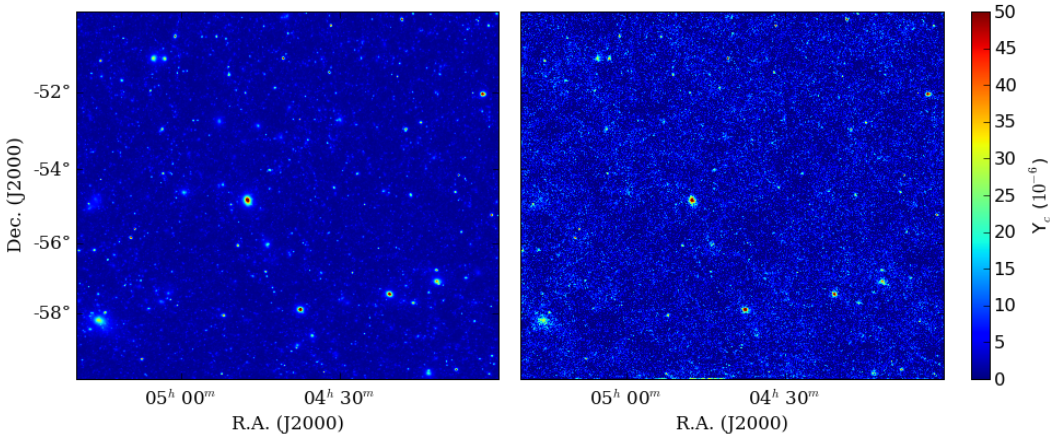

Figure 4.8: The 200 deg^2 input tSZ map (left) and filtered tSZ map (right) in Compton parameter units.

contributions from the primary CMB and galactic dust, moreover the weights in the 219 GHz and 277 GHz channels are opposite in sign to the weights in the 148 GHz channel to allow delicate cancellations of the CMB and galactic dust signals that are, respectively, constant and increasing in thermodynamic temperature of the CMB. At high multipoles ($\ell > 10000$) the filter weights go to zero to suppress the contamination from detector noise, if we were to include point sources in our filter then the filter weights would go to zero more rapidly at high multipoles.

The Wiener filter was applied in harmonic space to each of the three frequency maps, which were then summed and inverse Fourier transformed to obtain the filtered tSZ map in real space. We considered three tSZ surveys, a deep survey (ACT-Deep), a wide survey (ACT-Wide) with the same experimental sensitivities as those achieved by the ACT survey (Fowler et al., 2010) and similar to the SPT surveys (Lueker et al., 2009), and an extended deep (ACT-Extended) survey over the same area as the ACT-Deep survey but with greater sensitivity (as considered in Moodley et al. (2009) and Sehgal et al. (2007)). The experimental specifications for each of these surveys is given in Table 4.1.

The 200 deg^2 Wiener filtered tSZ map for the ACT-Deep survey is shown in the right panel of Fig. 4.8 where it is compared to the input tSZ map in the left panel. The input tSZ map is not

Table 4.1: Experimental specifications for a wide, deep and extended survey using ACT

Experiment	Area (deg^2)[a]	ν (GHz)[b]	σ_p (μK/beam)[c]	FWHM ($'$)[d]
ACT-Wide	800	148.0	28.6	1.4
		219.0	53.5	1.1
		277.0	133.8	0.9
ACT-Deep	200	148.0	14.3	1.4
		219.0	26.8	1.1
		277.0	66.9	0.9
ACT-Extended	200	148.0	2.0	1.4
		219.0	5.2	1.1
		277.0	8.8	0.9

[a] Sky area for particular survey.
[b] Instrumental frequency.
[c] Pixel noise per beam width.
[d] Full width at half-maximum of the beam related to the Gaussian beam width, $\theta_{\rm b}$, by FWHM $= \sqrt{8\ln 2}\,\theta_{\rm b}$.

convolved with the beam, unlike the filtered map, and both have the same pixelisation scale of $0.5'$. The dominant feature in the filtered tSZ map is the presence of detector noise on small scales which makes the smooth tSZ signals appear noisier. An examination of the power spectrum of the filtered tSZ map shows that there is a slight excess of power on large scales but this is hardly discernible in the map. Overall, halos in the input tSZ map with a central Compton distortion of $y \approx 4 \times 10^{-5}$ or higher stand out in the filtered tSZ map while halos with distortions as low as $y \approx 2 \times 10^{-5}$ are also visible.

To detect clusters in the filtered tSZ maps we first ran the source detection algorithm described in the previous section to identify peaks in the tSZ maps. We set the threshold high enough to increase the purity i.e., the ratio of true detections to total detections, in each of the maps to approximately 85% or better. We have considered two sets of maps for the different surveys corresponding to the standard and adiabatic model simulations described in Bode et al. (2009) and summarised in Appendix B. In the case of the standard model map, Fig. 4.9 illustrates that the wide survey only becomes complete at $7 \times 10^{14} M_{\odot}$ while the deep survey is complete

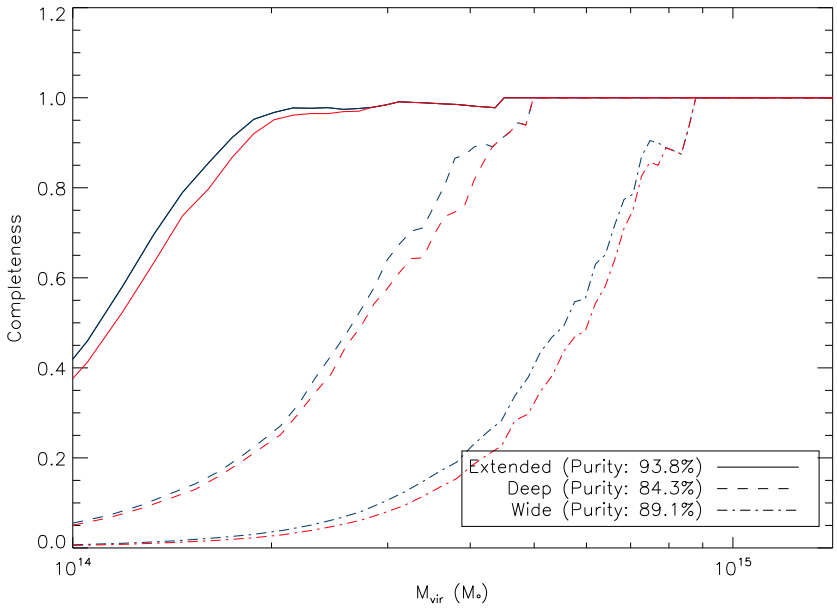

Figure 4.9: Completeness statistics for the ACT-Wide, ACT-Deep and ACT-Extended surveys using a standard model (red lines) and adiabatic model (blue lines) filtered tSZ map.

at $5 \times 10^{14} M_{\odot}$. Both of these surveys do not detect many low mass clusters and groups below $1 \times 10^{14} M_{\odot}$, though at lower masses the completeness of the deep survey is greater than that of the wide survey due to its lower pixel noise. The extended survey with its higher sensitivity is able to detect groups at $5 \times 10^{13} M_{\odot}$ with 10% completeness and clusters at $1 \times 10^{14} M_{\odot}$ with 40% completeness. The extended ACT survey becomes complete at approximately $2 \times 10^{14} M_{\odot}$, which agrees with the completeness reported for ACT by Sehgal et al. (2007) and Moodley et al. (2009) due to the consistency of the noise levels assumed in these papers.

To determine how many galaxy groups and clusters will be used for model parameter constraints in §4.5.3, we computed the abundance of detected tSZ halos in the standard model maps for the wide, deep and extended surveys. Fig. 4.10 displays the abundances as a function of mass above a mass limit of $1 \times 10^{14} M_{\odot}$. We note that the deep survey contains more low mass clusters above the detection threshold, while the wide survey has more high mass clusters detected resulting from the larger area. Due to the sensitivity to low mass clusters and the steep mass function for galaxy clusters overall, the deep survey comprises more clusters detections, approximately

100 in total, in comparison to the wide survey, which has approximately 40 in total. The extended survey, which contains much lower pixel noise, has significantly more cluster detections, over 700 in total, than both the wide and deep surveys. The majority of these clusters, roughly 550, are at masses below $2 \times 10^{14} M_{\odot}$ with few objects detected at the highest masses, due to the smaller area of sky covered in comparison to the wide survey.

Fig. 4.9 also shows the completeness of the adiabatic filtered tSZ maps for the different surveys. We expect that the adiabatic model map should contain a larger number of detected clusters in comparison to the standard model map as there is neither star formation in the adiabatic model, which increases the average entropy in the cluster centre, nor AGN and supernovae feedback, which pushes gas into the outskirts of the halo. Both these effects, which are present in the standard model map, reduce the central Compton distortion, making these halos harder to detect. The differences between the number of detections in the adiabatic and standard model maps are in fact quite small for the different surveys, with the completeness of the adiabatic model map not significantly higher than that of the standard model map. This could be due to the fact that the effects of star formation and feedback only slightly change the integrated Compton distortion i.e., the tSZ flux, in clusters as has been demonstrated in Motl et al. (2005); Nagai (2006); Reid and Spergel (2006) using numerical simulations.

As we will see in §4.5.2 the effects of star formation and feedback are more pronounced on the Compton profile, which suggests that this observable is more sensitive to physical cluster parameters, such as the feedback energy and the amount of star formation. For the halos detected in these maps we will use their radial Compton profiles to probe the underlying physical parameters that determine the distribution of hot gas in each cluster. In the next section we describe how the Compton profiles for each of the detected tSZ halos were extracted from the maps.

4.5.2 Compton Profiles of tSZ Halos

To extract the radial Compton profiles, $y_n(r)$, of individual halos we ran the deblender algorithm, described in §4.4, on objects detected in the filtered tSZ maps. The algorithm extracts postage stamp images around each cluster, in which the flux contribution from nearby clusters and groups

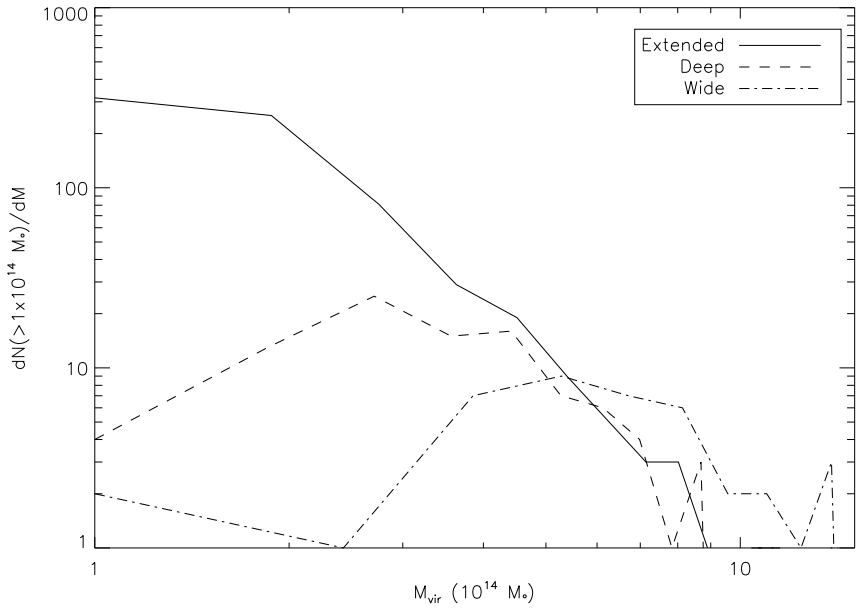

Figure 4.10: Abundance of detected tSZ halos in the standard model maps for the wide (dot-dashed), deep (dashed) and extended (solid) surveys.

has been deblended. As demonstrated in §4.4 the deblending process produces a more accurate radial Compton profile particularly in the outer regions of the cluster. We used angular bins corresponding to size of the ACT beam at the lowest frequency, 148 GHz, so that measurements of the Compton profile in each annulus would be uncorrelated by the beam. The error in the Compton profile, $\sigma(r)$, in each bin was estimated using the bootstrapping technique described in §4.4, and includes detector noise, residual contamination from Wiener filtering of the CMB, kSZ and dust, as well as fluctuations in the diffuse tSZ background.

In Fig. 4.11 we show the tSZ profile, $\Delta T(r)$, of a cluster extracted from the filtered adiabatic model tSZ maps as dotted points, with a set of three error bars that correspond to the tSZ profile errors for the wide, deep and extended survey maps. We observe that the profile error bars are the smallest in the extended survey, because of its lower noise level. However, the profile errors are only slightly larger in the deep and wide surveys, which is a consequence of the inverse noise weighting that results from using the Wiener filter. We have checked that if a uniform weighting of the noise was used instead, then the profile error bars in the wide survey are at least

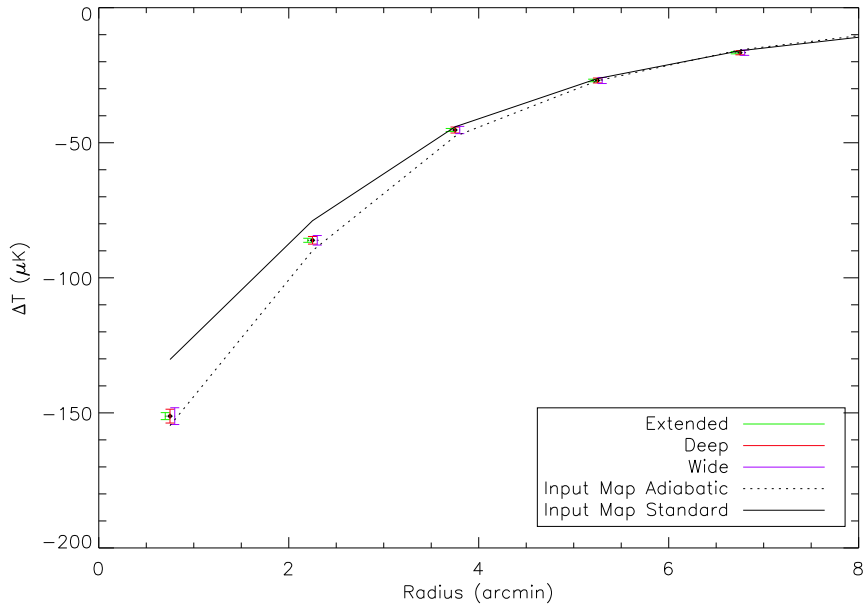

Figure 4.11: Radial profiles for a typical cluster in the simulation. The solid and dotted lines label the standard and adiabatic models respectively. Furthermore, the green, red and blue error bars specify the profile errors on the extended, deep and wide surveys respectively.

a factor of two larger. Also shown in Fig. 4.11 is the tSZ profile measured from the input map which in the case of the adiabatic model (dotted line) matches closely with the profile measured in the filtered maps. This indicates that any bias effect of the Wiener filter on the Compton profile is small. Finally to compare the differences of the underlying model on the tSZ profile, we extracted the Compton profile of the same cluster from the input standard model map which is shown as the solid line in Fig. 4.11. We note that the difference between the adiabatic and standard model profiles is larger than the error bars on the adiabatic model which indicates that we can distinguish these models for all three surveys.

In order to interpret the radial tSZ profiles in terms of cluster parameters, we have constructed models for the distribution of hot gas in clusters. Moreover, we consider two models studied in Bode et al. (2009), their ‘zero’ model which we refer to as the ‘adiabatic’ model, which contains no star formation or feedback, and the ‘standard’ model, which includes star formation and feedback. The gas models are described in detail in Appendix B but we summarise their main

features here. The dark matter profile of the halo is assumed to be a generalised, spherically symmetric, NFW profile with concentration, c, and inner slope, α, with its normalisation fixed by requiring that the integrated mass out to the virial radius equals the virial mass, $M_{\rm vir}$. The gas is assumed to be in hydrostatic equilibrium with the dark matter halo with polytropic index $\gamma = 1.2$, and to have mass which equals the baryonic mass less the stellar mass. Here the baryonic mass and stellar mass are, respectively, the baryon fraction, f_b, and stellar fraction, f_s, times the virial mass of the halo.

Removing gas that cools to form stars changes the average entropy of the halo. Other processes that increase the entropy of the halo include feedback from AGN and supernovae which we model as a term proportional to the mass in formed stars, with coefficient ϵ_F. The model also allows for a dynamical energy to be transferred from the dark matter halo to the gas, which we assume has a coefficient $\epsilon_D = 0.05$ and a non-thermal component of the gas pressure with fractional contribution, $\delta_{\rm rel}$, which we assume to be zero following Bode et al. (2009). These terms are incorporated into the energy conservation equation, together with a term that allows the halo to expand or contract adiabatically. The gas density and pressure are obtained by solving the energy conservation equation together with a conservation equation for surface pressure at the cluster boundary. Once the gas pressure profile is known we integrate it along the line of sight to obtain the projected Compton profile which can be compared to the simulated profile.

To test the accuracy of our models we compared the radial tSZ profile for each halo (with $M_{\rm vir} > 1 \times 10^{14} M_{\odot}$) in the standard model simulation, to the radial profile computed from our model for that halo. We avoided the contamination due to the projection of tSZ flux from other halos in the simulation along the line of sight by comparing to catalogue profiles, which are integrated over the cluster path length, rather than profiles extracted from the tSZ map. To calculate the cluster profile we needed to specify the parameters of the cluster model. The cluster mass and redshift were obtained directly from the halo catalogue. In the case of the concentration and the inner slope of the dark matter density profile we fitted to the dark matter mass and density profiles respectively. The feedback coefficient and stellar fraction were specified by the choice of model, in this case the standard model, as described in Appendix B. The baryon

fraction for each halo was calculated through the use of a scaling relation (see Eq. (4.5.13) for further explanation) – which was formulated by using the catalogue. We found that our models reproduced the simulated profiles with an accuracy better than 20% over a large range of radii,halo mass and redshift. The small discrepancy between the model and simulated profiles is likely due to the slight differences between the underlying parameters of the simulated halo and the model parameters, such as the concentration, inner slope of the dark matter density profile and the stellar and baryon fractions, that were fitted using the information available in the catalogue. Moreover, the simulation used the full three dimensional gravitational potential for the halo, which is in general aspherical, whereas our model uses a spherically symmetric gravitational potential that could in general have small differences with the spherically averaged simulated profile.

The fact that our implementation of the model reproduces the radial tSZ profiles with reasonable accuracy for clusters spanning a wide range in mass and redshift, indicates that the model provides a good description of the underlying physics of the simulated halos, in particular the change in cluster properties due to variations of the underlying cluster parameters. This suggests that our implementation of the cluster model can be used to study the constraints that radial tSZ profiles will set on the underlying cluster parameters, such as the stellar fraction, baryon fraction and feedback energy coefficient. We note that this model has also been used by Vanderlinde et al. (2010) to interpret the results from their tSZ cluster survey and has the advantage, over models like the β model, that have been used because of their simple parametric form for the Compton profile, that it makes a direct connection with the underlying gas physics. We turn to the objective of constraining cluster parameters in the next section.

4.5.3 Constraints on Cluster Parameters

Consider a cluster with Compton profile $y_{ij}(r)$ where the indices label the redshift bin, z_i, and mass bin, $M_j(z_i)$ of the cluster. We write the likelihood of the Compton profile for this cluster as

$$L^{ij} = \frac{1}{\sqrt{(2\pi)^{N^{ij}}\det(C^{ij})}} \times \exp\left(-\frac{1}{2}\sum_{n,n'=1}^{N_{ij}}[y_n^{ij} - \hat{y}_n^{ij}(\boldsymbol{\theta})][C_{nn'}^{ij}]^{-1}[y_{n'}^{ij} - \hat{y}_{n'}^{ij}(\boldsymbol{\theta})]\right) \tag{4.5.11}$$

where we have binned the radial profile, y_n^{ij}, into N^{ij} bins with $\hat{y}_n^{ij}(\boldsymbol{\theta})$ representing our model for the Compton profile that depends on the cluster parameters, $\boldsymbol{\theta}$, and $C_{nn'}^{ij}$ the covariance matrix of the binned radial profile. The finite beam induces covariance between pixels smaller than the beam size, so in estimating the Compton profiles we choose radial bins the size of the beam at the lowest frequency. In this way the covariance matrix becomes approximately diagonal and can be written in the form $C_{nn'} = \delta_{nn'}\sigma_n^{ij}$ where σ_n^{ij} is the Compton profile error estimated from the filtered tSZ map using the method described in §4.5.2. This error includes noise effects present in the maps and associated profiles.

Instead of computing the likelihood function directly, which is computationally intensive due to the high dimensionality of the parameter space being explored and the large number of detected clusters, we instead compute the Fisher matrix to infer marginalised errors on cluster parameters. The Fisher matrix is the second derivative of the log likelihood function with respect to the cluster parameters and characterises the curvature of the likelihood surface around the maximum likelihood fiducial model. As our models reproduce with reasonable accuracy the Compton profiles of the simulated halos and the variations of these profiles due to changes in the underlying cluster parameters, this approach is both fairly accurate and efficient at forecasting parameter constraints. Taking the second derivative of the log likelihood function the Fisher matrix for an individual halo detected in the tSZ map for a given survey is obtained as

$$F_{ab}^{ij} = \sum_{n=1}^{N^{ij}} \frac{\partial y_n^{ij}}{\partial a}\frac{\partial y_n^{ij}}{\partial b}\frac{1}{(\sigma_n^{ij})^2}, \tag{4.5.12}$$

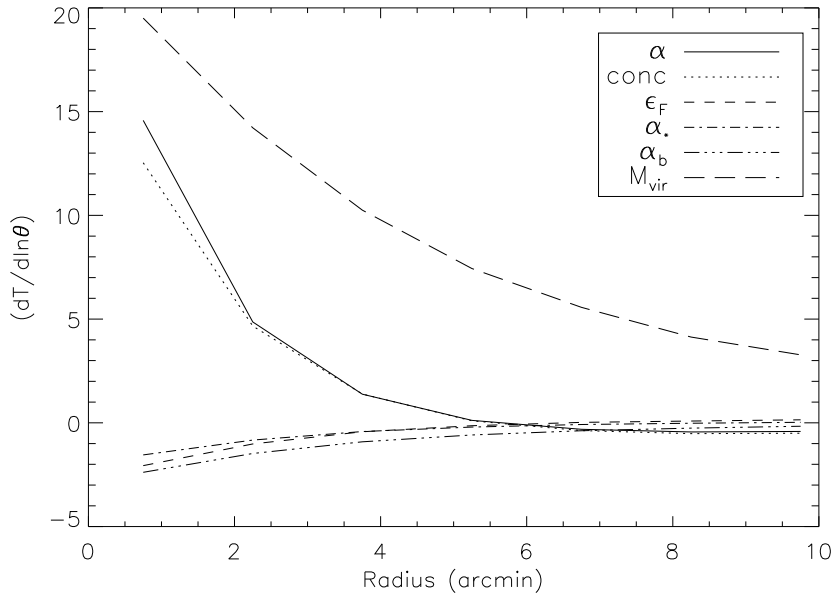

Figure 4.12: Fisher matrix derivatives for a low mass cluster. Each linestyle presents the derivative with respect to a particular parameter.

where the binned radial profile errors, σ_n^{ij}, are determined for the Compton profile of each halo extracted from the simulated maps.

We consider variations in the virial mass and concentration of the halo, the inner slope of the dark matter density profile, the feedback energy coefficient, and the stellar and total baryon mass fractions. Observations of these clusters with facilities operating in other wavelength bands will constrain or even measure a subset of these parameters for each halo in the survey, for example, weak lensing observations that measure the virial mass or infrared photometry that constrains the stellar mass. We do not place priors on any of the above parameters arising from these complementary observations of the cluster, apart from assuming that the redshift of the cluster will be well measured from follow-up spectroscopic observations. Hence, our full parameter set is $\boldsymbol{\theta} = \{c^{ij}, \alpha^{ij}, M_{\rm vir}^{ij}, \alpha_b, \alpha_*, \epsilon_F\}$ where the indices i and j are used to label parameters that vary from halo to halo. The parameter ϵ_F specifies the level of AGN and supernova feedback, which is assumed to be proportional to the mass of formed stars in the halo, while α_b and α_* specify the

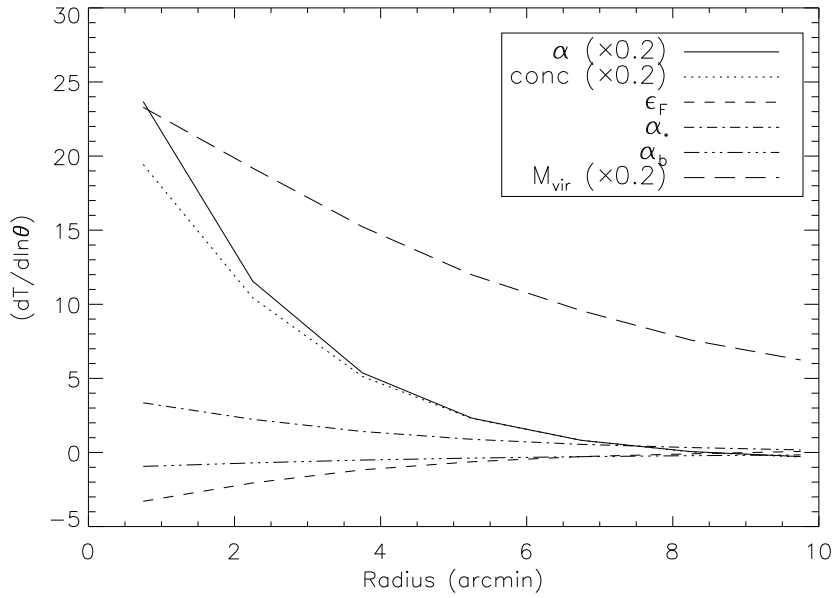

Figure 4.13: Fisher matrix derivatives for a high mass cluster. Each linestyle presents the derivative with respect to a particular parameter.

baryon and stellar mass fractions via the following scaling relations

$$f_b(M_{\rm vir}) = f_{b,0}\left[\frac{M_{\rm vir}}{1\times10^{15}M_\odot}\right]^{\alpha_b} \tag{4.5.13}$$

$$f_s(M_{\rm vir}) = f_{s,0}\left[\frac{M_{500}}{3\times10^{14}M_\odot}\right]^{-\alpha_*}, \tag{4.5.14}$$

where we have chosen a pivot mass of $M_{500} = 3\times10^{14}M_\odot$, following Bode et al. (2009) to normalise the stellar fraction scaling relation, and a sufficiently high pivot mass of $M_{\rm vir} = 1\times10^{15}M_\odot$, where we expect the baryon fraction to be well constrained, to normalise the baryon fraction scaling relation. Specifying the type of model fixes the stellar fraction scaling relation, for example, in the case of the standard model it is derived from Lin et al. (2003), while the baryon fraction scaling relation is inferred by fitting directly to the baryon fraction-mass relation in the corresponding simulation. Variations in the dynamical energy transfer between the gas and dark matter halo are not studied, but will form part of future work. To compute the Fisher matrix we need to specify a fiducial model, which we choose to be the standard model. In this case $f_{b,0} = 0.15, \alpha_b = 0.06, f_{s,0} = 0.0164$ and $\alpha_* = 0.26$. In the standard model simulation the

baryon and stellar fractions are found to be approximately constant from redshift $z = 0$ to $z = 1$ which spans the redshift range of the majority of detected clusters in the filtered maps, hence, we do not assume a redshift dependence for the baryon and stellar fraction scaling relations.

An important aspect of the Fisher matrix calculation is the sensitivity of the measured cluster profiles to variations in the cluster parameters. In Fig. 4.12 and Fig. 4.13, respectively, we show the derivatives of the Compton profile with respect to our set of parameters for a low mass halo with mass, $M_{\rm vir} = 1.0 \times 10^{14} M_{\odot}$, and at redshift, $z = 0.08$, and a high mass halo with mass, $M_{\rm vir} = 8.7 \times 10^{14} M_{\odot}$, and at redshift, $z = 0.09$. We notice that the derivative with respect to the virial mass is largest, which means that this parameter is better constrained, on a halo by halo basis, than the other parameters. The derivatives with respect to the concentration, c, and inner slope of the dark matter profile, α, are also large but are quite degenerate with each other, which is expected because an increase in concentration can be compensated by increasing the inner slope to leave the profile relatively unchanged. Our aim in this work is not to measure the mass, concentration and inner profile of individual halos using the tSZ profile, but rather to determine how well we can constrain feedback, star formation and the baryon fraction using the tSZ profiles from a set of observed clusters. Henceforth, we will treat $M_{\rm vir},\ c$ and α as nuisance parameters that will be marginalised over on a cluster by cluster basis, which means that the $c-\alpha$ degeneracy is only relevant if it projects strongly into the other parameter directions.

The derivatives of the parameters we are primarily interested in constraining, namely, $\epsilon_F,\ \alpha_b$ and α_* are much smaller and nearly degenerate for the low mass cluster. This means that a large set of cluster profiles is required to set strong constraints on these parameters. It is interesting that the relative shapes of the ϵ_F, α_b and α_* derivatives change for the high mass cluster which suggests that low mass clusters and high mass clusters could provide somewhat orthogonal constraints on the feedback energy, and stellar and baryon mass fractions.

As discussed above we are primarily interested in constraining the scaling relation parameters, such as the feedback coefficient, and stellar and baryon fractions, so we marginalise over nuisance parameters, such as the concentration, the inner slope of the dark matter profile, and the mass of individual halos. This is easily achieved in the Fisher matrix approach by considering

Table 4.2: Parameter constraints for the wide, deep and extended survey

Experiment	$\epsilon_F(4.0 \times 10^{-6})$	$\alpha_*(0.26)$	$\alpha_b(0.06)$
ACT-Wide	5.8×10^{-6}	0.39	0.11
ACT-Deep	3.9×10^{-6}	0.33	0.099
ACT-Extended	1.3×10^{-6}	0.09	0.045

only the corresponding sub-matrix of the inverse Fisher matrix, so that the marginalised inverse Fisher matrix for an individual halo is given by

$$\mathcal{F}^{-1}_{\alpha\beta,ij} = [F_{\alpha\beta,ij}]^{-1}, \tag{4.5.15}$$

where the physical parameters of interest to us, $\{\alpha, \beta\}$, are a subset of the full set of parameters, $\{a, b\}$. Summing the marginalised Fisher matrix over all halos detected in a given survey we obtain

$$\mathcal{F}_{\alpha\beta} = \sum_{i=1}^{N_z} \sum_{j=1}^{N_m(i)} \mathcal{F}_{\alpha\beta,ij}, \tag{4.5.16}$$

where each redshift bin in general contains a different number, $N_m(i)$, of detected halos in that survey.

In Fig. 4.14 we plot the joint two dimensional parameter constraints on the feedback coefficient, ϵ_F, and the baryon and stellar fraction scaling relation indices, α_b and α_*, for the wide, deep and extended surveys. We observe that the wide survey will be unable to constrain any of these parameters with any significance while the deep survey will just be able to measure the feedback coefficient. The marginalised 1-σ constraints on each parameter, $\sqrt{\mathcal{F}^{-1}_{\alpha\alpha}}$, is given in Table 4.2 with the fiducial value quoted after each parameter. It is interesting to note that the degeneracy directions between the different parameter combinations is different in the wide and deep surveys, as we will see this is likely due to the constraints coming from low mass clusters that are somewhat orthogonal to the constraints from high mass clusters.

In the case of the extended survey the constraints are significantly stronger than in the case of the deep and wide surveys, which is not surprising given its better sensitivity. Even though the

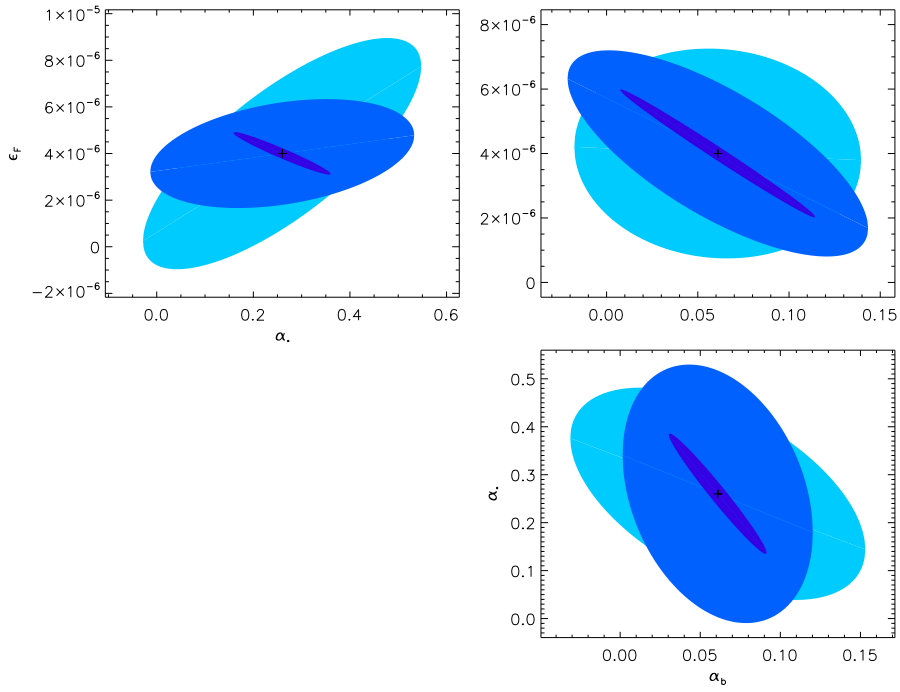

Figure 4.14: Error ellipses for physical cluster parameters: wide (turquoise), deep (blue), and extended (purple) surveys.

extended survey cannot break the degeneracies between the cluster parameters it is still able to set interesting constraints; the fractional errors on the feedback coefficient, stellar fraction index and baryon fraction index are 33%, 35% and 75%, respectively. We note that the degeneracy directions between the cluster parameters in the case of the extended survey are somewhat orthogonal to the degeneracies between these parameters in the deep and wide surveys. We investigated this point further and found that the information from low mass clusters provides tight constraints in a direction orthogonal to the degeneracy present in the observations of high mass clusters. In Fig. 4.15 we show the joint parameter constraints using low mass clusters ($M < 3 \times 10^{14} M_{\odot}$), high mass clusters ($M > 3 \times 10^{14} M_{\odot}$) and all clusters. We see that the drastic reduction in the errors on the cluster parameter arises from the orthogonal information that low mass clusters and high mass clusters provide.

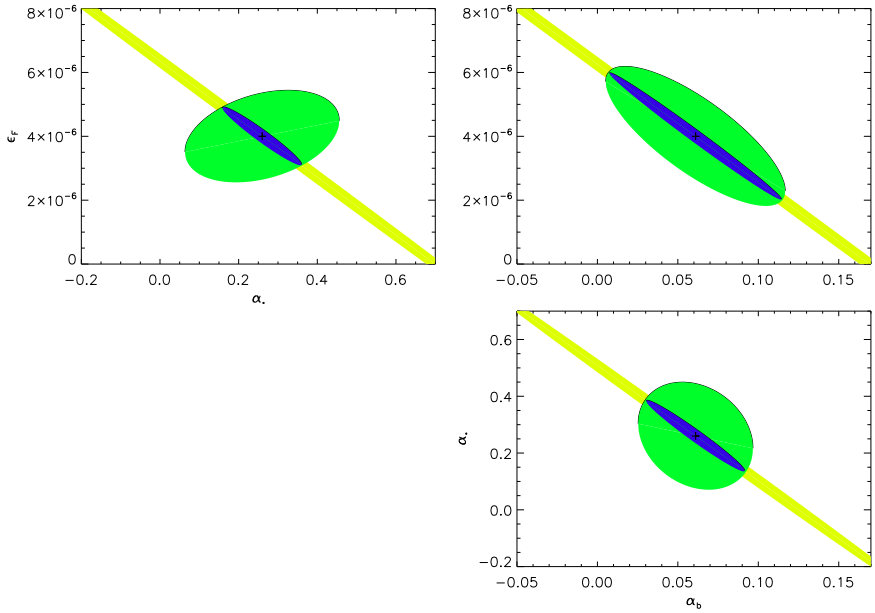

Figure 4.15: Error ellipses for physical cluster parameters: extended survey for clusters with virial mass below $3 \times 10^{14} M_{\odot}$ (yellow), clusters above $3 \times 10^{14} M_{\odot}$ (green) and all clusters (purple).

The measurement of the stellar fraction and baryon fraction indices in the extended survey means that these observations will be able to measure a departure from a constant scaling relation. In Fig. 4.16 we show the accuracy with which each survey will constrain the baryon and stellar fraction scaling relations. The pivot mass for the stellar fraction scaling relation is at a mass $M_{\rm vir} = 7 \times 10^{14} M_{\odot}$ while the pivot mass for the baryon fraction scaling relation is at a mass $M_{\rm vir} = 1 \times 10^{15} M_{\odot}$. We note that the extended survey will set interesting constraints on these scaling relations. In this work we have chosen not to place external priors on any of the cluster parameters, however, we do note that complementary measurements of these parameters are available from observations at other wavelengths.

Several authors have investigated the properties and scalings of the baryon, stellar and gas fractions within clusters and groups. For example, Lin et al. (2003) presented an analysis of 27 galaxy clusters using the Two Micron All Sky Survey (2MASS) and provided scaling relations

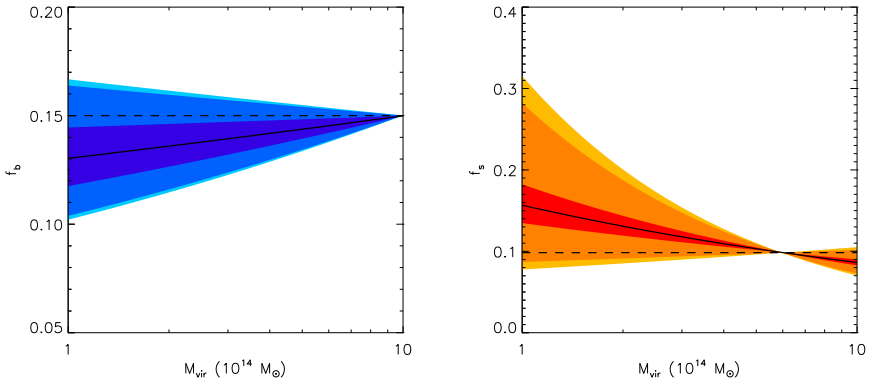

Figure 4.16: Constraint on the baryon fraction (left panel) and stellar fraction (right panel) scaling relations ellipses from the extended survey.

for the baryon and stellar fractions. In the case of the latter, they estimated α_* to be 0.26 with an error of 0.09. Using *Chandra* observations, Vikhlinin et al. (2006) derived estimates for the gas fraction within 13 clusters. They found that within r_{2500} the measured fraction was significantly lower than the observed universal baryon fraction. These results were corroborated by an analysis of 43 galaxy groups in Sun et al. (2009). More recently, Bode et al. (2009) presented joint constraints on the feedback and stellar fraction scaling index using measurements of the gas fraction from Vikhlinin et al. (2006) and Sun et al. (2009), although they did not minimise over other gas parameters. These complementary constraints will help to further reduce the parameter errors quoted in our work.

4.6 Discussion and Conclusions

In this chapter we have investigated how the tSZ can be used to contrain gas properties of clusters. We implemented a new deblending technique which not only recovered unbiased halo fluxes, but also accurate radial profiles over a large angular range. With regards to the former, we showed that the skewness of the error distribution was a factor of two better in the case of the deblender, due mainly to the excision of background halos. In the case of radial profile extraction, we compared direct profile versus deblended profile extraction and proved that the deblender produces

smaller errors over the entire angular range. The measurement of accurate radial profiles has a direct consequence on profile fitting and cosmological parameter estimation.

In the second part of this chapter we used a multi-frequency Wiener filter to obtain a map of the tSZ signal. From these maps we extracted halo profiles with error bars for each of the detected clusters, and compared them to tSZ profiles generated from gas models following the Bode et al. (2009) prescription. Assuming different surveys with ACT, we used a Fisher matrix analysis to investigate constraints on feedback and the stellar and baryon fractions in cluster halos. We found that the wide survey will be unable to place constraints on any of these parameters, while the deep survey will be able to constrain feedback. The extended survey however, will be able constrain the feedback parameter, stellar and baryon fraction indexes with fractional errors of 33%, 35%, 75% respectively. An interesting point to note is the fact that the degeneracies in the case of the extended survey are orthogonal to those in the wide and deep surveys - especially evident in the $\epsilon_F - \alpha_*$ plane. This is due to the additional information gained from low mass clusters detected within the extended survey. Following on from this, we also investigated how well each survey will constrain the baryon and stellar fraction scaling relations. It was found that the extended survey will be able to measure a departure from a constant scaling relation in both the stellar and baryon fractions.

In the future, several extensions are planned to this work. Deblending is a complicated procedure where one has to balance algorithm complexity with computational efficiency. To this end, we plan to streamline the deblender, thus speeding up its application particularly on large sky maps. Furthermore, we aim to apply the deblender to tSZ maps to assess how well projection effects from the tSZ background can be distinguished and removed from halo measurements. Shape variations in clusters, such as deviations from sphericity (triaxiality), will effect radial profile determination and parameter estimation. We plan to study the severity of these effects in future work.

With regards to the gas physics analysis, we have not investigated the effect of point sources on derived cluster statistics. We expect point sources to impact on purity and flux statistics, although with source excision these effects could mitigated to a large extent. Forthcoming studies

aim to investigate these effects thoroughly. In the case of the Fisher matrix analysis, no priors were placed on each of the parameters. By making use of complementary observations at other wavelengths, several priors could be placed on many of these parameters, such as mass, redshift, and the stellar mass fraction, which would have a positive effect on the derived constraints.

In conclusion, this study has shown that the tSZ effect is a powerful probe of gas physics within clusters. A sky survey, which can break the degeneracy in the various gas parameters, together with deblending techniques, will be able to probe the complicated physics within clusters to a new level. Such investigations will have direct consequences on derived cosmological parameters and conclusions.

CHAPTER 5

The Atacama Cosmology Telescope (ACT): Beam Profiles and First SZ Cluster Maps

5.1 Introduction

A new generation of experiments is measuring the cosmic microwave background (CMB) at arcminute resolutions. Within the past year alone, results from the South Pole Telescope (Staniszewski et al., 2009), ACBAR (Reichardt et al., 2009a), AMiBA (Umetsu et al., 2009), APEX-SZ (Reichardt et al., 2009b), the Cosmic Background Imager (Sievers et al., 2009), the Sunyaev-Zel'dovich Array (Sharp et al., 2009), and QUaD (Friedman et al., 2009) have revealed the $\sim$arcminute structure of the CMB with higher precision than ever. The angular power spectrum of temperature fluctuations at these scales ($\ell \gtrsim 1000$) will further constrain models of the early universe. Furthermore, secondary features such as the Sunyaev-Zel'dovich (SZ) effect and gravitational lensing will probe the growth of structure.

With its first scientific release, the Atacama Cosmology Telescope (ACT) now adds to these endeavours. A 6-meter, off-axis Gregorian telescope, was commissioned on Cerro Toco in northern Chile in October of 2007. Its current receiver is the Millimeter Bolometer Array Camera (MBAC), containing three 32×32 arrays of transition edge sensor (TES) bolometers observing at central frequencies of 148 GHz, 218 GHz, and 277 GHz, with beam full-widths at half-maxima

(FWHM) of $1.37'$, $1.01'$, and $0.91'$, respectively. It has operated for two seasons and is currently in its third season. In 2007 one month of science observations were made using only the 148 GHz array. The other two frequencies were added for the 2008 season, which lasted about 3.5 months. The telescopes optical design is described in Fowler et al. (2007). Hincks et al. (2008) and Switzer et al. (2008) report on the telescope performance and provide an overview of hardware and software systems. The MBAC design and details of TES detector properties and readout are in Niemack (2006), Marriage et al. (2006), Battistelli et al. (2008), Niemack et al. (2008), Swetz et al. (2008), Thornton et al. (2008), and Zhao et al. (2008).

ACT is located at one of the premier sites for millimetre astronomy because of the high altitude (5200 m) and the dry atmosphere. The precipitable water vapour (PWV) had a median value of 0.56 mm during the nights of our 2008 season. Nevertheless, atmospheric emission remains the largest signal external to the receiver in our raw data, a reality for any ground-based millimetre-wave telescope. The atmospheric power dominates only at low temporal frequencies and this is the main reason we observe while scanning our telescope in azimuth. Though much of the atmospheric power is below the frequency of our $0.0978\,\mathrm{Hz}$ scans, on typical nights the atmosphere dominates the detector noise up to about $2\,\mathrm{Hz}$.

In this chapter we present a map-making method designed to model and remove the atmospheric signal in a manner which is unbiased with respect to the celestial signal. The method currently produces its best results on small scales ($\lesssim 1^\circ$), so it is well suited to making maps of objects with small angular sizes. One of the most useful applications has been the study of our instrumental beam with high signal-to-noise maps of planets. The beam profile affects all aspects of data analysis, including calibration, and we provide the beam characteristics in this chapter. Additionally, we present new SZ measurements of eight known clusters.

We proceed as follows: in §5.2 we introduce the map-making method, showing both the theory and some qualitative properties; §5.3 describes how we analysed our beams, and presents the key measured parameters along with beam maps and radial profiles; window functions are derived in §5.4; §5.5 shows a selection of clusters imaged with the mapper; and we conclude in §5.6.

5.2 The Cottingham Mapping Method

In this section, we present a technique for removing the atmospheric power first described by Cottingham (1987) and used by Meyer et al. (1991), Boughn et al. (1992), and Ganga et al. (1993). The temporal variations in atmospheric signals are modelled using B-splines, a class of functions ideal for interpolation, discussed more below. The technique computes maximum-likelihood estimates of both the celestial and the atmospheric signals, using all available detectors in a single frequency band. We refer to it hereafter as the Cottingham Method.

In the following subsections, we give a mathematical description of the Cottingham Method (§5.2.1), followed by a discussion of its benefits and a comparison to the "destriping" method developed for PLANCK, which has close similarities (§5.2.2). Our approach for including the effects of spatial variability across the detector arrays is in §5.2.3. We discuss the use of B-splines in §5.2.4, and finish by outlining our implementation of the method (§5.2.5) and map-making steps (§5.2.6).

5.2.1 The Algorithm

The measured timestream $\boldsymbol{d}$ is modelled as a celestial signal plus an atmospheric component:

$$\boldsymbol{d} = \boldsymbol{P}\boldsymbol{m} + \boldsymbol{B}\boldsymbol{\alpha} + \boldsymbol{n}, \tag{5.2.1}$$

where the pointing matrix $\boldsymbol{P}$ projects the celestial map $\boldsymbol{m}$ into the timestream, $\boldsymbol{B}$ is a matrix of basis functions with amplitudes $\boldsymbol{\alpha}$ which model the temporal variation of atmospheric power, and $\boldsymbol{n}$ is the noise. The timestream of measurements $\boldsymbol{d}$ may be a concatenation of multiple detectors if they have been properly treated for relative gain differences. Throughout this paper, this is the case: all working detectors from one frequency band are processed simultaneously.

We seek $\widetilde{\boldsymbol{\alpha}}$ and $\widetilde{\boldsymbol{m}}$, estimates of the atmospheric amplitudes and the celestial map, respectively. Eq. (5.2.1) prescribes that we subtract the atmospheric term to obtain the map estimate: $\boldsymbol{d}' = \boldsymbol{d} - \boldsymbol{B}\widetilde{\boldsymbol{\alpha}}$. The maximum-likelihood estimator is then given by the standard map-making equation (e.g., Tegmark, 1997):

$$\widetilde{\boldsymbol{m}} = \left(\boldsymbol{P}^T\boldsymbol{N}^{-1}\boldsymbol{P}\right)^{-1}\boldsymbol{P}^T\boldsymbol{N}^{-1}\boldsymbol{d}' = \boldsymbol{\Pi}\left(\boldsymbol{d} - \boldsymbol{B}\widetilde{\boldsymbol{\alpha}}\right), \tag{5.2.2}$$

where

$$\mathbf{\Pi} \equiv \left(\boldsymbol{P}^T \boldsymbol{N}^{-1} \boldsymbol{P}\right)^{-1} \boldsymbol{P}^T \boldsymbol{N}^{-1} \tag{5.2.3}$$

the *projection matrix* and $\boldsymbol{N} \equiv \langle \boldsymbol{n}\boldsymbol{n}^T \rangle$ is the noise covariance. The projection matrix $\mathbf{\Pi}$ is designed in such a way that the map estimate is not biased, in the sense that the error, $\widetilde{\boldsymbol{m}} - \boldsymbol{m}$, does not depend on $\boldsymbol{m}$.

Given a set of basis functions $\boldsymbol{B}$, the Cottingham method minimises the variance of the map pixel residuals with respect to the amplitudes $\widetilde{\boldsymbol{\alpha}}$. The residuals are the differences between the celestial signals measured in the timestream and the map estimate:

$$\begin{aligned} \Delta \boldsymbol{d} &= \boldsymbol{d}' - \boldsymbol{P}\widetilde{\boldsymbol{m}} = \boldsymbol{d} - \boldsymbol{B}\widetilde{\boldsymbol{\alpha}} - \boldsymbol{P}\mathbf{\Pi}\left(\boldsymbol{d} - \boldsymbol{B}\widetilde{\boldsymbol{\alpha}}\right) \\ &= \left(\mathbf{1} - \boldsymbol{P}\mathbf{\Pi}\right)\left(\boldsymbol{d} - \boldsymbol{B}\widetilde{\boldsymbol{\alpha}}\right), \end{aligned} \tag{5.2.4}$$

where $\mathbf{1}$ is the identity matrix. We differentiate χ^2:

$$\begin{aligned} \frac{\partial \chi^2}{\partial \widetilde{\boldsymbol{\alpha}}} &= \frac{\partial}{\partial \widetilde{\boldsymbol{\alpha}}} \left(\Delta \boldsymbol{d}^T \boldsymbol{N}^{-1} \Delta \boldsymbol{d}\right) \\ &= -2\boldsymbol{B}^T \left(\mathbf{1} - \boldsymbol{P}\mathbf{\Pi}\right)^T \boldsymbol{N}^{-1} \left(\mathbf{1} - \boldsymbol{P}\mathbf{\Pi}\right)\left(\boldsymbol{d} - \boldsymbol{B}\widetilde{\boldsymbol{\alpha}}\right) \\ &= -2\boldsymbol{B}^T \boldsymbol{N}^{-1} \left(\mathbf{1} - \boldsymbol{P}\mathbf{\Pi}\right)\left(\boldsymbol{d} - \boldsymbol{B}\widetilde{\boldsymbol{\alpha}}\right). \end{aligned} \tag{5.2.5}$$

The last equality can be obtained by expanding $\mathbf{\Pi}$ to its constituent elements (c.f. Eq. (5.2.3)) and simplifying. If we define the following:

$$\mathbf{\Xi} \equiv \boldsymbol{B}^T \boldsymbol{N}^{-1} \left(\mathbf{1} - \boldsymbol{P}\mathbf{\Pi}\right), \quad \mathbf{\Theta} \equiv \mathbf{\Xi}\boldsymbol{B}, \quad \boldsymbol{\phi} \equiv \mathbf{\Xi}\boldsymbol{d}, \tag{5.2.6}$$

then when we set the derivative in Eq. (5.2.5) to zero, we have the simple expression:

$$\mathbf{\Theta}\widetilde{\boldsymbol{\alpha}} = \boldsymbol{\phi}. \tag{5.2.7}$$

This is a linear equation which is straightforward to solve for the atmospheric basis function amplitude estimates $\widetilde{\boldsymbol{\alpha}}$. These can then be used in Eq. (5.2.2) to estimate the map. In fact, both $\widetilde{\boldsymbol{\alpha}}$ and $\widetilde{\boldsymbol{m}}$ are the maximum-likelihood estimators of the atmosphere and celestial map, respectively, for a given set of basis functions $\boldsymbol{B}$. We show this explicitly in Appendix C.

There is an arbitrary overall offset to the computed $\boldsymbol{B}\widetilde{\boldsymbol{\alpha}}$ which must be estimated to remove the background from maps. We return to this point in §5.2.6.

5.2.2 Discussion

The chief strength of the Cottingham Method is that it estimates the atmospheric power in a way that is unbiased with respect to the map estimate itself. This important but subtle point is encapsulated in the term $(\mathbf{1} - \boldsymbol{P\Pi})$ in Eq. (5.2.5), whose effect is to project out the map estimate from the data. Therefore, the solution to Eq. (5.2.7) is not sensitive to the estimated celestial temperature, but only to a time-varying term which is represented by the atmospheric estimate $\boldsymbol{B\widetilde{\alpha}}$. This should be contrasted with high-pass filtering or fitting a slowly-varying function to the timestream to remove low-frequency power. Such approaches require masking of high signal-to-noise celestial objects (like planets or clusters) and/or multiple iterations to prevent corruption of the maps. They also remove low-frequency power without regard to its origin, the majority of it atmospheric, but also inevitably containing celestial signal, and therefore require extensive simulations to understand the effects of the filters on the final maps.

The Cottingham Method has close similarities to the "destriping" technique developed in particular for PLANCK analysis (Delabrouille, 1998; Burigana et al., 1999; Maino et al., 2002a). In fact, the linear algebra presented in §5.2.1 is identical to some versions of destriping (e.g., Keihänen et al., 2004). The destriping techniques are intended primarily to remove $1/f$ instrumental noise—thus, for example, Keihänen et al. (2005) impose a prior on the estimate $\boldsymbol{B\widetilde{\alpha}}$ based on detector noise. Sutton et al. (2009) also consider the effects of imposing a prior on the atmospheric noise. On the other hand, we use the Cottingham Method to remove atmospheric power with a flat prior. A distinct feature of our method is that we process multiple detectors simultaneously since the atmospheric signal is common across detectors (see, however, §5.2.3). Further, our approach differs in that it uses B-splines as the basis for modelling the atmosphere (§5.2.4).

5.2.3 Spatial Structure in the Atmosphere

The Cottingham Method as presented thus far assumes that the atmospheric signal $\boldsymbol{B\alpha}$ is common among all the detectors. In fact, we know that there is also spatial structure in the atmo-

sphere, meaning that in principle, each detector might see a different atmospheric signal. In practice, the finite telescope beam sets a lower limit on the spatial scale. We find that the atmospheric signal is coherent across a quarter to a third of the array, or about 5–7′. For reference, our 148 GHz channel, which has a $1.37'$ FWHM in the far-field (§5.3.2), is sensitive to an angular size of approximately $10'$ at a $1\,\mathrm{km}$ distance, roughly the distance to a typical turbulence layer in the atmosphere when pointed at 50° in altitude (Pérez-Beaupuits et al., 2005).

To account for this, we divide the 32×32 detector array into nine square *sub-arrays* of roughly equal size and fit for nine separate temporal atmospheric signals $\boldsymbol{B}_s\boldsymbol{\alpha}_s$, with the subscript s denoting the sub-array. These can all be done simultaneously if we adapt Eq. (5.2.1):

$$\begin{aligned}\boldsymbol{d} &= \boldsymbol{P}\boldsymbol{m} + \boldsymbol{S}\begin{pmatrix} \boldsymbol{B}_1 & \mathbf{0} & \dots & \mathbf{0} \\ \mathbf{0} & \boldsymbol{B}_2 & \dots & \mathbf{0} \\ \vdots & \vdots & \ddots & \vdots \\ \mathbf{0} & \mathbf{0} & \dots & \boldsymbol{B}_9 \end{pmatrix}\begin{pmatrix} \boldsymbol{\alpha}_1 \\ \boldsymbol{\alpha}_2 \\ \vdots \\ \boldsymbol{\alpha}_9 \end{pmatrix} + \boldsymbol{N} \\ &= \boldsymbol{P}\boldsymbol{m} + \boldsymbol{S}\boldsymbol{B}'\boldsymbol{\alpha}' + \boldsymbol{n}, \end{aligned} \tag{5.2.8}$$

where $\boldsymbol{S}$ is a book-keeping matrix that remembers from which sub-array each measurement in $\boldsymbol{d}$ came. The Cottingham Method proceeds exactly as before, except that we change $\boldsymbol{B} \to \boldsymbol{S}\boldsymbol{B}'$ and $\boldsymbol{\alpha} \to \boldsymbol{\alpha}'$.

5.2.4 The B-Spline as a Model of Atmospheric Signal

We follow Cottingham (1987) in choosing cubic basis B-splines for the basis functions **B**. B-splines are widely used in the field of geometrical modelling, and numerous textbooks cover them (e.g., Bojanov et al., 1993; de Boor, 2001; Schumaker, 2007); here we summarise basic properties. Basis B-splines are a basis of functions whose linear combination is called a B-spline. The basis B-splines are fully determined by a knot spacing τ_k and a polynomial order p; a B-spline is flexible on scales larger than τ_k, while on smaller scales it is relatively rigid. The basis B-splines $b_{j,p}(t)$ of order p are readily evaluated using the Cox–de Boor recursion on the

polynomial order. For m knots $\{t_j\}$ with $j = 0$ to $m - 1$:

$$\begin{aligned} b_{j,0}(t) &= \begin{cases} 1 & \text{if } t_j \leq t < t_{j+1} \\ 0 & \text{otherwise} \end{cases}, \\ b_{j,p}(t) &= \frac{t - t_j}{t_{j+p} - t_j} b_{j,p-1}(t) + \frac{t_{j+p+1} - t}{t_{j+p+1} - t_{j+1}} b_{j+1,p-1}(t), \end{aligned} \tag{5.2.9}$$

with j values restricted so that $j + p + 1 < m - 1$. For m knot times, $m + p - 1$ basis B-splines cover the interval between the first and last knot time. The individual basis B-splines $b_{j,p}(t)$ are compact functions, such that the B-spline receives support from no more than p of its bases at any point. For modelling the atmospheric signal, we always choose knots uniformly spaced in time and use $p = 3$ (cubic).

Due to their flexibility on large scales, B-splines are ideal for modelling the slowly varying atmospheric signal. The frequency f_k below which power will be removed is determined by the knot spacing τ_k. Empirically, we find:

$$f_k \approx 1/2\tau_k. \tag{5.2.10}$$

Figure 5.1 shows an example of atmospheric estimation using the Cottingham Method. The B-spline knot-spacing is $\tau_k = 0.25\,\mathrm{s}$, chosen for this example because it has $f_k = 2\,\mathrm{Hz}$, the approximate frequency at which the atmospheric power meets the detector noise level. Longer knot spacings produce qualitatively similar results, except that they cut off at lower frequencies, as per Eq. (5.2.10).

The Cottingham Method is effective at suppressing atmospheric contamination, but some covariance between atmospheric and celestial map estimates remains. This is typically at harmonics of the scan frequency ($\approx 0.1\,\mathrm{Hz}$), as exemplified in the bottom panel of Fig. 5.1. For this work we have used the white noise approximation for the detectors ($\boldsymbol{N} = 1$), which results in maps of bright sources which are clean down to the $-40\,\mathrm{dB}$ level in most cases (§5.3). The small residual atmospheric-celestial covariance is manifested as striping along lines of constant altitude since with our 7° peak-to-peak, $1.5^\circ\,\mathrm{s}^{-1}$ azimuthal scans (or 4.47° at $0.958^\circ\,\mathrm{s}^{-1}$ when projected on the sky at our observing altitude of 50.3°), the knot spacing ($\tau_k = 1.0\,\mathrm{s}$ for beam

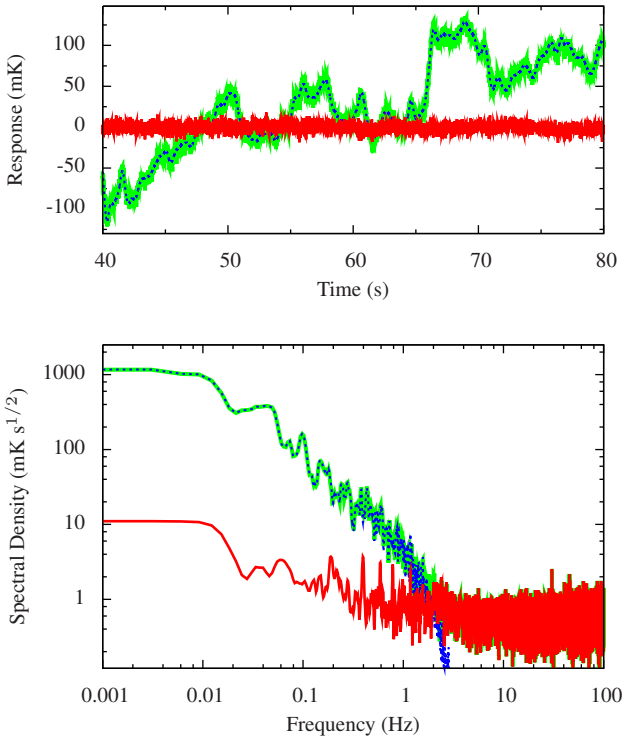

Figure 5.1: An example of the Cottingham Method. The fit is done using 300 s of data from 605 148 GHz detectors. The PWV was 0.8 mm, about 0.25 mm higher than the median in 2008. The knot spacing is 0.25 s and the order is cubic. In both plots, the original signal is plotted with a solid, light line, the B-spline atmosphere model with a dashed line and the signal minus the model with a solid, dark line. Each plot has been smoothed with a 5-sample boxcar filter for readability. The temperature units are with respect to a Rayleigh-Jeans spectrum. *Top:* A portion of one of the detectors' timestreams. *Bottom:* The spectral densities for the same single detector. A Welch window was applied before computing the Fourier transform.

maps (§5.3) and $0.5\,\mathrm{s}$ for cluster maps (§5.5)) corresponds to an angular scale smaller than the scan width. When noted, we fit straight lines to rows of pixels in the map, after masking out any bright source, and subtract them. We call this process "stripe removal". In both our beam analysis and our cluster studies, we have done tests which show that the bias introduced by this process is not significant—see §5.3.2 and §5.5.3. Nevertheless, future extensions of the Cottingham Method would benefit from the full treatment of the noise covariance.

5.2.5 Implementation

Before making maps with the Cottingham Method, some preprocessing must be done. The data, which are sampled at $400\,\mathrm{Hz}$, are divided into fifteen-minute time-ordered data (TOD) files and the preprocessing is performed on each individual TOD—a future paper will describe the steps which we only summarise here. The data acquisition electronics' digital anti-aliasing filter as well as measured detector time constants are deconvolved from the raw data. Low frequency signal due to cryogenic temperature drifts are measured with dark detectors (i.e., detectors uncoupled to sky signal) and removed from signal detectors; a sine wave with period $10.23\,\mathrm{s}$ is also fit to each timestream and removed to reduce scan-synchronous contamination. Calibration to units of power uses nightly load curves obtained by sweeping through detector bias voltages and measuring the response. Relative gain imprecisions are removed by using the large atmospheric signal itself to flat-field the detectors (e.g., Kuo et al., 2004); this is done independently in each of the nine sub-arrays (see §5.2.3). Finally, calibration to temperature units uses measurements of Uranus, which we estimate to have a net error of 6%. (The beam maps require no calibration to temperature—in fact, the temperature calibration is obtained from them.) The timestreams require no further preprocessing.

To improve the speed of the Cottingham algorithm, we exploit the fact that the map pixelisation used for calculating the atmospheric signal (Eqs. (5.2.5–5.2.7)) need not be the same as the map-making pixelisation. In general we only use a selection of the possible pixels on the map; additionally, we down-sample the number of hits in each pixel. We call the former "pixel down-sampling" and denote the fraction of retained pixels n_p; the latter we term "hit down-sampling" and denote the fraction of retained hits n_h. Consequently, the fraction of total available data used is $n_p \times n_h$. Each of these down-samplings is done in an even manner such that there are no large gaps in the remaining timestream.

We have specified four parameters for the Cottingham Method: the knot-spacing τ_k, the pixel size ξ, the pixel down-sampling fraction, n_p, and the hit down-sampling fraction, n_h. Of these, we always choose $\xi = 18''$ (about $1/3$ the 277 GHz beam size).

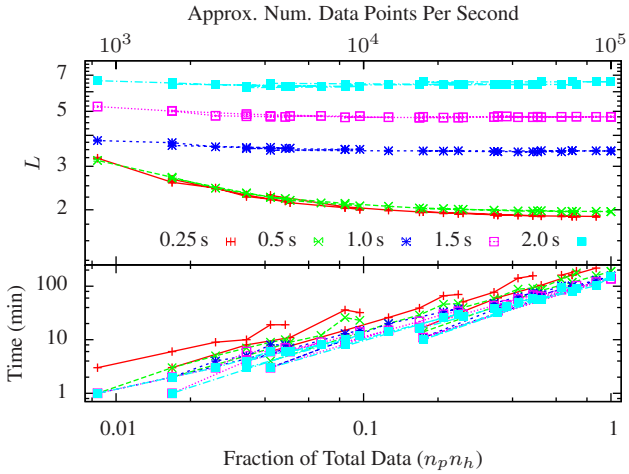

Figure 5.2: *Top panel:* The ratio L of low-frequency power to white noise after removing the atmospheric signal, as defined by Eq. (5.2.11). All data points are from the same TOD using all working detectors; only the parameters τ_k, n_p and n_h (see text) were varied to obtain each point. The x-axis is a product of the resamplings n_p and n_h, and the colours are different knot spacings τ_k as indicated in the plot key. *Bottom panel:* The computation time required for the data shown in the top panel. (The segmented lines are an artifact of how the data were recorded.) As the fraction $n_p n_h$ of total data used increases, the efficacy L of power removal flattens out and adding more data does not significantly improve the fit but only takes more computation time. In this example, there were ≈ 103000 possible map pixels with an average of 287 hits per pixel.

To evaluate the effect of varying the other three variables, we define a figure of merit which compares the average detector spectral density below 1 Hz to the white noise level, calculated in the range 5–25 Hz:

$$L \equiv \frac{1}{N_d} \sum_i^{N_d} \left[\frac{\int_{0\,\mathrm{Hz}}^{1\,\mathrm{Hz}} G_i(f) df}{\int_{0\,\mathrm{Hz}}^{1\,\mathrm{Hz}} df} \Big/ \frac{\int_{5\,\mathrm{Hz}}^{25\,\mathrm{Hz}} G_i(f) df}{\int_{5\,\mathrm{Hz}}^{25\,\mathrm{Hz}} df} \right], \tag{5.2.11}$$

where the sum runs over the N_d detectors used for the Cottingham calculation and G_i is the spectral density of the i^{th} detector *after* removing the estimated atmosphere signal. Fig. 5.2 shows a plot of measured values of L for a selection of knot-spacings and pixel down-samplings. As expected, shorter knot spacings remove more power: note however that only the $\tau_k = 0.5\,\mathrm{s}$ and $\tau_k = 0.25\,\mathrm{s}$ are capable of removing power up to the 1 Hz for which L is defined (c.f Eq. (5.2.10)). Because the curves flatten out as $n_p n_h$ increases, at a certain point adding more data does not

substantially improve the fit. This supports our conclusion that we only need to use a fraction of the data to estimate the atmosphere.

The timing data in the lower panel of Fig. 5.2 were measured on a 64-bit Intel Xeon® 2.5 GHz processor. Computation time is dominated by the calculation of the variables in Eq. (5.2.6). In general, these go linearly with the number of data points $\boldsymbol{d}$ and quadratically with the number of basis functions $\boldsymbol{B}$; in the case of B-splines, the compact support of the bases can be exploited so that the quadratic rate is subdominant to the linear, as the plot shows.

The number of basis B-splines is small enough that it is actually feasible to solve Eq. (5.2.7) exactly. For most cases, however, the conjugate gradient method (e.g., Press et al., 1992, p. 83ff) is much faster and yields indistinguishable results. Therefore, we use the latter in our implementation.

5.2.6 Map-Making

Once the atmospheric model $\boldsymbol{B\alpha}$ has been calculated for a TOD with the Cottingham Method, we create its celestial map. Maps are made in $(\Delta a,\ \Delta A\cos(a))$ coordinates, where Δa and ΔA are the distances from the altitude and azimuth of the map centre.[1] We use a pixel size of $10.6''$ per side, about 20% the size of the 277 GHz beam; note that this is different from the pixel size ξ used for calculating the atmosphere (§5.2.5).

We make the white noise approximation for each detector and weight it by the inverse of its variance in the map estimate. The detector variances are obtained iteratively: we make a map with equal detector weights and measure the variances of individual detector maps against the total map, remake the map with the new variances and repeat until the total map variance converges. The atmosphere estimates returned by the Cottingham Method have arbitrary offsets, which can be different for the nine sub-arrays we use (see §5.2.3). Thus, in the same iterative process, we also fit for the sub-array offsets and remove them when coadding detectors.

Co-addition of TOD maps is done after all of the steps described above. The maps are weighted by their inverse variances (calculated after masking bright sources or clusters).

[1] This is a very good approximation to the Gnomonic projection for the small map sizes we use.

Finally, we mention that the software used for the results in this chapter has a completely independent pipeline from our main map-making software which solves for the full survey area coverage. It has been especially useful for studying and optimising the signal extraction in small, targeted regions, and has provided important double-checks for our other pipeline.

5.3 Beam Maps and Properties

Understanding the telescope beams, or point-spread functions (PSF's), is of primary importance for the interpretation of our maps since they determine the relative response of the instrument to different scales on the sky and are central to calibration. For ACT's measurement of angular power spectra, the Legendre transform of our measured beam profile, called a window function, determines the response of the instrument as a function of angular scale.

Planets are excellent sources for measuring the telescope's beam because they are nearly point sources and are brighter than almost any other celestial object. The best candidates for the ACT are Saturn and Mars; of the rest, Jupiter is too bright and saturates the detectors, Venus is available too near to sunrise or sunset when the telescope is thermally settling, and the others are too dim for exploring the far sidelobes of the beam. (However, Uranus is useful as a calibrator.) The beam maps presented in this section are from observations of Saturn, which was available from early November through December of 2008.

5.3.1 Data Reduction

Maps were made for each night-time TOD of Saturn, using the Cottingham Method with $\tau_k = 1\,\mathrm{s}$, $n_p = 0.32$ and $n_h = 0.36$. We had more TODs than were needed to make low-noise beam maps, and we excluded about 1/3 of the maps which had higher residual background contamination, manifested by beam profiles that significantly diverged from those of the cleaner maps. The map sizes and number of TODs per frequency band are shown in Table 5.1.

In the analysis of §5.3.2, below, we sometimes compare unprocessed maps to stripe-removed maps. Stripe-removed map have been treated as outlined in §5.2.4, while unprocessed maps

Table 5.1: Summary of Beam Parameters

	148 GHz	218 GHz	277 GHz
Map Properties (§5.3.1)			
# TODs	16	15	11
Stripe-removal?	no	no	yes
Mask Radius (′)[a]	18	9,11,13	6,8,10,12
Beam Centres (§5.3.2)			
Major FWHM (′)	1.406 ± 0.003	1.006 ± 0.01	0.94 ± 0.02
Minor FWHM (′)	1.344 ± 0.002	1.001 ± 0.003	0.88 ± 0.02
Axis Angle (°)	62 ± 2	137 ± 9	98 ± 13
θ_W *Wing Fits (§5.3.2)*			
Fit Start, θ_1 (′)	7	5	4.5
Fit End, θ_2 (′)[b]	13	7–11	6–10
Best-fit θ_W (′)	0.526 ± 0.002	0.397 ± 0.01	0.46 ± 0.04
Solid Angles (§5.3.2)			
Solid Angle (nsr)	218.2 ± 4	118.2 ± 3	104.2 ± 6
% interpolated	2.8	4.3	7.2
Beam Fits (§5.4.1)			
θ_0 (′)	0.2137	0.1562	0.1367

[a] The 218 GHz and 277 GHz beam properties are averaged from the results at these mask radii—see text.
[b] The fit ranges for the 218 GHz and 277 GHz band are varied along with the mask radii so that θ_2 is never larger than the mask—see text.

have not been altered after map-making except for the subtraction of a background level. The planet is masked out before calculating the mean map value which estimates this level. The mask sizes for the three arrays, whether used for stripe removal or background estimation, are listed in Table 5.1.

In each frequency band, the selected TOD beam maps were coadded. Weights were determined from the RMS of the mean background level, calculated outside the mask radius. Relative pointing of individual detectors was measured to sub-arcsecond precision using the ensemble of Saturn observations. The overall telescope pointing was determined from each planet observation prior to map-making and used to centre each TOD map, so recentering of the maps was unnecessary before co-addition.

5.3.2 Beam Measurements

Fig. 5.3 shows coadded beam maps for the three arrays using a colour scale which highlights the features in the sidelobes. The 148 GHz and 218 GHz maps have striking similarities, most notably along the altitude (or vertical) direction where both exhibit more power near the top of the map. This is due to the off-axis design of the telescope (see Fowler et al., 2007): since the 148 GHz and 218 GHz arrays sit at about the same vertical offset from the centre of the focal plane, their resemblance along this axis is expected. Note that we recover structure in these map at a $< -40\,\mathrm{dB}$ level. The 277 GHz map is clearly inferior, showing residual striping in the scan direction, although this occurs below $-20\,\mathrm{dB}$. We believe this is from a combination of the brighter atmosphere at 277 GHz, as well as detector noise correlation induced by large optical loads (such as Saturn), which we are still investigating. Nonetheless we are still able to measure the 277 GHz solid angle to about 6% (see below), and work is underway to improve it.

For the 148 GHz and 218 GHz arrays, we do our beam analysis on maps which have not had stripe-removal because this process removes the real vertical gradient from the maps (see Fig. 5.3). Nonetheless, the solid angles (see below) from stripe-removed maps are within 1σ of the values from unprocessed maps. On the other hand, the larger residual striping in the 277 GHz maps necessitates the use of stripe-removed maps.

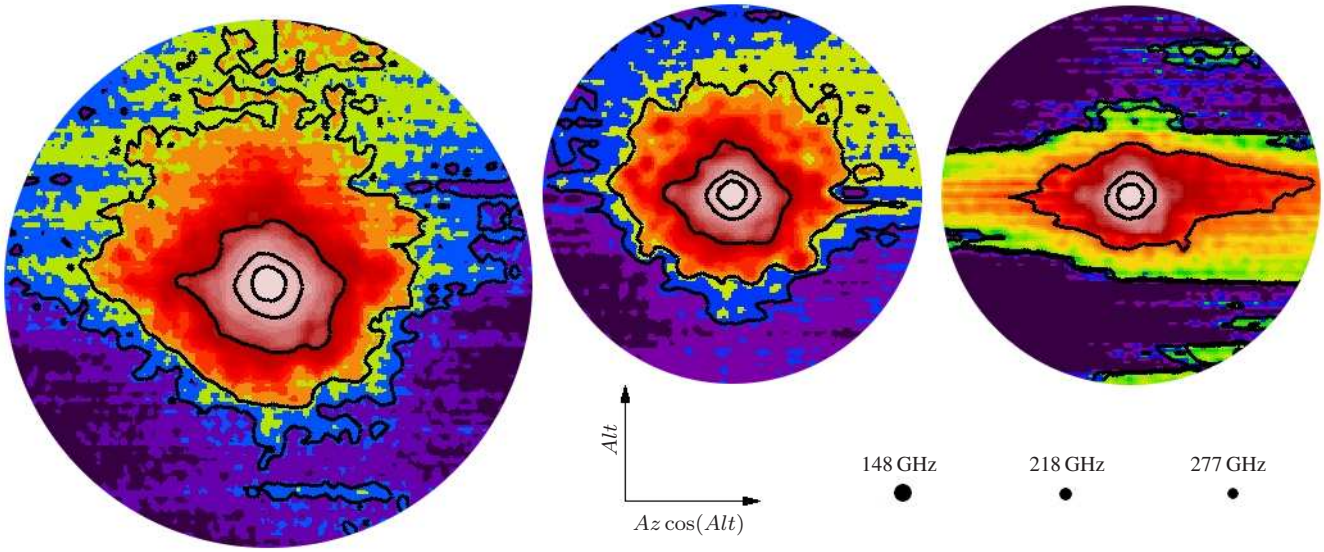

Figure 5.3: Beam maps for the three frequency bands: from left to right, 148 GHz, 218 GHz and 277 GHz. The maps are from coadded observations on 11–15 nights (see Table 5.1) and have radii of $21'$ (148 GHz) and $15'$ (218 GHz and 277 GHz). Maps are normalised to unity and contours are in decrements of -10 dB. The colour scale has been chosen to highlight the fact that we have made $< -40\,\mathrm{dB}$ beam measurements of our 148 GHz and 218 GHz bands. Even in the inferior 277 GHz map, striping is still below $-20\,\mathrm{dB}$. The circles show the sizes of the beam FWHM for each band (see Table 5.1). A Gaussian smoothing kernel with $\sigma = 0.54'$ has been applied to highlight large-scale structure; smoothing is not otherwise performed in the analysis. No stripe removal has been done on these maps.

The beam centre is characterised by fitting an elliptical Airy pattern—the function describing the beam of an optical system with a perfect aperture—to the top $\sim$3 dB of the beam map. This provides a measurement of the location of the beam centre, its FWHM along the major and minor axes of the ellipse, and its orientation, which we define as the angle of the major axis from the line of zero altitude relative to the beam centre. The uncertainties in these parameters are determined using the bootstrap method (Press et al., 1992, pp. 691ff) and give errors consistent with the standard deviation of values measured from the individual TOD maps. The FWHM and angles are listed in Table 5.1. They are included for reference but are not used in any analysis.

We denote the beam map by $B(\theta, \phi)$, where we use coordinates with radial distance θ from the beam centre and polar angle ϕ. By definition, $B(0, \phi) = 1$. The symmetrised beam is

averaged around the polar angle:

$$b^S(\theta) \equiv \frac{\int d\phi' B(\theta, \phi')}{\int d\phi'}. \tag{5.3.12}$$

Another quantity of interest is the accumulated solid angle, which measures the total normalised power within a given radius:

$$\Omega(\theta) = \int_0^{2\pi} d\phi' \int_0^{\theta} \theta' d\theta' B(\theta', \phi'). \tag{5.3.13}$$

The beam solid angle is $\Omega_A \equiv \Omega(\theta = \pi)$.

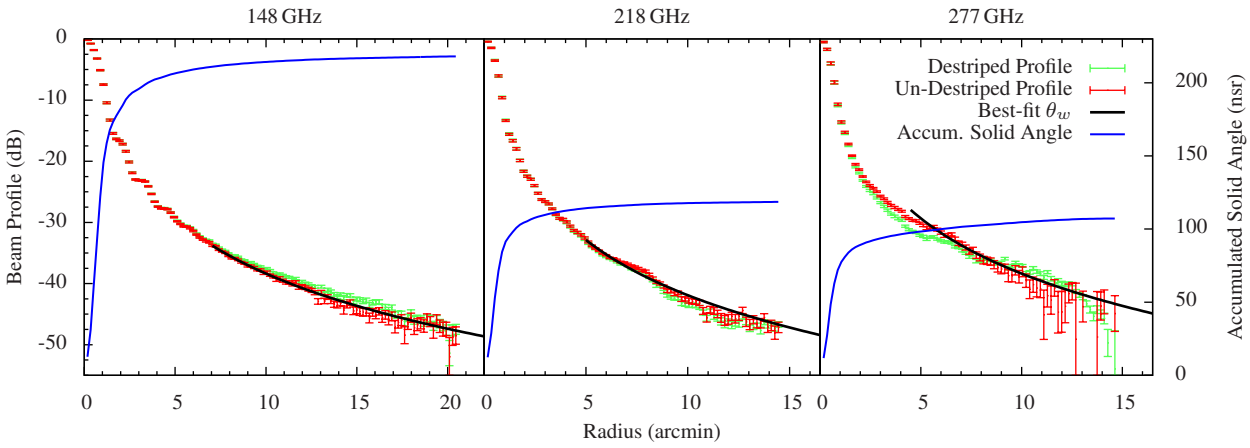

Figure 5.4: The beam profiles (Eq. (5.3.12)) and accumulated solid angles (Eq. (5.3.13)) for the three arrays, calculated from coadded maps (see text). The beam profiles are shown for both unprocessed maps, with dark errorbars, and stripe-removed maps, with light errorbars. Overplotted on each profile is the best fit of θ_W (Eq. (5.3.14)) to the unprocessed beam profiles. The error on the profiles are standard errors from the azimuthal average. The accumulated solid angles are from the unprocessed maps (without any solid angle extrapolation via Eq. (5.3.15)) for 148 GHz and 218 GHz, and from the stripe-removed map for 277 GHz. Saturn is bright enough that the rms power from the CMB falls below all the points in these plots.

Fig. 5.4 shows measured beam profiles and accumulated solid angles for the three arrays. We measure the beam profiles down to about $-45\,\mathrm{dB}$. If the beams exactly followed an Airy pattern, these data would account for 98% of the solid angle. Since systematic effects could corrupt our maps at the largest radii, we seek a way to robustly estimate the last few percent of the solid

angle on each beam. The method is to extrapolate the data with a fit to the asymptotic expression for the Airy Pattern:

$$b^S(\theta \gg \theta_F) = \left(\frac{\theta_W}{\theta}\right)^3, \tag{5.3.14}$$

where θ_F is the beam FWHM and θ_W defines the wing scale. Eq. (5.3.14) is good to better than 1% beyond about $5\theta_F$ (Schroeder, 2000, §10.2b).[2] Knowledge of θ_W allows us to infer the amount of unaccounted solid angle beyond the map boundary. A simple integration shows that the solid angle beyond a radius θ_b is:

$$\Omega_W(\theta > \theta_b) = 2\pi\frac{\theta_W^3}{\theta_b}. \tag{5.3.15}$$

We can also use this expression to estimate the amount of true beam power which was "mistakenly" included in the measurement of the background level outside the mask radius and subtracted from the map. In our analysis of the beam profiles and solid angles (including those displayed in Fig. 5.4), we use the fits of θ_W to calculate this missing power and add it back into the map. A new θ_W is then calculated from the corrected map; after two such iterations the θ_W fit converges.

Fig. 5.4 includes over-plots of the wing estimates from the best-fit values of θ_W on unprocessed maps. We denote the radii between which the fits were performed as θ_1–θ_2, and choose $\theta_1 \approx 5\theta_F$ for each array. For 148 GHz, we obtain good fits for any choice of θ_2 up to $13'$, or about the $-40\,\mathrm{dB}$ level in the profile. Thus, we use $\theta_2 = 13'$, for which we fit with χ^2 of 40 for 35 degrees of freedom. The fits to the other profiles are not as robust: 218 GHz has a reduced-χ^2 of 2.8 for $\theta_2 = 7'$ and 277 GHz has reduced-χ^2 of 25 for $\theta_2 = 6'$. Larger θ_2 gave poorer fits. Consequently, for these profiles we calculate θ_w at different mask sizes, as indicated in Table 5.1. At each mask size we varied θ_2 in $2'$ increments, always keeping it lower than the mask size. The average value from the whole ensemble of fits gives us θ_w and we take its standard error as the uncertainty. Although Eq. (5.3.14) may be too simple a model for these profiles, contributions to the solid angle at these radii are only a few percent of the total solid angle, which has an uncer-

[2] In full generality Eq. (5.3.14) is also proportional to $\cos(\pi D\theta/\lambda - 3\pi/4)$, where D is the telescope aperture diameter and λ the wavelength; we have smoothed over cosine cycles.

tainty dominated by the contribution of the beam at radii less than θ_2—see below. The values of θ_w for all three beam profiles are listed in Table 5.1.

Our θ_w fits allow us to calculate precise solid angles. At radii smaller than θ_2, we integrate the normalised power in the map (c.f. Eq. (5.3.13)). Beyond θ_2, we use Eq. (5.3.15) to extrapolate the remaining solid angle. (In the case of the 218 GHz and 277 GHz solid angles, we use the smallest θ_2 and the largest mask size in the ranges shown in Table 5.1. Other choices from these ranges do not significantly alter the results.) Finally, in the approximation that Saturn is a solid disk, it adds half of its solid angle Ω_S to the measured instrument solid angle—this is shown in Appendix D. Thus, the total solid angle is:

$$\Omega_A \;=\; \Omega(\theta \leq \theta_2) \;+\; \Omega_W(\theta > \theta_2) \;-\; \Omega_S/2. \tag{5.3.16}$$

During the period of our observations, Saturn subtended solid angles from 5.2 to 6.0 nanosteradians (nsr). We use the mean value of 5.6 nsr.

Determining the rest of the uncertainty in the solid angle is not straightforward since systematic errors dominate. For our total error, we add the estimated uncertainties of each of the terms on the RHS of Eq. (5.3.16) in quadrature. The uncertainty from Saturn's solid angle we take to be 1 nsr, both because of its varying angular size and to account for any systematic error due to the disk approximation.[3] The uncertainty of Ω_W is derived from the error of the fitted θ_W. For $\Omega(\theta < \theta_2)$, which dominates, we estimate the error by looking at the distribution of values from the individual TOD maps which comprise the coadded map. We did this in two ways. First, we calculated the mean and standard deviation of the solid angles measured in each individual map. This also reassures us that the coaddition step does not introduce any systematic error through, for example, pointing misalignments or changes in telescope focus from night to night. Second, we used the bootstrap method to generate 1000 coadded maps with random subsets of individual maps and used this ensemble to estimate the 68th percentile (i.e., $1\,\sigma$) of solid angles. These two error estimates were consistent with each other.

[3]The rings of Saturn add a layer of complication to its solid angle calculation, particularly since they have a different temperature than the disc. The ring inclination was low during our observations ($< 6^\circ$) and we have estimated that their contribution is negligible within the error budget.

The solid angles and their uncertainties are reported in Table 5.1. The formal uncertainties have been doubled and we quote them as $1\,\sigma$, in case there are systematic effects for which we have not accounted. In particular, the maps used for power spectrum estimation will come from an independent pipeline and will treat the instrumental response in slightly different ways—for example, by weighting detectors differently. We expect the beam uncertainties to decrease as our analysis evolves.

5.4 Window Functions

The statistics of the CMB are frequently characterised by an angular power spectrum C_ℓ:

$$\Delta T(\hat{\boldsymbol{n}}) = \sum_{\ell,m} a_{\ell m} Y_{\ell m}(\hat{\boldsymbol{n}}); \quad \langle a^*_{\ell' m'} a_{\ell m} \rangle = \delta_{\ell' \ell} \delta_{m' m} C_\ell, \tag{5.4.17}$$

where $\Delta T(\hat{\boldsymbol{n}})$ is the CMB temperature at position $\hat{\boldsymbol{n}}$ and $Y_{\ell m}$ is a spherical harmonic. In spherical harmonic space, the beam is encoded in a window function w_ℓ describing the response of the experiment to different multipoles ℓ, such that the total variance of a noiseless power spectrum is:

$$\mathrm{Var} = \sum_\ell \frac{2\ell + 1}{4\pi} C_\ell w_\ell. \tag{5.4.18}$$

In the case of a symmetric beam, the window function is the square of the Legendre transform of the beam radial profile (White and Srednicki, 1995; Bond, 1996):

$$w_\ell = b_\ell^2; \quad b_\ell \equiv \frac{2\pi}{\Omega_A} \int b^S(\theta) P_\ell(\theta) d(\cos\theta). \tag{5.4.19}$$

5.4.1 Basis Functions

For calculation of the window function and its covariance we model each beam with a set of basis functions which is complete but not necessarily orthogonal:

$$b^S(\theta) = \sum_{n=0}^{n_{\max}} a_n b_n(\theta). \tag{5.4.20}$$

Because the beam is truncated by a cold Lyot stop (Fowler et al., 2007), its Fourier transform is compact on a disk, which suggests that a natural basis with which to decompose the Fourier

transform of the beam image is the set of Zernike polynomials that form an orthonormal basis on the unit disk (Born and Wolf, 1999). The Zernike polynomials, expressed in polar coordinates ρ and φ on the aperture plane, are:

$$V_n^m(\rho, \varphi) = R_n^m(\rho) e^{im\varphi}, \tag{5.4.21}$$

where m and n are integers such that $n \geq 0$, $n > |m|$ and $n - |m|$ is even. In the case of an azimuthally symmetric beam, we need only consider the $m = 0$ radial polynomials, which can be expressed in terms of Legendre polynomials, $P_n(x)$ as:

$$R_{2n}^0(\rho) = P_n(2\rho^2 - 1). \tag{5.4.22}$$

The radial Zernike polynomials have a convenient analytic form for their Fourier transform:

$$\tilde{R}_{2n}^0(\theta) = \int \rho d\rho \, e^{-i\rho\theta} R_{2n}^0(\rho) = (-1)^n J_{2n+1}(\theta)/\theta, \tag{5.4.23}$$

where J_n is a Bessel function of the first kind. Motivated by this, we adopt

$$b_n(\theta) = \left(\frac{\theta}{\theta_0}\right)^{-1} J_{2n+1}\left(\frac{\theta}{\theta_0}\right) \tag{5.4.24}$$

as our set of basis functions to fit the radial beam profile.[4] Here, we have introduced a fitting parameter, θ_0, to control the scale of the basis functions.

5.4.2 Fitting Basis Functions to the Beam Profile

Below θ_1 (c.f. Table 5.1), we fit the bases b_n of Eq. (5.4.24) to the measured beam profile, and beyond θ_1, we use the power law defined in Eq. (5.3.14) with the parameters θ_w listed in Table 5.1. We assume vanishing covariance between the power law and the basis functions as they are fitted to independent sets of data points.

We employ a nonlinear, least-squares method to solve for the coefficients a_n and their covariance matrix $C_{mn}^{aa'}$. The algorithm uses a singular value decomposition to determine if the basis

[4] It may be asked why the Airy pattern, which was somewhat suitable for the high-θ fit in §5.3.2, is not used here. We find that at low θ, it is a poor fit since the optics are more complicated than the perfect-aperture model assumed by the Airy pattern.

functions accurately characterise the data and also computes a goodness-of-fit statistic (Press et al., 1992, §15.4). As inputs to the fitting procedure we are required to specify the scale parameter, θ_0, and polynomial order, $n_{\max}$. We searched the $\{\theta_0, n_{\max}\}$ parameter space until a reasonable fit was obtained that kept $n_{\max}$ as small as possible. For all three bands, $n_{\max} = 13$ gives a reduced $\chi^2 \approx 1$. No singular values is found for any of the fits. The parameters θ_0 we use for each frequency band are listed in Table 5.1.

5.4.3 Window Functions and their Covariances

Given the amplitudes a_n of the radial beam profile fitted to the basis functions and the covariance matrix $C_{mn}^{aa'}$ between the amplitudes a_m and a_n, the beam Legendre transform is:

$$b_\ell = \sum_{n=0}^{n_{\max}} a_n b_{\ell\, n}, \tag{5.4.25}$$

and the covariance matrix of the beam Legendre transforms b_ℓ and $b_{\ell'}$ is:

$$\Sigma_{\ell\ell'}^{b} = \sum_{m,n=0}^{n_{\max}} \frac{\partial b_\ell}{\partial a_m} C_{mn}^{aa'} \frac{\partial b_{\ell'}}{\partial a_n} \tag{5.4.26}$$

and therefore the covariance for the window function is:

$$\Sigma_{\ell\ell'}^{w} = 4 w_\ell w_{\ell'} \Sigma_{\ell\ell'}^{b}. \tag{5.4.27}$$

In Fig. 5.5 we show the window functions for each of the three frequency bands with diagonal error bars taken from the covariance matrix, $\Sigma_{\ell\ell'}^{w}$. We observe that the window function for each of the frequency bands has fallen to less than 15% of its maximum value at $\ell = 10000$. The statistical diagonal errors are at the 1.5%, 1.5%, and 6% levels for the 148 GHz, 218 GHz, and 277 GHz bands respectively, as shown in Fig. 5.5. They are computed following Eq. (17) of Page et al. (2003). The off-diagonal terms in the beam covariance matrix are comparable in magnitude to the diagonal terms. Singular value decompositions of $\Sigma_{\ell\ell'}^{b}$ yield only a handful of modes with singular values larger than 10^{-3} of the maximum values: 5 modes for 148 GHz, 4 for 218 GHz, and 2 for 277 GHz. Thus, the window function covariances can be expressed in a compact form which will be convenient for power spectrum analyses.

Table 5.2: Selection of SZ Clusters Detected by ACT

ACT Descriptor	Catalogue Name	J2000 Coordinates[a]		rms[b] [μK]	$t_{\rm int}$[c] [min]	$SNR\ (\theta)$[d]	ΔT_{SZ}[e] [μK]	$10^{10} \times Y(\theta)$[f]		
		RA	Dec.					$\theta \leq 2'$ (± 0.2)	$\theta \leq 4'$ (± 0.6)	$\theta \leq 6'$ (± 1.2)
ACT-CL J0245−5301	Abell S0295	$02^{\rm h}45^{\rm m}28^{\rm s}$	$-53°01'36''$	44	10.1	15.2 ($6.8'$)	−250	0.89	2.36	3.91
ACT-CL J0330−5228	Abell 3128 (NE)	$03^{\rm h}30^{\rm m}50^{\rm s}$	$-52°28'38''$	49	10.3	12.8 ($4.3'$)	−260	0.94	2.69	4.34
ACT-CL J0509−5345	SPT-CL 0509−5342	$05^{\rm h}09^{\rm m}20^{\rm s}$	$-53°45'00''$	47	10.1	7.7 ($5.2'$)	−70	0.33	1.07	1.50
ACT-CL J0516−5432	Abell S0520	$05^{\rm h}16^{\rm m}31^{\rm s}$	$-54°32'42''$	55	6.8	4.2 ($4.1'$)	−110	0.19	-0.11	-0.55
ACT-CL J0546−5346	SPT-CL 0547−5345	$05^{\rm h}46^{\rm m}35^{\rm s}$	$-53°46'04''$	46	9.5	13.9 ($5.8'$)	−250	0.91	2.36	3.67
ACT-CL J0638−5358	Abell S0592	$06^{\rm h}38^{\rm m}46^{\rm s}$	$-53°58'40''$	55	7.5	8.1 ($3.1'$)	−230	0.70	1.40	2.07
ACT-CL J0645−5413	Abell 3404	$06^{\rm h}45^{\rm m}29^{\rm s}$	$-54°13'52''$	59	9.3	2.8 ($2.0'$)	−120	0.12	-0.18	-0.69
ACT-CL J0658−5556	1E 0657−56 (Bullet)	$06^{\rm h}58^{\rm m}33^{\rm s}$	$-55°56'49''$	80	3.4	12.1 ($2.7'$)	−510	1.60	2.95	3.56

[a] Position of the deepest point in $2'$ FWHM Gaussian smoothed map, except for ACT-CL J0509−5345 which has a position which gives a maximal SNR (see text).
[b] Map rms measured outside a $6'$ mask and reported for a one square arcminute area.
[c] Integration time, defined as the approximate total time (in minutes) that the telescope was pointed in the map region.
[d] Maximum signal-to-noise ratio (Eq. (5.5.29)) and the radius θ at which it was obtained.
[e] Cluster depth, as measured in a $2'$ FWHM Gaussian smoothed map at the listed coordinates; intended as a guide to the magnitude of the decrement.
[f] See Eq. (5.5.32) and following discussion.

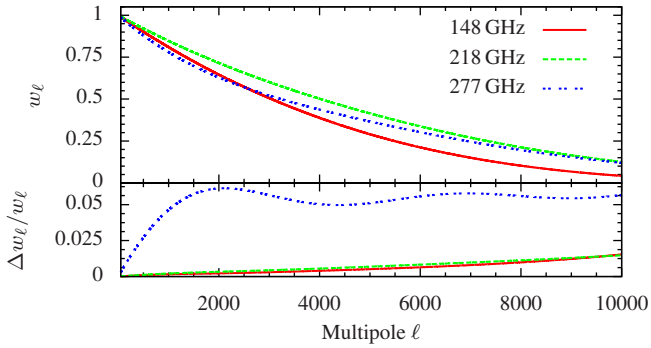

Figure 5.5: Normalised window functions *(top)* and diagonal errors *(bottom)* computed from the basis functions for each of the three frequency bands. The window functions have been normalised to unity at $\ell = 0$. In practice, the normalisation will take place over the range of multipoles corresponding to the best calibration. Only statistical errors are shown.

For 277 GHz we estimate a 10% systematic uncertainty from destriping. Another source of systematic error in the window functions arises from the beams not being perfectly symmetric. The symmetrised beam window function generally underestimates the power in the beam (e.g., Fig. 23, Hinshaw et al., 2007). In practice, the scans in our survey field are cross-linked (see §5.5.1) so that the quantity of relevance to the power spectrum calculation is the cross-linked window function i.e.,

$$w_\ell = \frac{1}{2\pi} \int_0^{2\pi} b(\boldsymbol{\ell})\, b^*(\boldsymbol{\ell})\, d\phi_\ell, \tag{5.4.28}$$

where ϕ_ℓ is the polar angle in spherical harmonic space and $b(\boldsymbol{\ell})$ is the transform of the beam profile. To study the magnitude of this effect on the window function we computed the fractional difference between the window function derived from the Legendre transform of the symmetrised beam and the cross-linked window function, derived for a typical cross-linking angle of $60°$. The difference between the two was found to be at the 1%, level for the 148 GHz and 218 GHz arrays, and at the 4% level for the 277 GHz array.

5.5 SZ Galaxy Clusters

In addition to beam maps, the Cottingham Method mapper has been used for making maps of SZ clusters. The maps and analysis presented in this section are the first results from ACT on SZ science. For this first overview, we present results from only the 148 GHz band, the most sensitive during our 2008 season. We focus on known clusters, including four new SZ measurements.

5.5.1 Data

Table 5.2 lists the clusters studied in this paper, including information on the maps and a summary of the results of our analysis (§5.5.2, §5.5.3). Fig. 5.6 shows the cluster maps and companion difference maps (see below).

Apart from planets, ACT has done no targeted observations of specific objects, so the cluster maps come from our regular survey data, which were taken at two different central azimuth pointings, one on the rising sky and the other on the setting sky. Therefore, the maps presented here are "cross-linked", i.e., they consist of data taken with two distinct angles between the azimuthal scan direction and the hour angle axis. The integration time is short, ranging from about 3 to 11 minutes—see Table 5.2.

The clusters were discovered in a full-survey 148 GHz map produced by our main map-maker. (Full maps will be shown and discussed in a future publication.) A Wiener filter was constructed using the polytropic model of Komatsu and Seljak (2001b) as an SZ template, and included detector noise, CMB power and point source contributions in the noise model. Clusters were then identified from the filtered maps. We make two points about the clusters presented in this chapter: first, although our template-based detection method has some built-in bias, the detections presented here are significant ($\geq 3\sigma$ in the filtered survey map); and second, we have only included a sample of our significant detections.

Cluster maps are made using the procedures outlined in §5.2.5 and §5.2.6. The knot spacing was $\tau_k = 0.5\,\mathrm{s}$ and the downsampling fractions were $n_p \approx 0.42$ and $n_h \approx 0.40$. All maps are

0.4° in diameter. Straight-line stripe removal (§5.2.6) has been performed, using a $6'$ radius mask over the cluster decrement.

We have made companion "difference" maps for each cluster from the same data. For each of the rising and setting observations, a map made from the first half of the nights' data is subtracted from the second half. The rising and setting difference maps are then coadded to produce the full, cross-linked coadded difference map—the same procedure used for the signal maps.

The map noise, listed in Table 5.2, is the rms of the map computed outside a $6'$ mask and converted to an effective pixel size of one square arcminute. By examining the power spectra of the maps we found that the rms values we quote are dominated by the white noise level and do not have significant contributions from residual low-frequency power.

5.5.2 Characterising the Detections

The cluster centre positions are determined by finding the coldest point in the map smoothed with a $2'$ FWHM Gaussian kernel. The one exception is ACT-CL J0509−5345 (SPT-CL 0509−5342), which has a complex structure. In this case, we choose a centre which gives a maximal signal-to-noise (see below). As a rough guide, we also quote the cluster depths, ΔT_{SZ}, from these smoothed maps in Table 5.2, but we stress that these values should not be used for quantitative analysis. All other cluster properties are measured from unsmoothed maps.

We quantify the significance of the detections by a signal-to-noise (SNR) measurement. Denoting the signal map m_{xy} and the difference map d_{xy}, we define the SNR within an aperture size θ as:

$$SNR(\theta) \equiv \min \left\{ \left| \frac{\sum\limits_{\sqrt{x^2+y^2}<\theta} (m_{xy} \pm d_{xy})}{\sqrt{N(\theta)\,(\sigma_m^2 + \sigma_d^2)}} \right| \right\}, \tag{5.5.29}$$

where the sum is over pixels which are within a radius θ from the cluster centre, $N(\theta)$ is the number of pixels in the sum, and σ_m^2 and σ_d^2 are the variances of the signal and difference maps, respectively, calculated outside a $6'$ mask. Because the sign of a difference map is arbitrary (we subtracted one half of the data from the other half), we take the smaller of the possible two SNR.

The purpose for including the subtraction is that coincident flux in the difference map indicates that the signal map probably contains spurious flux.

In Table 5.2, we quote $SNR(\theta_i)$ at the value of θ_i which maximised the SNR.

5.5.3 Integrated Compton-Y Values

The SZ effect occurs when CMB photons inverse Compton-scatter off hot electrons in clusters of galaxies (Sunyaev and Zeldovich, 1970). The imprint on the CMB is proportional to the integrated electron gas pressure:

$$\frac{\Delta T}{T_{CMB}} = y\, f(x); \quad y \equiv \frac{k_B \sigma_T}{m_e c^2} \int dl\, n_e T_e, \tag{5.5.30}$$

where the integral is along the line of sight, m_e, n_e, and T_e are the electron mass, number density, and temperature, respectively, σ_T is the Thomson scattering cross-section, and the variable y is the Compton-y parameter. The function $f(x)$ encodes the dependence on frequency:

$$f(x) = \left[x \coth(x/2) - 4\right] \left[1 + \delta_{SZ}(x, T_e)\right], \tag{5.5.31}$$

with $x \equiv h\nu / k_B T_{CMB}$. For hot clusters, a relativistic correction $\delta_{SZ}(x, T_e)$ may be required (Rephaeli, 1995), in which case f must be included in the integral of Eq. (5.5.30) in the non-isothermal case. However, in this paper we assume non-relativistic f for simplicity.

A robust measure of the SZ signal is the integrated Compton-y parameter, since it is model-independent and simply sums pixels in the maps (Benson et al., 2004):

$$Y(\theta) = \iint\limits_{|\boldsymbol{\theta}'|<\theta} d\Omega_{\boldsymbol{\theta}'} y(\boldsymbol{\theta}'), \tag{5.5.32}$$

where $\boldsymbol{\theta}$ is the angular distance from the cluster centre. We use steradians as the unit of solid angle, so Y is dimensionless. As an example, it is plotted for ACT-CL J0638−5358 in the lower panel of Fig. 5.7; the upper panels show its azimuthally symmetrised temperature profile. The values of Y at $2'$, $4'$, and $6'$ are shown for each cluster in Table 5.2. The errors were determined by calculating the standard deviation of Y values from maps of random patches of the CMB, made in the same way as the cluster maps. We find 1σ uncertainties of $0.2{\times}10^{-10}$, $0.6{\times}10^{-10}$

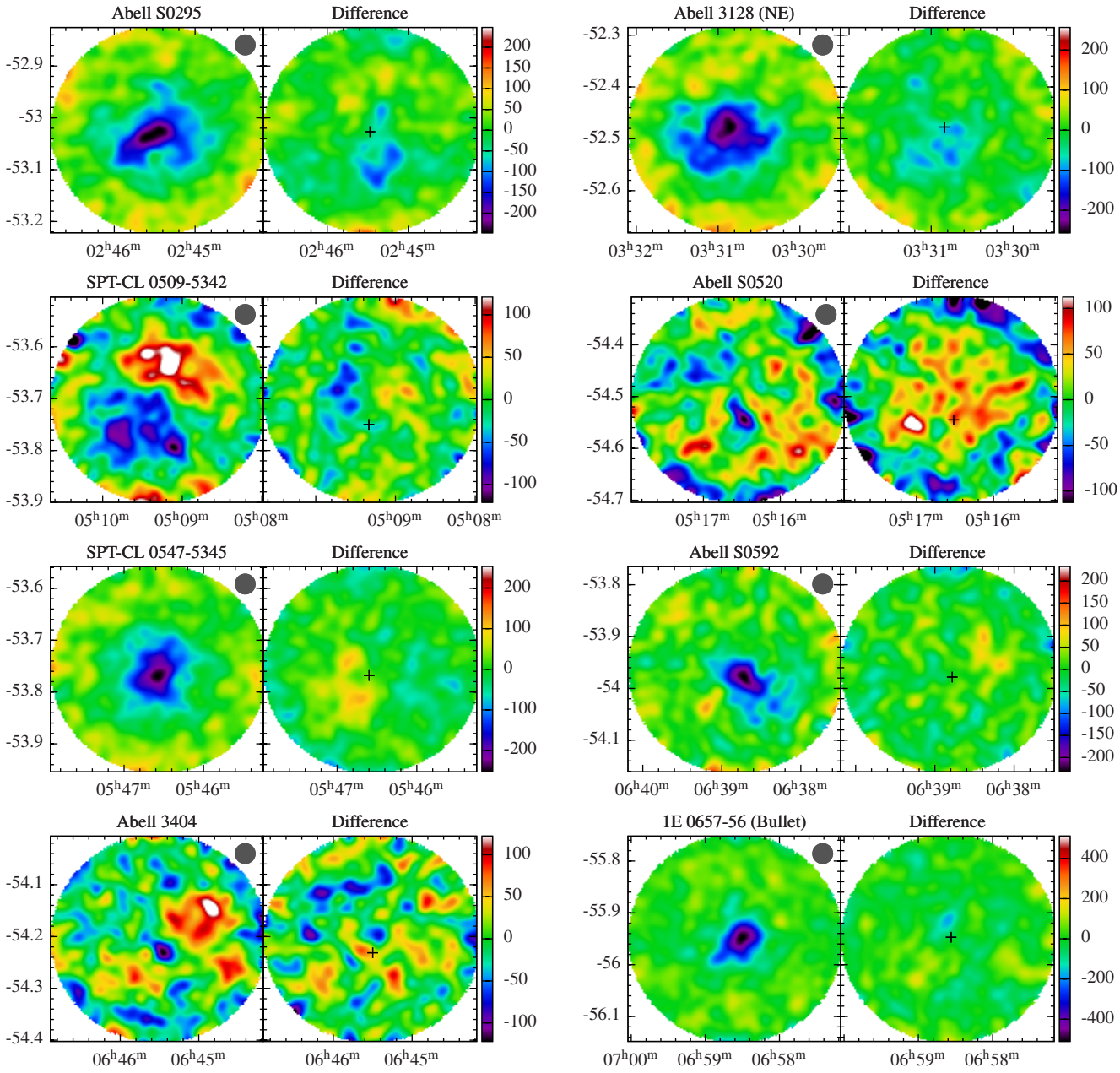

Figure 5.6: Cluster maps made using the Cottingham Method at 148 GHz, paired with their difference maps (see §5.5.1). The coordinates are J2000 right ascension (hours) and declination (degrees). The colour bars are μK (CMB); note that the scale is different for each cluster. The gray disc in the top corner of the the signal plots is 2.43′ in diameter, the FWHM size of the beam convolved with the Gaussian smoothing kernel which was applied to these images. In each difference plot, a cross shows the coordinates of the darkest spot in its corresponding signal map (except for SPT-CL 0509−5342 (ACT-CL J0509−5345)—see text).

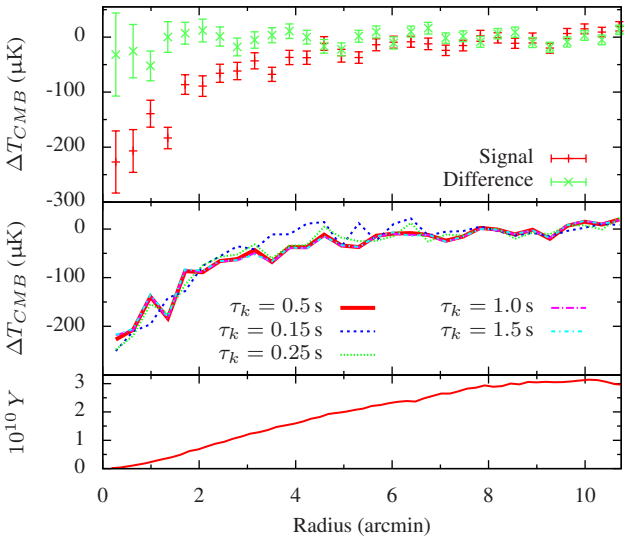

Figure 5.7: The radial profile *(top/middle)* and integrated Compton $Y(\theta)$ values *(bottom)* for the SZ decrement of ACT-CL J0638−5358 (Abell S0592). The profile data are averages from the maps in $22''$-wide annuli, and $Y(\theta)$ is the sum of the pixels within a radius θ, converted to the unitless Compton-y parameter (Eqs. (5.5.30) and (5.5.32)). The top panel shows the profile of the signal map and difference map. The middle panel compares profiles for maps made with different knot spacings τ_k, showing that only for very short spacings is the profile noticeably different from the $\tau = 0.5\,\mathrm{s}$ profile used for cluster analysis, and then not significantly so. In all of the panels, the profile centres were determined by the minimum of the map after smoothing with a $2'$ FWHM Gaussian profile. (The profiles were calculated from the unsmoothed map.)

and $1.2{\times}10^{-10}$ for Y at $2'$, $4'$, and $6'$, respectively. These values are dominated by systematic errors, including uncertainties in the background level, contributions from CMB in the map, and residual contamination from the stripe removal. Accordingly, they should not be interpreted as the significance of the detection; the SNR values (see Table 5.2) serve that purpose.

Note that in two clusters—ACT-CL J0516−5432 (Abell S0520) and ACT-CL J0645−5413 (Abell 3404)—we measure negative values of $Y(4')$ and $Y(6')$. Their maps show that the measured SZ signal is compact and the negative values are consistent with noise.

As a check that the choice of knot spacing ($\tau_k = 0.5$) is not creating a significant bias via covariance of the celestial signal with the low-frequency atmospheric estimate (see §5.2.4), we created maps with τ_k from $0.15\,s$ to $1.5\,s$ for ACT-CL J0245−5301 and ACT-CL J0638−5358.

The temperature profiles for the latter are plotted in the middle panel of Fig. 5.7. Even the shortest spacing does not produce a profile which is significantly different from the others. Its knot spacing, $\tau_k = 0.15\,\mathrm{s}$, is the only one from the ensemble with a corresponding angular scale smaller than the map size. We conclude that the results are not biased by having knots of too high a frequency.

5.5.4 Comparisons to Previous Measurements

The clusters shown in this paper are previously known X-ray, optical, and/or SZ clusters; all are massive systems. For four of the sources (Abell S0295, Abell 3128 (NE), Abell S0592, and Abell 3404), these are the first reported SZ detections. In this section, we briefly review measurements from the literature to provide context, and point out some of the contributions that our new measurements make to this body of knowledge.

Relevant parameters from the literature are listed in Table 5.3; references for these values are included below. Typical errors on L_X are small ($< 20\%$), while those on the inferred mass are more substantial ($\sim$50%). Temperatures are measured values from X-ray spectra. We use a flat ΛCDM cosmology with $\Omega_M = 0.3$ and $H_0 = 70\,\mathrm{km\,s^{-1}\,Mpc^{-1}}$. Masses are quoted in units of M_{500}, defined as the mass within a radius having a mean mass density $\langle\rho\rangle$ 500 times greater than the critical density, i.e., $\langle\rho\rangle = 500 \times 3H^2/(8\pi G)$. In the following we briefly discuss the clusters in the order in which they appear in Table 5.2, with the exception of the South Pole Telescope (SPT) clusters which are discussed together near the end of this section.

Abell S0295

Abell S0295 first appeared in Abell et al. (1989) in their table of supplementary southern clusters (i.e., clusters that were not rich enough or were too distant to satisfy the criteria for inclusion in the rich nearby cluster catalogue). It was also found to be a significant X-ray source in the *ROSAT* All Sky Survey (RASS) Bright Source Catalog (Voges et al., 1999). The spectroscopic redshift of Abell S0295 was obtained by Edge et al. (1994), who also reported the discovery of a giant strong-lensing arc near the brightest cluster galaxy. Efforts to detect the SZ effect at

Table 5.3: Summary of Cluster Properties from X-Ray and Optical Studies

ACT Descriptor	Catalogue Name	Redshift	D_A [Mpc]	L_X(0.1–2.4 keV) [10^{44} erg s^{-1}]	M_{500} [$10^{15} M_\odot$]	kT [keV]	$10^{10} \times Y_{2500}$[a]
ACT-CL J0245−5301	Abell S0295	0.3006	920	8.3	0.8	6.7 ± 0.7	$0.53^{+0.35}_{-0.21}$
ACT-CL J0330−5228	Abell 3128 (NE)	0.44	1172	3.9	0.3	5.1 ± 0.2	$0.15^{+0.10}_{-0.06}$
ACT-CL J0509−5345	SPT 0509−5342	0.36 (P)	1037	2.2	0.4	—	—
ACT-CL J0516−5432	Abell S0520	0.294	906	3.5	0.6	7.5 ± 0.3	$0.72^{+0.47}_{-0.28}$
ACT-CL J0546−5346	SPT 0547−5345	0.88 (P)	1596	4.7	0.6	—	—
ACT-CL J0638−5358	Abell S0592	0.2216	737	10.6	1.0	8.0 ± 0.4	$1.31^{+0.86}_{-0.52}$
ACT-CL J0645−5413	Abell 3404	0.167	589	8.2	0.7	7.6 ± 0.3	$1.87^{+1.23}_{-0.74}$
ACT-CL J0658−5556	1E 0657−56	0.296	910	20.5	1.4	10.6 ± 0.1	$1.61^{+1.16}_{-0.67}$

[a] Predicted value of Y within R_{2500} from the Y-kT scaling relation of Bonamente et al. (2008). Errors come from the uncertainty on the scaling relation parameters. Although we do not have R_{2500} values for our clusters, the $Y(2')$ measurements listed in Table 5.2 should be roughly comparable to these—see §5.5.4.

1.2-mm and 2-mm with the SEST were attempted, unsuccessfully, by Andreani et al. (1996b). *ASCA* observations (Fukazawa et al., 2004) yielded values (see Table 5.3) for average temperature and soft band X-ray flux(0.1–2.4 keV), from which we determined the corresponding X-ray luminosity. The cluster mass M_{500} was then estimated from the luminosity-mass (specifically L_X(0.1-2.4 keV) vs. M_{500}) relations from Reiprich and Böhringer (2002).

Abell 3128 (NE)

Until quite recently the north-east (NE) component of Abell 3128 was believed to be part of the Horologium-Reticulum supercluster at $z = 0.06$. The X-ray morphology is clearly double peaked with the two components separated on the sky by some $12'$. Rose et al. (2002) estimated the virial masses of the two components assuming the redshift of the supercluster and obtained a value for each of $\sim 1.5 \times 10^{14}\, M_\odot$. Fig. 5.8 shows our SZ measurement with overlaid X-ray contours.

Recently Werner et al. (2007) carried out a detailed study of this cluster using *XMM-Newton* data, which revealed a more distant and more massive cluster superposed on the northeastern component of Abell 3128. A significant portion of the X-ray emission comes from this background cluster. The values we quote in the table for redshift, X-ray luminosity, gas temperature, and M_{500} correspond to the background cluster and come from Werner et al. (2007).

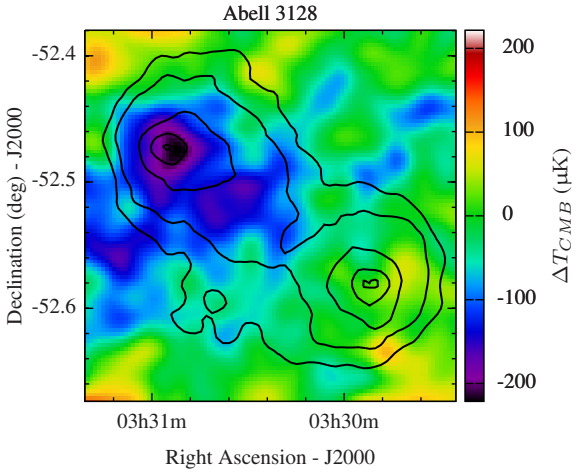

Figure 5.8: ACT-CL J0330-5228 (Abell 3128 (NE)) with overlaid contours of X-ray emission in black. The SZ detection is associated with the NE feature of Abell 3128, and confirms that it is due to a more massive, higher redshift cluster than that at the SW lobe—a compelling example of the redshift independent mass selection of the SZ effect. The X-ray data come from two separate *XMM-Newton* observations (Obs Ids 0400130101 and 0400130201) with a total exposure time of 104 ks. The two observations were mosaicked into a single image over the 0.2–2.0 keV. Contour values are from $1.25{\times}10^{-8}$ to $1.25{\times}10^{-7}$ photons/cm^2/s/arcsec^2.

The large SZ decrement ($SNR = 12.8$) seen in the ACT maps is clearly associated with the NE component where the $z = 0.44$ cluster is. We do not detect a significant decrement from the southwestern component which lies at $z = 0.06$. Werner et al. (2007) estimate the temperature of the higher redshift cluster to be 5.14 ± 0.15 keV, which is significantly hotter than that of the foreground cluster ($kT = 3.36 \pm 0.04$ keV). This system, therefore, is a compelling illustration of the mass selection, approximately independent of redshift, of the SZ effect. Werner et al. (2007) note that the temperature, luminosity and mass estimates of the $z = 0.44$ background cluster are all subject to large systematic errors, as the cluster properties depend upon the assumed properties of the foreground system. A joint X-ray/SZ/optical analysis should be able to better constrain the characteristics of both systems and thereby contribute to assessing the mass threshold of the ACT cluster survey.

Abell S0520

This optically-rich cluster (Abell et al., 1989) lies at a redshift of $z = 0.294$ (Guzzo et al., 1999). It is also an X-ray cluster, RXC J0516−5430 (Böhringer et al., 2004), and has been detected by SPT (Staniszewski et al., 2009) as SPT-CL 0517−5430. The X-ray temperature, soft X-ray flux and luminosity are based on *XMM-Newton* observations (Zhang et al., 2006) and the mass we quote in Table 5.3 comes from the X-ray–derived gas density and temperature profiles (Zhang et al., 2008).

Abell S0592

The galaxy cluster Abell S0592 was originally detected optically (Abell et al., 1989). *ROSAT* detected it as a bright source in the All Sky Survey and its redshift ($z = 0.2216$) was reported in de Grandi et al. (1999). The cluster is also known by its REFLEX designation of RXC J0638.7−5358 (Böhringer et al., 2004). The *ROSAT* flux and luminosity in the soft X-ray band (0.1-2.4 keV) are 7.5×10^{-12} erg cm^{-2} s^{-1} and 1.1×10^{45} erg s^{-1}. The X-ray spectrum of Abell S0592 from a *Chandra* observation (Hughes et al., 2009) yields an integrated gas temperature of $kT = 8.0 \pm 0.4$ keV. The soft X-ray luminosity implies a cluster mass of $M_{500} = 10^{15}\, M_{\odot}$.

Abell 3404

Abell 3404, at $z = 0.167$ (de Grandi et al., 1999), is the lowest redshift system in the ACT SZ-detected cluster sample presented here. It is REFLEX cluster RXC J0645.5−5413. The X-ray temperature, soft X-ray flux and luminosity are based on *XMM-Newton* observations (Zhang et al., 2008). These authors also provide the total cluster mass based on the X-ray–derived gas density and temperature profiles.

1E 0657−56 (Bullet Cluster)

We detect 1E 0657−56, the famous "Bullet" cluster, at high significance with a strong central decrement and large integrated Y. Previous detections of the mm-band SZ signal from this

cluster have been reported by ACBAR (Gomez et al., 2004) and APEX-SZ (Halverson et al., 2009).

The spectroscopic redshift of 1E 0657−56 was obtained by Tucker et al. (1998), the X-ray flux came from the Einstein Observatory (Markevitch et al., 2002), the X-ray gas temperature from *XMM-Newton* (Zhang et al., 2006), and the cluster mass, M_{500}, from a study by Zhang et al. (2008).

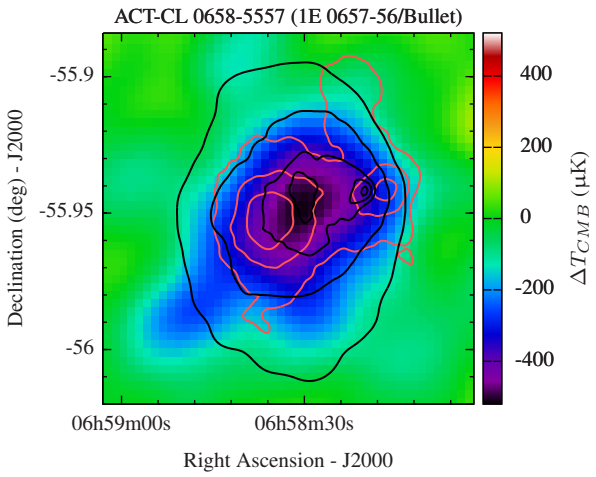

Figure 5.9: ACT-CL J0658-5556 (Bullet Cluster) with overlaid contours of X-ray emission (black) and dark matter distribution (orange). The X-ray contours come from an $85\,\mathrm{ks}$-long *Chandra* observation (Obs Id 3184) and correspond to the 0.5-2.0 keV band. Contour values are $4{\times}10^{-7}$ to $2{\times}10^{-9}$ photons/cm^2/s/arcsec^2. The lensing data are from Clowe et al. (2007) with contours running from $\kappa = 0.12$ to 0.39.

Fig. 5.9 shows a zoomed-in plot of our SZ map with X-ray contours from *Chandra* and lensing contours from Clowe et al. (2007). As expected, the SZ decrement follows the X-ray contours more closely than the lensing contours, since the collisonless dark matter is expected to be offset from the collisional gas in this merging system.

South Pole Telescope Clusters

Staniszewski et al. (2009) recently reported blind SZ detections of four galaxy clusters. Only one of them (SPT-CL 0517−5430) is a previously known cluster, Abell S0520 (see §5.5.4).

The physical properties of the SZ clusters—photometric redshifts, luminosities, and mass estimates—have been reported by Menanteau and Hughes (2009) based on optical and X-ray data. Here we summarise some of their findings (see Table 5.3). All four clusters have central elliptical galaxies associated with them whose luminosities are consistent with those of clusters in the Sloan Digital Sky Survey. Their mass estimates from their optical and X-ray luminosities also suggests that these are fairly massive systems. In Table 5.3 we list their M_{500} estimates from their X-ray luminosities.

We make strong detections of SPT-CL 0547−5345 and SPT-CL0509−5342 and also see Abell S0520 (SPT-CL 0517−5430) with moderate SNR (c.f., Table 5.2). There are visible similarities between the ACT maps presented here and those from SPT. An interesting feature is the bright spot to the north-west of SPT-CL 0509−5342 which figures prominently in both maps and for which we could find no radio or infrared catalogue source.

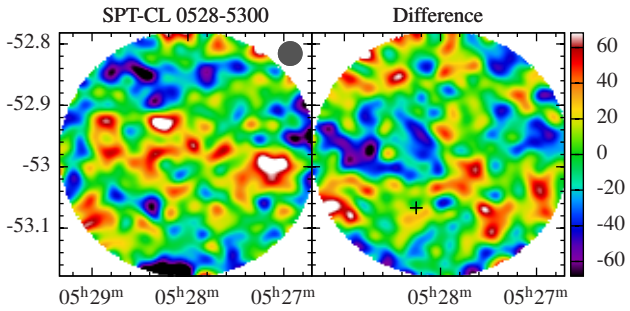

Figure 5.10: A map and corresponding difference map centred on the coordinates of SPT-CL 0528−5300, a cluster candidate detected by the South Pole Telescope but not yet detected with our instrument. The units of the axes are right ascension (hours) and declination (degrees), and the colour bar is ΔT_{CMB} (μK). The map rms noise is 45 μK.

We are unable to confirm the detection of SPT-CL 0528−5300. Fig. 5.10 shows a map centred on the cluster coordinates. There is no measureable SNR (Eq. (5.5.29)) for a putative decrement centred at its coordinates. Based on the map noise, we report a 2σ non-detection at the 90 μK level. Recent weak-lensing mass estimates for the SPT clusters (McInnes et al., 2009) indicate that SPT-CL 0528−5300 has a lower mass ($M_{500} \sim 2 \times 10^{14}\, M_{\odot}$, scaled from their M_{200} assuming a typical factor of 0.6, e.g., Reiprich and Böhringer (2002)) than any of the other

known clusters that we have detected in the SZ with ACT (see Table 5.3). Further study of the X-ray and optical properties of SPT-CL 0528−5300 will be necessary to more accurately predict its expected SZ signal.

Comparison with Previous SZ Measurements

Although the large masses of the ACT-detected clusters we report here offer strong support for the reality of our detections, we also compare the quoted integrated Compton-y parameters for consistency with expections from previous SZ cluster studies. For this we use the Y-kT scaling relation from Bonamente et al. (2008) (using values for "all clusters" from their Table 2). Predicted values are given in the last column of Table 5.3. The Y values in the scaling relation were integrated within R_{2500}, the radius where the average cluster mass density is 2500 times the critical density. We do not have precise R_{2500} values for our clusters, but estimates of R_{2500} range from about $1'$ to $3'$, so the predicted values of $Y(2500)$ should, to first order, be roughly comparable to our $Y(2')$ values. With that proviso, the predicted and measured Y values agree to within 2σ for all but two clusters: Abell 3404, whose X-ray temperature predicts a much higher Y value than we measure, and Abell 3128 (NE), where the cluster temperature predicts a much lower Y value than measured. The latter is a complex system which could have a larger mass than previously thought. Additionally, the Bonamente et al. (2008) scaling relation was measured at $30\,\mathrm{GHz}$. At 148 GHz, the point source contamination is different. This might explain why a measured Y value is lower than the prediction based on the $30\,\mathrm{GHz}$ scaling relation. A larger and better-studied sample of ACT-detected clusters will be necessary before drawing conclusions about scaling relations.

5.6 Conclusions

We have described a maximum-likelihood mapping algorithm which uses B-splines to model atmospheric signal and to remove it from the data.

The method has been used to make high precision ($< -40\,\mathrm{dB}$) beam maps, with solid angles in the 148 GHz, 218 GHz, and 277 GHz bands of $(218.2 \pm 4)\,\mathrm{nsr}$, $(118.2 \pm 3)\,\mathrm{nsr}$, and $(105.2 \pm$

$6)\,\mathrm{nsr}$, respectively. The beam profiles and window functions will be important for all subsequent analyses of ACT's data.

Additionally, we have made maps showing SZ detections of eight previously discovered galaxy clusters. Our high-σ detection of the $z = 0.44$ component of Abell 3128, and our current non-detection of the low-redshift part, corroborates existing evidence that the further cluster is more massive. This is a compelling example of the redshift-independent mass selection of the SZ effect.

The maps presented in this paper will eventually be made public through the LAMBDA site (http://lambda.gsfc.nasa.gov/) and ACT site (http://www.physics.princeton.edu/act/).

CHAPTER 6

Detection of Thermal SZ Clusters in Atacama Cosmology Telescope Maps

Galaxy clusters represent the largest virialised objects in the universe. Furthermore, their evolution and formation depends on a number of cosmological parameters as well as the dynamics of dark energy. In order to provide such constraints, a cluster catalogue, comprising mass and redshift estimates, fluxes, and a well-defined selection function is required. Such information is collated from a number of sources. Wide area SZ surveys (such as ACT, SPT and Planck) and realistic simulations will provide catalogues of cluster candidates with well defined selection functions and purity estimates, while targeted multi-wavelength observations including optical and X-ray instruments will provide estimates of cluster masses and redshifts.

In this chapter we present preliminary cluster detection analyses of the latest ACT sky maps at 148 GHz using the SZ effect. We compare our results to simulations presenting completeness, purity, number counts and fluxes. The cluster candidates presented here will form the basis for future follow-up investigations at other wavelengths.

6.1 Overview of ACT Data Maps

ACT was in operation in all three frequency channels from mid-August to late December 2008. The observing time was split between two regions situated away from the galactic plane. The analyses presented here uses 148 GHz data from observations covering ≈ 480 deg^2 of the southern sky in a 6° wide strip centred on a dec. of $\delta = -52^\circ$ with R.A. from $02^{\rm h}00^{\rm m}$ to $07^{\rm h}08^{\rm m}$. The beam FWHM for this frequency channel is $\approx 1.4'$ [1]. A thorough description of the data reduction and timestream mapping techniques can be found in Fowler et al. (2010).

6.2 Overview of ACT Simulation Maps

To understand cluster purity, completeness and flux recovery, we studied simulated sky maps comprising the same area as the ACT strip at 148 GHz. The simulated maps were chosen to cover approximately the same R.A. and dec. range in order to simulate cosmic variance and dust contamination. The input source maps, produced by Sehgal et al. (2010), included lensed CMB, thermal and kinetic SZ as well as dust. Point sources were not included in the current simulations, but their effects on purity and flux recovery will be studied in the future. The full sky map, which comprised all the forementioned sources, was then added to a realisation of actual ACT noise. The realistic noise map was produced by subtracting one half of the data from the other half. In this way, all astrophysical signals were removed, leaving only the noise properties in the map. An important point to note at this juncture is that these simulation maps were not mapped from time-stream data as is the case with the real ACT data maps, but are the result of large scale numerical simulations. Both the simulated and real ACT maps have a pixel scale of $0.5'$.

6.3 Map Filtering

Prior to map filtering, point sources in the ACT data maps were detected and removed using a nearest neighbour data interpolation. This step is crucial in mitigating the effects of point sources,

[1] Please refer to Chapter 5 for a complete description of the ACT beams.

particularly on purity estimates. The maps were then subject to single frequency Wiener filtering. Instead of applying the Wiener filter in one-dimension, as is typically the case which assumes symmetry in the power spectrum of the various sources, we implemented a two-dimensional Wiener filter. This filter is described as follows:

$$\tilde{W}(\mathbf{k}) = \frac{\tilde{S}(\mathbf{k})}{\tilde{S}(\mathbf{k}) + \tilde{N}(\mathbf{k})}, \tag{6.3.1}$$

where $\tilde{W}(\mathbf{k})$ is the two-dimensional weight function, $\tilde{S}(\mathbf{k})$ is the signal template power spectrum and $\tilde{N}(\mathbf{k})$ is the noise template power spectrum, all defined in Fourier space. We utilise a number of templates for the tSZ signal, ranging in mass from $M = 4 \times 10^{14} M_{\odot}$ to $1 \times 10^{15} M_{\odot}$, and redshift from $z = 0.2$ to 0.8. The templates follow the prescription given in Bode et al. (2009) - a description of our implementation of their models is presented in appendix B. The noise template characterises all contaminants in the map and as such includes models for the lensed CMB signal and dust. To assess the impact of model selection on cluster detection, we also investigated the situation where the noise template included the power spectrum of the data instead of theoretical models. This scenario was studied since the current ACT maps are noise and not signal dominated. In Fig. 6.1 we present an example of the two-dimensional weight function in harmonic space. The asymmetry in the weight function is clearly visible, arising from sources including correlated noise in the atmosphere. This filter removes striping (an artifact arising from the map making pipeline) and peaks on scales of $l \approx$ few thousand, where the tSZ signal dominates.

Application of the filter proceeds by Fourier transforming the sky map, applying the filter in harmonic space and inverse Fourier transforming to obtain the minimum variance Compton Y map. Fig. 6.2 presents a section of the ACT filtered map in units of μK at 148 GHz. The Bullet cluster (1ES 0657-56) can be seen in the lower left hand corner of the map, while two Abell clusters, Abell S0592 and Abell 3404 (Abell et al., 1989), can be seen in the top right hand corner (former to the left, latter to the right). For a more comprehensive list of known clusters and candidates detected in the ACT data, please refer to Table 6.1.

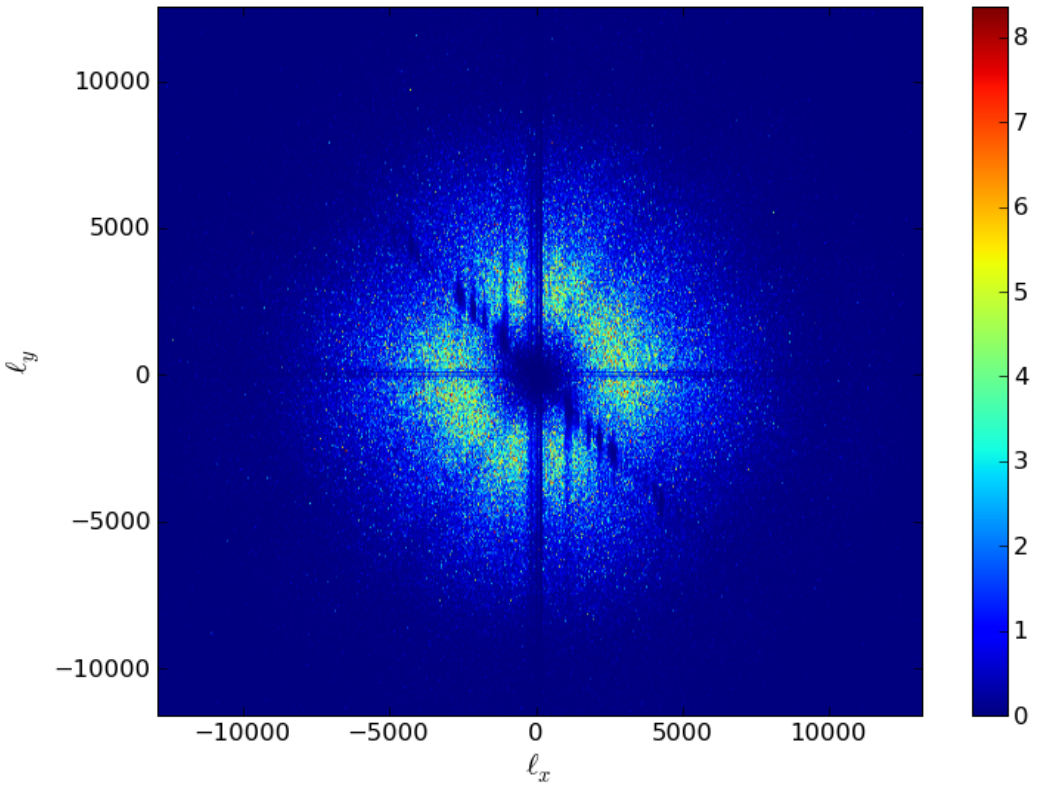

Figure 6.1: Two-dimensional weight function prescribed for the ACT data map, where the units are arbitrary. This particular filter weight uses the data within the filter description. The use of a two dimensional filtering scheme is motivated by the presence of asymmetric structure in the filter.

6.4 Detection Statistics: ACT and Simulated Maps

Once filtering of the simulated or data maps was completed, we applied a simple cluster detection algorithm to the maps, which detected all sources above a given signal-to-noise limit. We simply thresholded the filtered maps and enforced that candidate objects should have a minimum of ten connected pixels above a threshold of 3.5σ (where σ is the standard deviation of the filtered map). As alluded to earlier, nine templates were used in the filtering process. In cases where an object was detected in multiple templates, only the highest signal-to-noise detection was included in the final catalogue of cluster candidates. To remove any spurious detections related to noise

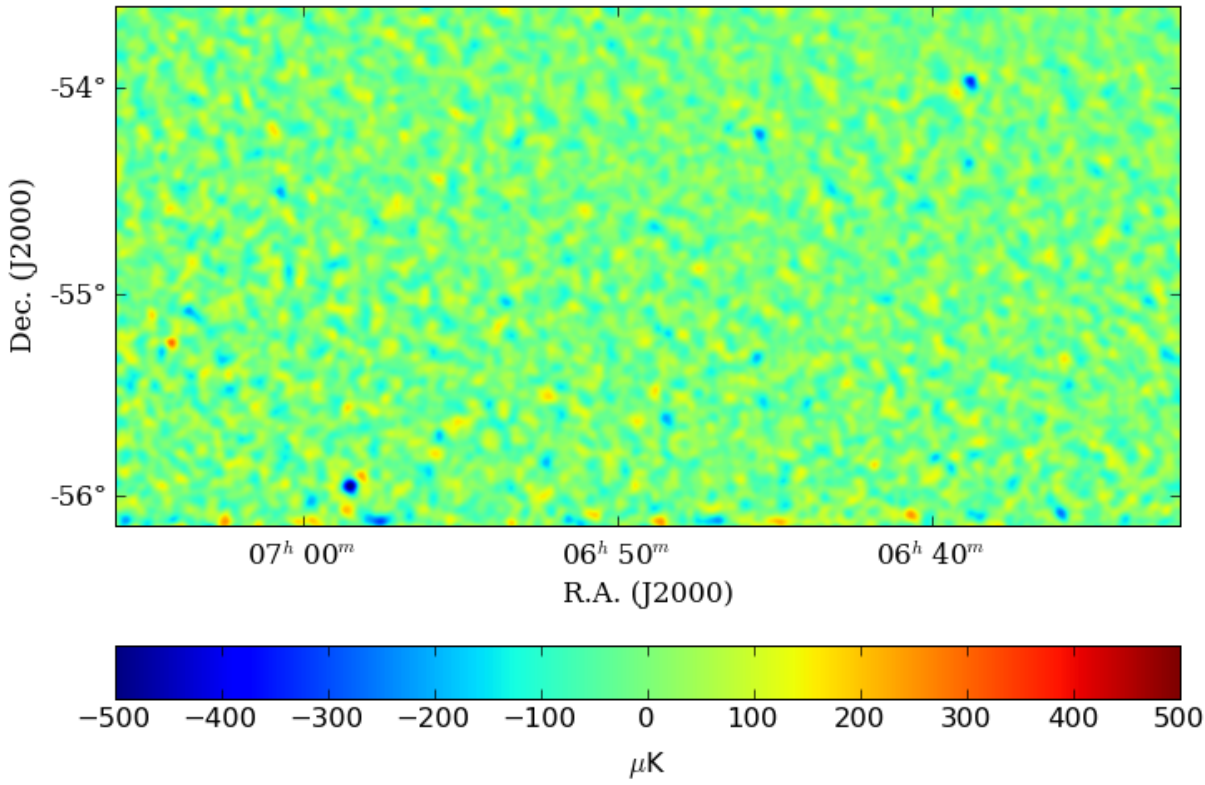

Figure 6.2: Sub-region of the filtered ACT data map at 148 GHz. The well known Bullet cluster (bottom left) and Abell S0592 (top right) are clearly discernible.

fluctuations, we utilised a data weight map in the detection process. A region of the weight map corresponding to the filtered region displayed above is presented in Fig. 6.3. The weight map comprises the number of times a pixel had been observed (defined as H in the figure). Consequently, high signal-to-noise regions were weighted more significantly than lower ones, reducing effects of noise stripes which are common in data, particularly in the outskirts of the survey region. The weight map was also used to produce signal-to-noise estimates for each of the cluster candidates, allowing one to produce completeness estimates as well as purity and number counts as a function of signal-to-noise.

In order to produce purity and completeness statistics, detected objects in the simulated maps were matched to the input cluster catalogue for the specified region. This was achieved by

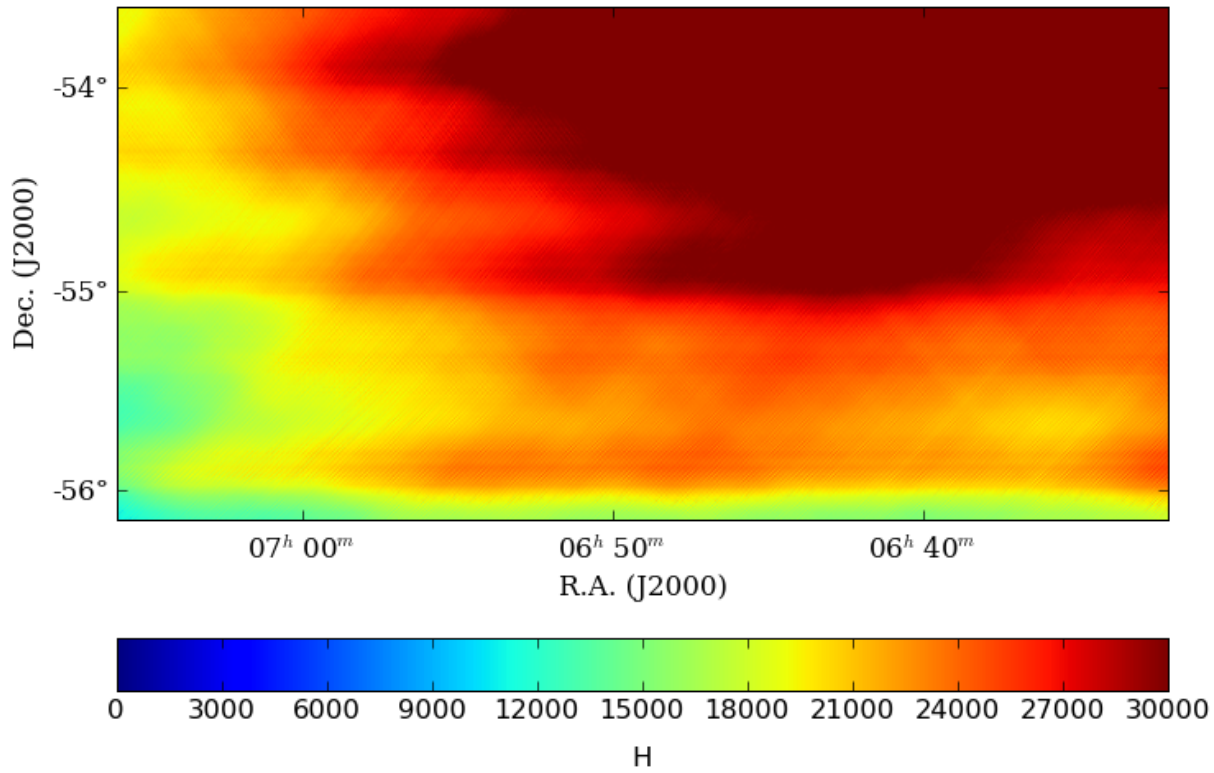

Figure 6.3: Sub-region of the ACT weight map at 148 GHz. The units are in terms of hit counts, designated by the variable, H.

locating all catalogue clusters contained within a radius of $\approx 1.2'$ from the detected object. The matched cluster was chosen to be the catalogue cluster with the highest mass found within the matching radius. The purity ($\tilde{P}$), above a particular signal-to-noise, σ^j_{SN}, was then calculated by the following

$$\tilde{P}(> \sigma^j_{SN}) = 100 \times \frac{N^j_{match}}{N^j_{obs}}, \tag{6.4.2}$$

where N^j_{match} and N^j_{obs} are the number of matched and detected objects, respectively, above a signal-to-noise limit. The completeness ($\tilde{C}$) for the sample (above a particular mass) is given by

$$\tilde{C}(> M^i) = \frac{N^i_{match}}{N^i_{cat}}, \tag{6.4.3}$$

where N^i_{cat} and N^i_{match} are the number of catalogue and matched halos respectively, above a given mass, M^i.

In Fig. 6.4 we present the purity of the cluster sample from the simulated maps of the ACT strip. We also present the number of matched clusters as a function of signal-to-noise. The black lines reflect the case where the data was used in the filter construction, while the red lines depict the case where models for the sky sources were used instead. Slightly more true clusters are

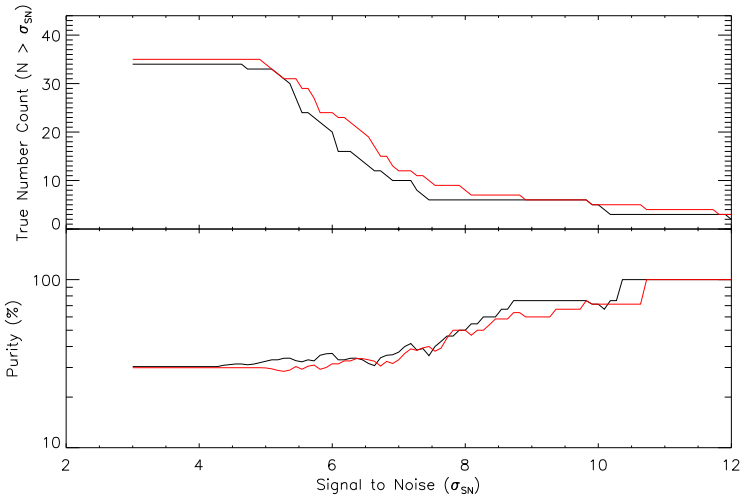

Figure 6.4: Cluster sample purity and true number counts versus signal-to-noise for the simulated ACT map. Black lines describe the case where data was used in the filter construction while the red lines indicate the scenario where astrophysical models were used instead.

detected in the simulation in the case where a model was used for the filter, with a relatively unchanged purity level. Considering the fact that we used the same source models (dust and lensed CMB) in the construction of the simulated map, this behaviour is not unexpected.

Studies of the completeness of the cluster sample, displayed in Fig. 6.5, show that we are approximately 80% complete above $7 \times 10^{14} M_\odot$ with a total contamination of 70%. The completeness and overall contamination proved to be approximately independent of filter construction (*i.e.* data or model used in the filter). The dip in the completeness at high mass is due to a single cluster that is asymmetric in shape. Thus, although we do detect this object, the peak is

located sufficiently far away from the position given in the input catalogue, that it is not flagged as a match.

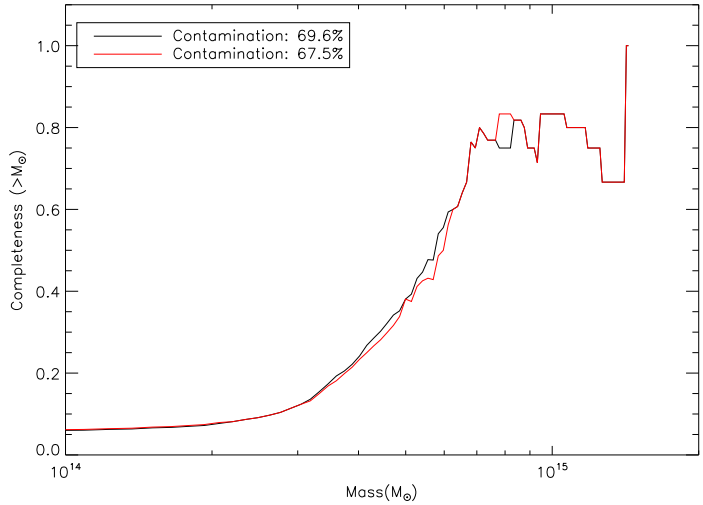

Figure 6.5: Cluster sample completeness and overall contamination for both filter construction cases.

The simulated cluster analysis is vital in quantifying the cluster detection results from the ACT data maps. In Fig. 6.6 we present the number counts from the ACT simulated and data maps. In both filter construction cases we see that the simulated maps produced more cluster detections. This discrepancy is more prominent in the situation where a model is used in the filter construction. This suggests that we are over-performing in the simulations with this assumption, and under-performing in the real data. Using the data in the filter construction produced a closer correlation between the real and simulation number counts. This can be explained by the fact that we are using the actual data properties to minimise noise sources, so both situations include the same priors. The fact that the simulation does not match the data precisely is due to a number of factors. Firstly, the noise properties (*e.g.* noise level) in the simulations could be slightly different from the real maps, which would translate into offset number counts. Secondly, the simulation has not been mapped in the same way as the ACT data, which could introduce noise correlations and other artifacts, which might impinge on detection statistics. Thirdly, the simulated galaxy clusters could have a larger than expected SZ signal, which would lead to an

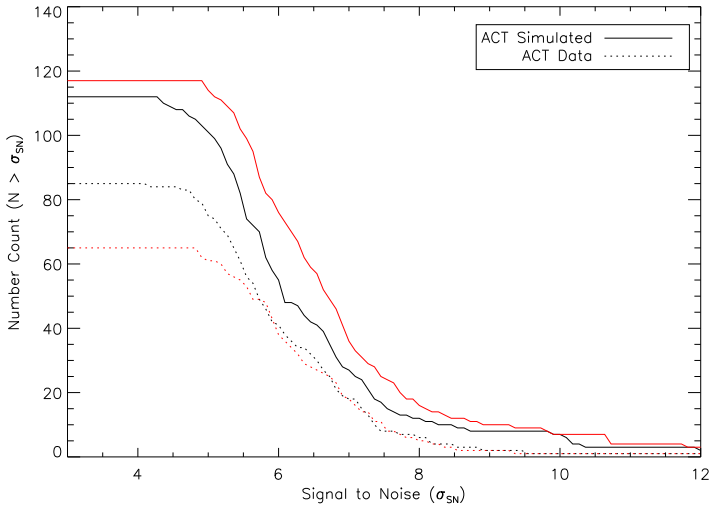

Figure 6.6: Cluster number counts from the ACT simulated and data maps against signal-to-noise. As previously stated, the black lines indicate a filter constructed using the data, while the red lines use a model in the filter prescription.

overestimate for the detection count. In future work, we will investigate whether this discrepancy remains after comparing to telescope simulations, where full synthetic timestream data is generated and fed into the ACT map making pipeline. These simulations will include a fuller, more realistic treatment of the correlated noise than the simulations used in this thesis. Finally, this investigation only used one noise and simulated map realisation. In a following study we will extend this procedure to multiple sky regions thus mitigating cosmic variance.

6.5 Flux Statistics: ACT and Simulated Maps

In addition to cluster detection statistics we present flux estimates for all detected objects. To calculate the latter, we used a fixed $3'$ aperture centred on each cluster detection. Object flux was then determined by totalling the flux contained within this aperture minus an estimate of the sky flux. The sky contribution was calculated by using 500 randomly placed apertures within $40'$ of the object position. We then took a pixel-by-pixel median of each aperture to create an 'averaged' sky map. The total of this map formed the estimate of the sky. Such a procedure was performed because the noise within the filtered maps is correlated. Thus, a simple per-pixel

estimate of the sky noise scaled to the aperture size is not robust and will be an underestimate of the true noise level. To determine the error in the flux, we totalled the sky contribution in each of the apertures and then calculated the standard deviation of this distribution. In this way we compensated for local noise variations in the map, which is of crucial importance when the map noise is non-white. Fig. 6.7 depicts the recovered versus catalogue flux (Compton parameter Y) for the simulated map analysis. From this flux distribution, we estimated the mean residual of the

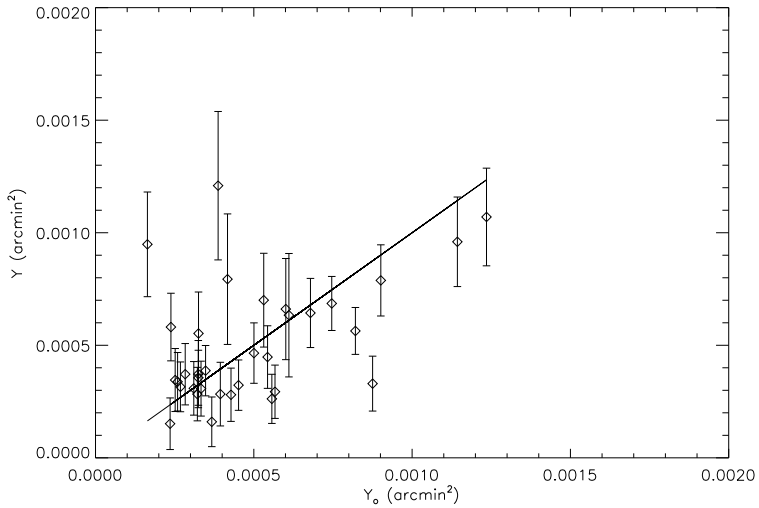

Figure 6.7: Recovered versus true flux for the simulated ACT map. The recovered flux (Y) is presented on the y-axis while the true flux (Y_o) is designated by the x-axis.

recovered fluxes to the input catalogue and found the deviation from zero to be $\approx +0.15\sigma$. This suggests that recovered fluxes are marginally biased, such that the recovered fluxes are slightly overestimated. This deviation is relatively small, and shows flux recovery from the filtered maps is reliable at least above 1×10^{-4} arcmin^2.

6.6 ACT Cluster Candidates

In this section we document cluster detection results from the real ACT data. In our sample we include both previously discovered clusters as well as a subset of our cluster candidates detected above a signal-to-noise of 6. Table 6.1 presents our cluster list, including cluster position, signal-

to-noise as well as flux estimates and errors. We used the NASA/IPAC Extragalactic Database (NED [2]) to cross-check our cluster list with known objects. In the case where a known object was close to our candidate, we present its catalogue name, separation in arcminutes as well as a reference to its first appearance in the literature. More information on the previously discovered clusters named in Table 6.1 can be found in Chapter 5.

Signal-to-noise estimates, object fluxes and errors were calculated in the same manner as for the simulations (see §6.5). The flux errors in the case of the real data vary between $15\% - 50\%$. For most of the clusters, the errors are similar to the simulated data flux errors, although there do exist outliers. Significant flux errors occur particularly in the case where clusters lie in high noise regions, for example in the outskirts of the survey region.

In Fig. 6.8 we present individual stamps of eight previously known clusters as well as eight new candidates. All maps are scaled in the same manner and the map units are given in μK. Each cluster map was derived by selecting a sub-region around each cluster in the filtered map. If a cluster was detected in more than one filtered map (since multiple signal templates were used), the map where the cluster was measured with the highest signal-to-noise was chosen. Each cluster stamp was then smoothed using a Gaussian with smoothing length, $0.5'$.

6.7 Conclusion

In this Chapter we have presented preliminary analyses of simulated and real ACT data. We have investigated the effects of two types of filter construction on cluster purity, number counts and completeness. We find that for the 480 deg^2 sky area studied, our sample is approximately 80% complete above $7 \times 10^{14} M_{\odot}$. In our study we demonstrated that the two-dimensional filtering procedure produces relatively reliable fluxes above 1×10^{-4}arcmin^2. In addition 36 new cluster candidates, along with 8 previously discovered clusters, have been detected in the ACT data and subsequently presented. Improvements to the cluster detection procedure have been planned. We propose using multiple realisations of the sky simulations to minimise cosmic variance, as well

[2]Website for NED can be found at: http://nedwww.ipac.caltech.edu

Table 6.1: Selection of SZ Clusters Detected by ACT

ACT Descriptor	Catalogue Name	J2000 Coordinates		SNR	Y_C
		RA	Dec.		10^{-6} arcmin^2
ACT-CL J0230-5553	-	$02^h30^m54.2^s$	$-55°53'26.2''$	6.84	1243.00 ± 284.50
ACT-CL J0235-5121	-	$02^h35^m55.3^s$	$-51°21'10.1''$	8.16	1892.00 ± 415.50
ACT-CL J0239-5118	-	$02^h39^m48.1^s$	$-51°18'12.4''$	6.15	1131.00 ± 294.50
ACT-CL J0245-5013	-	$02^h45^m27.8^s$	$-50°13'16.2''$	6.23	1736.00 ± 410.90
ACT-CL J0245-5302	Abell S0295[a] (1.15′)	$02^h45^m34.9^s$	$-53°02'18.3''$	8.84	1035.00 ± 269.60
ACT-CL J0247-5023	-	$02^h47^m13.0^s$	$-50°23'34.3''$	7.44	1943.00 ± 436.80
ACT-CL J0251-5544	-	$02^h51^m00.1^s$	$-55°44'11.3''$	6.10	1650.00 ± 578.60
ACT-CL J0307-5426	-	$03^h07^m16.0^s$	$-54°26'14.5''$	7.43	1796.00 ± 456.30
ACT-CL J0319-5224	-	$03^h19^m49.9^s$	$-52°24'53.2''$	6.98	1369.00 ± 382.30
ACT-CL J0330-5228	Abell 3128 NE[b]	$03^h30^m54.4^s$	$-52°28'17.6''$	6.50	953.80 ± 279.10
ACT-CL J0332-5551	-	$03^h32^m09.8^s$	$-55°51'19.1''$	7.31	1565.00 ± 416.00
ACT-CL J0400-5124	-	$04^h00^m27.1^s$	$-51°24'25.4''$	6.03	935.30 ± 278.70
ACT-CL J0425-5049	-	$04^h25^m38.7^s$	$-50°49'55.2''$	6.71	1710.00 ± 435.50
ACT-CL J0429-5400	-	$04^h29^m29.1^s$	$-54°00'12.2''$	8.15	1639.00 ± 406.50
ACT-CL J0435-5535	-	$04^h35^m57.4^s$	$-55°35'23.5''$	7.31	2053.00 ± 446.00
ACT-CL J0438-5418	-	$04^h38^m17.8^s$	$-54°18'58.7''$	6.05	443.30 ± 264.20
ACT-CL J0438-5339	-	$04^h38^m36.6^s$	$-53°39'49.9''$	6.76	1472.00 ± 403.70
ACT-CL J0441-5228	-	$04^h41^m57.1^s$	$-52°28'09.2''$	6.74	1672.00 ± 439.80
ACT-CL J0446-5201	-	$04^h46^m44.8^s$	$-52°01'32.4''$	7.16	1295.00 ± 293.40
ACT-CL J0453-5014	-	$04^h53^m01.9^s$	$-50°14'32.8''$	6.87	1259.00 ± 368.20
ACT-CL J0501-5308	-	$05^h01^m49.1^s$	$-53°08'59.0''$	7.19	1470.00 ± 477.50
ACT-CL J0503-5247	-	$05^h03^m04.9^s$	$-52°47'20.1''$	6.79	1658.00 ± 458.00
ACT-CL J0507-5147	-	$05^h07^m38.6^s$	$-51°47'09.7''$	6.56	1593.00 ± 559.60
ACT-CL J0508-5455	SUMSS J050810-545547[c] (1.52′)	$05^h08^m11.2^s$	$-54°55'05.0''$	6.63	1559.00 ± 492.50
ACT-CL J0516-5430	Abell S0520[d] (1.53′)	$05^h16^m34.4^s$	$-54°30'53.1''$	5.23	807.60 ± 303.00
ACT-CL J0525-5100	-	$05^h25^m33.7^s$	$-51°00'04.3''$	6.57	1315.00 ± 388.10
ACT-CL J0531-5124	-	$05^h31^m57.1^s$	$-51°24'27.9''$	7.91	1852.00 ± 504.20
ACT-CL J0539-5442	-	$05^h39^m05.3^s$	$-54°42'53.9''$	7.11	1673.00 ± 416.30
ACT-CL J0539-5154	-	$05^h39^m59.2^s$	$-51°54'36.8''$	6.76	1506.00 ± 466.40
ACT-CL J0546-5345	SPT-CL J0546-5345[e] (0.17′)	$05^h46^m37.6^s$	$-53°45'35.4''$	8.54	1615.00 ± 393.20
ACT-CL J0546-5326	-	$05^h46^m58.9^s$	$-53°26'46.5''$	6.04	1150.00 ± 330.40
ACT-CL J0556-5557	-	$05^h56^m41.2^s$	$-55°57'00.6''$	6.68	1678.00 ± 452.40
ACT-CL J0557-5027	-	$05^h57^m44.0^s$	$-50°27'28.4''$	6.20	1416.00 ± 359.60
ACT-CL J0559-5249	SPT-CL J0559-5249[f] (0.79′)	$05^h59^m45.2^s$	$-52°49'32.2''$	4.98	822.40 ± 292.30
ACT-CL J0614-5113	-	$06^h14^m03.0^s$	$-51°13'47.4''$	7.14	1756.00 ± 439.50
ACT-CL J0616-5227	SUMSS J061634-522716[g] (0.56′)	$06^h16^m38.0^s$	$-52°27'17.2''$	5.52	791.10 ± 351.10
ACT-CL J0622-5252	-	$06^h22^m20.5^s$	$-52°52'47.5''$	6.47	1598.00 ± 452.60
ACT-CL J0625-5317	-	$06^h25^m08.2^s$	$-53°17'57.6''$	7.22	1751.00 ± 522.90
ACT-CL J0627-5121	-	$06^h27^m07.9^s$	$-51°21'28.9''$	7.65	1675.00 ± 484.30
ACT-CL J0638-5358	Abell S0592[h] (1.15′)	$06^h38^m47.2^s$	$-53°58'45.4''$	9.49	1601.00 ± 320.50
ACT-CL J0645-5413	Abell 3404[i] (1.68′)	$06^h45^m29.0^s$	$-54°13'50.3''$	7.28	1110.00 ± 366.10
ACT-CL J0650-5244	-	$06^h50^m06.5^s$	$-52°44'50.8''$	6.41	1761.00 ± 528.80
ACT-CL J0658-5556	1ES 0657-56 (Bullet)[j] (0.31′)	$06^h58^m31.1^s$	$-55°56'59.7''$	11.12	2488.00 ± 473.50
ACT-CL J0706-5201	-	$07^h06^m34.5^s$	$-52°01'57.3''$	6.37	2055.00 ± 574.00

[a,d,h,i] Abell et al. (1989).
[b] Refers to north eastern counterpart of Abell 3128. Please refer to Chapter 5 for a discussion of this object.
[c,g] Radio point sources (Mauch et al., 2003).
[e,f] SPT clusters SPT-CL J0546-5345 (Staniszewski et al., 2009) and SPT-CL J0559-5249 (Vanderlinde et al., 2010) respectively.
[j] 1ES 0657-56 (Bullet) Tucker et al. (1995).

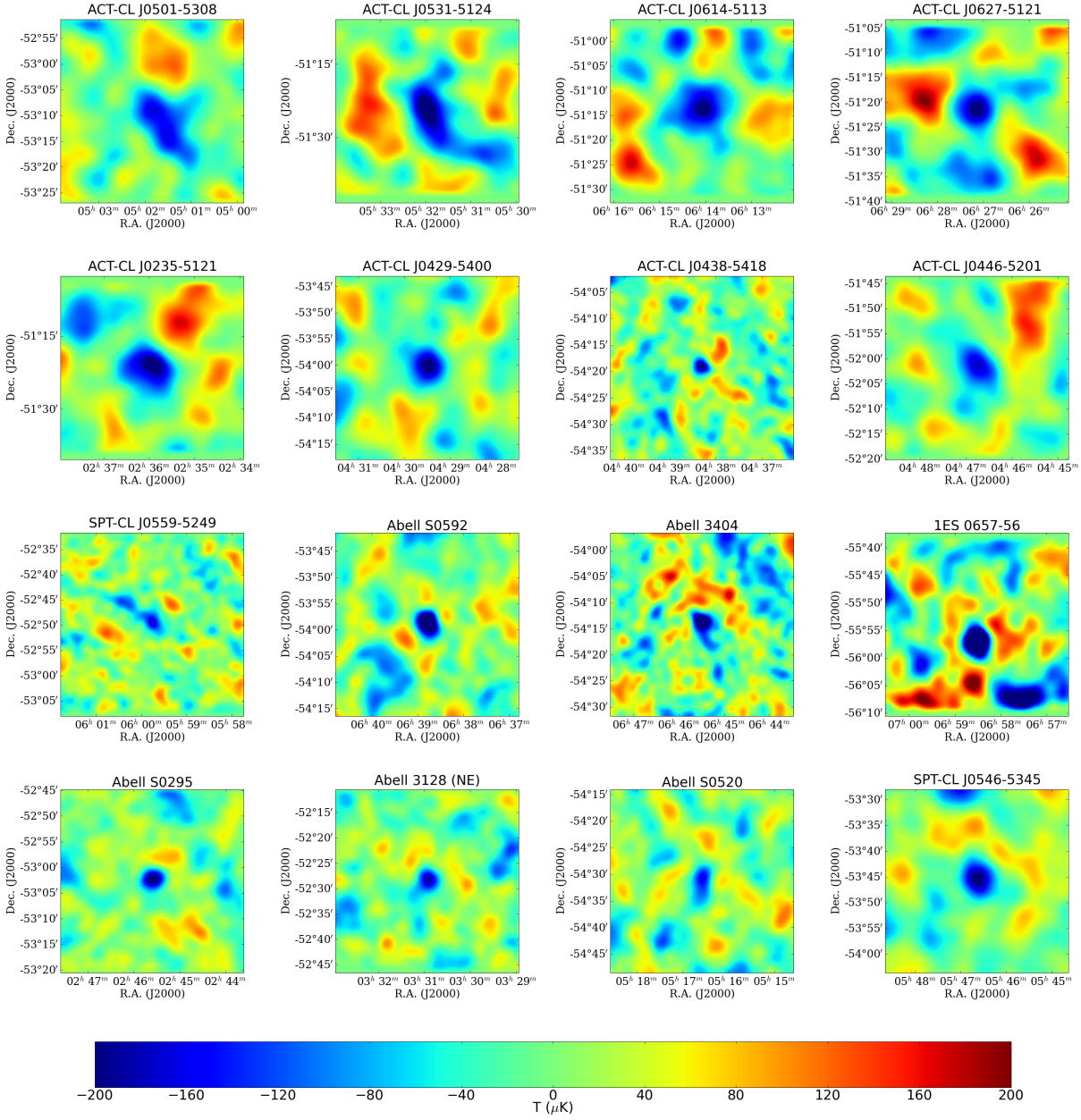

Figure 6.8: Subset of detected SZ clusters. The units of the stamps are μK.

as numerous realistic ACT noise realisations to quantify the effects of noise variations in the recovered maps. Furthermore, we plan to implement other filters such as the matched filter (*e.g.* Herranz et al., 2002b,a) to determine the dependence of the filtering process on cluster selection

and integrated Compton parameter estimation. To complement this, we also plan to study the effects of SZ template selection (such as various gas prescriptions and halo concentrations) and source modelling (such as lensed CMB and dust) on derived cluster properties. Finally, we plan to include realistic infrared and radio point sources in our simulations, which will impact on purity and other derived cluster properties. Several of the new cluster candidates will be followed up in upcoming targeted observations to confirm their existence and if so, to measure properties such as mass and redshift. This information will be used to place constraints on normalisation of the matter power spectrum, σ_8, and matter density, Ω_m.

CHAPTER 7

Conclusion

Galaxy clusters and groups provide a unique laboratory for studying the dynamics and evolution of our Universe. Their widescale distribution in the cosmos as well as their complicated dynamics poses significant challenges to astronomers and cosmologists alike. The SZ effect provides a possible means to mitigate at least some of these hindrances. Surveys employing such a technique benefit from a mass and not redshift limited catalogue. Such a property enables one to study these objects throughout a large range in redshift and thus over a large dynamic time frame.

In chapter 2 we provided a background to cosmology and large scale structure. Moreover, we discussed the development of such structure from perturbations in the Universe, into the observable galaxies, groups and clusters we see today. In addition we introduced the current or 'concordance' model of cosmology, as well as three new experiments aimed at constraining parameters within this model.

In chapter 3 we investigated the detectability of tSZ groups and low mass clusters using an analytic prescription for the hot gas contained within such halos. We studied two different models for the gas, one being a simple adiabatic formalism with a polytropic equation of state, and the other incorporating the effects of entropy through feedback effects. We found that the two models

were distinguishable through measurements of their tSZ distortion in clusters and even low mass galaxy groups. The detection of hot gas contained in low mass clusters and groups with current and upcoming CMB experiments such as ACT, SPT and PLANCK, will provide a novel probe of galaxy formation and its effect on the distribution and dynamics of the hot gas. Furthermore, a measurement of the tSZ effect in the outskirts of such halos will allow constraints to be placed on entropy injection levels as well as the baryon fraction. The latter provides a means of updating the current baryon census in the local universe.

In chapter 4 we investigated how well ACT will be able to constrain different gas parameters using the tSZ effect. We implemented a new deblending algorithm which measures accurate and unbiased halo fluxes as well as radial profiles. By comparing analytical simulations of Compton profiles for different gas models, against those derived from filtered sky maps, we placed constraints on different gas parameters using a Fisher matrix analysis. Moreover, we found that an extended survey with ACT will be able to constrain feedback, and stellar and baryon fraction indices with fractional errors of 33%, 35%, 75% respectively. On the other hand, studies using a deep survey will be able to constrain feedback effects only, while a wide survey will be unable to constrain any of these parameters. Furthermore, we also investigated how well each survey will be able to constrain baryon and stellar fraction scaling relations, with the conclusion that the extended survey will be able to measure a departure from a constant scaling relation.

In chapter 5 we presented a maximum-likelihood mapping algorithm which utilises B-splines to model the effects of atmospheric signals and remove them from data streams and the consequent maps. This method was used to construct beam maps for each of the ACT frequency channels, which are crucial in any further study of the ACT data. In addition, we presented SZ detections of 8 previously discovered clusters, which included a detection of an anomaly in Abell 3128. We detect the high redshift ($z = 0.44$) component of the cluster at high significance but fail to measure the low redshift counterpart. Our result corroborates other evidence that suggests the further cluster is more massive (Werner et al., 2007). This detection further confirms the redshift independent nature of the SZ effect.

In the final chapter we followed on from this work and presented a cluster detection analysis of ≈ 480 deg^2 of ACT data at 148 GHz. We used a two-dimensional Wiener filter incorporating two construction methods. The first method utilised the data in the filter prescription while the second method used models for the CMB and dust contamination. Map filtering and cluster detection was performed on real and simulated ACT maps in order to quantify sample purity, completeness and flux recovery statistics. Our analysis yielded 44 detections of which 8 are previously known and 36 are new candidates, with a completeness of $\approx 80\%$ above $7 \times 10^{14} M_{\odot}$. Furthermore, we also derived Compton parameters Y_{SZ} for each of the clusters and corroborated these estimates with simulations showing they were unbiased and reliable. The cluster catalogue will be used in upcoming targeted observations using optical and X-ray instruments to derive masses and redshifts. Such a catalogue incorporating a well-defined selection function, inherent to the SZ effect, as well as accurate halo properties derived from complementary studies, will be used to constrain cosmological parameters such as the normalisation of the matter power spectrum, the overall matter density of the universe and properties of the dark energy.

The plethora of data available from current and upcoming experiments will allow a unique probe into the evolution and dynamics of our Universe. The strength of the SZ effect as a cosmological probe is already being seen in cluster studies by ACT and SPT, and with new experiments coming online, such as PLANCK, the future is very exciting.

APPENDIX A

Gas profiles

We present here the radial profiles of the electron temperature, density, pressure and entropy for the polytropic model and entropy injection model (see Figs. A.2-A.4). For the higher mass halos ($\sim 10^{15} M_{\odot}$), the entropy injection model profiles are very similar to the corresponding polytropic model profiles, which indicates that the distribution of gas in large clusters is fairly insensitive to the injection of entropy.

For lower mass halos, the imposed heating is much more effective, resulting in a higher electron temperature especially in the central parts of the halo (see Fig. A.2). This reflects the fact that feedback effects are more significant for galaxy and group sized halos, raising the temperature above the shock-heated infall value. The density profiles of the polytropic and entropy injection models are significantly different for the low halo mass range, demonstrating that the entropy injection has a more marked effect on group sized halos, pushing gas into the outer regions of the halo and flattening the density profile. There is much more hot gas in the inner halo regions in the polytropic model which produces levels of X-ray emission in galaxy sized halos that are in violation of observational constraints, as we discuss below. Similarly, the imposed heating only significantly alters the pressure profiles for galaxy and group sized halos (see Fig. A.3), greatly lowering the central electron pressure. The heating term was modelled such that the pressure

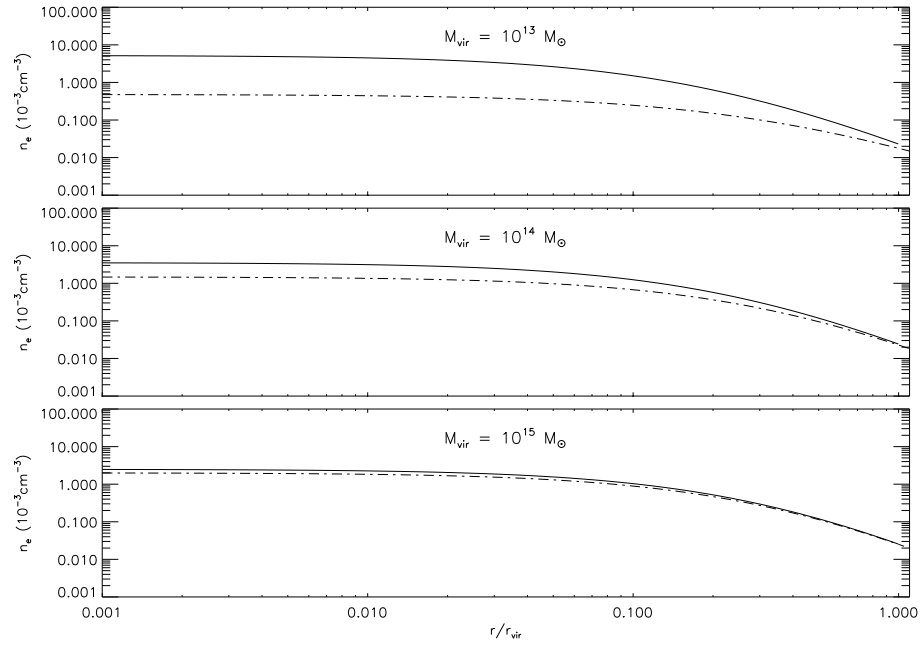

Figure A.1: Electron number density profiles, n_e (10^{-3}cm^{-3}), plotted against $r/r_{\rm vir}$ for the polytropic model (solid curves) and entropy model (dot-dashed curves). The panels from top to bottom show the density profiles for halo masses $M_{\rm vir} = 10^{13}, 10^{14}$ and 10^{15} $M_\odot$ respectively.

was unaltered at the virial radius, where we do not expect feedback to have an effect even for the lowest mass halos. The entropy injection model was constructed to have significantly more entropy than the polytropic model in the inner regions for the low mass halos, where the injected energy input is significant relative to the gravitational binding energy of the halo.

The cumulative X-ray luminosity profiles for the two models are shown in Fig. A.5. While the integrated luminosity profiles are similar for high mass halos, the X-ray luminosity in the polytropic model is significantly higher for low mass halos, in violation of the upper limits on the diffuse X-ray emission from hot gas in nearby galaxy halos like M31 (Taylor et al., 2003; Takahashi et al., 2001). The entropy model does not violate these constraints though, as the reduced central density in this model lowers the X-ray luminosity in the inner regions despite the increased temperature.

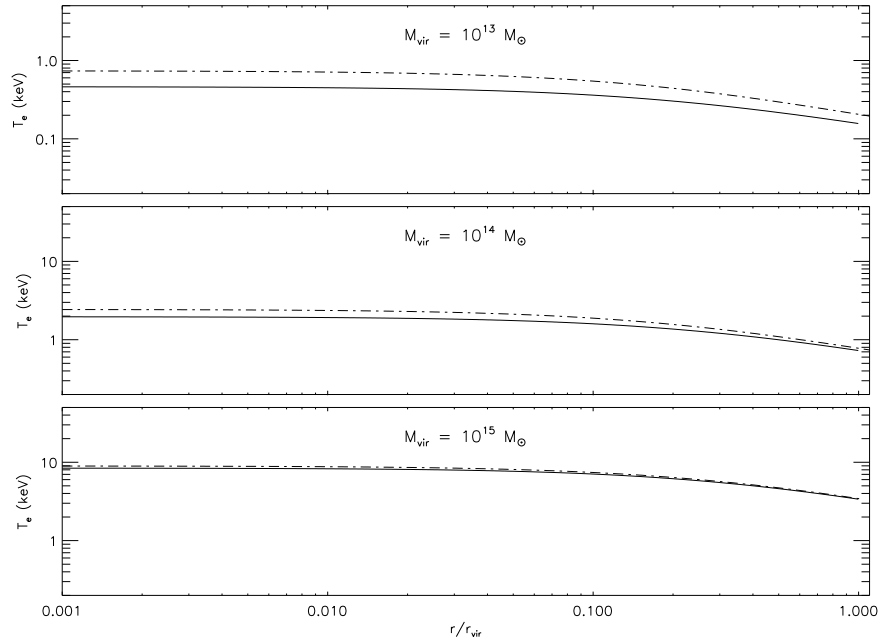

Figure A.2: Electron temperature profiles, T_e (keV), plotted against $r/r_{\rm vir}$ for the polytropic model (solid curves) and the entropy model (dot-dashed curves). The panels from top to bottom show the temperature profiles for halo masses $M_{\rm vir} = 10^{13}, 10^{14}$ and $10^{15}\ M_\odot$ respectively.

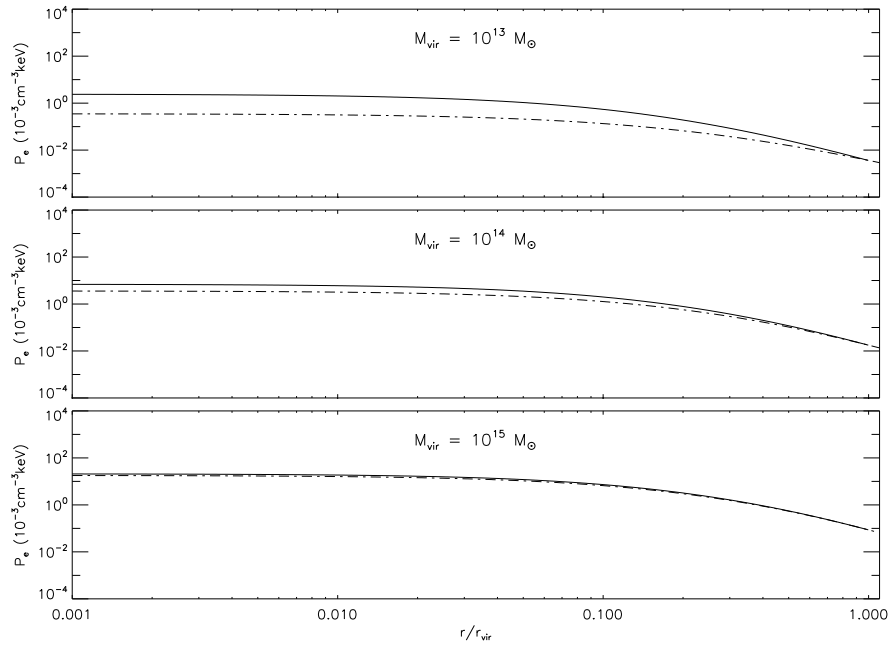

Figure A.3: Electron pressure profiles, P_e ($10^{-3}\,\mathrm{keV\,cm^{-3}}$), plotted against $r/r_{\rm vir}$ for the polytropic model (solid curves) and the entropy model (dot-dashed curves). The panels from top to bottom show the pressure profiles for halo masses $M_{\rm vir} = 10^{13}, 10^{14}$ and $10^{15}\ M_\odot$ respectively.

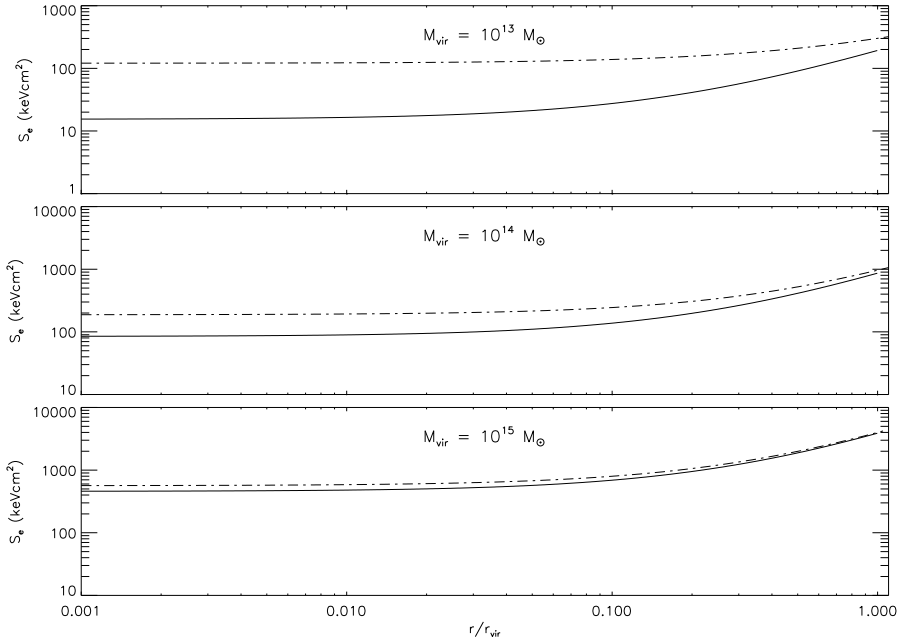

Figure A.4: Entropy profiles, S_e (keV cm^2), plotted against $r/r_{\rm vir}$ for the polytropic model (solid curves) and the entropy model (dot-dashed curves). The panels from top to bottom show the entropy profiles for halo masses $M_{\rm vir} = 10^{13}, 10^{14}$ and 10^{15} $M_\odot$ respectively.

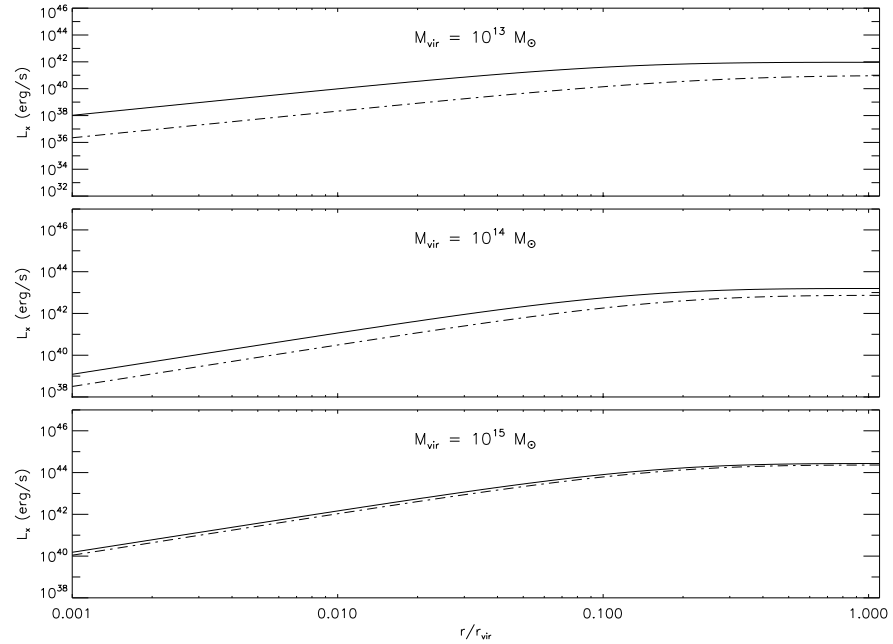

Figure A.5: Integrated X-ray luminosity, $L_X(< r/r_{\rm vir})$, plotted against $r/r_{\rm vir}$ for the polytropic (solid curves) and entropy (dot-dashed curves) models. The panels from top to bottom show the integrated luminosity profiles for halo masses $M_{\rm vir} = 10^{13}, 10^{14}$ and 10^{15} $M_\odot$ respectively.

APPENDIX B

Gas Model

We follow the prescription of Bode et al. (2009), following on earlier work by Ostriker et al. (2005), to construct a model for the gas in cluster and group halos.

Dark Matter Halo

We assume that the underlying dark matter halo has a density given by the generalised NFW profile

$$\rho_{\rm dm} = \frac{\rho_{\rm s}}{(r/r_{\rm s})^{\alpha}(1+r/r_{\rm s})^{3-\alpha}} = \rho_{\rm s} y_{\rm dm}(x) \tag{2.0.1}$$

where we define

$$y_{\rm dm}(x) = x^{-\alpha}(1+x)^{\alpha-3}, \qquad x = r/r_{\rm s}. \tag{2.0.2}$$

The formulae and model parameters described below assume an NFW profile ($\alpha = 1$ in Eq. (2.0.1)). However, these can be extended in a relatively straightforward manner for the generalised NFW profile with $\alpha \neq 1$, as we have done when comparing these models to the simulated halos.

Normalising the dark matter mass within the virial radius, $r_{\rm vir}$ to the virial mass, $M_{\rm vir}$ yields

$$\rho_s = \frac{M_{\rm vir} c^3}{4\pi r_{\rm vir}^3\, m(c)} \tag{2.0.3}$$

where we have used the concentration $c = r_{\rm vir}/r_{\rm s}$ and the dimensionless mass profile

$$m(x) = \int_0^x y_{\rm dm}(x')x'^2 dx' = \log(1+x) - \frac{x}{1+x}. \tag{2.0.4}$$

The virial radius is defined as the radius at which the dark matter halo has a characteristic average density equal to $\Delta_{\rm vir}(z)$ times the critical density,

$$\rho_c(z) = \frac{3H^2(z)}{8\pi G}\ . \tag{2.0.5}$$

The Hubble parameter relative to its present value is given by

$$\frac{H(z)}{H_0} = \left[\Omega_m(1+z)^3 + \Omega_{\rm de}(1+z)^{3(1+w_{\rm de})}\right]^{1/2}\ , \tag{2.0.6}$$

where $\Omega_{\rm m}$ and $\Omega_{\rm de}$ represent the density of the matter and dark energy components, respectively, relative to the critical density today. Using numerical simulations, Bryan and Norman (1998) found for ΛCDM cosmologies that the parametric form

$$\Delta_{\rm vir}(z) = 18\pi^2 + 82[\Omega(z) - 1] - 39[\Omega(z) - 1]^2\ , \tag{2.0.7}$$

where

$$\Omega(z) \equiv \Omega_m(1+z)^3 \left[\frac{H_0}{H(z)}\right]^2\ , \tag{2.0.8}$$

provides a good fit over a wide range of ΛCDM cosmological models. Once the characteristic average density is chosen, the virial mass and radius become uniquely related.

The concentration parameter is defined as $c = r_{\rm vir}/r_s$ and is derived by fitting the dark matter mass distribution (*e.g.* M_{vir}, M_{200}, M_{500}, M_{1500}, M_{2500}) as a function of radii (*e.g.* r_{vir}, r_{200}, r_{500}, r_{1500}, r_{2500}). Simulated dark matter halos exhibit scatter about the above concentration scaling relation. To account for this we allow the concentration to be a free parameter and fix it by fitting to the thermal SZ profile. Another effect that will cause scatter in our estimate of the concentration is the asymmetry of the dark matter distribution, which our model does not capture.

Once the dark matter density is specified we can obtain the gravitational potential of the halo as

$$\phi(x) = -GM(r)/r = \phi_0 f(x), \tag{2.0.9}$$

with $f(x)$ and ϕ_0 determined by

$$f(x) = m(x)/x, \qquad \phi_0 = -4\pi G\, r_{\rm s}^2 \rho_{\rm s}. \tag{2.0.10}$$

The velocity dispersion of the dark matter is defined as

$$\sigma^2(x) = \sigma_0^2 s(x), \qquad \sigma_0^2 = 4\pi G \rho_{\rm s} r_{\rm s}^2 \tag{2.0.11}$$

where

$$s(x) = x(1+x)^2 \left[\sigma_c - \int_x^c \frac{u - (1+u)\log(1+u)}{u^3(1+u)^3} du\right] \tag{2.0.12}$$

with σ_c is proportional to the surface pressure. For σ_c we adopt the expression

$$\begin{aligned} \sigma_c = \quad & \frac{\pi^2}{2} - \frac{\log(c)}{2} - \frac{1}{2c} - \frac{1}{2(1+c)^2} - \frac{3}{1+c} \\ & + \left(\frac{1}{2} + \frac{1}{2c^2} - \frac{2}{c} - \frac{1}{1+c}\right)\log(1+c) \\ & + \frac{3}{2}\log^2(1+c) + 3\int_{-c}^{0} \log(1-x) d\log(x) \end{aligned} \tag{2.0.13}$$

derived by Łokas and Mamon (2001) by solving the Jeans equation for a constant velocity anisotropy and isotropic orbits.

The total gravitational energy of the dark matter halo is given by

$$W^{\rm dm}(c) = \frac{1}{2} W_0^{\rm dm} \int_0^c f(x) y_{\rm dm}(x) x^2 dx, \tag{2.0.14}$$

with

$$W_0^{\rm dm} = 4\pi \phi_0 \rho_{\rm s} r_{\rm s}^3, \tag{2.0.15}$$

and the total kinetic energy is given by

$$T^{\rm dm}(c) = T_0^{\rm dm} \int_0^c s(x) y_{\rm dm}(x) x^2 dx, \tag{2.0.16}$$

where

$$T_0^{\rm dm} = 6\pi \sigma_0^2 \rho_{\rm s} r_{\rm s}^3. \tag{2.0.17}$$

Stellar Mass, Initial Gas Energy and Pressure

A fraction of the original baryons, f_* would have formed stars leaving a fraction $f_{\rm gas} = 1 - f_*$ of gas in the halo. We place the stars in the central region of the halo out to some radius x_s, which is obtained by integrating the mass profile of the stars (assumed proportional to the dark matter profile) out to x_s to give the total stellar mass, that is by solving

$$4\pi r_{\rm s}^3 \rho_s m(x_{\rm s}) f_b = M_* \tag{2.0.18}$$

The exact prescription for M_* follows that given in the appendix of Bode et al. (2009) and includes mass lost from winds and supernovae. The stellar mass exhibits a very weak dependence on redshift, particularly for $z < 1$. Note that removing stars also increases the average gas energy. The resulting gas energy, found by multiplying the energy in dark matter by the baryon fraction, is thus obtained by integrating the gravitational and kinetic energies from x_s to c, such that

$$W^{\rm gas}(c) = \frac{1}{2} W_0^{\rm gas} \int_{x_s}^{c} f(x) y_{\rm dm}(x) x^2 dx, \quad W_0^{\rm gas} = f_b W_0^{\rm dm} \tag{2.0.19}$$

and

$$T^{\rm gas}(c) = T_0^{\rm gas} \int_{x_s}^{c} s(x) y_{\rm dm}(x) x^2 dx, \quad T_0^{\rm gas} = f_b T_0^{\rm dm} \tag{2.0.20}$$

Applying the virial theorem: $W^{\rm dm}(c) + 2T^{\rm dm}(c) - 4\pi r_{\rm vir}^3 P_{\rm s} = 0$ to the halo allows us to find the initial surface pressure of the halo, and consequently the initial gas surface pressure given by $P_{\rm s}^{\rm gas} = f_b P_{\rm s}$.

Gas Equilibrium Distribution

We now present the equilibrium distributions after the gas has settled into the dark matter potential. Assuming that the gas is a polytrope

$$\rho_{\rm gas}(x) = \rho_0 y_{\rm gas}(x), \qquad P_{\rm gas}(x) = P_0 y_{\rm gas}^{\gamma}(x) \tag{2.0.21}$$

in hydrostatic equilibrium with the dark matter potential allows us to solve for the form of the gas profile

$$y_{\rm gas}(x) = (1 - \beta[\phi_0 - \phi(x)])^{1/(\gamma-1)}, \tag{2.0.22}$$

with

$$\beta = -\phi_0 \frac{\gamma - 1}{\gamma} \frac{1}{1 + \delta_{\rm rel}} \frac{\rho_0}{P_0} \equiv \beta_0 \frac{\rho_0}{P_0} \tag{2.0.23}$$

where $\delta_{\rm rel}$ is the fractional nonthermal contribution to the pressure from shocks and a magnetic field, for example.

The normalisation of the gas density and gas pressure is obtained by requiring the conservation of energy and constancy of the surface pressure. We model changes to the gas energy in terms of three contributions: expansion or contraction of the gas, dynamical transfer of energy from the dark matter, and feedback from collapsed objects such as supernovae and AGN. The change in energy of the gas due to a change in volume, reaching a final radius, $r_f = c_f\, r_{\rm s}$, is given by $\Delta E_P = \frac{4\pi}{3}(c^3 - c_f^3) P_{\rm s}^{\rm gas} r_{\rm s}^3$ while the dynamical energy transferred from the dark matter during virialisation is assumed to be proportional to the initial dark matter energy, $\Delta E_D = \epsilon_D |W^{\rm dm}(c) + T^{\rm dm}(c)|$, with ϵ_D measuring the fraction of energy transferred. The change in energy from AGN and supernovae feedback is assumed to be proportional to the mass in formed stars, $\Delta E_F = \epsilon_F M_F c^2$ which is derived from the stellar mass by taking gas recycling into account – for the redshift range that we are interested in, $0 < z < 1$, the mass in formed stars is roughly fifty percent larger than the stellar mass. We follow the prescription for M_F given in Bode et al. (2009), which makes use of the 'fossil' model by Nagamine et al. (2006). In this particular model, different stellar populations are considered as well as stellar mass loss due to supernovae and winds.

Taking into account energy conservation; i.e. $E_{initial} + \Delta E_P + \Delta E_D + \Delta E_F = E_{final}$, and matching the surface and exterior pressures of the gas gives two equations which can be solved to obtain the unknown parameters, c_f and β. These are, respectively,

$$\begin{aligned} 2W^{\rm gas}(c) \;+\; & T^{\rm gas}(c) + 4\pi(c^3 - c_f^3) r_{\rm s}^3 P_{\rm s}^{\rm gas} + \epsilon_D |W^{\rm dm}(c) \\ & + T^{\rm dm}(c)| + \epsilon_F M_F c^2 = \phi_0 M_{\rm gas} \frac{I_W^{\rm gas}(c_f, \beta)}{I_{\rm M}^{\rm gas}(c_f, \beta)} \\ & + \frac{3}{2}(1 + 2\delta_{\rm rel}) \left(\frac{\beta}{\beta_0}\right) M_{\rm gas} \frac{I_T^{\rm gas}(c_f, \beta)}{I_{\rm M}^{\rm gas}(c_f, \beta)} \end{aligned} \tag{2.0.24}$$

and

$$y^{\gamma}_{\rm gas}(c_f;\beta) = \frac{1+f_*}{1+\delta_{\rm rel}}\frac{\sigma_c\sigma_0^2}{m\,(c)}\left(\frac{\beta}{\beta_0}\right) I^{\rm gas}_{\rm M}(c_f,\beta). \tag{2.0.25}$$

Here we have defined

$$I^{\rm gas}_{W}(c_f,\beta) = \int_0^{c_f} f(x) y_{\rm gas}(x;\beta)x^2 dx \tag{2.0.26}$$

$$I^{\rm gas}_{T}(c_f,\beta) = \int_0^{c_f} y^{\gamma}_{\rm gas}(x;\beta)x^2 dx \tag{2.0.27}$$

$$I^{\rm gas}_{\rm M}(c_f,\beta) = \int_0^{c_f} y_{\rm gas}(x;\beta)x^2 dx \tag{2.0.28}$$

and the gas mass

$$M_{\rm gas} = f_{\rm gas} f_b M_{\rm vir} = 4\pi r_{\rm s}^3 \rho_0 I^{\rm gas}_{\rm M}(c_f,\beta). \tag{2.0.29}$$

The above equation, describing the conservation of gas mass, allows us to obtain ρ_0 once c_f is known, which in turn allows us to solve for P_0 from β.

Physical Gas Model Parameters

In our study we consider two different gas models which are characterised by various parameters. The first model is of an adiabatic type, where there is no feedback, star formation or dynamical energy exchange. This model is analogous to the 'zero model' in Bode et al. (2009). The second model we study is the standard model, which incorporates all the forementioned effects. For such a model we choose fiducial values for the feedback parameter, $\epsilon_F = 4 \times 10^{-6}$ and dynamical energy exchange parameter, $\epsilon_D = 0.05$. This model is similar to the one of the same name in Bode et al. (2009). The exact prescription for the baryon and stellar fractions encompassed within each of the models is presented in §4.5.3. All other parameters such as the concentration and dark matter profile index, α, are treated identically for each of the models.

APPENDIX C

The Cottingham Method as a Maximum Likelihood Estimator

Eq. (5.2.1) can be written in the matrix form,

$$\boldsymbol{d} = \begin{pmatrix} \boldsymbol{P} & \boldsymbol{B} \end{pmatrix} \begin{pmatrix} \boldsymbol{m} \\ \boldsymbol{\alpha} \end{pmatrix} + \boldsymbol{n}, \tag{3.0.1}$$

which has the maximum likelihood estimator:

$$\begin{aligned} \begin{pmatrix} \widetilde{\boldsymbol{m}} \\ \widetilde{\boldsymbol{\alpha}} \end{pmatrix} &= \left[\begin{pmatrix} \boldsymbol{P}^T \\ \boldsymbol{B}^T \end{pmatrix} \boldsymbol{N}^{-1} \begin{pmatrix} \boldsymbol{P} & \boldsymbol{B} \end{pmatrix} \right]^{-1} \begin{pmatrix} \boldsymbol{P}^T \\ \boldsymbol{B}^T \end{pmatrix} \boldsymbol{N}^{-1}\boldsymbol{d} \\ &= \begin{bmatrix} (\boldsymbol{PP}) & (\boldsymbol{PB}) \\ (\boldsymbol{BP}) & (\boldsymbol{BB}) \end{bmatrix}^{-1} \begin{pmatrix} \boldsymbol{P}^T\boldsymbol{N}^{-1}\boldsymbol{d} \\ \boldsymbol{B}^T\boldsymbol{N}^{-1}\boldsymbol{d} \end{pmatrix} \end{aligned} \tag{3.0.2}$$

where we use the shorthand notation $(\boldsymbol{XY}) \equiv \boldsymbol{X}^T\boldsymbol{N}^{-1}\boldsymbol{Y}$. The inverted matrix evaluates to:

$$\begin{bmatrix} \boldsymbol{w} & \boldsymbol{x} \\ \boldsymbol{y} & \boldsymbol{z} \end{bmatrix} \tag{3.0.3}$$

where

$$\begin{aligned} \boldsymbol{w} &= \left[(\boldsymbol{PP}) - (\boldsymbol{PB})(\boldsymbol{BB})^{-1}(\boldsymbol{BP})\right]^{-1} \\ \boldsymbol{x} &= -(\boldsymbol{PP})^{-1}(\boldsymbol{PB})\left[(\boldsymbol{BB}) - (\boldsymbol{BP})(\boldsymbol{PP})^{-1}(\boldsymbol{PB})\right]^{-1} \\ \boldsymbol{y} &= -(\boldsymbol{BB})^{-1}(\boldsymbol{BP})\left[(\boldsymbol{PP}) - (\boldsymbol{PB})(\boldsymbol{BB})^{-1}(\boldsymbol{BP})\right]^{-1} \\ \boldsymbol{z} &= \left[(\boldsymbol{BB}) - (\boldsymbol{BP})(\boldsymbol{PP})^{-1}(\boldsymbol{PB})\right]^{-1} \end{aligned} \tag{3.0.4}$$

Since this matrix is symmetric, and $(\boldsymbol{XY})^T = (\boldsymbol{YX})$, we can rewrite the lower-left component as:

$$\begin{aligned} &(\boldsymbol{BB})^{-1}(\boldsymbol{BP})\left[(\boldsymbol{PP}) - (\boldsymbol{PB})(\boldsymbol{BB})^{-1}(\boldsymbol{BP})\right]^{-1} \\ &\qquad = \left\{(\boldsymbol{PP})^{-1}(\boldsymbol{PB})\left[(\boldsymbol{BB}) - (\boldsymbol{BP})(\boldsymbol{PP})^{-1}(\boldsymbol{PB})\right]^{-1}\right\}^T \qquad (3.0.5) \\ &\qquad = \left[(\boldsymbol{BB}) - (\boldsymbol{BP})(\boldsymbol{PP})^{-1}(\boldsymbol{PB})\right]^{-1}(\boldsymbol{BP})(\boldsymbol{PP})^{-1}. \qquad (3.0.6) \end{aligned}$$

Thus, the solution for the atmosphere is:

$$\begin{aligned} \widetilde{\boldsymbol{\alpha}} &= \left[(\boldsymbol{BB}) - (\boldsymbol{BP})(\boldsymbol{PP})^{-1}(\boldsymbol{PB})\right]^{-1}\boldsymbol{B}^T\boldsymbol{N}^{-1}\boldsymbol{d} \\ &\quad - \left[(\boldsymbol{BB}) - (\boldsymbol{BP})(\boldsymbol{PP})^{-1}(\boldsymbol{PB})\right]^{-1}(\boldsymbol{BP})(\boldsymbol{PP})^{-1}\boldsymbol{P}^T\boldsymbol{N}^{-1}\boldsymbol{d}. \end{aligned} \tag{3.0.7}$$

To show that this is equivalent to the solution presented in §5.2.1, we observe that the definitions in Eqs. (5.2.3) and (5.2.6) of §5.2.1 can be recast:

$$\begin{aligned} \boldsymbol{\Theta} \equiv \boldsymbol{B}^T\boldsymbol{N}^{-1}(\mathbf{1} - \boldsymbol{P\Pi})\boldsymbol{B} &= (\boldsymbol{BB}) - (\boldsymbol{BP})(\boldsymbol{PP})^{-1}(\boldsymbol{PB}), \\ \boldsymbol{\phi} \equiv \boldsymbol{B}^T\boldsymbol{N}^{-1}(\mathbf{1} - \boldsymbol{P\Pi})\boldsymbol{d} &= \left[\boldsymbol{B}^T\boldsymbol{N}^{-1} - (\boldsymbol{BP})(\boldsymbol{PP})^{-1}\boldsymbol{P}^T\boldsymbol{N}^{-1}\right]\boldsymbol{d}. \end{aligned} \tag{3.0.8}$$

This reduces Eq. (3.0.7) to:

$$\widetilde{\boldsymbol{\alpha}} = \boldsymbol{\Theta}^{-1}\boldsymbol{\phi}, \tag{3.0.9}$$

which is the same as Eq. (5.2.7) of §5.2.1.

APPENDIX D

A Planet's Solid Angle Contribution to the Beam Solid Angle Measurement

Denote the instrument response with $P(\boldsymbol{n})$ and the power emitted by the planet with $P_0\Psi(\boldsymbol{n})$, where P_0 is the peak power emitted and Ψ is a normalised distribution describing its shape. The coordinate $\boldsymbol{n}$ is a two dimensional vector describing the position on the sky, with $\boldsymbol{n} = \boldsymbol{0}$ at the planet centre. The measured beam map, $\widetilde{B}$, is the convolution of the true beam, B, with the planet:

$$\widetilde{B}(\boldsymbol{n}) = \frac{P(\boldsymbol{n})}{P(\boldsymbol{0})} = \frac{\iint d\Omega_{\boldsymbol{n}'} B(\boldsymbol{n}-\boldsymbol{n}')\Psi(\boldsymbol{n}')}{\iint d\Omega_{\boldsymbol{n}'} B(-\boldsymbol{n}')\Psi(\boldsymbol{n}')}. \tag{4.0.1}$$

The measured solid angle is then (c.f. Eq. (5.3.13)):

$$\begin{aligned}\widetilde{\Omega}_A = \iint d\Omega_{\boldsymbol{n}} \frac{\iint d\Omega_{\boldsymbol{n}'} B(\boldsymbol{n}-\boldsymbol{n}')\Psi(\boldsymbol{n}')}{\iint d\Omega_{\boldsymbol{n}'} B(-\boldsymbol{n}')\Psi(\boldsymbol{n}')} &= \frac{\left[\iint d\Omega_{\boldsymbol{n}'}\Psi(\boldsymbol{n}')\right]\left[\iint d\Omega_{\boldsymbol{n}} B(\boldsymbol{n})\right]}{\iint d\Omega_{\boldsymbol{n}'} B(\boldsymbol{n}')\Psi(\boldsymbol{n}')} \\ &= \frac{\Omega_\Psi \Omega_A}{\iint d\Omega_{\boldsymbol{n}'} B(\boldsymbol{n}')\Psi(\boldsymbol{n}')},\end{aligned} \tag{4.0.2}$$

where in the second equality we brought the denominator outside the outer integral, and in the numerator we switched the order of and then shifted the dummy variable for the integral over B. In the last equality we recognised that the integrals in the numerator evaluate to the solid angles of the planet and the true instrument beam, respectively. If the planet is much smaller than the

beam, we can expand the beam appearing the integrand of the denominator in a Taylor series:

$$B(\boldsymbol{n}) = 1 \; + \; \nabla B(\boldsymbol{0}) \cdot \boldsymbol{n} \; + \; \frac{1}{2} \boldsymbol{n} \cdot \boldsymbol{H}(\boldsymbol{0}) \cdot \boldsymbol{n} \; + \; \ldots , \tag{4.0.3}$$

where $\boldsymbol{H}$ is the Hessian matrix of the beam. At the beam centre, being the peak, the gradient vanishes. If we assume a symmetric beam, then $\boldsymbol{n} \cdot \boldsymbol{H} \cdot \boldsymbol{n} = (\nabla^2 B/2)|\boldsymbol{n}|^2$, and we can write:

$$\begin{aligned} \widetilde{\Omega}_A \approx \frac{\Omega_\Psi \Omega_A}{\iint d\Omega_{\boldsymbol{n}'} \left[1 + \frac{1}{4} \nabla^2 B(\boldsymbol{0}) |\boldsymbol{n}'|^2\right] \Psi(\boldsymbol{n}')} &= \Omega_A \left[1 + \frac{\nabla^2 B(\boldsymbol{0})}{4\Omega_\Psi} \iint d\Omega_{\boldsymbol{n}'} |\boldsymbol{n}'|^2 \Psi(\boldsymbol{n}')\right]^{-1} \\ &= \Omega_A \left[1 + \frac{\nabla^2 B(\boldsymbol{0})}{4\Omega_\Psi} \mu_2^\Psi\right]^{-1} , \end{aligned} \tag{4.0.4}$$

where μ_2^Ψ is the second raw moment of the planet shape Ψ. In the small planet approximation we are making, the second term in the brackets is small. Thus:

$$\widetilde{\Omega}_A \approx \Omega_A - \frac{\Omega_A}{\Omega_\Psi} \frac{\nabla^2 B(\boldsymbol{0})}{4} \mu_2^\Psi . \tag{4.0.5}$$

For a disk, $\mu_2^\Psi = \Omega_\Psi^2 / 2\pi$, and both a Gaussian beam and an Airy pattern have $\nabla^2 B(\boldsymbol{0}) = -4\pi/\Omega_A$. (For the Airy pattern, this is easiest to see by expanding the Bessel function in a power series and differentiating.) Thus, we have the result that $\widetilde{\Omega}_A \approx \Omega_A + \Omega_\Psi/2$.

Bibliography

Abell, G. O., 1958, Astrophys. J. Supp., 3, 211

Abell, G. O., Corwin, H. G., Jr., and Olowin, R. P., 1989, Astrophys. J. Supp., 70, 1

Adelman-McCarthy, J. K., Agüeros, M. A., Allam, S. S., Anderson, K. S. J., Anderson, S. F., Annis, J., Bahcall, N. A., Baldry, I. K., Barentine, J. C., Berlind, A., Bernardi, M., Blanton, M. R., Boroski, W. N., Brewington, H. J., Brinchmann, J., Brinkmann, J., Brunner, R. J., Budavári, T., Carey, L. N., Carr, M. A., Castander, F. J., Connolly, A. J., Csabai, I., Czarapata, P. C., Dalcanton, J. J., Doi, M., Dong, F., Eisenstein, D. J., Evans, M. L., Fan, X., Finkbeiner, D. P., Friedman, S. D., Frieman, J. A., Fukugita, M., Gillespie, B., Glazebrook, K., Gray, J., Grebel, E. K., Gunn, J. E., Gurbani, V. K., de Haas, E., Hall, P. B., Harris, F. H., Harvanek, M., Hawley, S. L., Hayes, J., Hendry, J. S., Hennessy, G. S., Hindsley, R. B., Hirata, C. M., Hogan, C. J., Hogg, D. W., Holmgren, D. J., Holtzman, J. A., Ichikawa, S., Ivezić, Ž., Jester, S., Johnston, D. E., Jorgensen, A. M., Jurić, M., Kent, S. M., Kleinman, S. J., Knapp, G. R., Kniazev, A. Y., Kron, R. G., Krzesinski, J., Kuropatkin, N., Lamb, D. Q., Lampeitl, H., Lee, B. C., Leger, R. F., Lin, H., Long, D. C., Loveday, J., Lupton, R. H., Margon, B., Martínez-Delgado, D., Mandelbaum, R., Matsubara, T., McGehee, P. M., McKay, T. A., Meiksin, A., Munn, J. A., Nakajima, R., Nash, T., Neilsen, E. H., Jr., Newberg, H. J., Newman, P. R., Nichol, R. C., Nicinski, T., Nieto-Santisteban, M., Nitta, A., O'Mullane, W., Okamura, S.,

Owen, R., Padmanabhan, N., Pauls, G., Peoples, J., Jr., Pier, J. R., Pope, A. C., Pourbaix, D., Quinn, T. R., Richards, G. T., Richmond, M. W., Rockosi, C. M., Schlegel, D. J., Schneider, D. P., Schroeder, J., Scranton, R., Seljak, U., Sheldon, E., Shimasaku, K., Smith, J. A., Smolčić, V., Snedden, S. A., Stoughton, C., Strauss, M. A., SubbaRao, M., Szalay, A. S., Szapudi, I., Szkody, P., Tegmark, M., Thakar, A. R., Tucker, D. L., Uomoto, A., Vanden Berk, D. E., Vandenberg, J., Vogeley, M. S., Voges, W., Vogt, N. P., Walkowicz, L. M., Weinberg, D. H., West, A. A., White, S. D. M., Xu, Y., Yanny, B., Yocum, D. R., York, D. G., Zehavi, I., Zibetti, S., and Zucker, D. B., 2006, Astrophys. J. Supp., 162, 38

Aghanim, N., de Luca, A., Bouchet, F. R., Gispert, R., and Puget, J. L., 1997, Astron. Astrophys., 325, 9

Alpher, R. A. and Herman, R. C., 1948, Physical Review, 74, 1737

Alpher, R. A. and Herman, R. C., 1949, Physical Review, 75, 1089

Andreani, P., Böhringer, H., dall'Oglio, G., Martinis, L., Shaver, P., Lemke, R., Nyman, L., Booth, R., Pizzo, L., Whyborn, N., Tanaka, Y., and Liang, H., 1999, Astrophys. J., 513, 23

Andreani, P., Pizzo, L., dall'Oglio, G., Whyborn, N., Boehringer, H., Shaver, P., Lemke, R., Otarola, A., Nyman, L. A., and Booth, R., 1996a, Astrophys. J. Lett., 459, L49+

Andreani, P., Pizzo, L., dall'Oglio, G., Whyborn, N., Boehringer, H., Shaver, P., Lemke, R., Otarola, A., Nyman, L. A., and Booth, R., 1996b, Astrophys. J. Lett., 459, L49+

Arnaud, M. and Evrard, A. E., 1999, Mon. Not. R. Astron. Soc., 305, 631

Atrio-Barandela, F., Kashlinsky, A., Kocevski, D., and Ebeling, H., 2008, Astrophys. J. Lett., 675, L57

Bahcall, N. A., Ostriker, J. P., Perlmutter, S., and Steinhardt, P. J., 1999, Science, 284, 1481

Balogh, M. L., Babul, A., Voit, G. M., McCarthy, I. G., Jones, L. R., Lewis, G. F., and Ebeling, H., 2006, Mon. Not. R. Astron. Soc., 366, 624

Bartelmann, M. and Schneider, P., 2001, Phys. Rep., 340, 291

Bartlett, J. G., 2001, arXiv:astro-ph/0111211

Battistelli, E. S., Amiri, M., Burger, B., Devlin, M. J., Dicker, S. R., Doriese, W. B., Dünner, R., Fisher, R. P., Fowler, J. W., Halpern, M., Hasselfield, M., Hilton, G. C., Hincks, A. D., Irwin, K. D., Kaul, M., Klein, J., Knotek, S., Lau, J. M., Limon, M., Marriage, T. A., Niemack, M. D., Page, L., Reintsema, C. D., Staggs, S. T., Swetz, D. S., Switzer, E. R., Thornton, R. J., and Zhao, Y., 2008, in Society of Photo-Optical Instrumentation Engineers (SPIE) Conference Series, vol. 7020 of *Society of Photo-Optical Instrumentation Engineers (SPIE) Conference Series*

Battye, R. A. and Weller, J., 2003, Phys. Rev. D, 68, 8, 083506

Beard, S. M., MacGillivray, H. T., and Thanisch, P. F., 1990, Mon. Not. R. Astron. Soc., 247, 311

Bennett, C. L., Halpern, M., Hinshaw, G., Jarosik, N., Kogut, A., Limon, M., Meyer, S. S., Page, L., Spergel, D. N., Tucker, G. S., Wollack, E., Wright, E. L., Barnes, C., Greason, M. R., Hill, R. S., Komatsu, E., Nolta, M. R., Odegard, N., Peiris, H. V., Verde, L., and Weiland, J. L., 2003a, Astrophys. J. Supp., 148, 1

Bennett, C. L., Hill, R. S., Hinshaw, G., Nolta, M. R., Odegard, N., Page, L., Spergel, D. N., Weiland, J. L., Wright, E. L., Halpern, M., Jarosik, N., Kogut, A., Limon, M., Meyer, S. S., Tucker, G. S., and Wollack, E., 2003b, Astrophys. J. Supp., 148, 97

Benson, B. A., Church, S. E., Ade, P. A. R., Bock, J. J., Ganga, K. M., Henson, C. N., and Thompson, K. L., 2004, Astrophys. J., 617, 829

Bertin, E. and Arnouts, S., 1996, Astron. Astrophys. Supp., 117, 393

Bertschinger, E., 1985, Astrophys. J. Supp., 58, 39

Binney, J. and Tremaine, S., 1987, Galactic dynamics (Princeton University Press)

Birkinshaw, M., 1999, Phys. Rep., 310, 97

Birkinshaw, M., Gull, S. F., and Northover, K. J. E., 1978a, Nature, 275, 40

Birkinshaw, M., Gull, S. F., and Northover, K. J. E., 1978b, Mon. Not. R. Astron. Soc., 185, 245

Birkinshaw, M., Hughes, J. P., and Arnaud, K. A., 1991, Astrophys. J., 379, 466

Biswas, R. and Wandelt, B. D., 2009, arXiv:0903.2532

Bode, P., Ostriker, J. P., and Vikhlinin, A., 2009, Astrophys. J., 700, 989

Bode, P., Ostriker, J. P., Weller, J., and Shaw, L., 2007, Astrophys. J., 663, 139

Böhringer, H., Schuecker, P., Guzzo, L., Collins, C. A., Voges, W., Cruddace, R. G., Ortiz-Gil, A., Chincarini, G., De Grandi, S., Edge, A. C., MacGillivray, H. T., Neumann, D. M., Schindler, S., and Shaver, P., 2004, Astron. Astrophys., 425, 367

Bojanov, B. D., Hakopian, H. A., and Sahakian, A. A., 1993, Spline Functions and Multivariate Interpolations (Kluwer Academic Publishers)

Bonaldi, A., Tormen, G., Dolag, K., and Moscardini, L., 2007, Mon. Not. R. Astron. Soc., 378, 1248

Bonamente, M., Joy, M., LaRoque, S. J., Carlstrom, J. E., Nagai, D., and Marrone, D. P., 2008, Astrophys. J., 675, 106

Bond, J. R., 1996, in Cosmology and Large Scale Structure (Elsevier Science Press, Amsterdam)

Bond, J. R., Cole, S., Efstathiou, G., and Kaiser, N., 1991, Astrophys. J., 379, 440

Born, M. and Wolf, E., 1999, Principles of Optics, 7th edn. (Cambridge University Press)

Borys, C., Chapman, S., Halpern, M., and Scott, D., 2003, Mon. Not. R. Astron. Soc., 344, 385

Boughn, S. P., Cheng, E. S., Cottingham, D. A., and Fixsen, D. J., 1992, Astrophys. J. Lett., 391, L49

Bower, R. G., 1991, Mon. Not. R. Astron. Soc., 248, 332

Bryan, G. L. and Norman, M. L., 1998, Astrophys. J., 495, 80

Bullock, J. S., Kolatt, T. S., Sigad, Y., Somerville, R. S., Kravtsov, A. V., Klypin, A. A., Primack, J. R., and Dekel, A., 2001, Mon. Not. R. Astron. Soc., 321, 559

Burigana, C., Malaspina, M., Mandolesi, N., Danse, L., Maino, D., Bersanelli, M., and Maltoni, M., 1999, arXiv:astro-ph/9906360

Carlberg, R. G., Yee, H. K. C., Ellingson, E., Morris, S. L., Abraham, R., Gravel, P., Pritchet, C. J., Smecker-Hane, T., Hartwick, F. D. A., Hesser, J. E., Hutchings, J. B., and Oke, J. B., 1997, Astrophys. J. Lett., 485, L13+

Carlstrom, J. E., Holder, G. P., and Reese, E. D., 2002, Annu. Rev. Astron. Astrophys., 40, 643

Carroll, S. M., Press, W. H., and Turner, E. L., 1992, Annu. Rev. Astron. Astrophys., 30, 499

Cavaliere, A. and Fusco-Femiano, R., 1976, Astron. Astrophys., 49, 137

Cen, R. and Ostriker, J. P., 2006, Astrophys. J., 650, 560

Church, S., Knox, L., and White, M., 2003, Astrophys. J. Lett., 582, L63

Clowe, D., Randall, S. W., and Markevitch, M., 2007, Nuclear Physics B Proceedings Supplements, 173, 28

Cottingham, D. A., 1987, Ph.D. thesis, Princeton University

Crain, R. A., Eke, V. R., Frenk, C. S., Jenkins, A., McCarthy, I. G., Navarro, J. F., and Pearce, F. R., 2007, Mon. Not. R. Astron. Soc., 377, 41

Cyburt, R. H., Fields, B. D., and Olive, K. A., 2008, Journal of Cosmology and Astro-Particle Physics, 11, 12

da Silva, A. C., Kay, S. T., Liddle, A. R., and Thomas, P. A., 2004, Mon. Not. R. Astron. Soc., 348, 1401

Davé, R., Cen, R., Ostriker, J. P., Bryan, G. L., Hernquist, L., Katz, N., Weinberg, D. H., Norman, M. L., and O'Shea, B., 2001, Astrophys. J., 552, 473

Davis, M., Efstathiou, G., Frenk, C. S., and White, S. D. M., 1985, Astrophys. J., 292, 371

Davis, M., Efstathiou, G., Frenk, C. S., and White, S. D. M., 1992, Nature, 356, 489

de Boor, C., 2001, A Practical Guide to Splines, revised edn. (Springer)

de Grandi, S., Böhringer, H., Guzzo, L., Molendi, S., Chincarini, G., Collins, C., Cruddace, R., Neumann, D., Schindler, S., Schuecker, P., and Voges, W., 1999, Astrophys. J., 514, 148

Delabrouille, J., 1998, Astron. Astrophys. Supp., 127, 555

Desert, F., Benoit, A., Gaertner, S., Bernard, J., Coron, N., Delabrouille, J., de Marcillac, P., Giard, M., Lamarre, J., Lefloch, B., Puget, J., and Sirbi, A., 1998, New Astronomy, 3, 655

Dobbs, M., Halverson, N. W., Ade, P. A. R., Basu, K., Beelen, A., Bertoldi, F., Cohalan, C., Cho, H. M., Güsten, R., Holzapfel, W. L., Kermish, Z., Kneissl, R., Kovács, A., Kreysa, E., Lanting, T. M., Lee, A. T., Lueker, M., Mehl, J., Menten, K. M., Muders, D., Nord, M., Plagge, T., Richards, P. L., Schilke, P., Schwan, D., Spieler, H., Weiss, A., and White, M., 2006, New Astronomy Review, 50, 960

Dolag, K., Bartelmann, M., Perrotta, F., Baccigalupi, C., Moscardini, L., Meneghetti, M., and Tormen, G., 2004, Astron. Astrophys., 416, 853

Draine, B. T. and Lazarian, A., 1999, in de Oliveira-Costa, A. and Tegmark, M., eds., Microwave Foregrounds, vol. 181 of *Astronomical Society of the Pacific Conference Series*, 133–+

Dunkley, J., Komatsu, E., Nolta, M. R., Spergel, D. N., Larson, D., Hinshaw, G., Page, L., Bennett, C. L., Gold, B., Jarosik, N., Weiland, J. L., Halpern, M., Hill, R. S., Kogut, A., Limon,

M., Meyer, S. S., Tucker, G. S., Wollack, E., and Wright, E. L., 2009, Astrophys. J. Supp., 180, 306

Edge, A. C., Boehringer, H., Guzzo, L., Collins, C. A., Neumann, D., Chincarini, G., de Grandi, S., Duemmler, R., Ebeling, H., Schindler, S., Seitter, W., Vettolani, P., Briel, U., Cruddace, R., Gruber, R., Gursky, H., Hartner, G., MacGillivray, H. T., Schuecker, P., Shaver, P., Voges, W., Wallin, J., Wolter, A., and Zamorani, G., 1994, Astron. Astrophys., 289, L34

Eke, V. R., Cole, S., and Frenk, C. S., 1996, Mon. Not. R. Astron. Soc., 282, 263

Eke, V. R., Cole, S., Frenk, C. S., and Patrick Henry, J., 1998, Mon. Not. R. Astron. Soc., 298, 1145

Ettori, S., Borgani, S., Moscardini, L., Murante, G., Tozzi, P., Diaferio, A., Dolag, K., Springel, V., Tormen, G., and Tornatore, L., 2004, Mon. Not. R. Astron. Soc., 354, 111

Evrard, A. E., MacFarland, T. J., Couchman, H. M. P., Colberg, J. M., Yoshida, N., White, S. D. M., Jenkins, A., Frenk, C. S., Pearce, F. R., Peacock, J. A., and Thomas, P. A., 2002, Astrophys. J., 573, 7

Fabian, A. C., Guilbert, P. W., Blandford, R. D., Phinney, E. S., and Cuellar, L., 1986, Mon. Not. R. Astron. Soc., 221, 931

Fang, T., Sembach, K. R., and Canizares, C. R., 2003, Astrophys. J. Lett., 586, L49

Fillmore, J. A. and Goldreich, P., 1984, Astrophys. J., 281, 1

Finkbeiner, D. P., Davis, M., and Schlegel, D. J., 1999, Astrophys. J., 524, 867

Finkbeiner, D. P. and Schlegel, D. J., 1999, in de Oliveira-Costa, A. and Tegmark, M., eds., Microwave Foregrounds, vol. 181 of *Astronomical Society of the Pacific Conference Series*, 101–+

Finoguenov, A., Borgani, S., Tornatore, L., and Böhringer, H., 2003, Astron. Astrophys., 398, L35

Finoguenov, A., Ponman, T. J., Osmond, J. P. F., and Zimer, M., 2007, Mon. Not. R. Astron. Soc., 374, 737

Fowler, J. W., Acquaviva, V., Ade, P. A. R., Aguirre, P., Amiri, M., Appel, J. W., Barrientos, L. F., Battistelli, E. S., Bond, J. R., Brown, B., Burger, B., Chervenak, J., Das, S., Devlin, M. J., Dicker, S. R., Doriese, W. B., Dunkley, J., Dünner, R., Essinger-Hileman, T., Fisher, R. P., Hajian, A., Halpern, M., Hasselfield, M., Hernández-Monteagudo, C., Hilton, G. C., Hilton, M., Hincks, A. D., Hlozek, R., Huffenberger, K. M., Hughes, D. H., Hughes, J. P., Infante, L., Irwin, K. D., Jimenez, R., Juin, J. B., Kaul, M., Klein, J., Kosowsky, A., Lau, J. M., Limon, M., Lin, Y., Lupton, R. H., Marriage, T. A., Marsden, D., Martocci, K., Mauskopf, P., Menanteau, F., Moodley, K., Moseley, H., Netterfield, C. B., Niemack, M. D., Nolta, M. R., Page, L. A., Parker, L., Partridge, B., Quintana, H., Reid, B., Sehgal, N., Sievers, J., Spergel, D. N., Staggs, S. T., Swetz, D. S., Switzer, E. R., Thornton, R., Trac, H., Tucker, C., Verde, L., Warne, R., Wilson, G., Wollack, E., and Zhao, Y., 2010, arXiv:1001.2934

Fowler, J. W., Niemack, M. D., Dicker, S. R., Aboobaker, A. M., Ade, P. A. R., Battistelli, E. S., Devlin, M. J., Fisher, R. P., Halpern, M., Hargrave, P. C., Hincks, A. D., Kaul, M., Klein, J., Lau, J. M., Limon, M., Marriage, T. A., Mauskopf, P. D., Page, L., Staggs, S. T., Swetz, D. S., Switzer, E. R., Thornton, R. J., and Tucker, C. E., 2007, Applied Optics, 46, 3444

Freedman, W. L., Madore, B. F., Gibson, B. K., Ferrarese, L., Kelson, D. D., Sakai, S., Mould, J. R., Kennicutt, R. C., Jr., Ford, H. C., Graham, J. A., Huchra, J. P., Hughes, S. M. G., Illingworth, G. D., Macri, L. M., and Stetson, P. B., 2001, Astrophys. J., 553, 47

Frenk, C. S., White, S. D. M., Bode, P., Bond, J. R., Bryan, G. L., Cen, R., Couchman, H. M. P., Evrard, A. E., Gnedin, N., Jenkins, A., Khokhlov, A. M., Klypin, A., Navarro, J. F., Norman, M. L., Ostriker, J. P., Owen, J. M., Pearce, F. R., Pen, U.-L., Steinmetz, M., Thomas, P. A.,

Villumsen, J. V., Wadsley, J. W., Warren, M. S., Xu, G., and Yepes, G., 1999, Astrophys. J., 525, 554

Friedman, R. B., Ade, P., Bock, J., Bowden, M., Brown, M. L., Cahill, G., Castro, P. G., Church, S., Culverhouse, T., Ganga, K., Gear, W. K., Gupta, S., Hinderks, J., Kovac, J., Lange, A. E., Leitch, E., Melhuish, S. J., Memari, Y., Murphy, J. A., Orlando, A., O'Sullivan, C., Piccirillo, L., Pryke, C., Rajguru, N., Rusholme, B., Schwarz, R., Taylor, A. N., Thompson, K. L., Turner, A. H., Wu, E. Y. S., Zemcov, M., and QUa D collaboration, 2009, Astrophys. J. Lett., 700, L187

Frieman, J. A., Turner, M. S., and Huterer, D., 2008, Annu. Rev. Astron. Astrophys., 46, 385

Fukazawa, Y., Makishima, K., and Ohashi, T., 2004, Publications of the ASJ, 56, 965

Fukugita, M., Hogan, C. J., and Peebles, P. J. E., 1998, Astrophys. J., 503, 518

Fukugita, M. and Peebles, P. J. E., 2004, Astrophys. J., 616, 643

Gal, R. R., de Carvalho, R. R., Lopes, P. A. A., Djorgovski, S. G., Brunner, R. J., Mahabal, A., and Odewahn, S. C., 2003, Astron. J., 125, 2064

Gal, R. R., de Carvalho, R. R., Odewahn, S. C., Djorgovski, S. G., and Margoniner, V. E., 2000, Astron. J., 119, 12

Gal, R. R., Lopes, P. A. A., de Carvalho, R. R., Kohl-Moreira, J. L., Capelato, H. V., and Djorgovski, S. G., 2009, Astron. J., 137, 2981

Gamow, G., 1946, Physical Review, 70, 572

Ganga, K., Cheng, E., Meyer, S., and Page, L., 1993, Astrophys. J. Lett., 410, L57

Giacconi, R., Branduardi, G., Briel, U., Epstein, A., Fabricant, D., Feigelson, E., Forman, W., Gorenstein, P., Grindlay, J., Gursky, H., Harnden, F. R., Henry, J. P., Jones, C., Kellogg, E., Koch, D., Murray, S., Schreier, E., Seward, F., Tananbaum, H., Topka, K., Van Speybroeck,

L., Holt, S. S., Becker, R. H., Boldt, E. A., Serlemitsos, P. J., Clark, G., Canizares, C., Markert, T., Novick, R., Helfand, D., and Long, K., 1979, Astrophys. J., 230, 540

Gladders, M. D. and Yee, H. K. C., 2005, Astrophys. J. Supp., 157, 1

Gomez, P., Romer, A. K., Peterson, J. B., Chase, W., Runyan, M., Holzapfel, W., Kuo, C. L., Newcomb, M., Ruhl, J., Goldstein, J., and Lange, A., 2004, in G. Bertin, D. Farina, & R. Pozzoli, ed., Plasmas in the Laboratory and in the Universe: New Insights and New Challenges, vol. 703 of *American Institute of Physics Conference Series*, 361–366

Gonzalez, A. H., Zaritsky, D., and Zabludoff, A. I., 2007, Astrophys. J., 666, 147

Gunn, J. E., 1977, Astrophys. J., 218, 592

Gunn, J. E. and Gott, J. R., III, 1972, Astrophys. J., 176, 1

Guth, A. H., 1981, Phys. Rev. D, 23, 347

Guzzo, L., Böhringer, H., Schuecker, P., Collins, C. A., Schindler, S., Neumann, D. M., de Grandi, S., Cruddace, R., Chincarini, G., Edge, A. C., Shaver, P. A., and Voges, W., 1999, The Messenger, 95, 27

Haiman, Z., Mohr, J. J., and Holder, G. P., 2001, Astrophys. J., 553, 545

Hallman, E. J., Burns, J. O., Motl, P. M., and Norman, M. L., 2007a, Astrophys. J., 665, 911

Hallman, E. J., O'Shea, B. W., Burns, J. O., Norman, M. L., Harkness, R., and Wagner, R., 2007b, Astrophys. J., 671, 27

Halverson, N. W., Lanting, T., Ade, P. A. R., Basu, K., Bender, A. N., Benson, B. A., Bertoldi, F., Cho, H., Chon, G., Clarke, J., Dobbs, M., Ferrusca, D., Güsten, R., Holzapfel, W. L., Kovács, A., Kennedy, J., Kermish, Z., Kneissl, R., Lee, A. T., Lueker, M., Mehl, J., Menten, K. M., Muders, D., Nord, M., Pacaud, F., Plagge, T., Reichardt, C., Richards, P. L., Schaaf, R., Schilke, P., Schuller, F., Schwan, D., Spieler, H., Tucker, C., Weiss, A., and Zahn, O., 2009, Astrophys. J., 701, 42

Herbig, T., Lawrence, C. R., Readhead, A. C. S., and Gulkis, S., 1995, Astrophys. J. Lett., 449, L5+

Hernández-Monteagudo, C., Trac, H., Verde, L., and Jimenez, R., 2006, Astrophys. J. Lett., 652, L1

Herranz, D., Sanz, J. L., Barreiro, R. B., and Martínez-González, E., 2002a, Astrophys. J., 580, 610

Herranz, D., Sanz, J. L., Hobson, M. P., Barreiro, R. B., Diego, J. M., Martínez-González, E., and Lasenby, A. N., 2002b, Mon. Not. R. Astron. Soc., 336, 1057

Hicken, M., Wood-Vasey, W. M., Blondin, S., Challis, P., Jha, S., Kelly, P. L., Rest, A., and Kirshner, R. P., 2009, Astrophys. J., 700, 1097

High, F. W., Stalder, B., Song, J., Ade, P. A. R., Aird, K. A., Allam, S. S., Armstrong, R., Barkhouse, W. A., Benson, B. A., Bertin, E., Bhattacharya, S., Bleem, L. E., Brodwin, M., Buckley-Geer, E. J., Carlstrom, J. E., Challis, P., Chang, C. L., Crawford, T. M., Crites, A. T., de Haan, T., Desai, S., Dobbs, M. A., Dudley, J. P., Foley, R. J., George, E. M., Gladders, M., Halverson, N. W., Hamuy, M., Hansen, S. M., Holder, G. P., Holzapfel, W. L., Hrubes, J. D., Joy, M., Keisler, R., Lee, A. T., Leitch, E. M., Lin, H., Lin, Y., Loehr, A., Lueker, M., Marrone, D., McMahon, J. J., Mehl, J., Meyer, S. S., Mohr, J. J., Montroy, T. E., Morell, N., Ngeow, C., Padin, S., Plagge, T., Pryke, C., Reichardt, C. L., Rest, A., Ruel, J., Ruhl, J. E., Schaffer, K. K., Shaw, L., Shirokoff, E., Smith, R. C., Spieler, H. G., Staniszewski, Z., Stark, A. A., Stubbs, C. W., Tucker, D. L., Vanderlinde, K., Vieira, J. D., Williamson, R., Wood-Vasey, W. M., Yang, Y., Zahn, O., and Zenteno, A., 2010, arXiv:1003.0005

Hincks, A. D., Acquaviva, V., Ade, P., Aguirre, P., Amiri, M., Appel, J. W., Barrientos, L. F., Battistelli, E. S., Bond, J. R., Brown, B., Burger, B., Chervenak, J., Das, S., Devlin, M. J., Dicker, S., Doriese, W. B., Dunkley, J., Dünner, R., Essinger-Hileman, T., Fisher, R. P., Fowler, J. W., Hajian, A., Halpern, M., Hasselfield, M., Hernández-Monteagudo, C., Hilton, G. C., Hilton,

M., Hlozek, R., Huffenberger, K., Hughes, D., Hughes, J. P., Infante, L., Irwin, K. D., Jimenez, R., Juin, J. B., Kaul, M., Klein, J., Kosowsky, A., Lau, J. M., Limon, M., Lin, Y., Lupton, R. H., Marriage, T., Marsden, D., Martocci, K., Mauskopf, P., Menanteau, F., Moodley, K., Moseley, H., Netterfield, C. B., Niemack, M. D., Nolta, M. R., Page, L. A., Parker, L., Partridge, B., Quintana, H., Reid, B., Sehgal, N., Sievers, J., Spergel, D. N., Staggs, S. T., Stryzak, O., Swetz, D., Switzer, E., Thornton, R., Trac, H., Tucker, C., Verde, L., Warne, R., Wilson, G., Wollack, E., and Zhao, Y., 2009, arXiv:0907.0461

Hincks, A. D., Ade, P. A. R., Allen, C., Amiri, M., Appel, J. W., Battistelli, E. S., Burger, B., Chervenak, J. A., Dahlen, A. J., Denny, S., Devlin, M. J., Dicker, S. R., Doriese, W. B., Dünner, R., Essinger-Hileman, T., Fisher, R. P., Fowler, J. W., Halpern, M., Hargrave, P. C., Hasselfield, M., Hilton, G. C., Irwin, K. D., Jarosik, N., Kaul, M., Klein, J., Lau, J. M., Limon, M., Lupton, R. H., Marriage, T. A., Martocci, K. L., Mauskopf, P., Moseley, S. H., Netterfield, C. B., Niemack, M. D., Nolta, M. R., Page, L., Parker, L. P., Sederberg, A. J., Staggs, S. T., Stryzak, O. R., Swetz, D. S., Switzer, E. R., Thornton, R. J., Tucker, C., Wollack, E. J., and Zhao, Y., 2008, in Society of Photo-Optical Instrumentation Engineers (SPIE) Conference Series, vol. 7020 of *Society of Photo-Optical Instrumentation Engineers (SPIE) Conference Series*

Hinshaw, G., Nolta, M. R., Bennett, C. L., Bean, R., Doré, O., Greason, M. R., Halpern, M., Hill, R. S., Jarosik, N., Kogut, A., Komatsu, E., Limon, M., Odegard, N., Meyer, S. S., Page, L., Peiris, H. V., Spergel, D. N., Tucker, G. S., Verde, L., Weiland, J. L., Wollack, E., and Wright, E. L., 2007, Astrophys. J. Supp., 170, 288

Hinshaw, G., Weiland, J. L., Hill, R. S., Odegard, N., Larson, D., Bennett, C. L., Dunkley, J., Gold, B., Greason, M. R., Jarosik, N., Komatsu, E., Nolta, M. R., Page, L., Spergel, D. N., Wollack, E., Halpern, M., Kogut, A., Limon, M., Meyer, S. S., Tucker, G. S., and Wright, E. L., 2009, Astrophys. J. Supp., 180, 225

Ho, P. T. P., Altamirano, P., Chang, C., Chang, S., Chang, S., Chen, C., Chen, K., Chen, M., Han, C., Ho, W. M., Huang, Y., Hwang, Y., Ibañez-Romano, F., Jiang, H., Koch, P. M., Kubo, D. Y., Li, C., Lim, J., Lin, K., Liu, G., Lo, K., Ma, C., Martin, R. N., Martin-Cocher, P., Molnar, S. M., Ng, K., Nishioka, H., O'Connell, K. E., Oshiro, P., Patt, F., Raffin, P., Umetsu, K., Wei, T., Wu, J., Chiueh, T., Chiueh, T., Chu, T., Huang, C., Hwang, W. Y. P., Liao, Y., Lien, C., Wang, F., Wang, H., Wei, R., Yang, C., Kesteven, M., Kingsley, J., Sinclair, M. M., Wilson, W., Birkinshaw, M., Liang, H., Lancaster, K., Park, C., Pen, U., and Peterson, J. B., 2009, Astrophys. J., 694, 1610

Hobson, M. P., Barreiro, R. B., Toffolatti, L., Lasenby, A. N., Sanz, J., Jones, A. W., and Bouchet, F. R., 1999, Mon. Not. R. Astron. Soc., 306, 232

Hobson, M. P., Jones, A. W., Lasenby, A. N., and Bouchet, F. R., 1998, Mon. Not. R. Astron. Soc., 300, 1

Holder, G., Haiman, Z., and Mohr, J. J., 2001, Astrophys. J. Lett., 560, L111

Holder, G. P., McCarthy, I. G., and Babul, A., 2007, Mon. Not. R. Astron. Soc., 382, 1697

Holland, W. S., Robson, E. I., Gear, W. K., Cunningham, C. R., Lightfoot, J. F., Jenness, T., Ivison, R. J., Stevens, J. A., Ade, P. A. R., Griffin, M. J., Duncan, W. D., Murphy, J. A., and Naylor, D. A., 1999, Mon. Not. R. Astron. Soc., 303, 659

Holzapfel, W. L., Wilbanks, T. M., Ade, P. A. R., Church, S. E., Fischer, M. L., Mauskopf, P. D., Osgood, D. E., and Lange, A. E., 1997, Astrophys. J., 479, 17

Hubble, E., 1929, Proceedings of the National Academy of Science, 15, 168

Hughes, J. P., Menanteau, F., Sehgal, N., Infante, L., and Barrientos, F., 2009, in Bulletin of the American Astronomical Society, vol. 41 of *Bulletin of the American Astronomical Society*, 336–+

Hui, L. and Gnedin, N. Y., 1997, Mon. Not. R. Astron. Soc., 292, 27

Jarvis, J. F. and Tyson, J. A., 1981, Astron. J., 86, 476

Jenkins, A., Frenk, C. S., White, S. D. M., Colberg, J. M., Cole, S., Evrard, A. E., Couchman, H. M. P., and Yoshida, N., 2001, Mon. Not. R. Astron. Soc., 321, 372

Jing, Y. P., 2000, Astrophys. J., 535, 30

Jones, M., Saunders, R., Alexander, P., Birkinshaw, M., Dilon, N., Grainge, K., Hancock, S., Lasenby, A., Lefebvre, D., and Pooley, G., 1993, Nature, 365, 320

Kay, S. T., da Silva, A. C., Aghanim, N., Blanchard, A., Liddle, A. R., Puget, J., Sadat, R., and Thomas, P. A., 2007, Mon. Not. R. Astron. Soc., 377, 317

Kay, S. T., Thomas, P. A., Jenkins, A., and Pearce, F. R., 2004, Mon. Not. R. Astron. Soc., 355, 1091

Keihänen, E., Kurki-Suonio, H., and Poutanen, T., 2005, Mon. Not. R. Astron. Soc., 360, 390

Keihänen, E., Kurki-Suonio, H., Poutanen, T., Maino, D., and Burigana, C., 2004, Astron. Astrophys., 428, 287

Kessler, R., Becker, A. C., Cinabro, D., Vanderplas, J., Frieman, J. A., Marriner, J., Davis, T. M., Dilday, B., Holtzman, J., Jha, S. W., Lampeitl, H., Sako, M., Smith, M., Zheng, C., Nichol, R. C., Bassett, B., Bender, R., Depoy, D. L., Doi, M., Elson, E., Filippenko, A. V., Foley, R. J., Garnavich, P. M., Hopp, U., Ihara, Y., Ketzeback, W., Kollatschny, W., Konishi, K., Marshall, J. L., McMillan, R. J., Miknaitis, G., Morokuma, T., Mörtsell, E., Pan, K., Prieto, J. L., Richmond, M. W., Riess, A. G., Romani, R., Schneider, D. P., Sollerman, J., Takanashi, N., Tokita, K., van der Heyden, K., Wheeler, J. C., Yasuda, N., and York, D., 2009, Astrophys. J. Supp., 185, 32

Kirkman, D., Tytler, D., Suzuki, N., O'Meara, J. M., and Lubin, D., 2003, Astrophys. J. Supp., 149, 1

Knox, L., 1995, Phys. Rev. D, 52, 4307

Koester, B. P., McKay, T. A., Annis, J., Wechsler, R. H., Evrard, A., Bleem, L., Becker, M., Johnston, D., Sheldon, E., Nichol, R., Miller, C., Scranton, R., Bahcall, N., Barentine, J., Brewington, H., Brinkmann, J., Harvanek, M., Kleinman, S., Krzesinski, J., Long, D., Nitta, A., Schneider, D. P., Sneddin, S., Voges, W., and York, D., 2007, Astrophys. J., 660, 239

Komatsu, E., Dunkley, J., Nolta, M. R., Bennett, C. L., Gold, B., Hinshaw, G., Jarosik, N., Larson, D., Limon, M., Page, L., Spergel, D. N., Halpern, M., Hill, R. S., Kogut, A., Meyer, S. S., Tucker, G. S., Weiland, J. L., Wollack, E., and Wright, E. L., 2009, Astrophys. J. Supp., 180, 330

Komatsu, E., Kitayama, T., Suto, Y., Hattori, M., Kawabe, R., Matsuo, H., Schindler, S., and Yoshikawa, K., 1999, Astrophys. J. Lett., 516, L1

Komatsu, E., Matsuo, H., Kitayama, T., Hattori, M., Kawabe, R., Kohno, K., Kuno, N., Schindler, S., Suto, Y., and Yoshikawa, K., 2001, Publications of the ASJ, 53, 57

Komatsu, E. and Seljak, U., 2001a, Mon. Not. R. Astron. Soc., 327, 1353

Komatsu, E. and Seljak, U., 2001b, Mon. Not. R. Astron. Soc., 327, 1353

Komatsu, E. and Seljak, U., 2002, Mon. Not. R. Astron. Soc., 336, 1256

Komatsu, E., Smith, K. M., Dunkley, J., Bennett, C. L., Gold, B., Hinshaw, G., Jarosik, N., Larson, D., Nolta, M. R., Page, L., Spergel, D. N., Halpern, M., Hill, R. S., Kogut, A., Limon, M., Meyer, S. S., Odegard, N., Tucker, G. S., Weiland, J. L., Wollack, E., and Wright, E. L., 2010, arXiv:1001.4538

Kompaneets, A. S., 1956, Zh.E.F.T., 31, 876, translation in Sov. Phys. JETP, 4, 730 (1957)

Koopmans, L. V. E., Treu, T., Bolton, A. S., Burles, S., and Moustakas, L. A., 2006, Astrophys. J., 649, 599

Kosowsky, A., 2006, New Astronomy Review, 50, 969

Kowalski, M., Rubin, D., Aldering, G., Agostinho, R. J., Amadon, A., Amanullah, R., Balland, C., Barbary, K., Blanc, G., Challis, P. J., Conley, A., Connolly, N. V., Covarrubias, R., Dawson, K. S., Deustua, S. E., Ellis, R., Fabbro, S., Fadeyev, V., Fan, X., Farris, B., Folatelli, G., Frye, B. L., Garavini, G., Gates, E. L., Germany, L., Goldhaber, G., Goldman, B., Goobar, A., Groom, D. E., Haissinski, J., Hardin, D., Hook, I., Kent, S., Kim, A. G., Knop, R. A., Lidman, C., Linder, E. V., Mendez, J., Meyers, J., Miller, G. J., Moniez, M., Mourão, A. M., Newberg, H., Nobili, S., Nugent, P. E., Pain, R., Perdereau, O., Perlmutter, S., Phillips, M. M., Prasad, V., Quimby, R., Regnault, N., Rich, J., Rubenstein, E. P., Ruiz-Lapuente, P., Santos, F. D., Schaefer, B. E., Schommer, R. A., Smith, R. C., Soderberg, A. M., Spadafora, A. L., Strolger, L., Strovink, M., Suntzeff, N. B., Suzuki, N., Thomas, R. C., Walton, N. A., Wang, L., Wood-Vasey, W. M., and Yun, J. L., 2008, Astrophys. J., 686, 749

Kravtsov, A. V., Nagai, D., and Vikhlinin, A. A., 2005, Astrophys. J., 625, 588

Kuo, C. L., Ade, P. A. R., Bock, J. J., Cantalupo, C., Daub, M. D., Goldstein, J., Holzapfel, W. L., Lange, A. E., Lueker, M., Newcomb, M., Peterson, J. B., Ruhl, J., Runyan, M. C., and Torbet, E., 2004, Astrophys. J., 600, 32

Lacey, C. and Cole, S., 1993, Mon. Not. R. Astron. Soc., 262, 627

Lahav, O., Lilje, P. B., Primack, J. R., and Rees, M. J., 1991, Mon. Not. R. Astron. Soc., 251, 128

Lancaster, K., Birkinshaw, M., Gawroński, M. P., Browne, I., Feiler, R., Kus, A., Lowe, S., Pazderski, E., and Wilkinson, P., 2007, Mon. Not. R. Astron. Soc., 378, 673

LaRoque, S. J., Bonamente, M., Carlstrom, J. E., Joy, M. K., Nagai, D., Reese, E. D., and Dawson, K. S., 2006a, Astrophys. J., 652, 917

LaRoque, S. J., Bonamente, M., Carlstrom, J. E., Joy, M. K., Nagai, D., Reese, E. D., and Dawson, K. S., 2006b, Astrophys. J., 652, 917

Lewis, A. D., Buote, D. A., and Stocke, J. T., 2003, Astrophys. J., 586, 135

Lin, Y.-T., Mohr, J. J., and Stanford, S. A., 2003, Astrophys. J., 591, 749

Lloyd-Davies, E. J., Ponman, T. J., and Cannon, D. B., 2000, Mon. Not. R. Astron. Soc., 315, 689

Łokas, E. L. and Mamon, G. A., 2001, Mon. Not. R. Astron. Soc., 321, 155

Lueker, M., Reichardt, C. L., Schaffer, K. K., Zahn, O., Ade, P. A. R., Aird, K. A., Benson, B. A., Bleem, L. E., Carlstrom, J. E., Chang, C. L., Cho, H. M., Crawford, T. M., Crites, A. T., de Haan, T., Dobbs, M. A., George, E. M., Hall, N. R., Halverson, N. W., Holder, G. P., Holzapfel, W. L., Hrubes, J. D., Joy, M., Keisler, R., Knox, L., Lee, A. T., Leitch, E. M., McMahon, J. J., Mehl, J., Meyer, S. S., Mohr, J. J., Montroy, T. E., Padin, S., Plagge, T., Pryke, C., Ruhl, J. E., Shaw, L., Shirokoff, E., Spieler, H. G., Staniszewski, Z., Stark, A. A., Vanderlinde, K., Vieira, J. D., and Williamson, R., 2009, arXiv:0912.4317

Lupton, R. H., 2001, Sdss image processing i: The deblender

Lynden-Bell, D., 1967, Mon. Not. R. Astron. Soc., 136, 101

Maino, D., Burigana, C., Górski, K. M., Mandolesi, N., and Bersanelli, M., 2002a, Astron. Astrophys., 387, 356

Maino, D., Farusi, A., Baccigalupi, C., Perrotta, F., Banday, A. J., Bedini, L., Burigana, C., De Zotti, G., Górski, K. M., and Salerno, E., 2002b, Mon. Not. R. Astron. Soc., 334, 53

Malte Schäfer, B. and Bartelmann, M., 2007, Mon. Not. R. Astron. Soc., 377, 253

Marian, L. and Bernstein, G. M., 2006, Phys. Rev. D, 73, 12, 123525

Markevitch, M., Gonzalez, A. H., David, L., Vikhlinin, A., Murray, S., Forman, W., Jones, C., and Tucker, W., 2002, Astrophys. J. Lett., 567, L27

Marriage, T. A., Chervenak, J. A., and Doriese, W. B., 2006, Nuclear Instruments and Methods in Physics Research A, 559, 551

Mason, B. S., Myers, S. T., and Readhead, A. C. S., 2001, Astrophys. J. Lett., 555, L11

Mauch, T., Murphy, T., Buttery, H. J., Curran, J., Hunstead, R. W., Piestrzynski, B., Robertson, J. G., and Sadler, E. M., 2003, Mon. Not. R. Astron. Soc., 342, 1117

Mauskopf, P. D., Ade, P. A. R., Allen, S. W., Church, S. E., Edge, A. C., Ganga, K. M., Holzapfel, W. L., Lange, A. E., Rownd, B. K., Philhour, B. J., and Runyan, M. C., 2000, Astrophys. J., 538, 505

McCarthy, I. G., Balogh, M. L., Babul, A., Poole, G. B., and Horner, D. J., 2004, Astrophys. J., 613, 811

McCarthy, I. G., Bower, R. G., and Balogh, M. L., 2007, Mon. Not. R. Astron. Soc., 377, 1457

McInnes, R. N., Menanteau, F., Heavens, A. F., Hughes, J. P., Jimenez, R., Massey, R., Simon, P., and Taylor, A., 2009, Mon. Not. R. Astron. Soc., 399, L84

Melin, J.-B., Bartlett, J. G., and Delabrouille, J., 2006, Astron. Astrophys., 459, 341

Mellier, Y., 1999, Annu. Rev. Astron. Astrophys., 37, 127

Menanteau, F. and Hughes, J. P., 2009, Astrophys. J. Lett., 694, L136

Meyer, S. S., Cheng, E. S., and Page, L. A., 1991, Astrophys. J. Lett., 371, L7

Moodley, K., Warne, R., Goheer, N., and Trac, H., 2009, Astrophys. J., 697, 1392

Motl, P. M., Hallman, E. J., Burns, J. O., and Norman, M. L., 2005, Astrophys. J. Lett., 623, L63

Muchovej, S., Mroczkowski, T., Carlstrom, J. E., Cartwright, J., Greer, C., Hennessy, R., Loh, M., Pryke, C., Reddall, B., Runyan, M., Sharp, M., Hawkins, D., Lamb, J. W., Woody, D., Joy, M., Leitch, E. M., and Miller, A. D., 2007, Astrophys. J., 663, 708

Myers, S. T., Baker, J. E., Readhead, A. C. S., Leitch, E. M., and Herbig, T., 1997, Astrophys. J., 485, 1

Nagai, D., 2006, Astrophys. J., 650, 538

Nagamine, K., Ostriker, J. P., Fukugita, M., and Cen, R., 2006, Astrophys. J., 653, 881

Navarro, J. F., Frenk, C. S., and White, S. D. M., 1997, Astrophys. J., 490, 493

Navarro, J. F., Hayashi, E., Power, C., Jenkins, A. R., Frenk, C. S., White, S. D. M., Springel, V., Stadel, J., and Quinn, T. R., 2004, Mon. Not. R. Astron. Soc., 349, 1039

Niemack, M. D., 2006, in Society of Photo-Optical Instrumentation Engineers (SPIE) Conference Series, vol. 6275 of *Society of Photo-Optical Instrumentation Engineers (SPIE) Conference Series*

Niemack, M. D., Zhao, Y., Wollack, E., Thornton, R., Switzer, E. R., Swetz, D. S., Staggs, S. T., Page, L., Stryzak, O., Moseley, H., Marriage, T. A., Limon, M., Lau, J. M., Klein, J., Kaul, M., Jarosik, N., Irwin, K. D., Hincks, A. D., Hilton, G. C., Halpern, M., Fowler, J. W., Fisher, R. P., Dünner, R., Doriese, W. B., Dicker, S. R., Devlin, M. J., Chervenak, J., Burger, B., Battistelli, E. S., Appel, J., Amiri, M., Allen, C., and Aboobaker, A. M., 2008, Journal of Low Temperature Physics, 151, 690

Nolta, M. R., Dunkley, J., Hill, R. S., Hinshaw, G., Komatsu, E., Larson, D., Page, L., Spergel, D. N., Bennett, C. L., Gold, B., Jarosik, N., Odegard, N., Weiland, J. L., Wollack, E., Halpern, M., Kogut, A., Limon, M., Meyer, S. S., Tucker, G. S., and Wright, E. L., 2009, Astrophys. J. Supp., 180, 296

Olive, K. A., Steigman, G., and Walker, T. P., 2000, Phys. Rep., 333, 389

Ostriker, J. P., Bode, P., and Babul, A., 2005, Astrophys. J., 634, 964

Pace, F., Maturi, M., Bartelmann, M., Cappelluti, N., Dolag, K., Meneghetti, M., and Moscardini, L., 2008, Astron. Astrophys., 483, 389

Padin, S., Shepherd, M. C., Cartwright, J. K., Keeney, R. G., Mason, B. S., Pearson, T. J., Readhead, A. C. S., Schaal, W. A., Sievers, J., Udomprasert, P. S., Yamasaki, J. K., Holzapfel,

W. L., Carlstrom, J. E., Joy, M., Myers, S. T., and Otarola, A., 2002, Publications of the Astronomical Society of the Pacific, 114, 83

Page, L., Barnes, C., Hinshaw, G., Spergel, D. N., Weiland, J. L., Wollack, E., Bennett, C. L., Halpern, M., Jarosik, N., Kogut, A., Limon, M., Meyer, S. S., Tucker, G. S., and Wright, E. L., 2003, Astrophys. J. Supp., 148, 39

Peebles, P. J. E., 1980, The large-scale structure of the universe (Princeton University Press)

Penton, S. V., Shull, J. M., and Stocke, J. T., 2000, Astrophys. J., 544, 150

Penton, S. V., Stocke, J. T., and Shull, J. M., 2004, Astrophys. J. Supp., 152, 29

Penzias, A. A. and Wilson, R. W., 1965, Astrophys. J., 142, 419

Percival, W. J., Baugh, C. M., Bland-Hawthorn, J., Bridges, T., Cannon, R., Cole, S., Colless, M., Collins, C., Couch, W., Dalton, G., De Propris, R., Driver, S. P., Efstathiou, G., Ellis, R. S., Frenk, C. S., Glazebrook, K., Jackson, C., Lahav, O., Lewis, I., Lumsden, S., Maddox, S., Moody, S., Norberg, P., Peacock, J. A., Peterson, B. A., Sutherland, W., and Taylor, K., 2001, Mon. Not. R. Astron. Soc., 327, 1297

Pérez-Beaupuits, J. P., Rivera, R. C., and Nyman, L.-A., 2005, Height and velocity of the turbulence layer at chajnantor estimated from radiometric measurements, memo 542, Atacama Large Millimeter Array (ALMA)

Perlmutter, S., Aldering, G., Goldhaber, G., Knop, R. A., Nugent, P., Castro, P. G., Deustua, S., Fabbro, S., Goobar, A., Groom, D. E., Hook, I. M., Kim, A. G., Kim, M. Y., Lee, J. C., Nunes, N. J., Pain, R., Pennypacker, C. R., Quimby, R., Lidman, C., Ellis, R. S., Irwin, M., McMahon, R. G., Ruiz-Lapuente, P., Walton, N., Schaefer, B., Boyle, B. J., Filippenko, A. V., Matheson, T., Fruchter, A. S., Panagia, N., Newberg, H. J. M., Couch, W. J., and The Supernova Cosmology Project, 1999, Astrophys. J., 517, 565

Pierpaoli, E., Anthoine, S., Huffenberger, K., and Daubechies, I., 2005, Mon. Not. R. Astron. Soc., 359, 261

Pierpaoli, E., Borgani, S., Scott, D., and White, M., 2003, Mon. Not. R. Astron. Soc., 342, 163

Plagge, T., Benson, B. A., Ade, P. A. R., Aird, K. A., Bleem, L. E., Carlstrom, J. E., Chang, C. L., Cho, H., Crawford, T. M., Crites, A. T., de Haan, T., Dobbs, M. A., George, E. M., Hall, N. R., Halverson, N. W., Holder, G. P., Holzapfel, W. L., Hrubes, J. D., Joy, M., Keisler, R., Knox, L., Lee, A. T., Leitch, E. M., Lueker, M., Marrone, D., McMahon, J. J., Mehl, J., Meyer, S. S., Mohr, J. J., Montroy, T. E., Padin, S., Pryke, C., Reichardt, C. L., Ruhl, J. E., Schaffer, K. K., Shaw, L., Shirokoff, E., Spieler, H. G., Stalder, B., Staniszewski, Z., Stark, A. A., Vanderlinde, K., Vieira, J. D., Williamson, R., and Zahn, O., 2009, arXiv:0911.2444

Pointecouteau, E., Giard, M., Benoit, A., Désert, F. X., Aghanim, N., Coron, N., Lamarre, J. M., and Delabrouille, J., 1999, Astrophys. J. Lett., 519, L115

Pointecouteau, E., Giard, M., Benoit, A., Désert, F. X., Bernard, J. P., Coron, N., and Lamarre, J. M., 2001, Astrophys. J., 552, 42

Ponman, T. J., Cannon, D. B., and Navarro, J. F., 1999, Nature, 397, 135

Ponthieu, N., Macías-Pérez, J. F., Tristram, M., Ade, P., Amblard, A., Ansari, R., Aumont, J., Aubourg, É., Benoît, A., Bernard, J.-P., Blanchard, A., Bock, J. J., Bouchet, F. R., Bourrachot, A., Camus, P., Cardoso, J.-F., Couchot, F., de Bernardis, P., Delabrouille, J., Désert, F.-X., Douspis, M., Dumoulin, L., Filliatre, P., Fosalba, P., Giard, M., Giraud-Héraud, Y., Gispert, R., Grain, J., Guglielmi, L., Hamilton, J.-C., Hanany, S., Henrot-Versillé, S., Kaplan, J., Lagache, G., Lange, A. E., Madet, K., Maffei, B., Masi, S., Mayet, F., Nati, F., Patanchon, G., Perdereau, O., Plaszczynski, S., Piat, M., Prunet, S., Puget, J.-L., Renault, C., Rosset, C., Santos, D., Vibert, D., and Yvon, D., 2005, Astron. Astrophys., 444, 327

Postman, M., Lubin, L. M., Gunn, J. E., Oke, J. B., Hoessel, J. G., Schneider, D. P., and Christensen, J. A., 1996, Astron. J., 111, 615

Postman, M., Lubin, L. M., and Oke, J. B., 2001, Astron. J., 122, 1125

Pratt, G. W. and Arnaud, M., 2002, Astron. Astrophys., 394, 375

Press, W. H. and Schechter, P., 1974, Astrophys. J., 187, 425

Press, W. H., Teukolsky, S. A., Vetterling, W. T., and Flannery, B. P., 1992, Numerical Recipes in C: The Art of Scientific Computing, 2nd edn. (Cambridge University Press)

Ramella, M., Geller, M. J., Pisani, A., and da Costa, L. N., 2002, Astron. J., 123, 2976

Rasia, E., Tormen, G., and Moscardini, L., 2004, Mon. Not. R. Astron. Soc., 351, 237

Reichardt, C. L., Ade, P. A. R., Bock, J. J., Bond, J. R., Brevik, J. A., Contaldi, C. R., Daub, M. D., Dempsey, J. T., Goldstein, J. H., Holzapfel, W. L., Kuo, C. L., Lange, A. E., Lueker, M., Newcomb, M., Peterson, J. B., Ruhl, J., Runyan, M. C., and Staniszewski, Z., 2009a, Astrophys. J., 694, 1200

Reichardt, C. L., Zahn, O., Ade, P. A. R., Basu, K., Bender, A. N., Bertoldi, F., Cho, H., Chon, G., Dobbs, M., Ferrusca, D., Halverson, N. W., Holzapfel, W. L., Horellou, C., Johansson, D., Johnson, B. R., Kennedy, J., Kneissl, R., Lanting, T., Lee, A. T., Lueker, M., Mehl, J., Menten, K. M., Nord, M., Pacaud, F., Richards, P. L., Schaaf, R., Schwan, D., Spieler, H., Weiss, A., and Westbrook, B., 2009b, Astrophys. J., 701, 1958

Reid, B. A. and Spergel, D. N., 2006, Astrophys. J., 651, 643

Reiprich, T. H. and Böhringer, H., 2002, Astrophys. J., 567, 716

Rephaeli, Y., 1995, Astrophys. J., 445, 33

Riess, A. G., Filippenko, A. V., Challis, P., Clocchiatti, A., Diercks, A., Garnavich, P. M., Gilliland, R. L., Hogan, C. J., Jha, S., Kirshner, R. P., Leibundgut, B., Phillips, M. M., Reiss, D., Schmidt, B. P., Schommer, R. A., Smith, R. C., Spyromilio, J., Stubbs, C., Suntzeff, N. B., and Tonry, J., 1998, Astron. J., 116, 1009

Riess, A. G., Strolger, L., Casertano, S., Ferguson, H. C., Mobasher, B., Gold, B., Challis, P. J., Filippenko, A. V., Jha, S., Li, W., Tonry, J., Foley, R., Kirshner, R. P., Dickinson, M., MacDonald, E., Eisenstein, D., Livio, M., Younger, J., Xu, C., Dahlén, T., and Stern, D., 2007, Astrophys. J., 659, 98

Riess, A. G., Strolger, L., Tonry, J., Casertano, S., Ferguson, H. C., Mobasher, B., Challis, P., Filippenko, A. V., Jha, S., Li, W., Chornock, R., Kirshner, R. P., Leibundgut, B., Dickinson, M., Livio, M., Giavalisco, M., Steidel, C. C., Benítez, T., and Tsvetanov, Z., 2004, Astrophys. J., 607, 665

Righi, M., Hernández-Monteagudo, C., and Sunyaev, R. A., 2008, Astron. Astrophys., 478, 685

Rosati, P., Borgani, S., and Norman, C., 2002, Annu. Rev. Astron. Astrophys., 40, 539

Rose, J. A., Gaba, A. E., Christiansen, W. A., Davis, D. S., Caldwell, N., Hunstead, R. W., and Johnston-Hollitt, M., 2002, Astron. J., 123, 1216

Rubin, V. C., Ford, W. K. J., and . Thonnard, N., 1980, Astrophys. J., 238, 471

Ruhl, J., Ade, P. A. R., Carlstrom, J. E., Cho, H.-M., Crawford, T., Dobbs, M., Greer, C. H., Halverson, N. w., Holzapfel, W. L., Lanting, T. M., Lee, A. T., Leitch, E. M., Leong, J., Lu, W., Lueker, M., Mehl, J., Meyer, S. S., Mohr, J. J., Padin, S., Plagge, T., Pryke, C., Runyan, M. C., Schwan, D., Sharp, M. K., Spieler, H., Staniszewski, Z., and Stark, A. A., 2004, in Bradford, C. M., Ade, P. A. R., Aguirre, J. E., Bock, J. J., Dragovan, M., Duband, L., Earle, L., Glenn, J., Matsuhara, H., Naylor, B. J., Nguyen, H. T., Yun, M., and Zmuidzinas, J., eds., Millimeter and Submillimeter Detectors for Astronomy II., vol. 5498 of *Presented at the SPIE Conference*, 11–29

Sachs, R. K. and Wolfe, A. M., 1967, Astrophys. J., 147, 73

Sahlén, M., Viana, P. T. P., Liddle, A. R., Romer, A. K., Davidson, M., Hosmer, M., Lloyd-Davies, E., Sabirli, K., Collins, C. A., Freeman, P. E., Hilton, M., Hoyle, B., Kay, S. T., Mann,

R. G., Mehrtens, N., Miller, C. J., Nichol, R. C., Stanford, S. A., and West, M. J., 2009, Mon. Not. R. Astron. Soc., 397, 577

Sanderson, A. J. R., Ponman, T. J., Finoguenov, A., Lloyd-Davies, E. J., and Markevitch, M., 2003, Mon. Not. R. Astron. Soc., 340, 989

Sarazin, C. L., 1986, Reviews of Modern Physics, 58, 1

Schlegel, D. J., Finkbeiner, D. P., and Davis, M., 1998, Astrophys. J., 500, 525

Schroeder, D. J., 2000, Astronomical Optics, 2nd edn. (Academic Press)

Schumaker, L. L., 2007, Spline Functions: Basic Theory, 3rd edn. (Cambridge University Press)

Sehgal, N., Bode, P., Das, S., Hernandez-Monteagudo, C., Huffenberger, K., Lin, Y., Ostriker, J. P., and Trac, H., 2010, Astrophys. J., 709, 920

Sehgal, N., Trac, H., Huffenberger, K., and Bode, P., 2007, Astrophys. J., 664, 149

Seljak, U., 2000, Mon. Not. R. Astron. Soc., 318, 203

Sembach, K. R., Wakker, B. P., Savage, B. D., Richter, P., Meade, M., Shull, J. M., Jenkins, E. B., Sonneborn, G., and Moos, H. W., 2003, Astrophys. J. Supp., 146, 165

Sharp, M. K., Marrone, D. P., Carlstrom, J. E., Culverhouse, T., Greer, C., Hawkins, D., Hennessy, R., Joy, M., Lamb, J. W., Leitch, E. M., Loh, M., Miller, A., Mroczkowski, T., Muchovej, S., Pryke, C., and Woody, D., 2009, arXiv:0901.4342

Shaw, L. D., Holder, G. P., and Bode, P., 2008, Astrophys. J., 686, 206

Sheth, R. K., Mo, H. J., and Tormen, G., 2001, Mon. Not. R. Astron. Soc., 323, 1

Sheth, R. K. and Tormen, G., 1999, Mon. Not. R. Astron. Soc., 308, 119

Sievers, J. L., Mason, B. S., Weintraub, L., Achermann, C., Altamirano, P., Bond, J. R., Bronfman, L., Bustos, R., Contaldi, C., Dickinson, C., Jones, M. E., May, J., Myers, S. T., Oyarce, N., Padin, S., Pearson, T. J., Pospieszalski, M., Readhead, A. C. S., Reeves, R., Shepherd, M. C., Taylor, A. C., and Torres, S., 2009, arXiv:0901.4540

Smoot, G. F., Bennett, C. L., Kogut, A., Wright, E. L., Aymon, J., Boggess, N. W., Cheng, E. S., de Amici, G., Gulkis, S., Hauser, M. G., Hinshaw, G., Jackson, P. D., Janssen, M., Kaita, E., Kelsall, T., Keegstra, P., Lineweaver, C., Loewenstein, K., Lubin, P., Mather, J., Meyer, S. S., Moseley, S. H., Murdock, T., Rokke, L., Silverberg, R. F., Tenorio, L., Weiss, R., and Wilkinson, D. T., 1992, Astrophys. J. Lett., 396, L1

Spergel, D. N., Bean, R., Doré, O., Nolta, M. R., Bennett, C. L., Dunkley, J., Hinshaw, G., Jarosik, N., Komatsu, E., Page, L., Peiris, H. V., Verde, L., Halpern, M., Hill, R. S., Kogut, A., Limon, M., Meyer, S. S., Odegard, N., Tucker, G. S., Weiland, J. L., Wollack, E., and Wright, E. L., 2007, Astrophys. J. Supp., 170, 377

Staniszewski, Z., Ade, P. A. R., Aird, K. A., Benson, B. A., Bleem, L. E., Carlstrom, J. E., Chang, C. L., Cho, H., Crawford, T. M., Crites, A. T., de Haan, T., Dobbs, M. A., Halverson, N. W., Holder, G. P., Holzapfel, W. L., Hrubes, J. D., Joy, M., Keisler, R., Lanting, T. M., Lee, A. T., Leitch, E. M., Loehr, A., Lueker, M., McMahon, J. J., Mehl, J., Meyer, S. S., Mohr, J. J., Montroy, T. E., Ngeow, C., Padin, S., Plagge, T., Pryke, C., Reichardt, C. L., Ruhl, J. E., Schaffer, K. K., Shaw, L., Shirokoff, E., Spieler, H. G., Stalder, B., Stark, A. A., Vanderlinde, K., Vieira, J. D., Zahn, O., and Zenteno, A., 2009, Astrophys. J., 701, 32

Steigman, G., 2007, Annual Review of Nuclear and Particle Science, 57, 463

Stolyarov, V., Hobson, M. P., Ashdown, M. A. J., and Lasenby, A. N., 2002, Mon. Not. R. Astron. Soc., 336, 97

Sun, M., Voit, G. M., Donahue, M., Jones, C., Forman, W., and Vikhlinin, A., 2009, Astrophys. J., 693, 1142

Sunyaev, R. A. and Zeldovich, Y. B., 1970, Astrophys. Space Sci., 7, 3

Sunyaev, R. A. and Zeldovich, Y. B., 1972, Comments on Astrophysics and Space Physics, 4, 173

Sutton, D., Johnson, B. R., Brown, M. L., Cabella, P., Ferreira, P. G., and Smith, K. M., 2009, Mon. Not. R. Astron. Soc., 393, 894

Swetz, D. S., Ade, P. A. R., Allen, C., Amiri, M., Appel, J. W., Battistelli, E. S., Burger, B., Chervenak, J. A., Dahlen, A. J., Das, S., Denny, S., Devlin, M. J., Dicker, S. R., Doriese, W. B., Dünner, R., Essinger-Hileman, T., Fisher, R. P., Fowler, J. W., Gao, X., Hajian, A., Halpern, M., Hargrave, P. C., Hasselfield, M., Hilton, G. C., Hincks, A. D., Irwin, K. D., Jarosik, N., Kaul, M., Klein, J., Knotek, S., Lau, J. M., Limon, M., Lupton, R. H., Marriage, T. A., Martocci, K. L., Mauskopf, P., Moseley, S. H., Netterfield, C. B., Niemack, M. D., Nolta, M. R., Page, L., Parker, L. P., Reid, B. A., Reintsema, C. D., Sederberg, A. J., Sehgal, N., Sievers, J. L., Spergel, D. N., Staggs, S. T., Stryzak, O. R., Switzer, E. R., Thornton, R. J., Tucker, C., Wollack, E. J., and Zhao, Y., 2008, in Society of Photo-Optical Instrumentation Engineers (SPIE) Conference Series, vol. 7020 of *Society of Photo-Optical Instrumentation Engineers (SPIE) Conference Series*

Switzer, E. R., Allen, C., Amiri, M., Appel, J. W., Battistelli, E. S., Burger, B., Chervenak, J. A., Dahlen, A. J., Das, S., Devlin, M. J., Dicker, S. R., Doriese, W. B., Dünner, R., Essinger-Hileman, T., Gao, X., Halpern, M., Hasselfield, M., Hilton, G. C., Hincks, A. D., Irwin, K. D., Knotek, S., Fisher, R. P., Fowler, J. W., Jarosik, N., Kaul, M., Klein, J., Lau, J. M., Limon, M., Lupton, R. H., Marriage, T. A., Martocci, K. L., Moseley, S. H., Netterfield, C. B., Niemack, M. D., Nolta, M. R., Page, L., Parker, L. P., Reid, B. A., Reintsema, C. D., Sederberg, A. J., Sievers, J. L., Spergel, D. N., Staggs, S. T., Stryzak, O. R., Swetz, D. S., Thornton, R. J., Wollack, E. J., and Zhao, Y., 2008, in Society of Photo-Optical Instrumentation Engineers (SPIE) Conference Series, vol. 7019 of *Society of Photo-Optical Instrumentation Engineers (SPIE) Conference Series*

Tago, E., Einasto, J., Saar, E., Einasto, M., Suhhonenko, I., Jõeveer, M., Vennik, J., Heinämäki, P., and Tucker, D. L., 2006, Astronomische Nachrichten, 327, 365

Takahashi, H., Okada, Y., Kokubun, M., and Makishima, K., 2001, Publications of the ASJ, 53, 875

Taylor, J. E., Moodley, K., and Diego, J. M., 2003, Mon. Not. R. Astron. Soc., 345, 1127

Tegmark, M., 1997, Astrophys. J. Lett., 480, L87+

Tegmark, M. and Efstathiou, G., 1996, Mon. Not. R. Astron. Soc., 281, 1297

Tegmark, M., Eisenstein, D. J., Hu, W., and de Oliveira-Costa, A., 2000, Astrophys. J., 530, 133

Tegmark, M., Eisenstein, D. J., Strauss, M. A., Weinberg, D. H., Blanton, M. R., Frieman, J. A., Fukugita, M., Gunn, J. E., Hamilton, A. J. S., Knapp, G. R., Nichol, R. C., Ostriker, J. P., Padmanabhan, N., Percival, W. J., Schlegel, D. J., Schneider, D. P., Scoccimarro, R., Seljak, U., Seo, H., Swanson, M., Szalay, A. S., Vogeley, M. S., Yoo, J., Zehavi, I., Abazajian, K., Anderson, S. F., Annis, J., Bahcall, N. A., Bassett, B., Berlind, A., Brinkmann, J., Budavari, T., Castander, F., Connolly, A., Csabai, I., Doi, M., Finkbeiner, D. P., Gillespie, B., Glazebrook, K., Hennessy, G. S., Hogg, D. W., Ivezić, Ž., Jain, B., Johnston, D., Kent, S., Lamb, D. Q., Lee, B. C., Lin, H., Loveday, J., Lupton, R. H., Munn, J. A., Pan, K., Park, C., Peoples, J., Pier, J. R., Pope, A., Richmond, M., Rockosi, C., Scranton, R., Sheth, R. K., Stebbins, A., Stoughton, C., Szapudi, I., Tucker, D. L., vanden Berk, D. E., Yanny, B., and York, D. G., 2006, Phys. Rev. D, 74, 12, 123507

The Planck Collaboration, 2006, arXiv:astro-ph/0604069

Thornton, R. J., Ade, P. A. R., Allen, C., Amiri, M., Appel, J. W., Battistelli, E. S., Burger, B., Chervenak, J. A., Devlin, M. J., Dicker, S. R., Doriese, W. B., Essinger-Hileman, T., Fisher, R. P., Fowler, J. W., Halpern, M., Hargrave, P. C., Hasselfield, M., Hilton, G. C., Hincks, A. D., Irwin, K. D., Jarosik, N., Kaul, M., Klein, J., Lau, J. M., Limon, M., Marriage, T. A.,

Martocci, K. L., Mauskopf, P., Moseley, S. H., Niemack, M. D., Page, L., Parker, L. P., Reidel, J., Reintsema, C. D., Staggs, S. T., Stryzak, O. R., Swetz, D. S., Switzer, E. R., Tucker, C., Wollack, E. J., and Zhao, Y., 2008, in Society of Photo-Optical Instrumentation Engineers (SPIE) Conference Series, vol. 7020 of *Society of Photo-Optical Instrumentation Engineers (SPIE) Conference Series*

Tinker, J., Kravtsov, A. V., Klypin, A., Abazajian, K., Warren, M., Yepes, G., Gottlöber, S., and Holz, D. E., 2008, Astrophys. J., 688, 709

Treu, T. and Koopmans, L. V. E., 2004, Astrophys. J., 611, 739

Tripp, T. M., Savage, B. D., and Jenkins, E. B., 2000, Astrophys. J. Lett., 534, L1

Tucker, W., Blanco, P., Rappoport, S., David, L., Fabricant, D., Falco, E. E., Forman, W., Dressler, A., and Ramella, M., 1998, Astrophys. J. Lett., 496, L5+

Tucker, W. H., Tananbaum, H., and Remillard, R. A., 1995, Astrophys. J., 444, 532

Tumlinson, J., Shull, J. M., Giroux, M. L., and Stocke, J. T., 2005, Astrophys. J., 620, 95

Umetsu, K., Birkinshaw, M., Liu, G., Wu, J., Medezinski, E., Broadhurst, T., Lemze, D., Zitrin, A., Ho, P. T. P., Huang, C., Koch, P. M., Liao, Y., Lin, K., Molnar, S. M., Nishioka, H., Wang, F., Altamirano, P., Chang, C., Chang, S., Chang, S., Chen, M., Han, C., Huang, Y., Hwang, Y., Jiang, H., Kesteven, M., Kubo, D. Y., Li, C., Martin-Cocher, P., Oshiro, P., Raffin, P., Wei, T., and Wilson, W., 2009, Astrophys. J., 694, 1643

Vale, C. and White, M., 2006, New Astronomy, 11, 207

Vanderlinde, K., Crawford, T. M., de Haan, T., Dudley, J. P., Shaw, L., Ade, P. A. R., Aird, K. A., Benson, B. A., Bleem, L. E., Brodwin, M., Carlstrom, J. E., Chang, C. L., Crites, A. T., Desai, S., Dobbs, M. A., Foley, R. J., George, E. M., Gladders, M. D., Hall, N. R., Halverson, N. W., High, F. W., Holder, G. P., Holzapfel, W. L., Hrubes, J. D., Joy, M., Keisler, R., Knox, L., Lee, A. T., Leitch, E. M., Loehr, A., Lueker, M., Marrone, D. P., McMahon, J. J., Mehl, J., Meyer,

S. S., Mohr, J. J., Montroy, T. E., Ngeow, C., Padin, S., Plagge, T., Pryke, C., Reichardt, C. L., Rest, A., Ruel, J., Ruhl, J. E., Schaffer, K. K., Shirokoff, E., Song, J., Spieler, H. G., Stalder, B., Staniszewski, Z., Stark, A. A., Stubbs, C. W., van Engelen, A., Vieira, J. D., Williamson, R., Yang, Y., Zahn, O., and Zenteno, A., 2010, arXiv:1003.0003

Vielva, P., Martínez-González, E., Cayón, L., Diego, J. M., Sanz, J. L., and Toffolatti, L., 2001, Mon. Not. R. Astron. Soc., 326, 181

Vikhlinin, A., Kravtsov, A., Forman, W., Jones, C., Markevitch, M., Murray, S. S., and Van Speybroeck, L., 2006, Astrophys. J., 640, 691

Voges, W., Aschenbach, B., Boller, T., Bräuninger, H., Briel, U., Burkert, W., Dennerl, K., Englhauser, J., Gruber, R., Haberl, F., Hartner, G., Hasinger, G., Kürster, M., Pfeffermann, E., Pietsch, W., Predehl, P., Rosso, C., Schmitt, J. H. M. M., Trümper, J., and Zimmermann, H. U., 1999, Astron. Astrophys., 349, 389

Voit, G. M., 2005, Reviews of Modern Physics, 77, 207

Voit, G. M., Balogh, M. L., Bower, R. G., Lacey, C. G., and Bryan, G. L., 2003, Astrophys. J., 593, 272

Voit, G. M., Bryan, G. L., Balogh, M. L., and Bower, R. G., 2002, Astrophys. J., 576, 601

Wang, L. and Steinhardt, P. J., 1998, Astrophys. J., 508, 483

Weinberg, N. N. and Kamionkowski, M., 2003, Mon. Not. R. Astron. Soc., 341, 251

Werner, N., Churazov, E., Finoguenov, A., Markevitch, M., Burenin, R., Kaastra, J. S., and Böhringer, H., 2007, Astron. Astrophys., 474, 707

White, M., 2001, Astron. Astrophys., 367, 27

White, M. and Majumdar, S., 2004, Astrophys. J., 602, 565

White, M. and Srednicki, M., 1995, Astrophys. J., 443, 6

Wood-Vasey, W. M., Miknaitis, G., Stubbs, C. W., Jha, S., Riess, A. G., Garnavich, P. M., Kirshner, R. P., Aguilera, C., Becker, A. C., Blackman, J. W., Blondin, S., Challis, P., Clocchiatti, A., Conley, A., Covarrubias, R., Davis, T. M., Filippenko, A. V., Foley, R. J., Garg, A., Hicken, M., Krisciunas, K., Leibundgut, B., Li, W., Matheson, T., Miceli, A., Narayan, G., Pignata, G., Prieto, J. L., Rest, A., Salvo, M. E., Schmidt, B. P., Smith, R. C., Sollerman, J., Spyromilio, J., Tonry, J. L., Suntzeff, N. B., and Zenteno, A., 2007, Astrophys. J., 666, 694

Wright, E. L., 1998, Astrophys. J., 496, 1

Yang, X., Mo, H. J., van den Bosch, F. C., Pasquali, A., Li, C., and Barden, M., 2007, Astrophys. J., 671, 153

Younger, J. D. and Bryan, G. L., 2007, Astrophys. J., 666, 647

Zhang, Y., Böhringer, H., Finoguenov, A., Ikebe, Y., Matsushita, K., Schuecker, P., Guzzo, L., and Collins, C. A., 2006, Astron. Astrophys., 456, 55

Zhang, Y., Finoguenov, A., Böhringer, H., Kneib, J., Smith, G. P., Kneissl, R., Okabe, N., and Dahle, H., 2008, Astron. Astrophys., 482, 451

Zhao, Y., Allen, C., Amiri, M., Appel, J. W., Battistelli, E. S., Burger, B., Chervenak, J. A., Dahlen, A. J., Denny, S., Devlin, M. J., Dicker, S. R., Doriese, W. B., Dünner, R., Essinger-Hileman, T., Fisher, R. P., Fowler, J. W., Halpern, M., Hilton, G. C., Hincks, A. D., Irwin, K. D., Jarosik, N., Klein, J., Lau, J. M., Marriage, T. A., Martocci, K. L., Moseley, S. H., Niemack, M. D., Page, L., Parker, L. P., Sederberg, A., Staggs, S. T., Stryzak, O. R., Swetz, D. S., Switzer, E. R., Thornton, R. J., and Wollack, E. J., 2008, in Society of Photo-Optical Instrumentation Engineers (SPIE) Conference Series, vol. 7020 of *Society of Photo-Optical Instrumentation Engineers (SPIE) Conference Series*

Zwicky, F., 1933, Helvetica Physica Acta, 6, 110